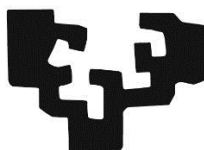


eman ta zabal zazu



Universidad del País Vasco Euskal Herriko Unibertsitatea

Departamento de Química Orgánica I / Kimika Organikoa I Saila

Facultad de Química / Kimika Fakultatea

**Design, chemical synthesis and biological evaluation of
new synthetic conjugates of ursodeoxycholic acid for
the inhibition of cystogenesis in experimental models
of polycystic liver disease**

Tesis Doctoral / Doktorego Tesia

Francisco Javier Caballero Camino

Directores / Zuzendariak:

Fernando P. Cossío Mora, Jesús María Bañales Asurmendi

Programa de Doctorado en Química Sintética e Industrial / Kimika Sintetiko
eta Industrialak Doktorego Programa

Donostia-San Sebastian 2019

INDEX

INTRODUCTION	
I.1 Polycystic liver diseases (PLDs)	1
I.1.1 Genetics and molecular mechanisms of PLDs	2
I.2 Ursodeoxycholic acid (UDCA)	5
I.3 Histone deacetylases (HDACs)	10
I.3.1 HDACs in pathobiology	13
I.3.2 Inside HDACs catalytic domain: general model of HDAC inhibition	15
I.3.4 HDACis: from the pharmacophore model to their particular structures	17
<i>I.3.4.a Hydroxamic acids</i>	17
<i>I.3.4.b Benzamides</i>	19
<i>I.3.4.c Short chain fatty acids (SCFAs)</i>	21
<i>I.3.4.d Macrocycles</i>	21
<i>I.3.4.e Hybrid HDACis</i>	22
I.3.5 HDAC6	24
I.4 The primary cilium	27
I.4.1 The primary cilium in cholangiocytes.	29
I.4.2 HDAC6 and primary cilium in cholangiopathies and polycystic diseases	29
<i>I.4.2.a Polycystic diseases</i>	30
<i>I.4.2.b Cholangiocarcinoma (CCA)</i>	32
HYPOTHESIS	36
OBJECTIVES	38

RESULTS

R.1 Design and chemical synthesis of new synthetic conjugates of UDCA	42
R.2 General methods for the synthesis of UDCA-HDAC6is	44
R.2.a.1) Coupling of UDCA with spacers	44
R.2.a.2) Synthesis of hydroxamic acids	45
R.2.b.1) Hydrolysis of methyl ester 3	46
R.2.b.2) Synthesis of tert-butyl (3-amino-[1,1'-biphenyl] 4-yl) carbamate: D	47
R.2.b.3) Coupling of benzamide chelating groups	49
R.2.b.4) Deprotection of the tert-butoxycarbamate	50
R.2.c.1) Coupling of the spacers	51
R.2.c.2) Synthesis of hydroxamic acids	52
R.3 UDCA-HDAC6is exhibit binding affinities for HDAC6 CD1 and C2 <i>in silico</i> and UDCA is determinant in these interactions	53
R.4 UDCA actively contributes to the selective HDAC6 inhibitory activity of UDCA-HDAC6is	61
R.5 Chemical and structural factors that determine inhibitory activity and selectivity of UDCA-HDAC6is	66
R.6 Potency and selectivity, pharmacokinetic properties and synthetic cost make UDCA-HDAC6 #1 the best candidate for potential clinical translation	74
R.7 UDCA-HDAC6i #1 halts hepatorenal cystogenesis in PCK rats	77

R.8 UDCA-HDAC6i #1 modulates the bile acid pool and increases the levels of unconjugated UDCA in PCK rats	82
R.9 UDCA-HDAC6i #1 halts liver cystogenesis <i>in vivo</i>, and this event is linked to the restoration of the cholangiocyte primary cilium length and inhibition of cell proliferation	85
R.10 Hepatotropic properties of UDCA-HDAC6i #1	89
DISCUSSION	94
CONCLUSIONS	107
MATERIALS AND METHODS	
M.1 Docking	110
M.2 Homology modeling	110
M.3 Chemical synthesis and characterization	111
M.4 HDAC activity assays	149
M.5 Treatment of PCK rats with HDAC6i-UDCA #1	151
M.6 Liver histological analysis	151
M.6.1 Tissue slides hydration	151
M.6.2 Haematoxylin and eosin (H&E) staining	152
M.6.3 CK19 Immunohistochemistry	152
M.7 Bile acid measurement	153
M.8 Cell lines and culture conditions	153
M.9 Experimental overexpression of human transporters in cells	154

M.10 Transport assays	155
M.11 Reverse transcription quantitative polymerase chain reaction (RT-qPCR)	156
M.11.1 RNA extraction	156
M.11.2 Reverse transcription	156
M.11.3 Quantitative real time polymerase chain reaction (qPCR)	157
M.12 Immunoblotting	157
M.12.1 Protein extraction	157
M.12.2 Protein quantification	158
M.12.3 Protein expression or post-translational modification analysis	158
M.13 Ciliary length analysis	159
M.14 Cell proliferation	160
M.15 3D culturing	160
M.16 Statistical analysis	161
SUMMARY IN SPANISH (RESUMEN EN CASTELLANO)	
Introducción	165
Hipótesis	168
Objetivos	169
Resultados y discusión	170
Conclusiones	177
BIBLIOGRAPHY	183

ABBREVIATIONS

3-D , 3-dimensional	CDCA , chenodeoxycholic acid
AMC , 7-amino-4-methylcoumarin	CK19 , cytokeratin 19
a/bMCA , α/β murocholic acid	DAB , 3,3-diaminobenzidine
ADPKD , autosomal dominant polycystic kidney disease	DMF , N,N-dimethylformamide
ADPLD , autosomal dominant polycystic liver disease	DMEM , Dulbecco's modified eagle Medium
ALG8 , asparagine-linked glycosylation protein 8 homolog	EGF , epidermal growth factor
ARPKD , autosomal recessive polycystic kidney disease	ERK , extracellular signal-regulated kinase
ASBT , apical sodium-dependent bile salt transporter	ESI , electrospray ionization
BA , bile acid	FBS , fetal bovine serum
BUZ , Zn finger ubiquitin binding domain	GANAB , neutral alpha-glucosidase AB
CA , cholic acid	GAPDH , glyceraldehyde 3-phosphate dehydrogenase
cAMP , cyclic 3',5'-adenosine monophosphate	GCA , glycocholic acid
CCA , cholangiocarcinoma	GQDCA , glycochenodeoxycholic acid
CD , catalytic domain	GUDCA , glyoursodeoxycholic aci
	H3K9 , lysine 9 of histone 3

H&E , haematoxylin and eosin	mRNA , messenger ribonucleic acid
HDAC , histone deacetylase	NCTP , sodium-taurocholate cotransporting polypeptide
HDAC6 , histone deacetylase 6	NES , nuclear export signal
HDACi , histone deacetylase inhibitor	OATP , organic anion transporting polypeptide
HDAC6is , histone deacetylase 6 inhibitors;	OCT , organic cation transporter
HPLC-MS/MS , high performance liquid chromatography-tandem mass spectrometry	ORF , open reading frame
HyoDCA , hyodeoxycholic acid	PBC , primary biliary cholangitis
Hsp90 , heat shock protein 90	PBS , phosphate buffered saline
IC50 , Half-maximal inhibitory concentration	PC-1 , polycystin-1
iCa²⁺ , intracellular calcium	PDB , protein data bank
K40 , lysine 40	PFA , paraformaldehyde
LCA , lithocholic acid	PKD , polycystic kidney disease
LRP5 , low-density lipoprotein receptor-related protein 5	PKD1 , polycystic kidney disease
MRM , multiple reaction monitoring	PKD2 , polycystic kidney disease 2
	PKHD1 , polycystic kidney and hepatic disease 1
	PLD , polycystic liver disease

PRKCSH, protein kinase C

substrate 80K-H

PSC, primary sclerosing cholangitis

qPCR, quantitative real time

polymerase chain reaction

RPL22, 60S ribosomal protein L22

RT-qPCR, reverse transcription

quantitative polymerase chain

reaction

SCFA, short chain fatty acid

SD, sprague dawley

SDS, sodium dodecyl sulfate

SEC61B, protein transport protein

Sec61 subunit beta

SEC63, translocation protein SEC63

homolog

SIRT, sirtuin

SLCA, sulpholithocholic

Ta/bMCA, tauro α/β murocholic acid

TBTU, 2-(1H-Benzotriazole-1-yl)-

1,1,3,3-tetramethyluronium

tetrafluoroborate

TCA, taurocholic acid; TQDCA,

taurochenodeoxycholic acid

TLV, total liver volume

TQDCA, taurochenodeoxycholic

acid

TUDCA, tauroursodeoxycholic acid

UDCA, ursodeoxycholic acid

UDCA-HDAC6i, synthetic conjugate

of ursodeoxycholic acid

VPA, valproic acid

WT, wild-type

INTRODUCTION

I.1 Polycystic liver diseases (PLDs)

Polycystic liver diseases (PLDs) comprise a heterogeneous group of hereditary genetic disorders characterized by bile duct dilatation and development of multiple fluid-filled biliary cysts.¹ Although, it has been classically established that the minimum number of liver cysts to define PLD is 20, recent consensus reached by the international PLD Registry steering committee has revised this definition to consider hepatic disorders comprising more than 10 liver cysts.² Some of the currently known risk factors for disease progression are age, female sex, pregnancies and use of estrogens.^{3,4} Patients with PLD frequently refer to symptoms such as abdominal distention, pain and early satiety and commonly display hepatic manifestations such as hepatomegaly, biliary and portal obstruction and cyst infection or rupture. Autosomal dominant polycystic liver disease (ADPLD, ~1:100,000 prevalence) is characterized by the development of cysts exclusively in the liver, which are the main cause of morbidity, whereas autosomal dominant polycystic kidney disease (ADPKD, ~1:1,000 prevalence) and autosomal recessive polycystic kidney disease (ARPKD, ~1:20,000 prevalence) also present renal cystogenesis, potentially leading to hypertension and ultimately end-stage renal disease.² Importantly, a recent international cross-sectional study revealed a significant difference in the liver phenotype between patients with ADPLD *versus* ADPKD, being more frequent to observe dominant cysts in the patients suffering only from hepatic manifestations, and observing differences in the most frequently applied clinical strategies for each group.³

Current therapies for PLDs include surgical procedures such as aspiration-sclerotherapy, fenestration, segmental hepatic resection and trans-catheter arterial embolization. It is important to note that, even in the cases of severe PLD,

liver function usually remains essentially preserved, and disease does not evolve to liver failure or death.^{2,3} For these reasons, and due to the short-term and modest beneficial effects of these surgical interventions together with the potential therapy-related complications, these procedures are only indicated in highly symptomatic patients in which symptoms severely affect quality of life.² In addition to the mentioned surgical procedures, pharmacological treatment with somatostatin analogs has been applied to the treatment of PLDs.⁵ Somatostatin analogs such as octreotide or lanreotide base their therapeutic effects on their ability to modulate the increased levels of intracellular cyclic adenosine monophosphate (cAMP) found in cystic cholangiocytes that lead to increased proliferative activity and altered fluid secretion on these cells via PKA, EPAC and ERK1/2/MEK.⁶ These pharmacological treatments improve quality of life of symptomatic PLD patients by significantly reducing total liver volume (TLV) of these patients.⁵ However, the modest effect, high costs and related side effects of these therapies restrict their use to only particular cases.⁷ Therefore, providing the mild therapeutic outcome of current surgical and pharmacological approaches, liver transplantation remains as the only curative option. However, this last alternative turns into a very limited option due to the non-lethal nature of the disease and accompanied by the common issues linked to organ transplantation.⁸

I.1.1 Genetics and molecular mechanisms of PLDs

As mentioned above, PLDs constitute a group of genetic disorders that share some common features mainly in terms of clinical manifestations, being liver cystogenesis the central event for all PLDs. In this regard, liver cysts are thought to be originated either from embryological defects during ductal plate formation

and/or as a result of a somatic second hit mutations during adulthood. These mutations can result in loss of heterozygosity in particular disease-related genes, leading to deficient glycoproteins assembly and control and, ultimately, decreased polycystin-1 (PC-1) expression.^{2,9-11}

Although liver cystogenesis is a common event in all PLDs, these can differ in other features such as the severity of the hepatic manifestations and symptoms or the presence or absence of extrahepatic manifestations. Importantly, these differences seem to be very closely related to the genetic background triggering disease.^{12,13} In this regard, exhaustive research in the last decades, and in particular increasing efforts made in the last 20 years have allowed a better understanding of the pathophysiology and the molecular mechanisms involved in the development and progression of PLDs.

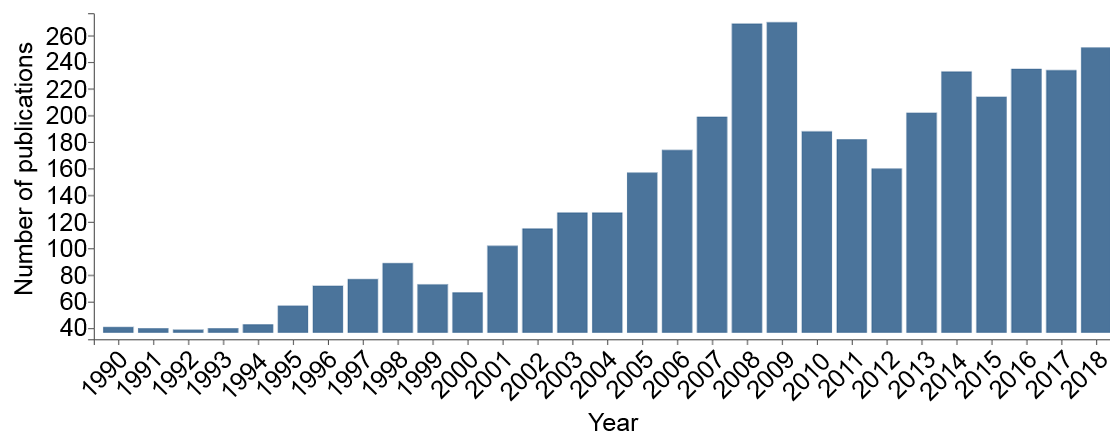


Figure 11. Number of publications between years 1990 and 2018 reported by Web of Science for the search topic "polycystic liver disease". (Accessed database at <https://apps.webofknowledge.com> on 06/09/2019).

To date germline mutations in nine different genes have been described to be related to development and progression of PLDs (Table I1).^{9,14}

Gene	Encoded protein	Cellular localization	Function	Associated PLD
<i>PRKCSH</i>	Glucosidase II subunit β	ER	N-glycan metabolism	ADPLD
<i>GANAB</i>	Glucosidase II subunit α	ER	N-glycan metabolism	ADPLD and ADPKD
<i>SEC63</i>	Translocation protein SEC63 homolog	ER	Protein translocation	ADPLD
<i>SEC61B</i>	Protein transport protein Sec61 subunit β	ER	Protein translocation	ADPLD
<i>ALG8</i>	Asparagine-linked glycosylation protein 8 homolog	ER	Protein glycosylation	ADPLD
<i>LRP5</i>	Low-density lipoprotein receptor-related protein 5	Plasma membrane	Receptor in canonical Wnt pathway	ADPLD and ADPKD
<i>PKD1</i>	Polycystin-1	Primary cilium Plasma membrane Cell junctions	Mechanochemical sensor linked to calcium signaling and tubulogenesis	ADPKD
<i>PKD2</i>	Polycystin-2	Primary cilium ER	Nonselective calcium channel	ADPKD
<i>PKHD1</i>	Fibrocystin or polyductin	Primary cilium	Receptor linked to tubulogenesis and biliary differentiation	ADPLD and ADPKD

Table I1. Genes for which somatic mutations have been described to be related in development and progression of PLDs. Modified from refs. 9,14

Mutations on these genes produce several functional alterations in cholangiocytes that are directly associated to increased levels of cAMP and decreased intracellular calcium (iCa^{2+}) concentration.¹ These alterations include hyperproliferation,^{6,15} hypersecretion,¹⁶ increased matrix metalloproteolytic activity,¹⁷ changes in microRNAs expression patterns¹⁸ and morphological and functional alterations of the primary cilium,¹⁹ and are the responsible for the pathobiology of PLDs. Thus, the increasing knowledge on the pathophysiology of PLDs is proposing new potential targets for therapy. In particular, due to its hepatoprotective and choleric properties, together with its strong capacity to regulate iCa^{2+} , ursodeoxycholic acid (UDCA) has been tested as a potential pharmacological approach for the treatment of PLDs. In this regard, treatment

with this endogenous bile acid (BA) has been shown to produce significant inhibition of hepatobiliary cystogenesis, providing substantial beneficial effects both, in experimental models of PLD (PCK rats) and a subgroup of patients with ADPKD (Phase II clinical trial).^{15,20} On the other hand, histone deacetylase 6 (HDAC6) has been shown to be upregulated in cystic cholangiocytes.²¹ This enzyme catalyzes deacetylation of α -tubulin, an important component of cholangiocyte primary cilium, and its enzymatic activity has been directly linked to ciliary disassembly.²² Therefore, and providing the importance of primary cilium in cholangiocyte pathobiology, pharmacological HDAC6 selective inhibition has also been tested as a potential therapeutic strategy for the treatment of PLDs.^{21,23}

I.2 Ursodeoxycholic acid (UDCA)

BAs are synthesized in the liver by hydroxylation and modification of cholesterol to yield a number of different amphipathic chemical entities that contribute to the emulsification, absorption and transport of nutrients, fats and vitamins from the gastrointestinal tract.²⁴ The multistep process of BA synthesis within hepatocytes involves participation of different enzymes located to the endoplasmic reticulum, mitochondria, cytosol and peroxisomes.²⁵

UDCA is a choleric and hepatoprotective BA that possesses antioxidant, anti-inflammatory and cytoprotective properties.²⁶ This endogenous BA has been extensively applied in the clinic for the treatment of hepatobiliary cholestatic disorders. Nowadays, UDCA is the first-line pharmacological treatment in patients with primary biliary cholangitis (PBC) with abnormal serum liver tests.²⁷

Importantly, unlike the major portion of bile acids within human bile, UDCA is synthesized in the gastrointestinal tract by bacterial metabolism.²⁸

From a chemical perspective, UDCA is a C₂₄ BA with a cyclopentane-perhydro[a]phenanthrene scaffold carrying 3 α and 7 β hydroxylations and a C₄ side chain methylated in C-20 and ended on a carboxylic acid (Figure I2C).

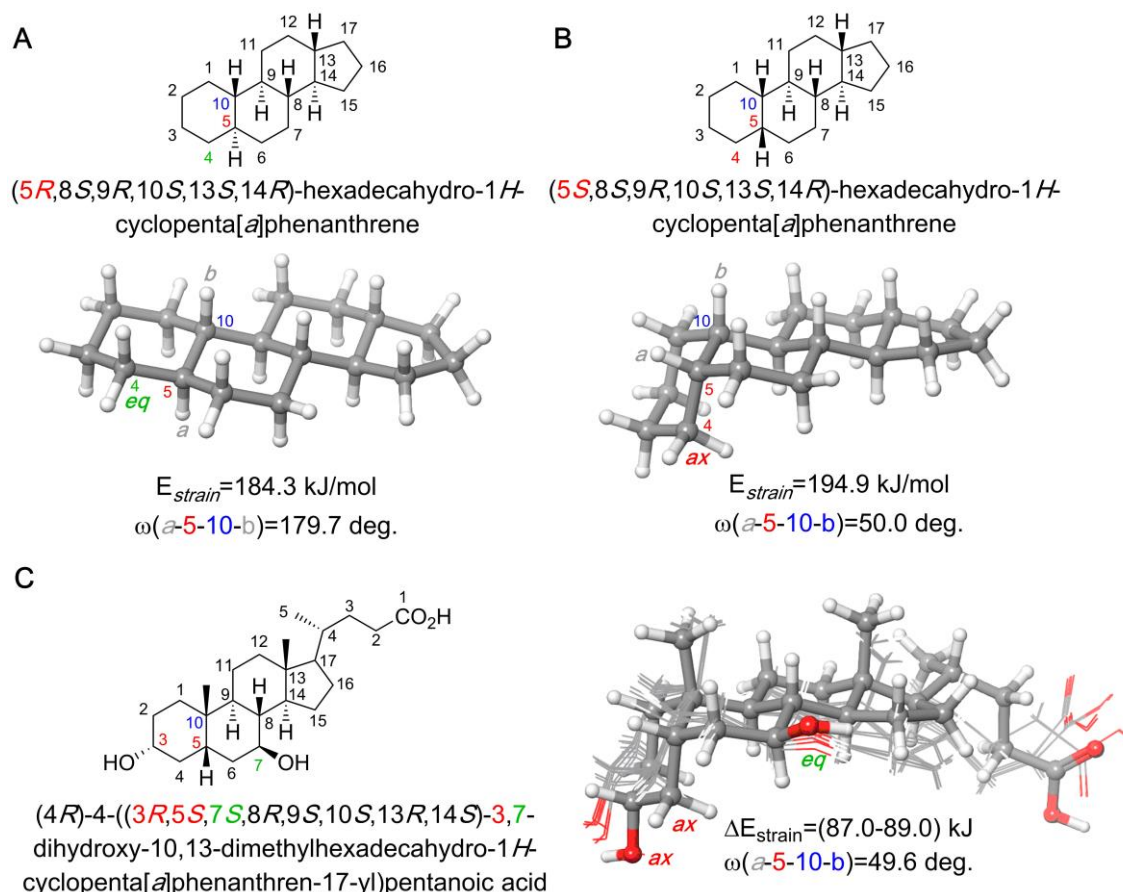


Figure I2. Fully optimized and strain energies (OPLS_2005 force field²⁹ in water) of (A) (5*R*)-cyclopentanepерhydro[*a*]phenanthrene (cholestane scaffold), (B) (5*S*)-cyclopentanepерhydro[*a*]phenanthrene (coprostanе scaffold), and (C) ursodeoxycholic acid. The significant axial and equatorial positions are highlighted in red and green, respectively. The ten most stable conformations in UDCA within 3 kJ/mol are also represented in (C).

It is important to note that the structure of the steroidal scaffold of cyclopentanepерhydro[*a*]phenanthrene presents two configurations in the

junction of rings A and B. If these two cyclohexane rings are fused in *trans* (Figure I2A), the C4 carbon atom occupies an equatorial position thus presenting an all-trans geometry for the whole tetracyclic system. This skeleton can be found in the cholestane series of steroids. When the (5,10) fusion results in a *cis* configuration for the A-B rings, the chair conformation of the perhydrophenantrene moiety generates an axial disposition for the resulting structure (Figure I2B). This gives rise to the coprostane series of steroids, which is thermodynamically *ca.* 10 kJ/mol less stable than the cholestane series (see Figure I2A and B). As far as the UDCA structure is concerned, inspection of its stereochemistry shows that it belongs to the coprostane series. In addition, the two hydroxy groups at C-3 and C-7 occupy axial and equatorial positions, respectively (Figure I2C). This results in thermodynamically less stable geometries. Importantly, although the coprostane scaffold is quite rigid, the pentanoic acid chain is flexible (Figure I2C). This allows to hypothesize that UDCA conjugates will combine the rigidity of the coprostane polycyclic moiety with the conformational flexibility of the lateral chain, thus resulting in a good trade-off between preorganization and adaptative character, as we will see later.

Similar to the rest of BAs, UDCA displays poor water solubility in its protonated form. Actually, it precipitates in water at a pH value of 7.0-7.1 and shows a solubility in this solvent of 53 μM .³⁰ Its pK_a value at 20°C, 10 mM in water, is 5.24.³⁰ However, the presence of the two hydroxy groups as well as the β position of the C-7 hydroxylation provide UDCA with higher hydrophilicity when compared to mono-hydroxylated BAs like lithocholic acid (LCA) or 7 α -hydroxylated BAs like cholic acid (CA) or chenodeoxycholic acid (CDCA).^{31,32} Upon oral administration of pharmacological doses (10-15 mg/ kg day) of its

unconjugated protonated form, UDCA is solubilized in the proximal jejunum by formation of mixed micelles with endogenous bile acids, and is mostly absorbed in the small intestine by dissolution-limited passive nonionic diffusion.³³ Therefore, UDCA absorption is directly influenced by endogenous BA concentration in the intestinal lumen, being enhanced during meals and substantially decreased in cholestatic patients.³⁴ After absorption, UDCA reaches the liver through the portal circulation where is actively uptaken by hepatocytes by means of specific bile acid transporters sodium-taurocholate cotransporting polypeptide (NTCP) and organic anion transporting polypeptides (OATPs).^{31,35} Once inside hepatocytes, UDCA is effectively amidated to its glycine (preferentially in humans) and taurine (preferentially in rats) conjugates and actively secreted into bile.³³ After reaching the gastrointestinal tract, UDCA conjugates are reabsorbed by enterocytes in the distant ileum through the apical sodium-dependent bile salt transporter (ASBT) and are re-circularized into the liver accomplishing an effective enterohepatic circulation.³⁴ Finally, the portion of UDCA and its conjugates that is not absorbed is metabolized by colon microbiota into LCA that is further eliminated via feces.³⁴ This restricted biodistribution circuit is a clear advantage for the therapeutic use of UDCA and its derivatives in hepatobiliary disorders.

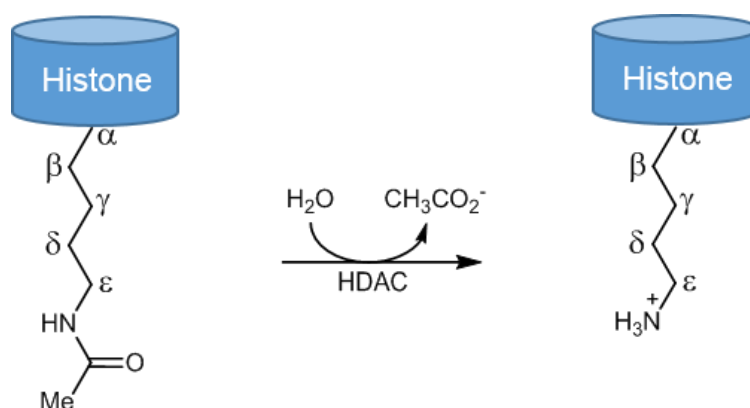
At the cellular level, UDCA and its conjugates are potent signaling molecules able to stimulate iCa^{2+} levels.^{36,37} Importantly, they have been proven to exert significant cytoprotective effect against cytotoxic BAs.²⁶ UDCA and/or its conjugates are able to modulate a number of important cellular processes carried out by cholangiocytes and hepatocytes. These processes include, hepatobiliary

secretion; transcriptional, post-transcriptional and functional regulation of specific transporters; and finally cell survival.^{27,34}

As mentioned before, one of the central events in hepatic cystogenesis is the decreased iCa^{2+} levels of cystic cholangiocytes that lead to hyperproliferation and impaired secretory activity of these cells. Therefore, providing the capacity of UDCA to rise the iCa^{2+} concentration, as well as its safety and tolerability, *Banales JM and co-workers* proposed the administration of UDCA as a potential pharmacological strategy for the treatment of PLDs.¹⁵ In this study, *Munoz-Garrido P. et al* demonstrated that chronic oral administration to PCK rats (animal model of ARPKD) with UDCA reduced hepatic cystogenesis and fibrosis as well as improved their symptomatology (motor behavior). Furthermore, the analysis of the BA profile of PCK rats revealed that UDCA administration decreased the intrahepatic accumulation of toxic BAs, which promote cystogenesis. Based on these results, an International Multicenter Phase II Clinical Trial was conducted to test the potential therapeutic value of UDCA for the treatment of patients with PLD.²⁰ In highly symptomatic patients, administration of UDCA for 6 months did not modified the total liver volume but significantly reduced the liver cystic volume of patients with ADPKD. On the other hand, this effect was not observed in patients with ADPLD. Moreover, UDCA improved the symptomatology and reduced the levels of markers of cholestasis in patients with PLD, and showed promising tendencies on the inhibition of the renal volume in ADPKD patients.

I.3 Histone deacetylases (HDACs)

Histone deacetylases (HDACs) are a family of hydrolase enzymes that catalyze deacetylation of lysine residues located within different histone and non-histone protein substrates (Scheme I1). These enzymes are essential for the correct functioning of a wide number of cellular processes, since they are key modulators of both gene expression and protein activity.^{38,39}



Scheme I1. N-deacetylation of an acetyl lysine residue of a histone catalyzed by HDACs.

Current consensus classification of HDAC family includes a total number of four subclasses (Figure I3). Class III is the most largely differing from the others, being composed by a particular type of HDACs called sirtuins (SIRT1-7) that involve participation of NAD^+ as a cofactor to carry out catalytic activity. On the other hand, the so-called “classical HDACs” gather into classes I, II (divided into IIa and IIb), and IV. Class I comprises HDAC1-3 and 8, while class II is subsequently subdivided into IIa, composed of HDAC4, 5, 7 and 9 and IIb that includes HDAC6 and 10. Finally, HDAC11 is the only member of class IV (Figure I3).⁴⁰

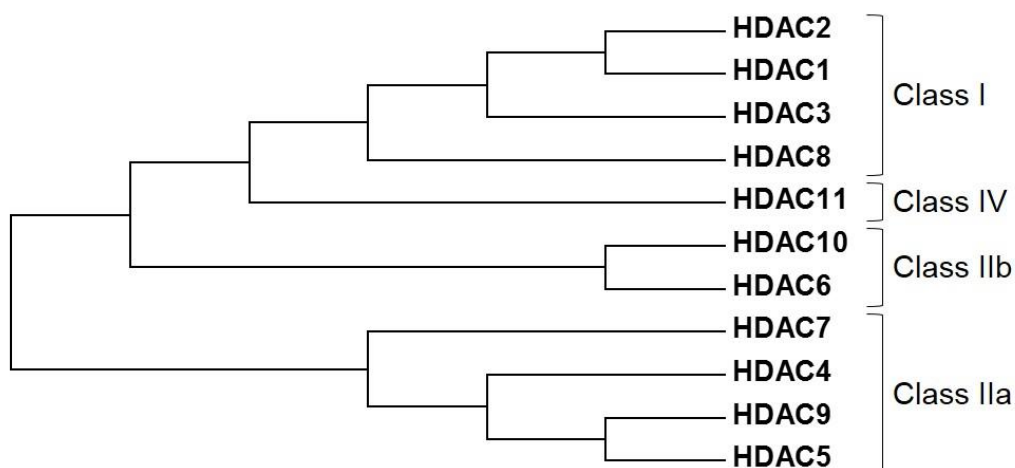


Figure I3. Molecular phylogenetic classification by the Maximum Likelihood method. The evolutionary history was inferred by using the Maximum Likelihood method based on the JTT matrix-based model. Calculations were performed with MEGA6 software.⁴¹

Members of classes I, IIa, IIb and IV contain a Zn(II) cation in their active sites to participate in the catalytic activity. These enzymes show distinct preferential cellular localizations (Table I2), and participate in the modulation of a wide range of physiological processes, such as differentiation, cell cycle regulation, modulation of cytoskeletal dynamics, metabolic processes, autophagy and apoptosis among many others.⁴²⁻⁴⁴

Class	Protein	Localization
I	HDAC1	Nuclear
	HDAC2	Nuclear
	HDAC3	Nuclear
	HDAC8	Nuclear / Cytoplasmic
IIA	HDAC4	Nuclear / Cytoplasmic
	HDAC5	Nuclear / Cytoplasmic
	HDAC7	Nuclear / Cytoplasmic
	HDAC9	Nuclear / Cytoplasmic
IIB	HDAC6	Cytoplasmic
	HDAC10	Cytoplasmic
IV	HDAC11	Nuclear / Cytoplasmic

Table I2. Class arrangement and subcellular localization of Zn(II)-dependent HDACs. Modified from ref. 42

Members of the HDAC family considerably differ in sequence length, from the 347 aminoacid sequence of HDAC11 (Uniprot id: Q96DB2) to the 1,215 residues contained in HDAC6 (Uniprot id: Q9UBN7). However, in spite of the significant differences in terms of substrate preference and subsequent biological function, all members of the mentioned subclasses share highly conserved catalytic domains (CDs) (Figure I4).

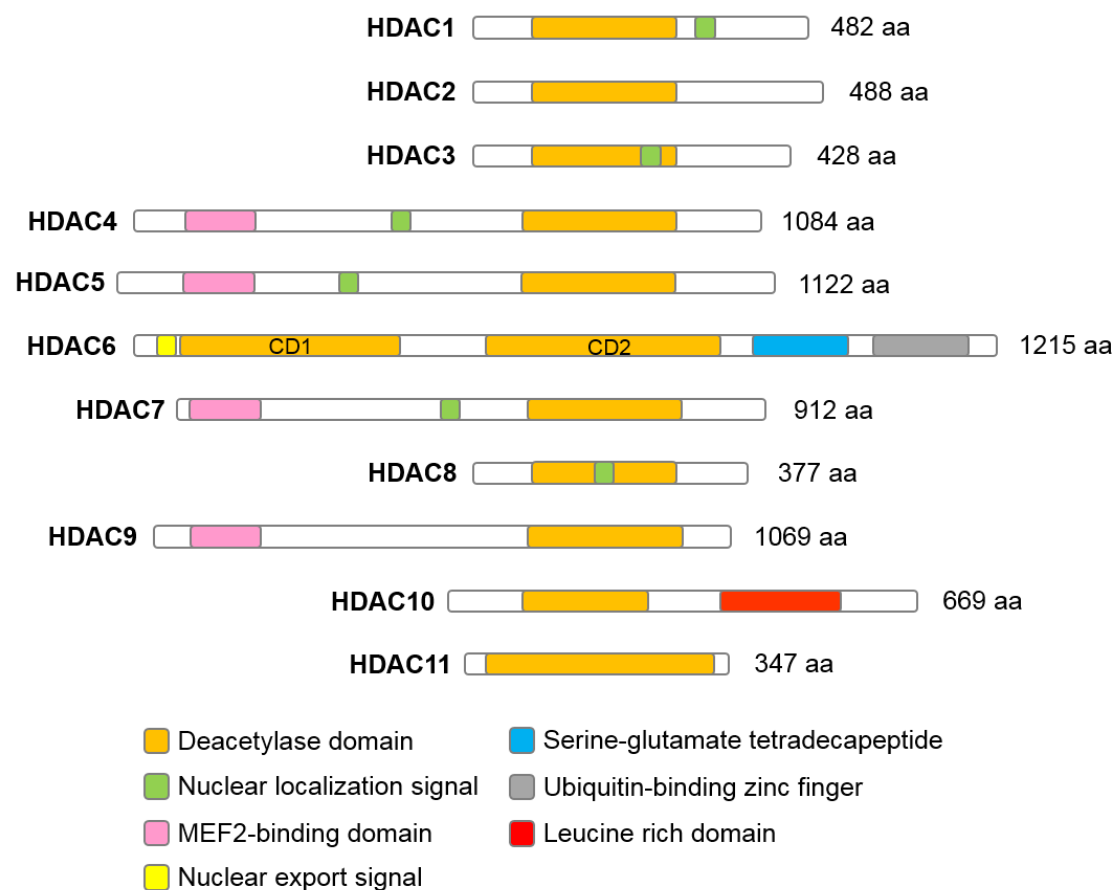


Figure I4. Schematic representation of the domains organization and amino acid sequence length of HDACs 1-11. In HDAC6, CD1 and CD2 refer to catalytic domains 1 and 2 respectively. Modified from refs. 45,46

I.3.1 HDACs in pathobiology

Expression and/or activity of different HDACs has been found impaired in a considerable number of pathological situations, and therefore have been proposed as potential therapeutic targets for the treatment these.^{43,47-50} In this regard, the particular architectural features of the active sites of HDACs make them highly druggable targets. However, the high degree of evolutionary conservation in their CDs has become a limitation to achieve isoform selective inhibition. In this regard, although a considerable number of clinical trials has been carried out with several HDAC inhibitors (HDACis), to date only five of these drugs have obtained FDA approval for clinical applications. Moreover, their use has been restricted to very particular indications, mainly hematological malignancies (Table I3).⁵¹

Valproic acid (VPA) is a weak HDACi that can be considered the exception to the rule since it has been extensively used for years in the treatment of epilepsy and has also been involved in a high number of clinical trials.⁵² More recently, four new inhibitors have been approved by FDA for different indications: Vorinostat,⁵³ also known as SAHA, and Romidepsin⁵⁴ for the treatment of cutaneous T-cell lymphoma, Belinostat⁵⁵ for the treatment of peripheral T-cell lymphoma, and finally Panobinostat⁵⁶ for the treatment of multiple myeloma (Table I3). Interestingly, three of these four drugs are hydroxamic acids, and only Romidepsin belongs to a different group, being classified as a cyclic depsipeptide.

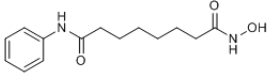
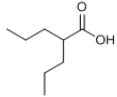
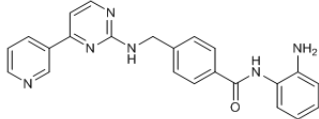
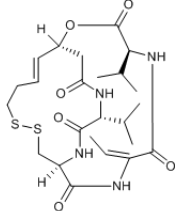
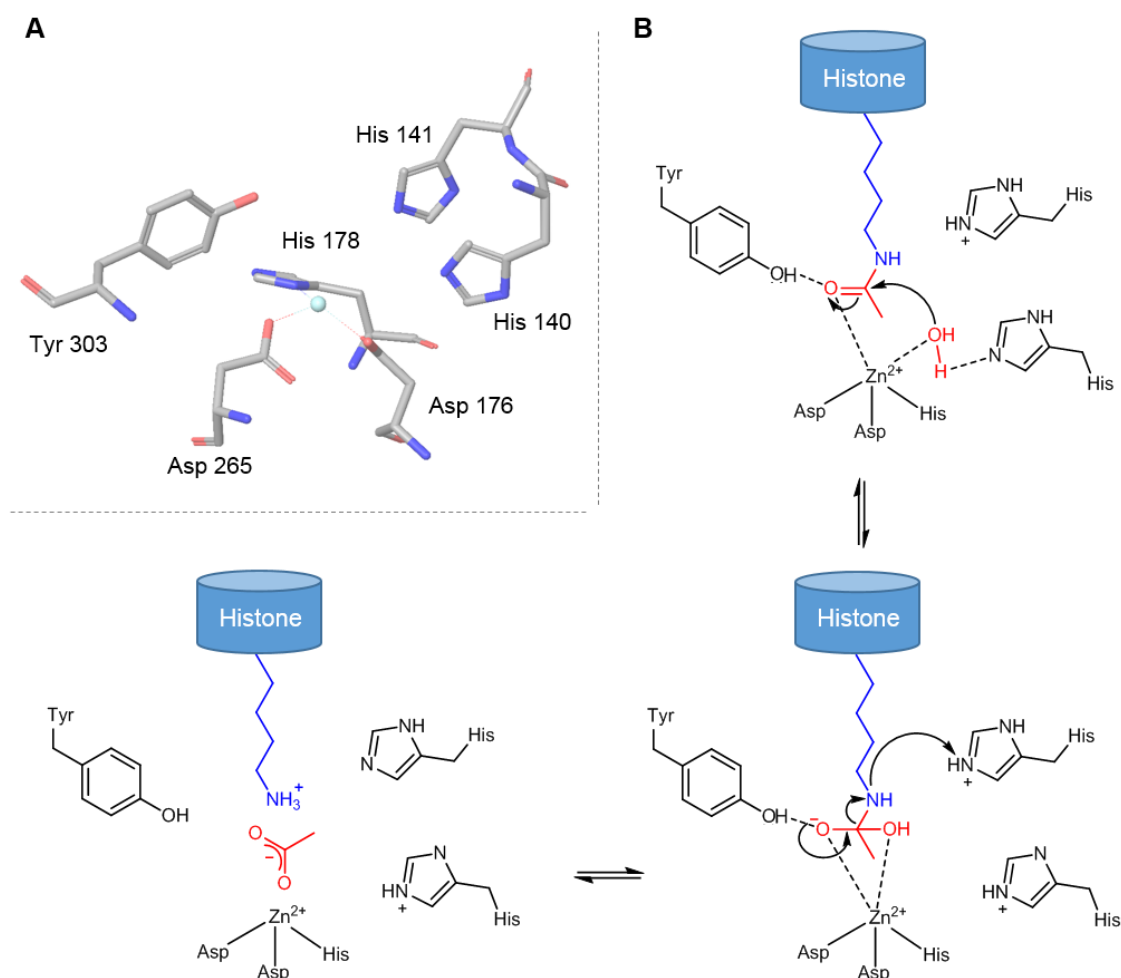
Inhibitor type	Inhibitor	Selectivity	Clinical status
Hydroxamic acids 	<u>Vorinostat (SAHA)</u>	pan	FDA approved (Cutaneous T-cell lymphoma)
	Belinostat	pan	FDA approved (Peripheral T-cell lymphoma)
	Panabostat	pan	FDA approved (Multiple myeloma)
	Trichostatin A	pan	Clinical trials
	Givinostat	pan	Clinical trials
	Resminostat	pan	Clinical trials
	Abexinosta	pan	Clinical trials
	Quisinostat	pan	Clinical trials
	Rocilinostat	II	Clinical trials
	Practinostat	I, II and IV	Clinical trials
	CHR-3996	I	Clinical trials
Short chain fatty acids 	<u>Valproic acid</u>	I and IIa	FDA approved (epilepsia, bipolar disorders and migraine)
	Butyric acid	I and II	Clinical trials
	Phenylbutyric acid	I and II	Clinical trials
Benzamides 	Entinostat	I	Clinical trials
	Tacedinaline	I	Clinical trials
	4SC202	I	Clinical trials
	<u>Mocetinostat</u>	I and IV	Clinical trials
Cyclic peptides 	<u>Romidepsin</u>	I	FDA approved (Cutaneous T-cell lymphoma)

Table I3. Examples of the main HDACi types applied in clinical practice. Table modified from ref.

I.3.2 Inside HDACs catalytic domain: general model of HDAC inhibition

As mentioned above, all Zn(II)-dependent HDAC isoforms present highly conserved CDs to carry out deacetylation catalysis. Several reaction mechanisms have been proposed to explain HDAC hydrolase activity.^{58,59} Among them, the first and most broadly accepted reaction mechanism was proposed in 1999 by *Finnin et al.* (Scheme I2).⁶⁰



Scheme I2. (A) Three-dimensional distribution of the main residues responsible of the catalytic activity within human HDAC1 active site. (B) Reaction mechanism proposed for HDAC-catalyzed deacetylation of acetyl lysine residues. Modified from ref. 60

This consists of a two-step mechanism that starts with the coordination of a water molecule and the carboxy group of the acetyl lysine to the Zn(II) cation. This allows the nucleophilic attack of the water molecule to the carboxamide group of the acetyl lysine to form an unstable tetrahedral intermediate. The instability of this fleeting species induces the formation of the carboxylate anion and the protonated amino group via hydrogen donation of a histidine residue to the lysine amino group. (Scheme I2).

HDAC CDs can be schematically described as an ensemble of shallowed external cavities connected through a hydrophobic channel with a Zn(II) containing catalytic site (Figure I5A). In addition, some HDAC isoforms, but not all, contain what is called the acetate release channel (Figure I5A).⁶¹

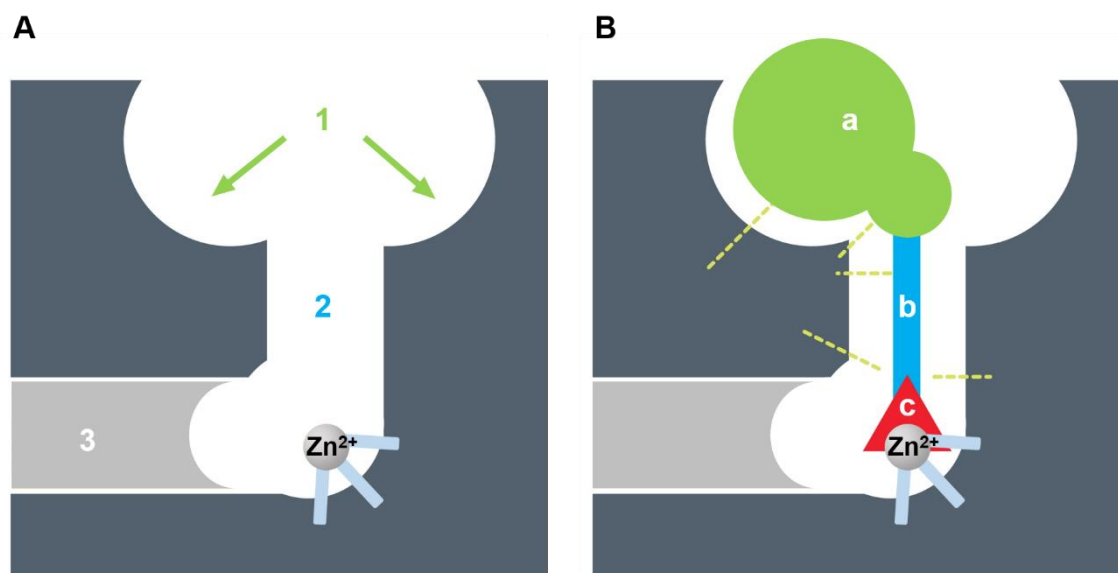


Figure I5. (A) Schematic representation of the architecture of HDACs deacetylation domains. 1: external cavities; 2: hydrophobic channel; 3: acetate release channel. (B) General pharmacophore model of HDACs. a: van der Waals cap; b: hydrophobic linker; c: Zn(II)-chelating group.

According to the structural features of HDACs, a general pharmacophore model has been extensively applied in our group for the design and development of HDACis.^{62,63} This model divides the entire inhibitor structure into three main substructures. These consist of: *i*) an external van der Waals cap (denoted as *a* in Figure I5B), that would ideally accommodate and interact with amino acids present on the external cavities, *ii*) a hydrophobic linker (denoted as *b* in Figure I5B) of adequate length that would enter and cross the hydrophobic channel, and finally *iii*) a Zn (II) chelating agent (denoted as *c* in Figure I5B) that would strongly interact with the Zn (II) cation present in the active site (Figure I5).⁶² Importantly, although this model is applicable to the majority of HDACis developed to date, it cannot be taken as a rule of thumb, since there is a non-negligible number of HDACis that do not match this general model.⁶⁴⁻⁶⁶

I.3.4 HDACis: from the pharmacophore model to their particular structures

Many different strategies have been developed for the design of effective HDACis. A wide number of chemical entities has been designed and structurally refined in the search for HDACis with optimized activity and selectivity. The most extensively studied inhibitor types are described below.

I.3.4.a Hydroxamic acids

Hydroxamic acids are usually obtained by reaction of an activated carboxy group with the hydroxylamine promoted by a base, such as sodium methoxide (Scheme I3).⁶⁷⁻⁷⁰



Scheme I3. General equation describing the synthesis of hydroxamic acids by reaction of an activated acyl group with the hydroxylamine. Modified from ref. 68

Hydroxamic derivatives are weak acids with a strong chelating capacity to form very stable mono or bidentate complexes with different metal ions, being this ability the main responsible for their pharmacological properties (Figure I6).^{70,71}

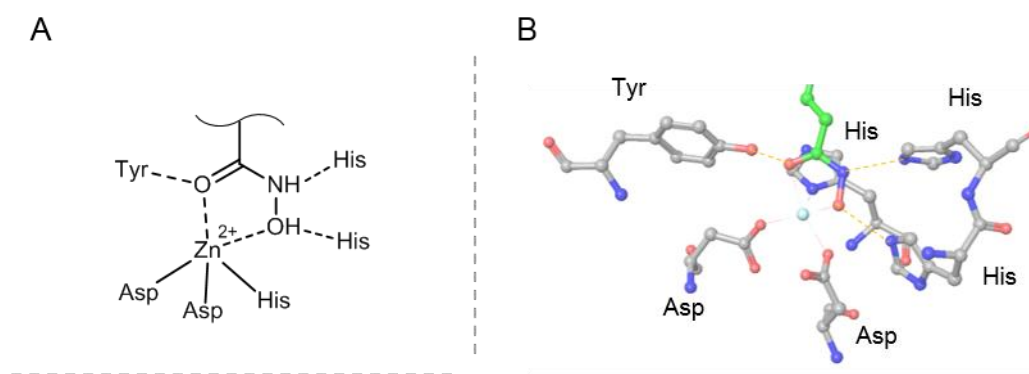


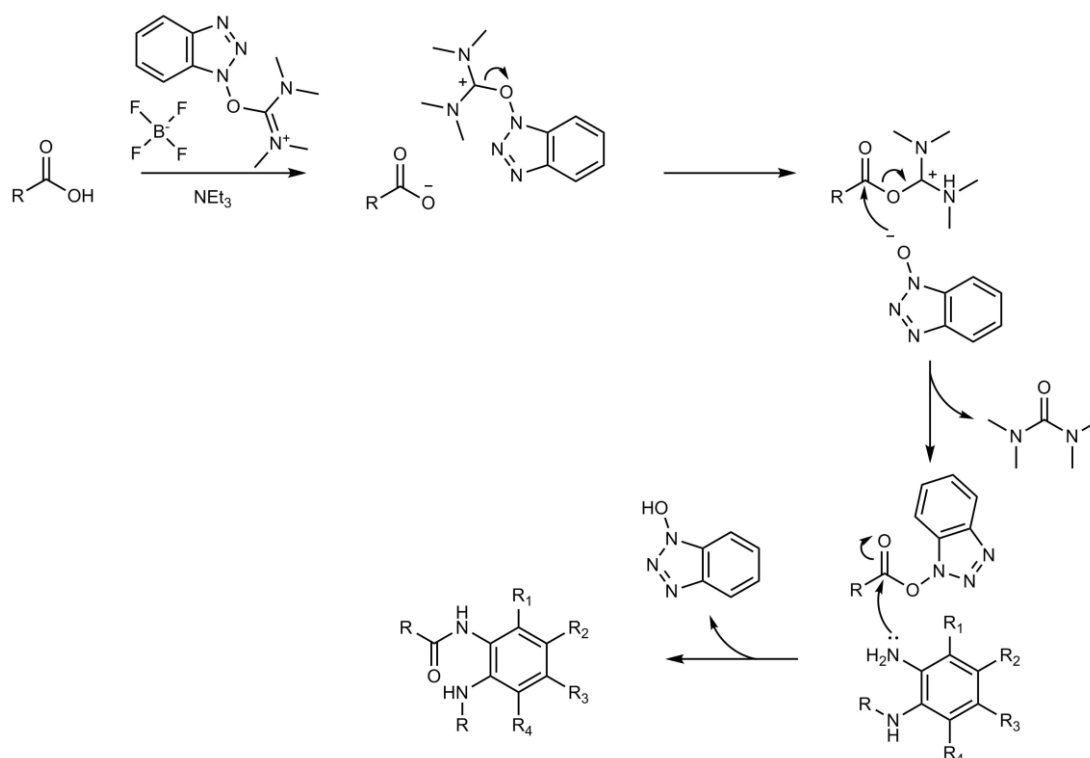
Figure I6. (A) Usual coordination mode of hydroxamic acids to Zn(II) catalytic centers. (B) X-ray structure of hydroxamic acid trichostatin bound to HDAC homolog from *Aquifex aeolicus* (PDB code: 1C3R).

Different hydroxamic acid derivatives have been extensively shown to be effective inhibitors of a wide number of Zinc metalloproteases.⁷² In accordance, hydroxamic acids are most probably the type of HDACis with the largest number of examples developed to date. Interestingly, Trichostatin A, a potent HDAC hydroxamic pan-inhibitor is produced in nature by *Streptomyces hygroscopicus*.⁷³ In particular, three of the five FDA approved HDACis (i.e., Vorinostat, Belinostat and Panabinstat) are hydroxamic acids. Nowadays, a high number of

compounds belonging to this group are currently involved in different phases of clinical trials (Table I3), emphasizing the considerable potential of this type of chemical entities for the future development of new HDACis.

1.3.4.b Benzamides

Benzamide HDACis can be obtained by amide bond formation between a carboxylic acid and an orthophenylenediamine eventually substituted in different positions of the aromatic ring. This type of reaction requires the activation of the carbonyl carbon by introduction of an electron withdrawing group provided by a *peptide coupling reagent* in order to allow the attack of the amino group (Scheme I4).⁷⁴



Scheme I4. Schematic representation of benzamide formation mechanism using 2-(1H-Benzotriazole-1-yl)-1,1,3,3-tetramethyluronium tetrafluoroborate (TBTU) as peptide coupling reagent. Modified from ref. 75

Benzamide groups exhibit good Zn(II) binding capacity what provides them with their HDAC inhibitory potential (Figure 17)

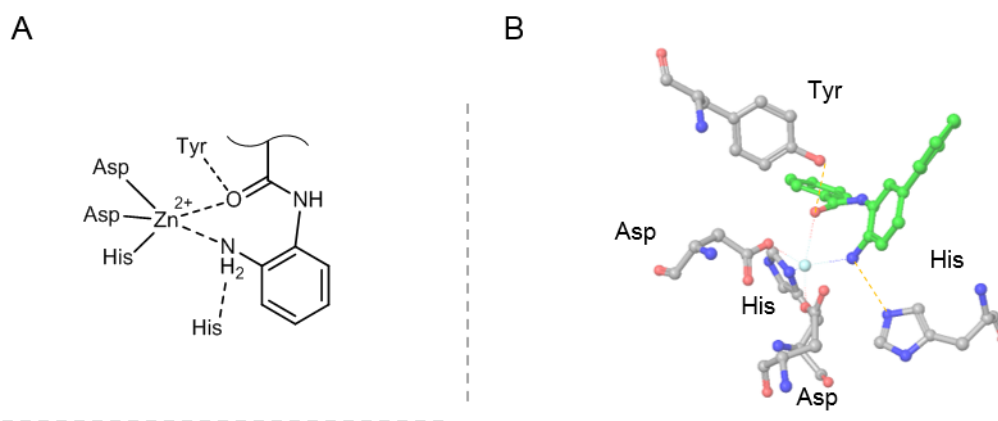


Figure 17. (A) Usual coordination mode of ortho-aminobenzamides to Zn(II) catalytic centers. (B) X-ray structure of N-(4-aminobiphenyl-3-yl)benzamide bound to human HDAC2 (PDB code: 3MAX).

However, experiments performed in purified HDACs have shown that benzamides show considerably slower association and dissociation kinetic rates than those of hydroxamic acids.⁷⁶ Importantly, this type of HDACs display a high degree of selectivity mainly towards class I HDACs (Table I3).^{77,78} In this regard, the increased bulkiness and rigidity of benzamides compared to hydroxamic acids may be determinant for the particular selectivity of these compounds. Several examples of benzamide HDACis have been involved in clinical trials such as Entinostat,⁷⁹ Tacedinaline⁸⁰ and Mocetinostat^{81,82} among others. However, to date none of these drugs has received FDA approval for a particular clinical indication.

1.3.4.c Short chain fatty acids (SCFAs)

Short chain fatty acids (SCFAs) such as Valproic and Butyric acids are HDACis of relatively simple chemical structure. This type of inhibitors usually exert HDAC inhibition in the micromolar range, being substantially less potent than members belonging to other inhibitor types. In this regard, although Valproic acid has proved to be effective for the treatment of epilepsy, the use of this type of inhibitors for other pathological conditions such as cancer is strongly limited by their low potency and selectivity and their fast metabolic elimination.⁸³ A fascinating feature of this type of inhibitors is that they are continuously being produced in the human organism by metabolic processes carried out by gut microbiota.⁸⁴ In this regard, there is an increasing number of works describing the important role of SCFAs as endogenous epigenetic modulators of different physiological and pathophysiological processes, mainly related to the immune system.⁸⁵⁻⁸⁸ Therefore, it cannot be discarded that the link between the gut microbiome and the development of other disorders, in which epigenetic impairments have been observed, could be somehow related to the HDAC inhibitory capacity of SCFAs.

1.3.4.d Macrocycles

Macrocyclic HDACis are the type of inhibitors carrying the most complex van der Waals cap moieties. Depending on their chemical nature, these can be classified into peptide macrocycles including cyclic tetrapeptides and cyclic depsipeptides, peptide mimetic macrocycles, and non-peptide macrocycles.⁸⁹ Importantly, the substantial structural complexity of the cap moieties of macrocyclic HDACis

confers them very interesting properties in terms of isoform selectivity.⁹⁰ From a classical HDACi perspective, the main reason for this would be that the largest degree of sequence disparity between the CDs of the different HDAC isoforms is found in the external cavities surrounding the hydrophobic channels,⁹¹ being excellent targets for selective inhibition. Interestingly, HDACs are often found forming complexes with other proteins to carry out specific activities. For this reason, novel strategies based on the use of macrocycles to disrupt HDAC-multiprotein complexes rather than focusing in Zn(II) chelation into the active site have been recently proposed to finer tune HDAC inhibitory selectivity.^{92,93}

Focusing on peptide macrocycles, a considerable number of these compounds possessing HDAC inhibitory capacity has been found to be naturally produced by different microbial sources.⁹⁴ An striking example of these peptide macrocyclic HDACis is Romidepsin, also known as FK228, which is a cyclic depsipeptide produced by *Chromobacterium violaceum*,⁹⁵ being the only macrocyclic HDACi approved by FDA for a particular clinical indication (Table I3), in this case cutaneous T-cell lymphoma.⁹⁶ Interestingly, Romidepsin does not exert any HDAC inhibitory activity by itself but rather consists of a stable prodrug that acquires HDAC inhibitory capacity upon *in vivo* disulfide bond reduction to form two thiol groups, being one of them able to act as an effective Zn(II) chelating group to drive HDAC inhibition.⁹⁷

1.3.4.e Hybrid HDACis

An interesting concept that has attracted great interest in the field of cancer treatment is the development of what has been called “hybrid or chimeric” drugs.

The design of this type of drugs is usually based on the combination of two pharmacophore models for different targets into the same chemical structure to provide the drug with multi-targeting capacities.⁹⁸ The use of hybrid drugs has been proposed to be an effective strategy to overcome the compensatory mechanisms often displayed by tumor cells to develop resistance to monotherapy.⁸⁹ Furthermore, the forced concomitant presence of the two distinct pharmacologically active entities into the same cell could be the key advantage to prevail the use of hybrid drugs over conventional combinatorial pharmacological treatments.⁹⁹ A proposed strategy for the design of new hybrid drugs has been the covalent combination of two pharmacologically active moieties into what has been called a mutual pro-drug by means of an inert linker that would ideally be enzymatically cleaved in the target cell or tissue to exert additive or synergistic effects.^{100,101} Hybrid strategies have been also proposed for delivering classical chemotherapy with improved targeting selectivity and reduced toxicity. A striking example of this strategy have been the development Bamet compounds that consist of the combination of a transition metal containing molecule such as cisplatin with different bile acids resulting in excellent antitumor activity with significantly improved liver vectorization and subsequently reduced systemic side effect events.¹⁰²⁻¹⁰⁴

In a slightly different way, the importance of the cap moiety for dictating inhibitory activity and selectivity of HDACis makes these excellent candidates for the development of new hybrid drugs. In this regard, the van der Waals cap of HDACis can be extensively modified to fulfil the requirements of a wide number of pharmacophore models, while directly influencing both HDACi activity and selectivity. Therefore, by joining the right components, HDACis would allow to

develop hybrid drugs in which both substructures could cooperate to optimize HDACi performance and subsequently provide additional pharmacological effects.

Some interesting examples have been developed by combining the classical pharmacophore model for HDAC inhibition with other components able to modulate activity of distinct cancer-related targets such as protein kinases, nuclear receptors, and epigenetic effectors, among others.^{98,100}

1.3.5 HDAC6

HDAC6 is a member of the Zn(II)-dependent family of HDACs that possesses some interesting structural particularities (Figure 14). Its amino acid sequence containing 1,215 residues is the longest of the HDAC family. Unlike the other HDAC isoforms, HDAC6 incorporates two tandem Zn(II)-containing CDs (CD1 and CD2). This enzyme also possesses a C-terminal Zn finger ubiquitin binding domain (BUZ) that allows it to bind ubiquitinated proteins.¹⁰⁵ This particular motif converts HDAC6 in an important effector for aggresome formation and autophagosome maturation, two events involved in the clearance of misfolded proteins that are essential for the maintenance of cell homeostasis.¹⁰⁶⁻¹¹⁰ Another interesting feature that distinguishes HDAC6 from most of the other HDAC isoforms is its preferential localization to the cell cytoplasm that is promoted by the presence of a N-terminal nuclear export signal (NES) and a serine-glutamate tetradecapeptide also known as SE14 motif that acts as cytoplasmic retention signal.^{111,112} In addition, HDAC6 exerts its deacetylation activity on several cytoplasmic protein substrates such as heat shock protein 90 (Hsp90), α -tubulin,

cortactin, or β -catenin.¹¹³⁻¹¹⁶ For many years, the individual catalytic role of each CD within HDAC6 has remained a matter of controversy.¹¹⁷ However, recently published directed mutagenesis experiments combined with structural crystallographic and enzymatic activity analysis provided important information for the understanding of the biological significance of both HDAC6 CDs.^{118,119} These studies revealed that despite the high degree of structural homology between both CDs, they possess some differences that significantly affect their respective catalytic activities. In this regard, although both CDs are catalytically active, CD1 seems to display very stringent substrate selectivity towards C-terminal acetylated lysines, while CD2 exhibits much broader substrate tolerance, being the responsible for HDAC6-mediated α -tubulin deacetylation, either in its monomeric form or as part of microtubule polymers.¹²⁰

HDAC6 is involved in many important cellular processes, such as cell proliferation, ciliary disassembly, cell motility and migration, cytoskeletal dynamics, misfolded protein degradation and control, and even innate immunity-driven pathogen sensing and destruction.^{22,121-126} For this reason it is not surprising that impaired HDAC6 expression and/or activity have been directly linked to a large number of pathological situations. Therefore, given its high druggability potential, HDAC6 inhibition has been proposed as a promising therapeutic target for the treatment of several pathologies.¹²⁷ In this regard, exhaustive efforts during the last decades have yielded promising drug candidates for selective HDAC6 inhibition, being Tubastatin A, Tubacin, ACY-1215 and QTX125 probably the ones most extensively applied for further development (Figure I8).^{63,128-131}

Nowadays, HDAC6 is considered a hot-spot target for several neurodegenerative and tumor-related disorders.^{117,130,132-136} Furthermore, since HDAC6 plays a central role in microtubule destabilization and ciliary disassembly, it is attracting a significant degree of interest as a potential target for the treatment of several types of so-called ciliopathies.^{22,137} Within this context, development of new HDAC6is with strong and selective inhibitory capacity, additional therapeutic properties, improved pharmacokinetics, and optimal tissue selectivity are warranted and may have significant therapeutic implications.

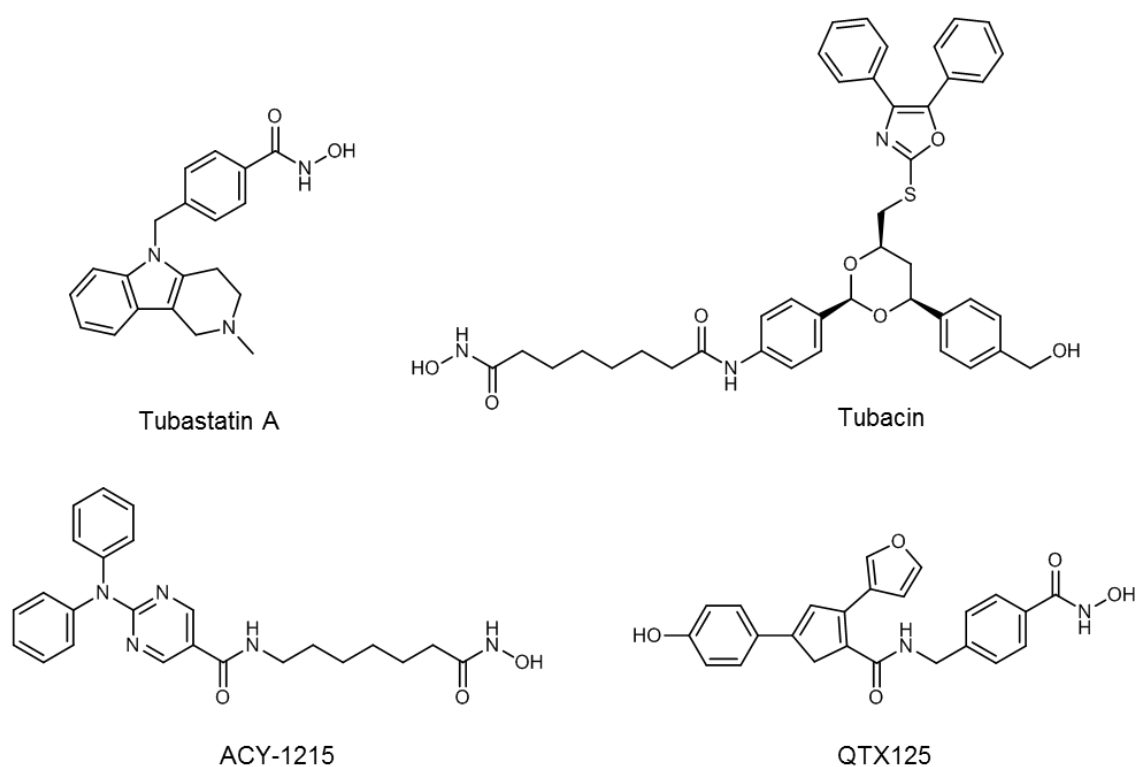


Figure 18. Chemical structures of HDAC6 selective inhibitors Tubastatin A, Tubacin, ACY-1215 and QTX125.

I.4 The primary cilium

The primary cilium is a microtubule-based organelle present in most mammalian cell types, and is commonly found as a thin projection of the apical membrane of different epithelial cells, including cholangiocytes.¹³⁸⁻¹⁴⁰ Although for long time this organelle was considered to be simply vestigial, in the last two decades, advances in the understanding of primary cilium biology have granted it as an important sensory organelle with a critical role in microenvironmental sensing and cell cycle regulation.^{139,141-143}

The structural scaffold of primary cilium consists of an axoneme formed by nine microtubule doublets that protrude from a basal body and is covered by a specialized domain extension of the plasma membrane called ciliary membrane (Figure I9A).¹⁴⁴ The primary cilium axoneme (9+0) differs from the one present in motile cilia (9+2) in the absence of central microtubules as well as other key proteins usually involved in cilia motility (Figure I9B).¹⁴⁴

Tubulin within the axonemal microtubules can be subjected to several post-translational modifications directly affecting microtubule dynamics, organization, and interaction with other cellular components.¹⁴⁶ Importantly, long-lived ciliary axonemal microtubules are highly enriched in α -tubulin acetylated in lysine 40 (K40), and therefore a causal relation between tubulin acetylation and cilia stabilization has been largely suggested.¹⁴⁷⁻¹⁴⁹ Interestingly, α -tubulin K40 acetylation by tubulin acetyl transferase enzymes is enhanced in microtubules over unpolimerized tubulin.^{148,150} This finding seems to indicate that tubulin acetylation within microtubules is an important post-polymerization hallmark of stability rather than a pre-requisite for microtubule polymerization. In accordance

HDAC6 overexpression and/or increased activity has been tightly linked to cilia shortening and resorption in a large number of experimental models. Most importantly, pharmacological inhibition of its deacetylase activity has been shown to result in significant improvement in the number of ciliated cells, cilia structure and biological function.¹⁵¹⁻¹⁵⁷

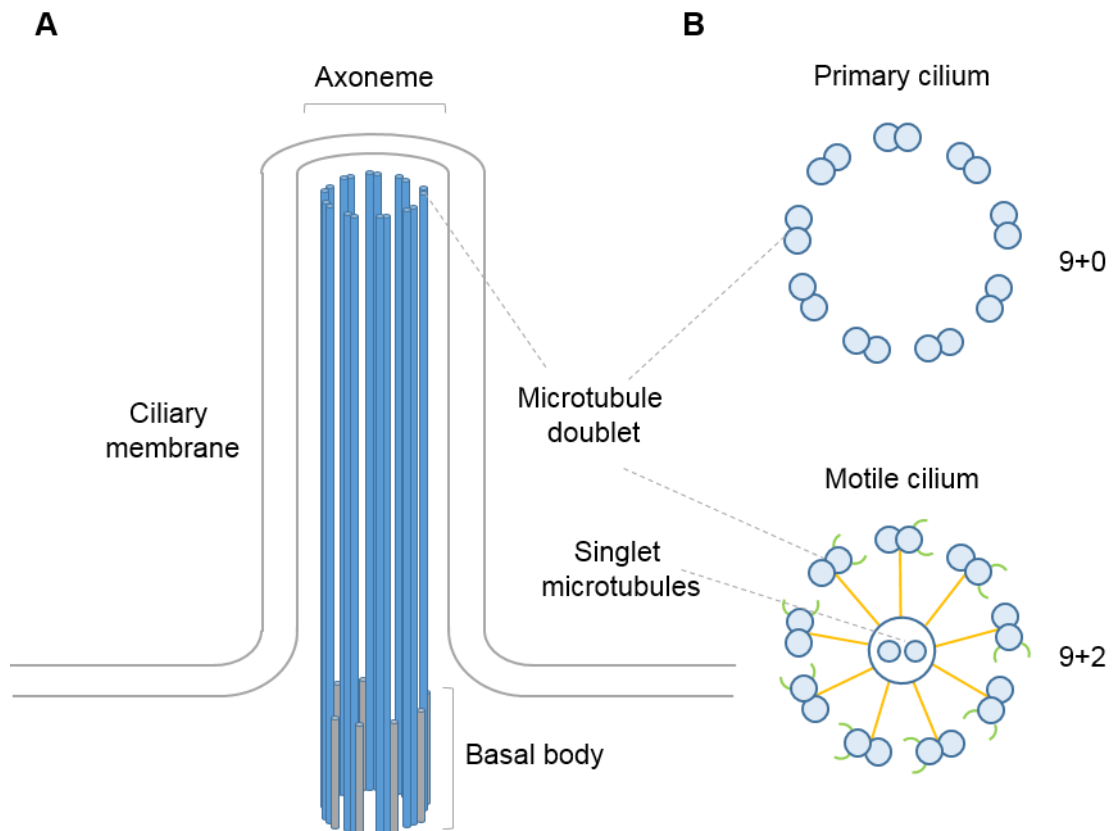


Figure 19. (A) Schematic representation of the scaffolding structure of primary cilium. (B) Schematic representation of a cross-section of the axoneme of a primary cilium and a motile cilium. (9+0) refers to the radial disposition of the nine microtubule doublets within primary cilium axoneme. (9+2) refers to the radial disposition of the nine microtubule doublets and the presence of an additional pair of central microtubules in motile cilium axoneme. In the motile cilium, yellow lines represent radial protein spokes and dynein arms are depicted in green. Modified from ref. 145

I.4.1 The primary cilium in cholangiocytes

Cholangiocytes are the epithelial cells lining the intra and extrahepatic bile ducts.¹⁵⁸ In addition to other important physiological implications, these cells carry out highly specialized transport functions that are essential to modulate bile composition.¹⁵⁹ In healthy biliary epithelia, primary cilia extend from the apical plasma membranes of cholangiocytes into the ductal lumen. This sort of “cellular antenna” or “mechano-osmo-chemical” sensor is able to detect changes in bile flow, bile composition and biliary osmolality and trigger distinct intracellular signals in response to these.^{160,161} In this regard, it has been demonstrated that cholangiocyte primary cilium is able to detect hypotonicity through the Ca²⁺-permeable channel TRPV4, what induces an increase in [iCa²⁺], subsequent release of ATP and finally bicarbonate secretion.¹⁶² This finding highlights the importance of cholangiocyte primary cilia for the regulation of the fine-tuned cholangiocyte driven mechanism of bile fluidization and alkalization through HCO₃⁻ secretion.^{163,164} Interestingly, it has also been shown that primary cilia of cholangiocytes are able to interact and respond to biliary exosomes, clearly suggesting a potential implication of this organelle in distant cell communication events.¹⁶⁵ Finally, the primary cilium is a pivotal regulator of cell cycle and polarity, depicting the critical importance of this organelle for normal cholangiocyte biology.¹¹

I.4.2 HDAC6 and primary cilium in cholangiopathies and polycystic diseases

Experimental evidences have largely demonstrated that primary cilium is a master regulator of cholangiocyte biology and function.¹⁵⁸ For this reason, it is not

surprising that structural and/or functional abnormalities in this organelle have been found in several cholangiopathies, being particularly relevant in PLDs and cholangiocarcinoma (CCA).¹⁶⁶

1.4.2.a Polycystic diseases

A previous report by *Gradilone* and collaborators demonstrated that HDAC6 is overexpressed in cystic cholangiocytes *in vitro* and *in vivo*.²¹ This finding encouraged authors to analyze the therapeutic potential of Tubastatin-A, Tubacin, and ACY-1215, three well-known selective HDAC6is for the treatment of PLDs. Interestingly, they found that pharmacological HDAC6 inhibition resulted in decreased cystic cholangiocyte proliferation accompanied by a significant decrease in β -catenin expression, and important activator of transcription and cell cycle progression through Wnt signaling.¹⁶⁷ Importantly, translation of this treatment into PCK rats, an animal model of PLDs, resulted in significant decrease of hepatorenal cystogenesis upon 4-week treatment (daily intraperitoneal treatment with 30 mg/kg day of ACY-1215).²¹

Since somatostatin analogues are currently the only available pharmacological treatment for PLDs, *Pisarello* and collaborators explored a combinatorial approach based in co-administration of a somatostatin analogue (i.e. Pasireotide) together with a HDAC pan inhibitor (i.e., Panabinstat) or selective HDAC6is (i.e., ACY-1215, ACY-738, and ACY-241). Then, these authors compared the therapeutic potential of the combined treatment *versus* individual administration of each drug alone to reduce hepatorenal cystogenesis.²³ In this study, authors reported that combination of HDAC6i ACY-

1215 and Pasireotide resulted in the highest levels of cAMP reduction and antiproliferative effect in cholangiocytes. Interestingly, the HDAC6 selective inhibitor ACY-1215 inhibited hepatorenal cystogenesis significantly more than HDAC pan-inhibitor Panabinstat. Finally, it was found that combination of ACY-1215 and Pasireotide was the treatment that provided the best therapeutic outcome in terms of cilia length restoration and hepatorenal cystogenesis inhibition. Therefore, these two studies highlight the promising therapeutic potential of HDAC6is for the treatment of PLDs, and also suggest that combining HDAC6is with chemical entities modulating other important disease-related targets, such as cAMP or iCa^{2+} , could be an effective strategy to circumvent virtual compensatory mechanisms leading to monotherapy failure.

In parallel to these studies, *Li et al.* reported the cytoplasmic accumulation of HDAC6 in cyst-lining epithelial cells in human ADPKD renal tissue and kidneys of an animal model of PKD.¹⁶⁸ In accordance, *Cebotaru et al.* and *Yanda et al.* reported significant inhibition of renal cystogenesis and improved renal function in *Pkd1^{fl/fl};Pax8^{rtTA};TetO-cre* mice (induced animal model of PKD) upon treatment with Tubacin and ACY-1215, two selective HDAC6is.¹⁶⁹⁻¹⁷¹ These studies reinforce the conclusions reported by *Gradilone et al.* and *Pisarello et al.* in the PCK rats. Importantly, taking all these studies together, HDAC6 emerges as a potential molecular bridge between PLDs and PKDs, two pathologies that often arise in parallel. Therefore, these findings point selective HDAC6is as promising therapeutic tools that, in combination with modulators of other polycystic disease-related pathways, could settle the basis for next generation pharmacological approaches with improved therapeutic outcome.

1.4.2.b Cholangiocarcinoma (CCA)

Regarding CCA, another study reported by *Gradilone and collaborators* depicted the strong relation between cholangiocyte primary cilium impairment and CCA pathobiology.¹⁷² In this study, these authors demonstrated that the primary cilia were impaired or absent in CCA cells *in vitro* and *in vivo*, and experimentally-induced deciliation of normal cholangiocytes resulted in acquisition of a pro-malignant phenotype through activation of Hedhehog and MAPK signaling pathways. Importantly, cilia abnormalities appeared to be directly related to HDAC6 overexpression in CCA. In this regard, molecular downregulation and pharmacological inhibition of HDAC6 restored primary cilia in CCA cells leading to a significant reduction of cell proliferation, anchorage-independent growth and invasion, and ultimately *in vivo* tumor growth. Inspired by these results, interesting findings have been recently reported about the regulatory functions of primary cilium chemosensation in CCA migration, invasion and tumor growth; the importance of miR-433 and miR-22 for HDAC6-induced cilia impairment in CCA or even the potential implication of cilia loss in the development of primary sclerosing cholangitis (PSC)-derived CCA.¹⁷³⁻¹⁷⁵ Moreover, the importance of the ciliary-associated localization of the bile acid receptor TGR5 for cholangiocyte pathobiology, together with the increasing evidence of the critical role of TGR5 overexpression in CCA development and progression, may provide important insights for the understanding and treatment of CCA in the coming future.^{176,177}

HYPOTHESIS AND OBJECTIVES

Pharmacological approaches based on the administration of either UDCA or HDAC6is have provided very promising, but still partial, results for the treatment of PLDs have been obtained so far.^{15,20,21,23} For this reason we hypothesized that new chemical entities combining UDCA and HDAC6i activity into the same chemical structure could provide added and/or synergistic value for the treatment of PLDs. In this regard, it is known that pre-organized macrocyclic systems can exhibit high non-covalent binding constants with the external cavities close to the rim that connects the active sites of HDACs with the surface of these enzymes.^{91,178,179} For this reason, and considering the polycyclic nature of the UDCA scaffold, we rationalized that this endogenous BA could be a suitable conformationally restricted analogue to these macrocyclic systems, and therefore an excellent structural element for the development of high performance HDAC6is. Furthermore, we reasoned that some of the inherent hepatotropic properties of UDCA could be transferred to these new HDAC6is, thus improving liver targeting and entero-hepatic re-circularization, as well as active transport into cystic cholangiocytes. Importantly, metabolic cleavage of the amide bond by intestinal microbiota is not expected to generate potentially toxic metabolites but rather could result in the release of therapeutic concentrations of free UDCA that could further improve the effectiveness of the treatment.

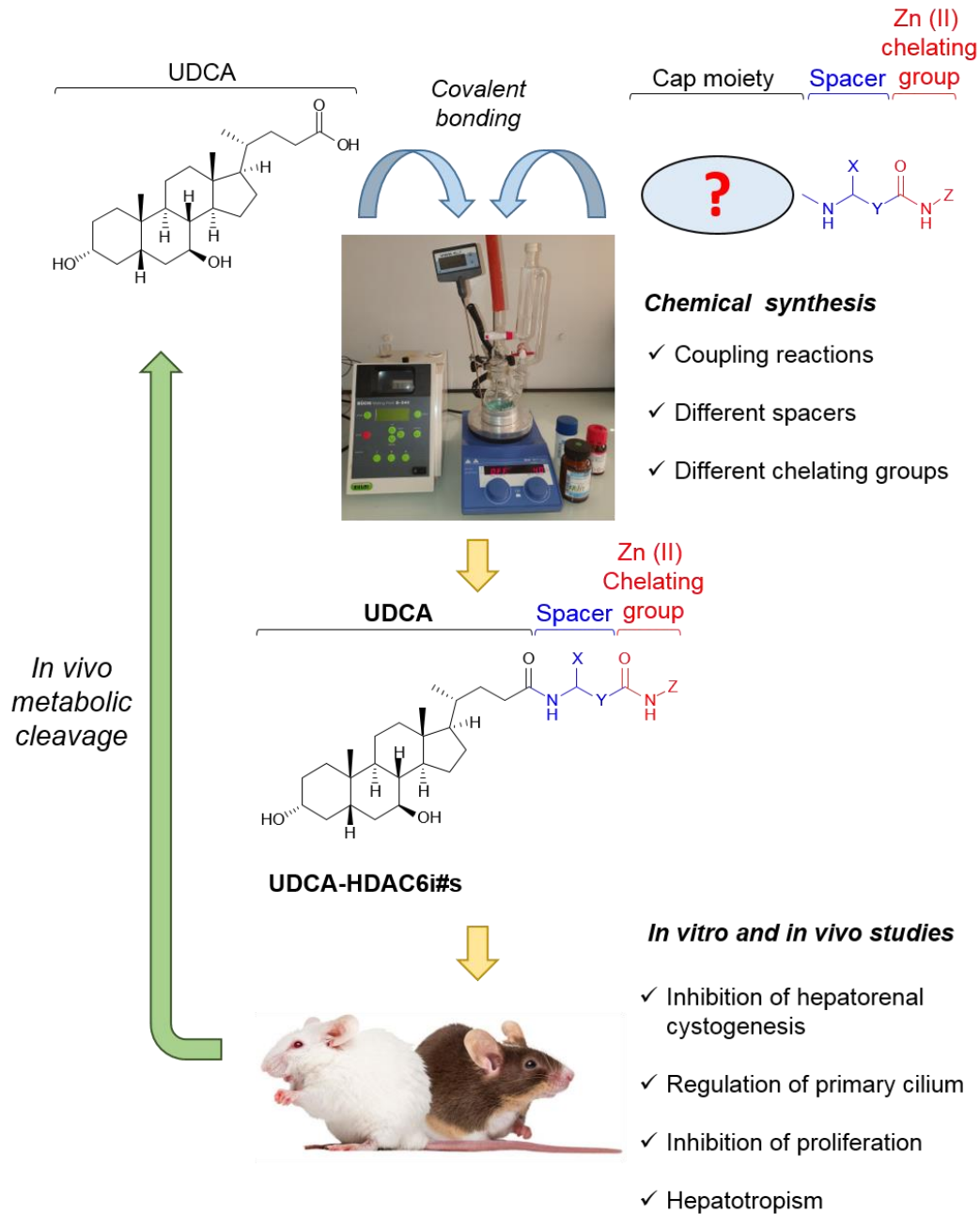


Figure H1. Graphical representation of the general hypothesis in this dissertation.

In order to evaluate the described hypothesis, the following objectives were proposed:

- i. Design, chemical synthesis and characterization of new synthetic conjugates of UDCA.
- ii. Computational prediction of the binding affinities of UDCA-HDAC6is for HDAC6 CD1 and C2.
- iii. In vitro evaluation of the HDAC inhibitory activity and selectivity of UDCA-HDAC6is on individual HDACs and cystic cholangiocytes.
- iv. Computational and experimental study of the chemical and structural factors that drive HDAC6 activity and selectivity in UDCA-HDAC6is.
- v. Evidence-based selection of the UDCA-HDAC6i with higher translational potential for further in vivo and in vitro studies.
- vi. In vivo evaluation of the therapeutic potential of UDCA-HDAC6is for the treatment of PLDs.
- vii. In vitro characterization of the therapeutic effect of UDCA-HDAC6is.

RESULTS

R.1 Design and chemical synthesis of new synthetic conjugates of UDCA

We applied to the X-ray structure of the CD2 of human HDAC6 (PDB code: 5EDU)¹¹⁹ a HDAC inhibition model previously described by our group⁶² (Figure R1). According to this model, HDAC6 active sites can be schematically described as an ensemble of external shallow cavities connected through a hydrophobic channel with a Zn(II) cation containing catalytic site. Following this general model, we designed a family of new synthetic UDCA conjugates (i.e., UDCA-HDAC6i #1-10), in which the tetracyclic skeleton of UDCA acted as the external van der Waals cap of the inhibitor, followed by a number of different hydrophobic spacers ended on a Zn(II) chelating group (Figure R1).

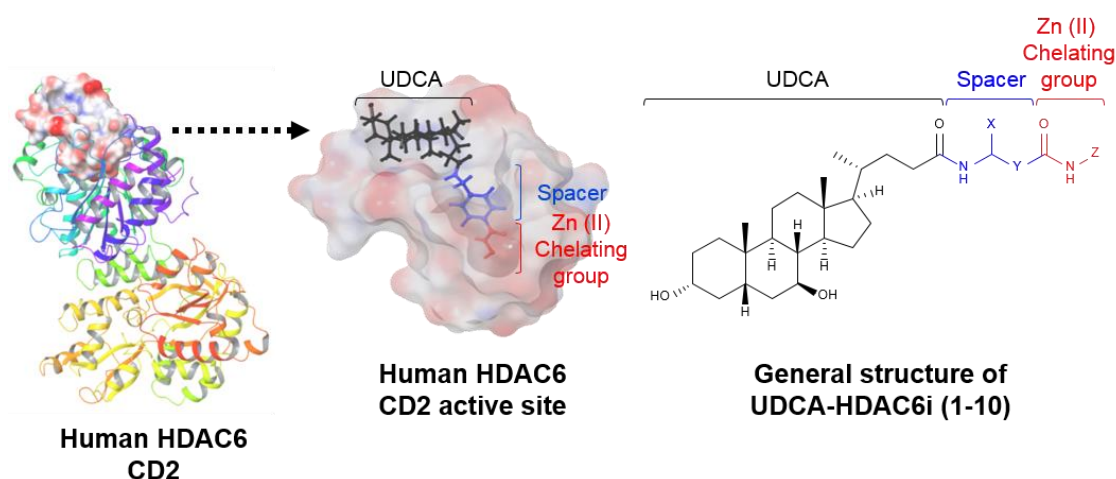


Figure R1. X-ray structure of human HDAC6 catalytic domain 2 (PDB entry 5EDU). General model of HDAC6 inhibition. Description of the common chemical structural features of HDAC6 inhibitors and translation into UDCA synthetic conjugates.

The chemical synthesis of the UDCA-HDAC6i molecules started with the coupling reaction of UDCA (**1**) with amines **2** to yield amide esters **3**. Hydrolysis of these latter intermediates and *in situ* reaction with hydroxylamine permitted the obtaining and characterization of UDCA-hydroxamic acids UDCA-HDAC6i **#1**,

#3-6 and **#10**, which possess different lengths and stereoelectronic features depending on the nature of the X-residues, as shown in Figure R2.

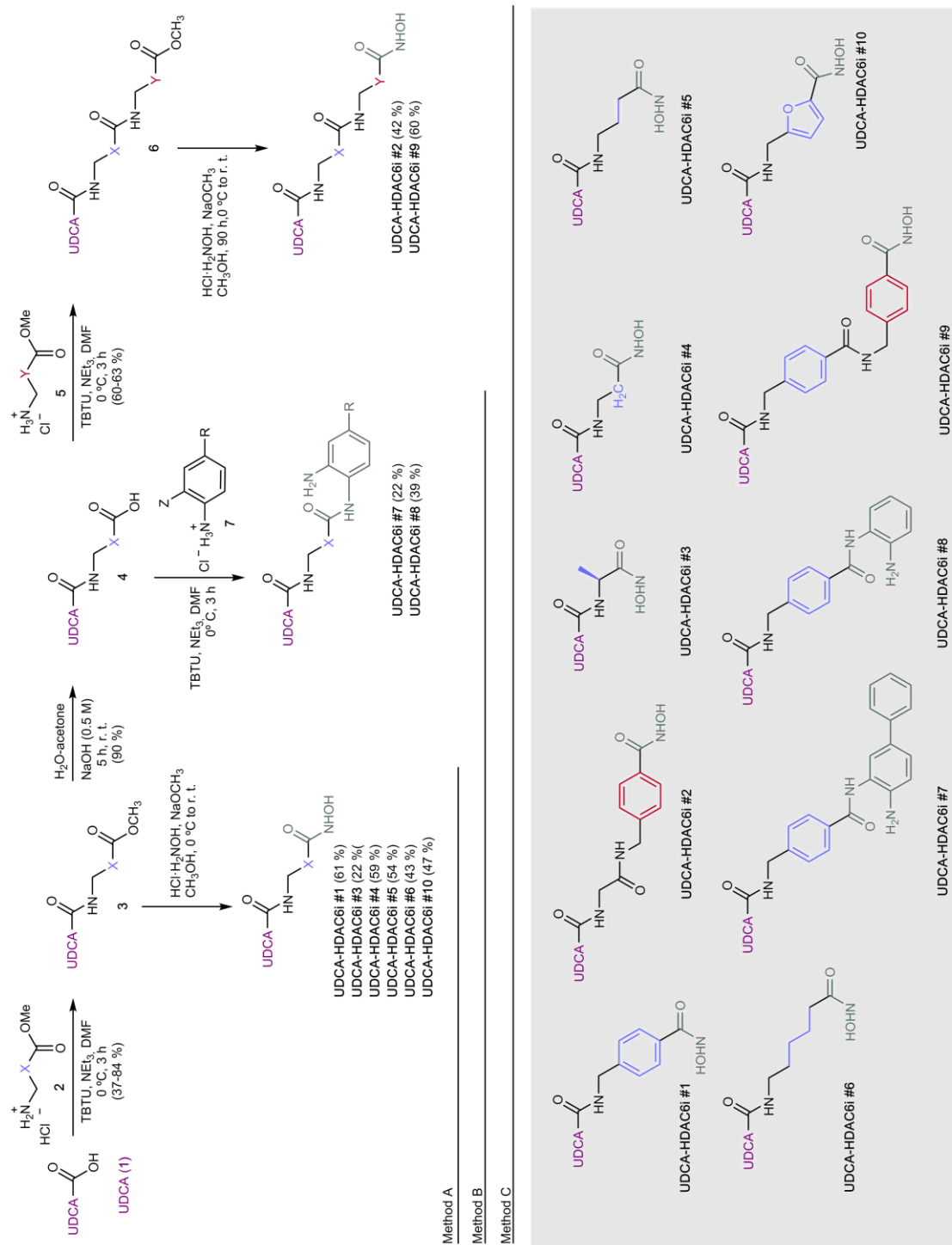
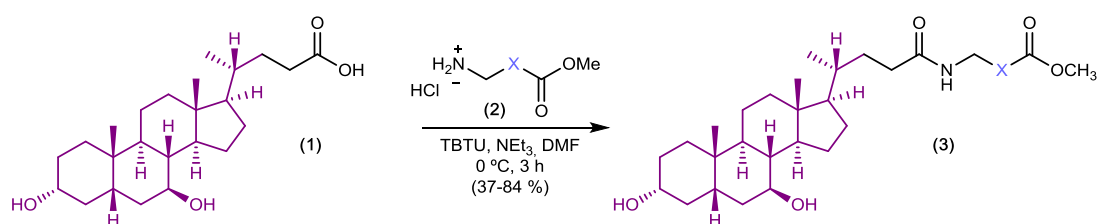


Figure R2. Graphical representation of the synthetic routes followed for the chemical synthesis of the different UDCA-HDAC6is

In particular, these candidates incorporate alkyl, phenyl, heteroaryl and chiral groups in their respective spacers. Alternatively, hydrolysis of esters **3** permitted the preparation of carboxylic acids **4**, whose subsequent coupling with orthophenylenediamines **7** yielded amide candidates UDCA-HDAC6i **#7**, **#8**. In other examples, the spacer between the chelating group and the UDCA component was further elongated by an additional hydrolysis-coupling sequence thus yielding esters **6**. Deprotection of these methyl esters and reaction with hydroxylamine permitted the isolation and characterization of candidates UDCA-HDAC6i **#2**, **#9**. In summary, the synthetic scheme shown in Figure R2 yielded an ensemble of potential HDAC inhibitors possessing different spacers, chelating groups, and sharing an UDCA moiety as a common hydrophobic terminal cap. Therefore, this focused ensemble of candidates covered the configurational space around the conformationally restricted UDCA moiety.

R.2 General methods for the synthesis of UDCA-HDAC6is

R.2.a.1) Coupling of UDCA with spacers

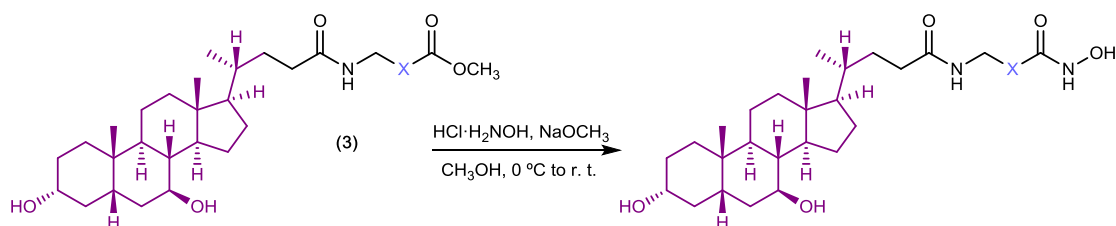


Scheme R1. General example of peptide coupling reaction of UDCA with aminoester spacers.

To a solution of UDCA (393 mg, 1 mmol) in N,N-Dimethylformamide (DMF) (2.5 mL) the hydrochloride of the corresponding methyl or ethyl amino ester (1 mmol)

and 2-(1H-Benzotriazole-1-yl)-1,1,3,3-tetramethyluronium tetrafluoroborate (TBTU) (385 mg, 1.2 mmol) were added. The solution was brought to 0 °C in an inert atmosphere and a solution of Et₃N (0.5 mL) in DMF (0.6 mL) with a concentration of 3.26 M was added dropwise. Reaction was followed by thin layer chromatography. The reaction mixture was stirred for 3 hours. The solvent was then evaporated under reduced pressure, and the residue was dissolved in ethyl acetate (20 mL) and washed successively with 1N HCl (3 × 10 mL), saturated NaHCO₃ (2 × 10 mL) and saturated NaCl (1 × 10 mL). The organic phase was dried over MgSO₄ and evaporated under reduced pressure. The solid obtained was purified by chromatography obtaining the desired product. Compounds (**3a-f**) were obtained following this method.

R.2.a.2) Synthesis of hydroxamic acids

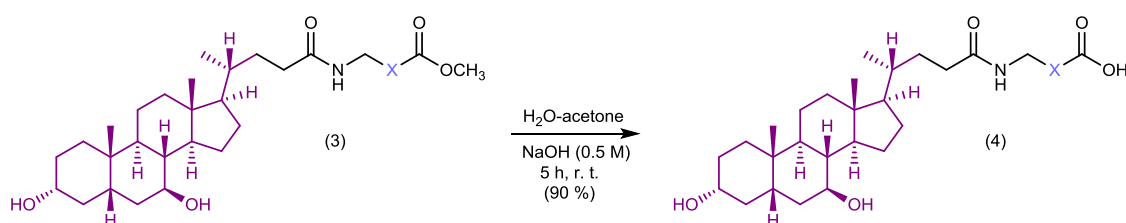


Scheme R2. General example of the synthesis of hydroxamic acids from UDCA ester derivatives.

To a solution of hydroxylamine hydrochloride (695 mg, 10 mmol) and phenolphthalein (1 mg) in dry methanol (5 mL) at 0°C under inert atmosphere, an aliquot of previously prepared suspension of sodium methoxide in methanol (2 g,

37 mmol, 5 mL) was added dropwise until a permanent color switch to intense pink color. Then, the corresponding methyl or ethyl ester **3** (1 mmol) dissolved in dry methanol (1 mL) was added followed by addition of 1 mL of the previously prepared sodium methoxide suspension. Reaction was monitored by thin layer chromatography. The reaction mixture was stirred for 90 hours. Subsequently, distilled water (10 mL) was added and the reaction medium was acidified with glacial acetic acid. The product was then extracted with diethyl ether (3 × 20 mL) and the combined organic fractions were dried over MgSO₄ and evaporated under reduced pressure. The product thus obtained was redissolved in methanol (1 mL) and precipitated with water. This precipitate was filtered and washed with water and diethyl ether to obtain the desired product. Compounds UDCA-HDAC6i #1, #3, #4, #5, #6 and #10 were obtained following this method.

R.2.b.1) Hydrolysis of methyl ester **3**

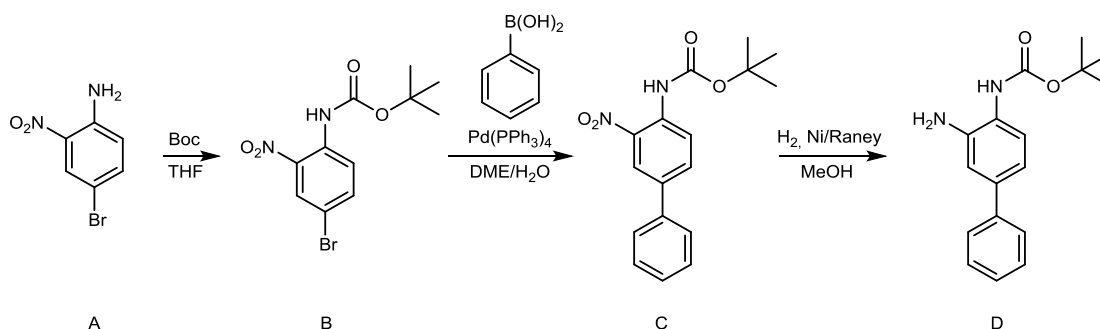


Scheme R3. Reaction scheme of hydrolysis of UDCA ester derivatives.

A solution of NaOH (2.15 mmol) in distilled water (4.35 mL) was slowly added to a solution of the corresponding UDCA ester derivative **3**, (1 mmol) in acetone (4.35 mL). The mixture was stirred for 5 hours. The reaction mixture was then acidified with 1N HCl and kept under stirring for additional 15 minutes at 0°C. The

formed precipitate was filtered and washed successively with cold water, thereby obtaining the desired product. Compound **4a** was obtained following this method.

R.2.b.2) Synthesis of tert-butyl (3-amino- [1,1'-biphenyl] -4-yl) carbamate: **D**



Scheme R4. Reaction scheme of the synthesis of tert-butyl (3-amino- [1,1'-biphenyl] -4-yl) carbamate.

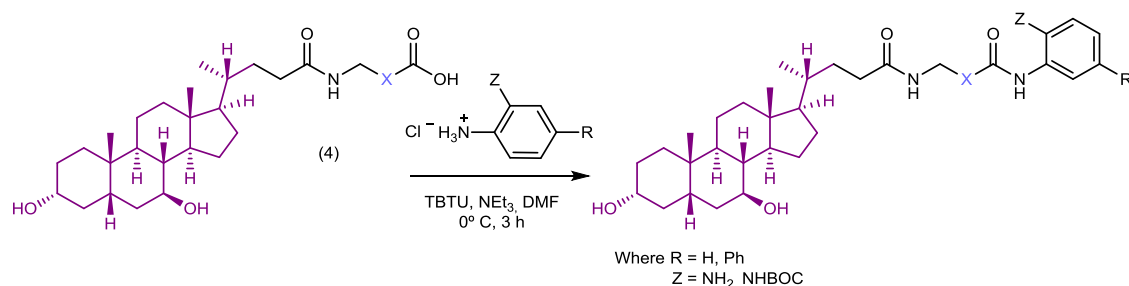
To a solution of 4-bromo-2-nitroaniline **A** (2.4 g, 11.05 mmol) and Boc-anhydride (di-tert-butyl dicarbonate) (5.08 mL, 22.11 mmol) in THF (20 mL) a catalytic amount of DMAP (4-dimethylamino pyridine) was added. The reaction was stirred for 90 minutes at room temperature. The solvent was then evaporated at low pressure and the oil obtained was dissolved in THF (10 mL). NaOH (10 mL, from a 2N solution) was then added and the reaction was stirred for 18 hours at 65°C. Afterwards, NaOH (400 mg, 10 mmol) was added and the reaction was stirred for additional 4 hours at 65°C. The progress of the reaction was monitored by thin layer chromatography. The solvent was removed in vacuo yielding a solid residue, which was filtered and washed with distilled water (2 x 20 mL) obtaining

the desired product as a yellow solid **B**, which was used directly for the next reaction step to obtain **C**.

$\text{Pd}(\text{PPh}_3)_4$ (400 mg, 0.346 mmol) was added to a reaction mixture in DME/ H_2O (2:1,5 mL) containing the corresponding tert-butyl carbamate **B** (1 g, 3.15 mmol), obtained above, phenylboronic acid (423 mg 3.46 mmol) and sodium carbonate (492 mg, 4.73 mmol). The solution was stirred for 20 hours at 110°C and under inert atmosphere. After this reaction time, water was added, and the product was extracted with ethyl acetate (3 x 20 mL). The organic phases were combined and washed with water (2 x 10 mL), dried over magnesium sulfate, filtered and the solvent was evaporated under reduced pressure. The yellow solid thus obtained was purified by column chromatography obtaining the desired product **C**.

The last step involved the reduction of the group nitro to obtain the corresponding primary amine, which was carried out using a modular catalytic hydrogenator (H-Cube Pro of THALESNano) and a Ni/Ra supported cartridge catalytic system. Compound **C** was dissolved in 500 mL of MeOH and passed through the catalyst system at a flow rate of 1 mL/min, 50°C and under a pressure of 10 bar. The solvent was removed in vacuo giving the desired product **D** as a white solid.

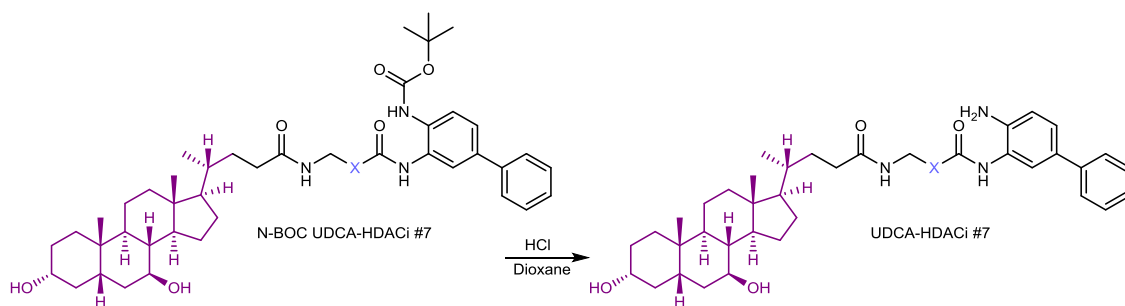
R.2.b.3) Coupling of benzamide chelating groups



Scheme R5. General example of the coupling of orthophenylenediamines.

To a solution of the carboxylic acid **4** obtained in b.1 (206 mg, 0.38 mmol) in DMF (2.5 mL), the corresponding orthophenylenediamine (0.38 mmol) and TBTU (148 mg, 0.46 mmol) were added. The solution was brought to 0°C in an inert atmosphere and a solution of Et₃N (0.2 mL) in DMF (0.24 mL) with a concentration of 3.26 M was added dropwise. The mixture was stirred for 3 hours at 0°C. The reaction was monitored by thin layer chromatography. The solvent was then evaporated under reduced pressure, and the residue was dissolved in ethyl acetate (7.5 mL) and washed successively with 1 N HCl (3 × 5 mL), saturated NaHCO₃ (2 × 5 mL) and saturated NaCl (1 × 5 mL). The organic phase was dried over MgSO₄ and then evaporated under reduced pressure. The solid obtained was purified by column chromatography obtaining the desired product. Compound UDCA-HDAC6i **#8** and N-BOC protected precursor of UDCA-HDAC6i **#7** were obtained following this methodology.

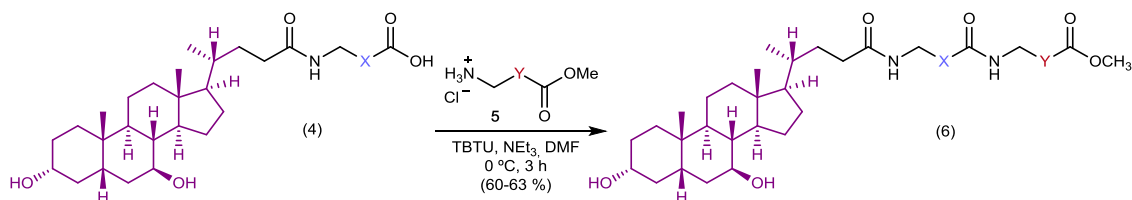
R.2.b.4) Deprotection of the tert-butoxycarbamate



Scheme R6. Reaction scheme of the carbamate deprotection of N-BOC protected UDCA-HDAC6i #7.

A solution of 4N HCl in dioxane (0.3 mL) was added dropwise to a suspension of the N-BOC protected compound (53 mg, 0.067 mmol) in a mixture of CH_2Cl_2 (0.63 mL) and dioxane (0.63 mL). The progress of the reaction was monitored by thin layer chromatography. The mixture was kept under stirring for 3 hours. The solvent was then evaporated under reduced pressure. The solid thus obtained was suspended in AcOEt (10 mL) and washed with saturated NaHCO_3 solutions (3 x 5mL) and NaCl (3 x 5mL), then dried over magnesium sulfate, filtered and evaporated. Finally, it was dissolved in MeOH and precipitated in Et_2O , obtaining the desired product. Compound UDCA-HDAC6i #7 was obtained following this methodology.

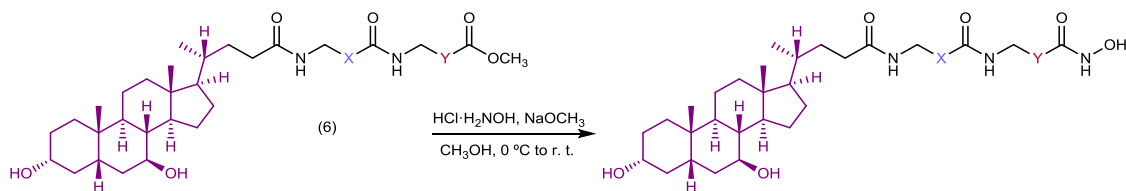
R.2.c.1) Coupling of the spacers



Scheme R7. General scheme of the peptide coupling of aminoester spacers.

To a solution of the corresponding carboxylic acid (0.38 mmol) in DMF (2.5 mL) the hydrochloride of methyl 4-(aminomethyl)benzoate (76 mg, 0.38 mmol) and TBTU (148 mg, 0.46 mmol) were added. The solution was brought to 0°C in an inert atmosphere and a solution of Et₃N (0.2 mL) in DMF (0.24 mL) with a concentration of 3.26 M was added dropwise. Reaction was monitored by thin layer chromatography. The mixture was stirred for 3 hours. The solvent was then evaporated under reduced pressure, and the residue was dissolved in ethyl acetate (7.5 mL) and washed successively with 1N HCl (3 x 5 mL), saturated NaHCO₃ (2 x 5 mL) and saturated NaCl (1 x 5 mL). The organic phase was dried over MgSO₄ and evaporated under reduced pressure. The solid obtained was purified by chromatography obtaining the desired product. Compounds **6a** and **6b** were obtained following this methodology.

R.2.c.2) Synthesis of hydroxamic acids

**Scheme R8.** General scheme of the synthesis of hydroxamic acids.

To a solution of hydroxylamine hydrochloride (139 mg, 2 mmol) and phenolphthalein (1 mg) in dry methanol (5 mL) at 0°C under inert atmosphere, an aliquot of previously prepared suspension of sodium methoxide in methanol (2.0 g, 37 mmol, 5 mL) was added dropwise until a permanent intense pink color was observed. Then, the corresponding methyl ester (0.2 mmol) dissolved in dry methanol (0.2 mL) and 1 mL of the previously prepared sodium methoxide suspension were added. The evolution of the reaction was monitored by thin layer chromatography. The reaction mixture was stirred for 90 hours. Subsequently, distilled water (2 mL) was added and the reaction mixture was acidified with glacial acetic acid. The product was then extracted with diethyl ether (3×5 mL) and the organic fractions were combined and dried over MgSO_4 and evaporated under reduced pressure. The product thus obtained was redissolved in methanol (1 mL) and precipitated with water. This precipitate was filtered and washed with water and diethyl ether to obtain the desired product. Compounds UDCA-HDAC6i #2 and #9 were obtained following this methodology.

R.3 UDCA-HDAC6is exhibit binding affinities for HDAC6 CD1 and C2 *in silico* and UDCA is determinant in these interactions

The potential HDAC6 inhibitory capacity of this new UDCA derivatives was first evaluated *in silico* with a docking model based on the crystallographic structure of human HDAC6 CD2 (PDB code: 5EDU) (Figure R1 and R3).

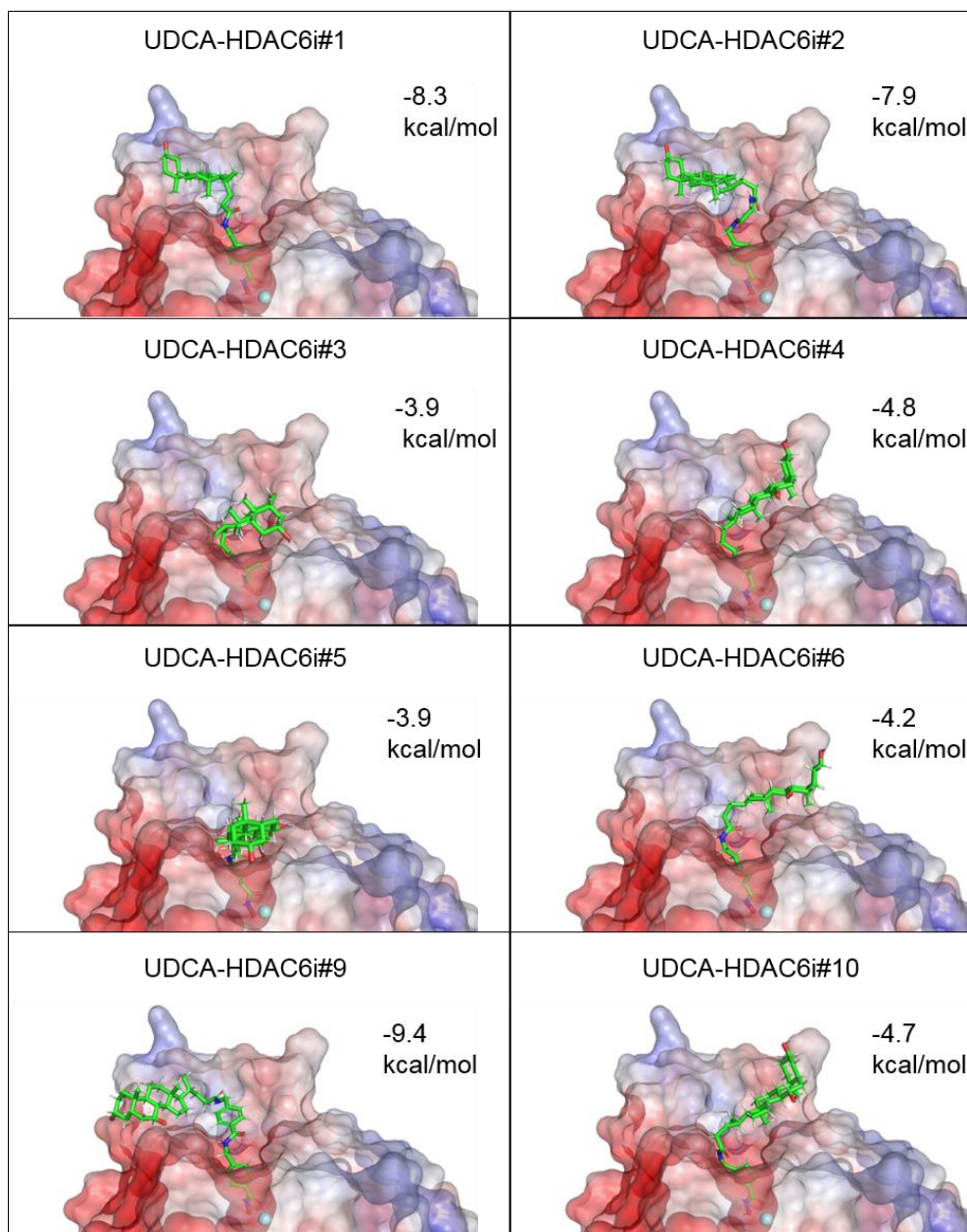


Figure R3. *In silico* docking studies. Graphical representation of the binding of different UDCA-HDAC6is on human HDAC6 CD2. The values of the score functions for each inhibitor are represented in kcal/mol.

According to our results, eight of the ten designed compounds presented significant binding affinities for HDAC6, being UDCA-HDAC6i #1, #2 and #9 the compounds that displayed the highest energy scores (-8.3, -7.9 and -9.4 kcal/mol, respectively; Figures R3 and R4). Interestingly, these three compounds oriented the tetracyclic skeleton scaffold of UDCA towards the same region of the protein surface (Figures R3 and R4).

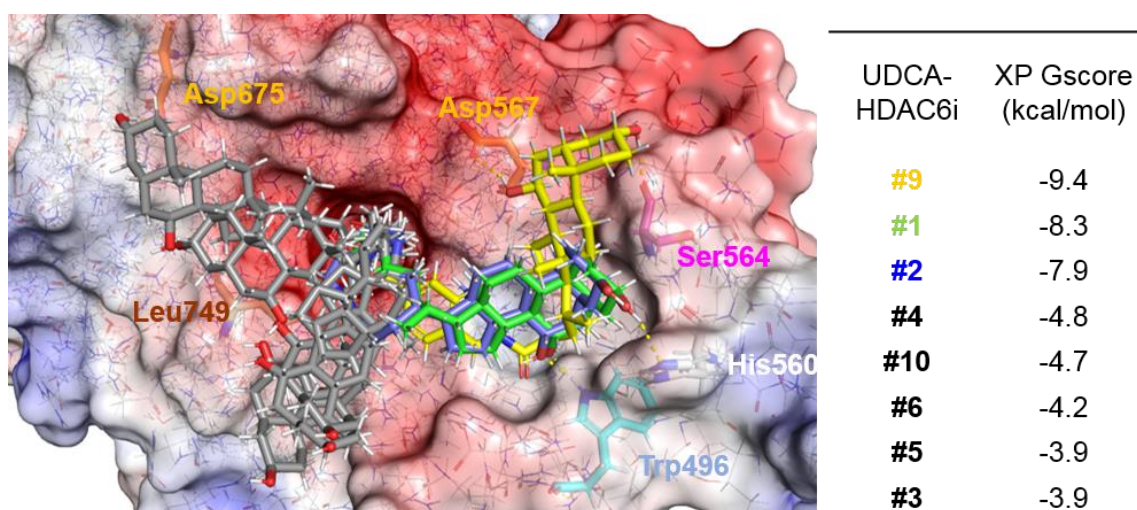


Figure R4. Graphical representation of the orientations of UDCA hydrocarbon skeleton in the different UDCA-HDAC6is (yellow #9, green #1, blue #2, grey #4, #10, #6, #5 and #3) docked to the CD2 domain of human HDAC6. Dashed yellow lines represent hydrogen bond interactions between hydroxyl groups of UDCA and different amino acids located in the surface cavities of the enzyme. The table displays all the predicted binding energies reported in the docking studies for the UDCA-HDAC6is.

Based on this observation, we decided to carry out a more detailed analysis of the binding modes of all compounds in order to understand the potential contribution of the different pharmacologically active substructures conforming each inhibitor (i.e., UDCA and chelating group) to the overall binding affinity (Figure R5).

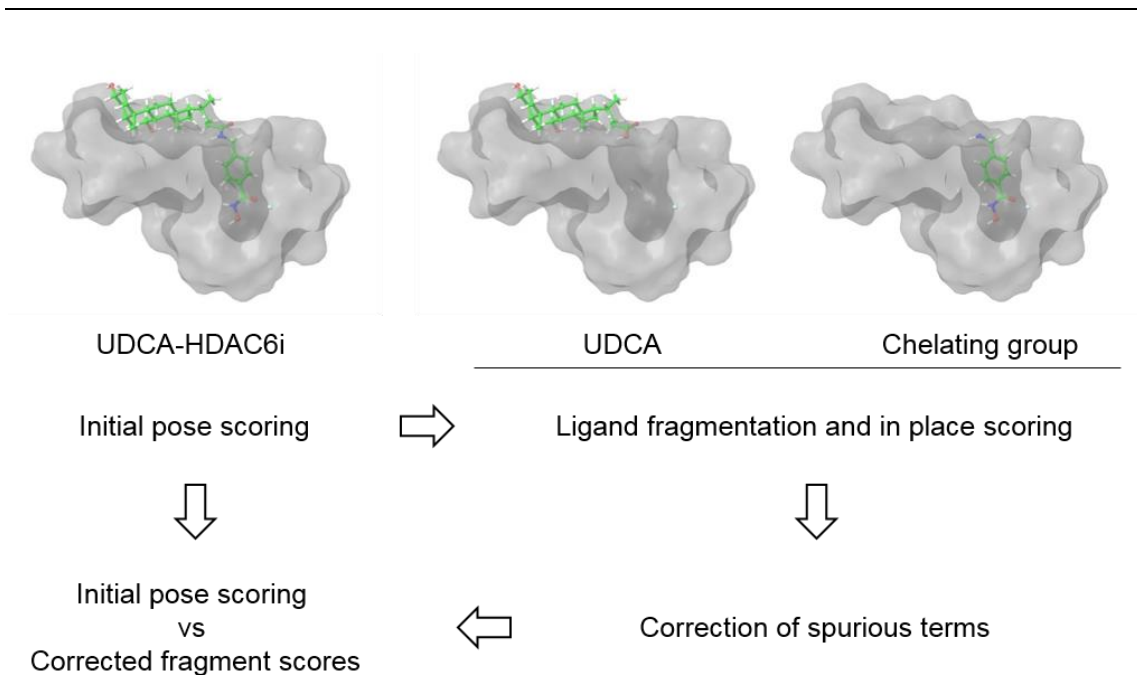


Figure R5. Schematic representation of the workflow followed to determine the contribution of the different substructures to the total binding affinity of each UDCA-HDAC6i.

For that purpose, we decomposed the total binding energy of each synthetic derivative into the contribution of the following descriptors to the final score.

- XP GScore: Total GlideScore, sum of XP terms
- Lipophilic EvdW: Lipophilic term derived from hydrophobic grid potential and fraction of the total protein-ligand vdW energy.
- PhobEn: Hydrophobic enclosure reward.
- PhobEnHB: Reward for hydrophobically packed H-bond.
- PhobEnPairHB: Reward for hydrophobically packed correlated H-bonds.
- HBond: ChemScore H-bond pair term.
- Electro: Electrostatic rewards.
- SiteMap: SiteMap ligand/receptor non-H bonding polar/hydrophobic and hydrophobic/hydrophilic complementarity terms.

-
- π Cat: Reward for pi-cation interactions.
 - CIBr: Reward for Cl or Br in a hydrophobic environment that pack against Asp or Glu.
 - LowMW: Reward for ligands with low molecular weight.
 - Penalties: Polar atom burial and desolvation penalties, and penalty for intra-ligand contacts.
 - HBPenal: Penalty for ligands with large hydrophobic contacts and low H-bond scores.
 - ExposPenal: Penalty for exposed hydrophobic ligand groups.
 - RotPenal: Rotatable bond penalti.
 - EpikState Penalty: Penalty for ionization or tautomeric states calculated by Epik.
 - Corrected GScore: XP GScore corrected by elimination of spurious terms generated by structure fragmentation.

Next, taking as starting point the optimal binding mode of each inhibitor, we separately calculated the binding energy of each substructure on its initial position, decomposing this energy into the previously mentioned descriptors. Finally, after correction of the spurious terms generated by separation of the substructures (i.e., rotational penalties, low molecular weight rewards...) we obtained the contribution of each substructure to the total binding energy of the corresponding compound. The energies are gathered as corrected GScores in Table R1.

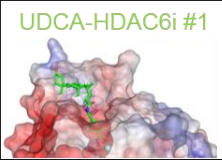
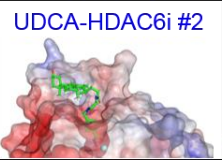
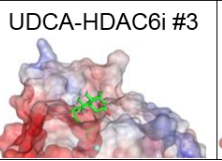
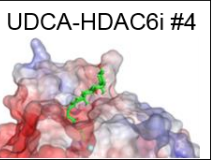












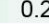
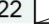
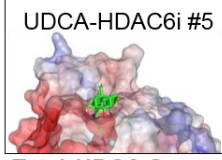
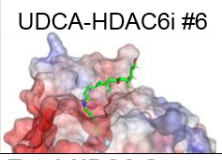
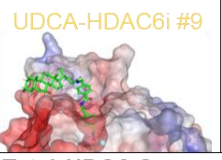
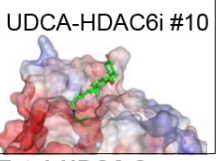











	UDCA-HDAC6i #1			UDCA-HDAC6i #2			UDCA-HDAC6i #3			UDCA-HDAC6i #4		
												
	Total UDCA Spacer			Total UDCA Spacer			Total UDCA Spacer			Total UDCA Spacer		
UDCA-HDAC6i	UDCA-HDAC6i #1			UDCA-HDAC6i #2			UDCA-HDAC6i #3			UDCA-HDAC6i #4		
XP GScore	-8.3	-3.4	-6	-7.9	-1.7	-5.3	-3.9	-3.3	-1.2	-4.8	-0.6	-2.2
Lipophilic EvdW	-4.5	-1.91	-2.72	-4.38	-1.68	-2.7	-2.18	-1.66	-0.53	-2.57	-1.48	-1.13
PhobEn	-0.66	0	-0.73	-0.39	0	-0.39	0	0	0	0	0	0
PhobEnHB	0	0	0	0	0	0	0	0	0	0	0	0
PhobEnPair HB	0	0	0	0	0	0	0	0	0	0	0	0
HBond	-2.25	-1.18	-1.67	-2.17	-0.7	-1.59	-1.66	-1.18	-1.01	-1.81	-0.48	-1.81
Electro	-1.43	-0.63	-0.81	-1.25	-0.37	-0.84	-1.14	-0.37	-0.87	-0.85	-0.08	-0.8
Sitemap	0	0	0	-0.14	-0.09	-0.04	-0.33	-0.33	0	-0.28	-0.28	0
PiCat	0	0	0	0	0	0	0	0	0	0	0	0
CIBr	0	0	0	0	0	0	0	0	0	0	0	0
LowMW	0			0			0			0		
Penalties	0	0	0	0		0	0.96	0	1.26	0	0	
HBPenal	0	0	0	0	0	0	0	0	0	0	0	0
ExposPenal	0.22	0.31	0	0.17	0.16	0.01	0.19	0.19	0	0.33	1.7	0
RotPenal	0.27	0.22		0.25	0.22		0.3	0.22		0.34	0.22	
EpikState Penalty	0.01	0.01	0.01	0.01	0.01	0.01	0.01	0.01	0.01	0	0	0
Corrected GScore	-9.1	-3.18	-5.92	-7.99	-2.45	-5.54	-4.26	-3.12	-1.14	-4.14	-0.4	-3.74
	UDCA-HDAC6i #5			UDCA-HDAC6i #6			UDCA-HDAC6i #9			UDCA-HDAC6i #10		
												
	Total UDCA Spacer			Total UDCA Spacer			Total UDCA Spacer			Total UDCA Spacer		
UDCA-HDAC6i	UDCA-HDAC6i #5			UDCA-HDAC6i #6			UDCA-HDAC6i #9			UDCA-HDAC6i #10		
XP GScore	-3.9	-0.7	-1.2	-4.2	-0.2	-5	-9.4	-3.3	-6.1	-4.7	-0.3	-4.9
Lipophilic EvdW	-2.9	-1.61	-1.41	-2.95	-1.05	-1.97	-4.8	-1.53	-3.3	-2.85	-0.74	-1.7
PhobEn	0	0	-0.18	0	0	-0.13	-0.61	0	-0.61	-0.5	0	-0.53
PhobEnHB	0	0	0	0	0	0	0	0	0	0	0	0
PhobEnPair HB	0	0	0	0	0	0	0	0	0	0	0	0
HBond	-1.33	-0.35	-1.03	-2.17	-0.96	-1.59	-3.34	-2.04	-1.6	-2.17	-0.96	-1.86
Electro	-1.5	-0.41	-1.1	-1.13	-0.39	-0.81	-1.6	-0.56	-1.11	-1.12	-0.33	-0.82
Sitemap	-0.17	-0.17	0	0	0	0	-0.04	0	-0.04	-0.02	-0.02	0
PiCat	0	0	0	0	0	0	0	0	0	0	0	0
CIBr	0	0	0	0	0	0	0	0	0	0	0	0
LowMW	0			0			0			0		
Penalties	0	0		0	0	0	0	0	0	0	0	0
HBPenal	0	0	0	0	0	0	0	0	0	0	0	0
ExposPenal	1.99	1.85	0	2.03	2.16	0	0.79	0.79	0	1.68	1.69	0
RotPenal	0	0.22	0	0	0.22	0	0.19	0.22		0.28	0.22	
EpikState Penalty	0	0	0	0	0	0	0.01	0.01	0.01	0.16	0.16	0.16
Corrected GScore	-4.19	-0.47	-3.72	-4.52	-0.02	-4.5	-9.76	-3.11	-6.65	-4.73	0.02	-4.75

Table R1. Contribution of the different molecular descriptors (see text) to the total binding affinities on UDCA-HDAC6is and their forming substructures after ligand fragmentation.

It is interesting to note that the difference between the obtained initial XP GScore for each compound and the sum of the corrected XP GScores for its forming substructures was in all cases ≤ 0.8 kcal/mol, confirming the reliability of the method. Importantly, we observed that in the cases of UDCA-HDAC6i #1, #2 and #9, the three compounds that displayed the highest binding energies, the contribution of UDCA to the final binding energy was approximately one third of the total value, being this contribution mainly integrated by van der Waals interactions and hydrogen bonds. (Table R1).

As mentioned before, one of the main distinctive features of HDAC6 with respect to other HDACs is the presence of tandem catalytic domains CD1 and CD2. Although most catalytic potential of HDAC6 has been commonly attributed to CD2,¹⁸⁰ two recently published studies using different HDAC6 constructs in directed mutagenesis, activity and crystallography experiments, have pointed out the potential importance of HDAC6 CD1 for HDAC6 catalytic activity.^{118,119} For this reason, we decided to submit our UDCA-HDAC6is to docking simulations on HDAC6 CD1 in order to evaluate their inhibitory potential on this domain. Since there is not crystallographic structure of human HDAC6 CD1 available, we attempted to generate a homology model of the human catalytic domain based on the X-ray structure of HDAC6 CD1 from zebrafish (PDB code: 5G0G). For that purpose, we aligned the predicted secondary structures of both sequences (i.e., human HDAC6 CD1 and zebrafish HDAC6 CD1) (Figure R6) and generated a knowledge-based 3D model using Prime^{181,182} software included in the Maestro 10.4 software package.

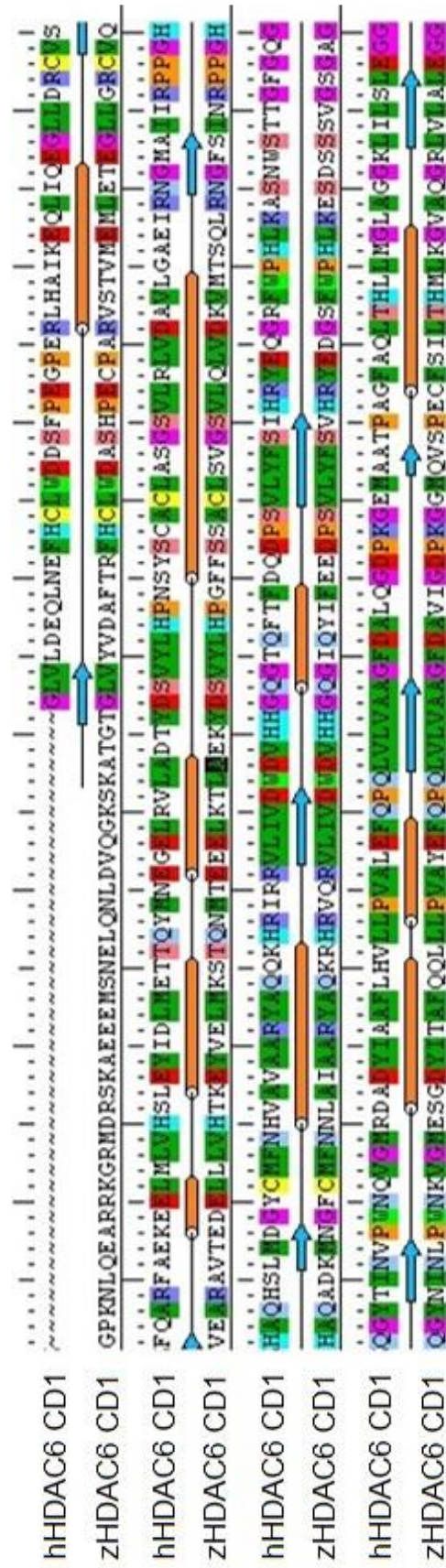


Figure R6. Secondary structure prediction and sequence alignment of human HDAC6 CD1 (hHDAC6 CD1) and zebrafish HDAC6 CD1 (zHDAC6 CD1 (PDB code: 5G0G)) performed with Prime software.^{181,182}

Once we obtained the 3D homology model, we optimized and minimized the protein structure and used it in docking experiments with the previously described synthetic UDCA derivatives. Our results (Table R2) showed that as observed for HDAC6 CD2, UDCA-HDAC6i #9 and #2 maintained high affinity for CD1. On the other hand, while UDCA-HDAC6i #1 showed lower affinity for CD1 when compared to CD2, compound #10 showed substantially higher affinity for CD1 than for CD2, being the second best ranked compound for CD1.

UDCA-HDAC6i	CD1		CD2	
	XP GScore (kcal/mol)	Rank	XP GScore (kcal/mol)	Rank
#1	-6.3	(4)	-8.3	(2)
#2	-7.4	(3)	-7.9	(3)
#3	-5.1	(8)	-3.9	(6)
#4	-5.3	(7)	-4.8	(4)
#5	-5.6	(6)	-3.9	(6)
#6	-5.9	(5)	-4.2	(5)
#9	-8.6	(1)	-9.4	(1)
#10	-7.9	(2)	-4.7	(4)

Table R2. Predicted binding affinities (XP GScore) of the different UDCA-HDAC6is for the catalytic site of human HDAC6 CD1 homology model. The data obtained for HDAC6 CD2 are shown for comparative purposes.

R.4 UDCA actively contributes to the selective HDAC6 inhibitory activity of UDCA-HDAC6is

We confirmed by immunoblot the previously reported²¹ overexpression of HDAC6 in human cystic cholangiocytes compared to normal human cholangiocytes in culture (Figure R7).

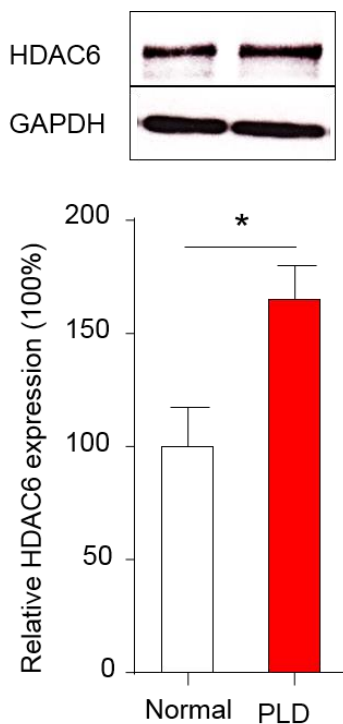


Figure R7. Representative immunoblot and graphical representation of the relative HDAC6 protein expression in human PLD and normal cholangiocytes.

Since acetylated α -tubulin is one of the main deacetylation targets of HDAC6, the levels of acetylated α -tubulin in cholangiocytes are considered a good marker of HDAC6 expression and activity on these cells. Therefore, in order to evaluate the HDAC6 inhibitory potential of UDCA-HDAC6is, the levels of acetylated α -tubulin were measured by immunoblot in cell cultures of human cystic cholangiocytes incubated with the aforementioned synthetic UDCA

conjugates (Figure R8). In addition, acetylation levels of lysine 9 of the nuclear histone 3 (H3K9) were measured as a control of selectivity (negative control).

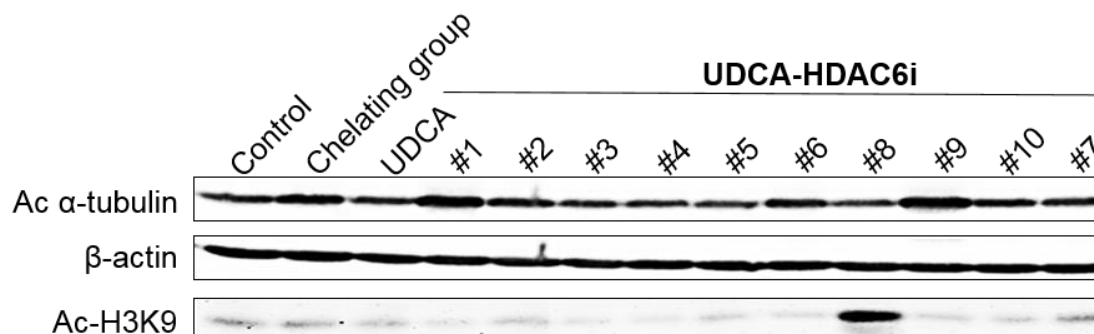


Figure R8. *In vitro* HDACi activity in PLD cells. Representative immunoblot of the acetylation levels of α -tubulin and Histone 3 (H3K9) after 24h treatment with 2 μ M of each compound. Chelating agent refers to the spacer ended on a Zn(II) chelating motif directly bonded to UDCA in UDCA-HDAC6i #1.

Our results (Figure R8) revealed that at low concentration (2 μ M), at least four of the synthesized UDCA conjugates (#1, #2, #6 and #9) induced an increase in the levels of acetylated α -tubulin in cystic cholangiocytes, without affecting the acetylation of the nuclear H3K9 residue (negative control), thus indicating selective inhibitory activity on HDAC6. In contrast, one of the new synthesized UDCA conjugates (#8) substantially increased the levels of H3K9 in cystic cholangiocytes without increasing the acetylation of α -tubulin, being a potential inhibitor of nuclear HDACs (Figure R8). It is interesting to note that, comparison between the *in silico* predicted binding energies of the aforementioned UDCA conjugates on HDAC6 CD2 and their effect on the HDAC6-dependent levels of acetylated α -tubulin in cystic cholangiocytes showed significant correlation

($r^2=0.8031$) for these two parameters, confirming the predictive accuracy of our computational approach (Figure R9).

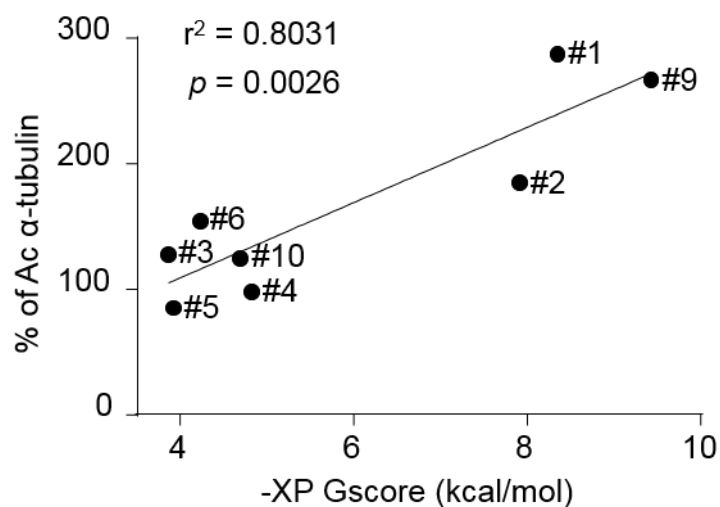
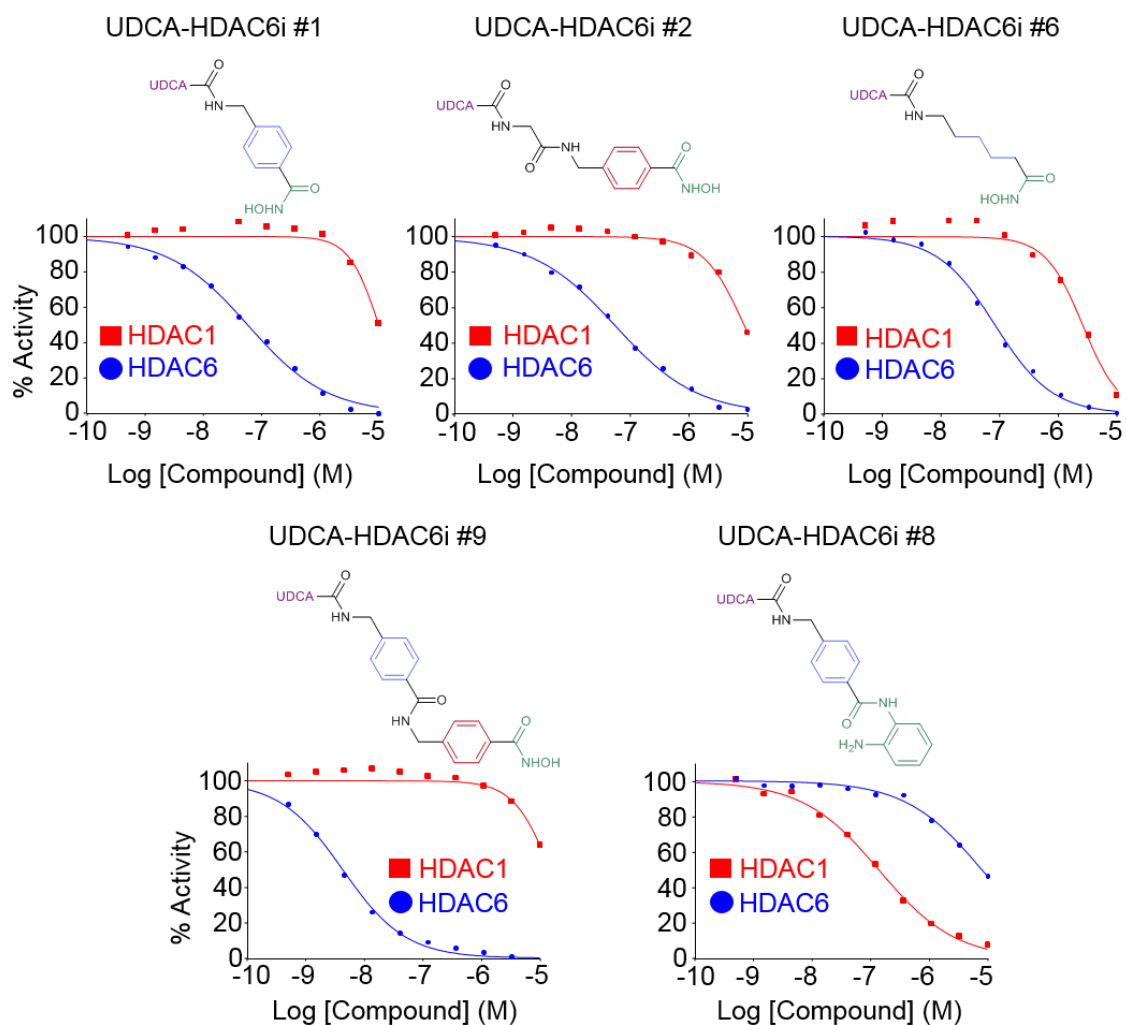


Figure R9. Experimental validation of the *in silico* docking model. Graphical representation of predicted binding energies *versus* the normalized HDAC6 inhibitory activity in PLD cells.

Next, the inhibitory capacity of UDCA-HDAC6i #1, #2, #6, #8 and #9 on purified HDAC1 and HDAC6 enzymes was measured by monitoring the dose-dependent deacetylation of a fluorogenic acetylated peptide (Figure R10). Data showed that UDCA-HDAC6i #1, #2, #6 and #9 displayed nanomolar half-maximal inhibitory concentration (IC_{50}) values (58 nM, 56.1 nM, 82.1 nM, 4.26 nM, respectively) for HDAC6 inhibition, concomitantly with a high degree of selectivity, calculated as the HDAC6i/HDAC1i ratio, particularly in the case of compounds #1, #2, and #9 (Figure R10). On the other hand, UDCA-HDAC6i #8 showed both high inhibitory activity and selectivity for HDAC1 ($IC_{50} = 140$ nM) (Figure R10).



Enzyme	UDCA-HDAC6i					Chelating group	UDCA
	#1	#2	#6	#9	#8		
HDAC1	1.01E-05	9.01E-06	2.57E-06	1.52E-05	1.40E-07	ND	ND
HDAC6	5.80E-08	5.61E-08	8.21E-08	4.26E-09	8.08E-06	6.89E-07	ND
Selectivity	HDAC6/HDAC1	174	160	31	3574	-	-
	HDAC1/HDAC6	-	-	-	-	58	-

Figure R10. Dose response curves and IC₅₀ values of the inhibitory activity of UDCA-HDAC6i #s #1 (n=9), #2 (n=9), #6 (n=3), #8 (n=3) and #9 (n=3) on HDAC6 and HDAC1. For curve fitting and IC₅₀ calculation, log (inhibitor) versus normalized response with variable slope equation was obtained by means of GraphPad6 software. Chelating group is (4-(hydroxycarbonyl)phenyl)methanaminium chloride.

Importantly, UDCA itself did not exhibit any direct HDAC inhibitory activity; however, its covalent bonding with the structure of the chelating group in order to form UDCA-HDAC6i #1, significantly increased (~12 fold) its HDAC6 inhibitory capacity (IC₅₀ = 58 nM) with respect to that measured for the isolated chelating group unit (IC₅₀ = 689 nM). In addition, the effect of UDCA-HDAC6i #1 and #2 was also evaluated on purified HDAC2-5 and HDAC7-11 enzymes, showing similar inhibitory capacity than in HDAC1 and significantly less compared to HDAC6 (Table R3).

Enzyme	UDCA-HDAC6i						Chelating group	UDC A
	#1	#2	#6	#9	#8			
HDAC1	1.01E-05	9.01E-06	2.57E-06	1.52E-05	1.40E-07	ND	ND	
HDAC2	1.88E-05	1.32E-05	-	-	5.16E-07	ND	ND	
HDAC3	8.37E-06	9.99E-06	-	-	-	ND	ND	
HDAC4	1.65E-05	ND	-	-	-	ND	ND	
HDAC5	1.41E-05	ND	-	-	-	4.35E-04	ND	
HDAC6 IC ₅₀ (M)	5.80E-08	5.61E-08	8.21E-08	4.26E-09	8.08E-06	6.89E-07	ND	
HDAC7	7.47E-06	1.76E-05	-	-	-	1.47E-05	ND	
HDAC8	8.94E-07	6.15E-07	-	-	-	1.36E-05	ND	
HDAC9	1.34E-05	1.16E-05	-	-	-	ND	ND	
HDAC10	2.45E-05	2.18E-05	-	-	-	ND	ND	
HDAC11	2.33E-06	2.56E-06	-	-	-	ND	ND	
Selectivity	HDAC6/ HDAC1	174	160	31	3574	-	-	
	HDAC1/ HDAC6	-	-	-	-	58	-	

Table R3. IC₅₀ values of UDCA-HDAC6i #1, #2, #6, #9 and #8 in HDAC (1-11). ND: non-determined. (-), not analyzed.

All these data demonstrate that the presence of UDCA in the UDCA-HDAC6i structure provides a synergic effect on their inhibitory capacity on HDAC6, pointing out the active and critical contribution of UDCA to the pharmacological effect of these synthetic derivatives.

R.5 Chemical and structural factors that determine inhibitory activity and selectivity of UDCA-HDAC6is

The analysis of the interactions between the individual protein residues of human HDAC6 CD2 and the different UDCA-HDAC6is revealed important information about some events that seem to be critical to determine the activity and selectivity of UDCA-HDAC6is (Table R4). First, our docking experiments showed that, contrary to what was first expected, in 7 of the 8 docked compounds (UDCA-HDAC6i #1, #2, #3, #4, #6, #9, and #10), the hydroxamate moiety exhibited a monodentate coordination geometry to the Zn(II) cation of HDAC6 CD2 by interaction between the carboxyl group of the inhibitor and the metal ion of the enzyme. According to this, in 6 of the mentioned cases (#1, #2, #4, #6, #9, and #10), the NH group of the hydroxamic acid preferentially established a hydrogen bond with the carboxamide group of glycine 619. This generated a shift of the hydroxy group of the hydroxamate far from the coordination sphere of Zn(II) cation, therefore avoiding the possibility of establishing a classical bidentate coordination geometry (Table R4).

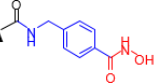
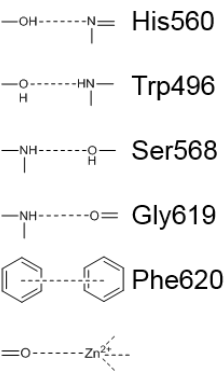
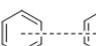
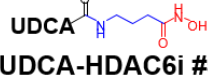
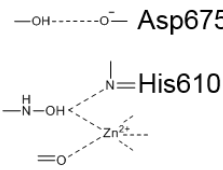
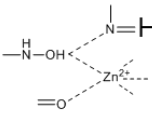
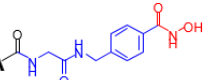
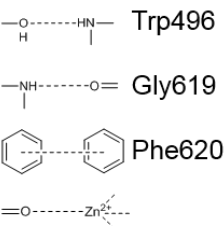
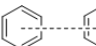
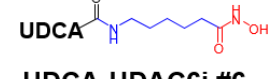
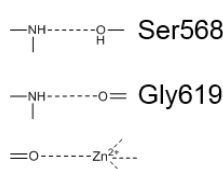
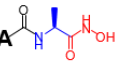
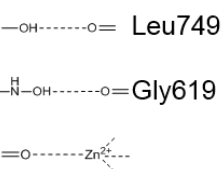
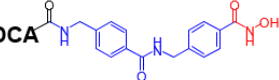
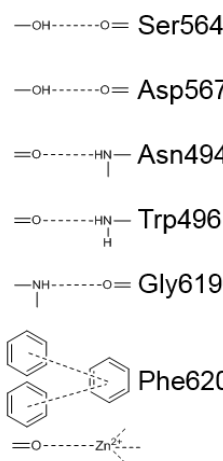
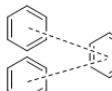
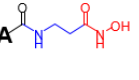
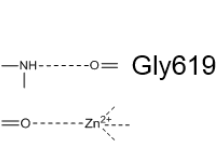
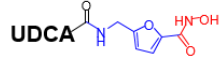
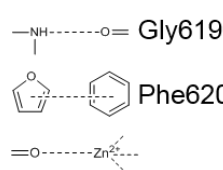
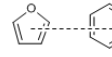
Compound	Interaction	Compound	Interaction
 <p>UDCA-HDAC6i #1</p> <p>-8.3 kcal/mol</p>	 <p>—OH····N= His560 —O—H····HN— Trp496 —NH····O— Ser568 —NH····O= Gly619  Phe620 =O····Zn²⁺</p>	 <p>UDCA-HDAC6i #5</p> <p>-3.9 kcal/mol</p>	 <p>—OH····O⁻ Asp675  N=His610</p>
 <p>UDCA-HDAC6i #2</p> <p>-7.9 kcal/mol</p>	 <p>—O—H····HN— Trp496 —NH····O= Gly619  Phe620 =O····Zn²⁺</p>	 <p>UDCA-HDAC6i #6</p> <p>-4.2 kcal/mol</p>	 <p>—NH····O— Ser568 —NH····O= Gly619 =O····Zn²⁺</p>
 <p>UDCA-HDAC6i #3</p> <p>-3.9 kcal/mol</p>	 <p>—OH····O= Leu749 —N—OH····O= Gly619 =O····Zn²⁺</p>	 <p>UDCA-HDAC6i #9</p> <p>-9.4 kcal/mol</p>	 <p>—OH····O= Ser564 —OH····O= Asp567 =O····HN— Asn494 =O····HN— Trp496 —NH····O= Gly619  Phe620 =O····Zn²⁺</p>
 <p>UDCA-HDAC6i #4</p> <p>-4.8 kcal/mol</p>	 <p>—NH····O= Gly619 =O····Zn²⁺</p>	 <p>UDCA-HDAC6i #10</p> <p>-4.7 kcal/mol</p>	 <p>—NH····O= Gly619  Phe620 =O····Zn²⁺</p>

Table R4. Schematic representation of the main protein-ligand interactions observed in the docking model of human HDAC6 CD2.

Importantly, the three compounds that exhibited the strongest binding energies as well as the highest levels of activity and selectivity (UDCA-HDAC6i #1, #2 and #9) were the ones containing one or two 1,4-phenylene moieties acting as the linker of the inhibitor, and a hydroxamic acid as the Zn(II) chelating group. As mentioned above, these three compounds oriented the steroid skeleton

of UDCA towards the same region of the protein surface (Figures R3 and R4). When comparing the interactions displayed by these three compounds we could observe some interesting similarities. In this regard, these three compounds established π - π interactions between the 1,4-phenylene groups of the inhibitors and phenylalanine 620 flanking the hydrophobic channel that connects the outer rim with the internal active site (Table R4). Importantly, in the three cases hydrogen bonds were established between the hydroxy groups located in the hydrocarbon skeleton of UDCA and different aminoacids of the protein surface. Finally, these three compounds interacted by hydrogen bonding with tryptophan 496 located in one of the outer cavities surrounding the active site (Figure R4 and Table R4).

Interestingly, structural comparison of UDCA-HDAC6i #1 with UDCA-HDAC6i #6 revealed that the respective distance between C-24 and the carboxamide group of the hydroxamate moiety were 7.64 Å and 8.66 Å respectively (Figure R11), thus showing a difference of only 1 Å.

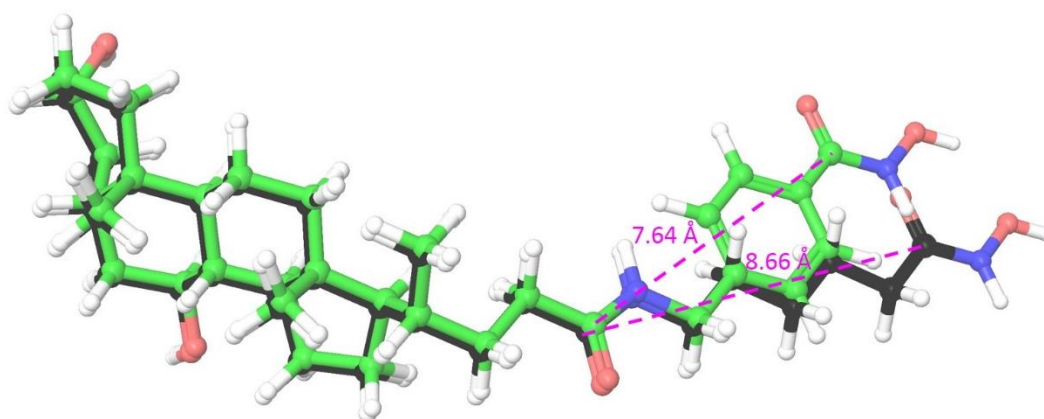
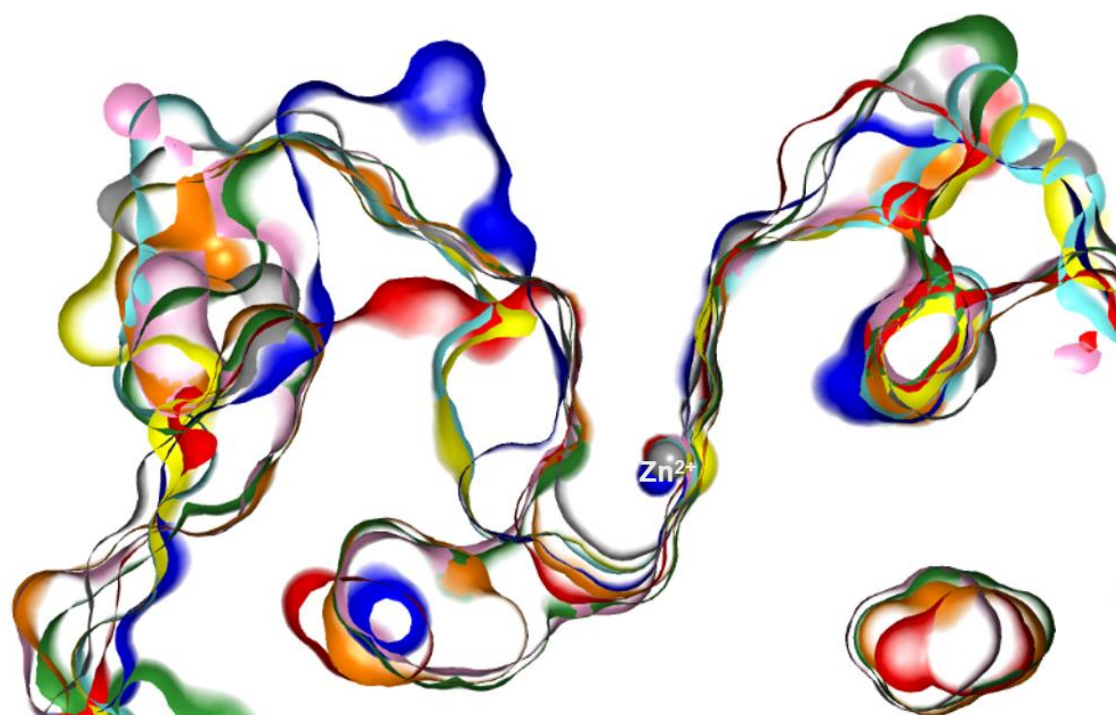
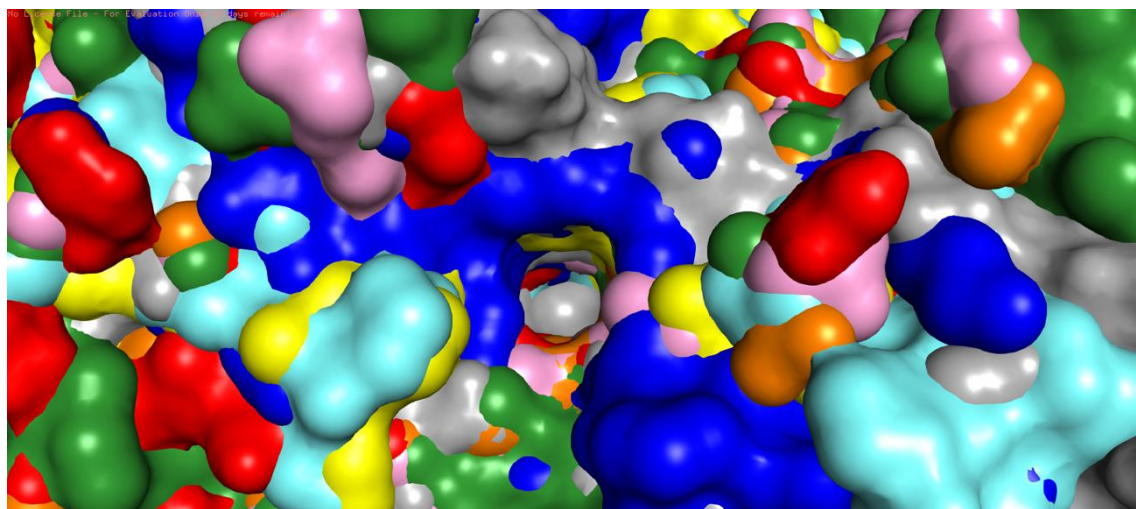


Figure R11. Structural comparison of UDCA-HDAC6i #1 and #6. Dashed pink line shows the distance between C-24 and the carboxamide group of the hydroxamate moiety on each compound.

Furthermore, the only structural difference between UDCA-HDAC6i #1 and #2 is the presence of a glycine residue in UDCA-HDAC6i #2 that elongates the length of the linker around 2.5 Å in respect to UDCA-HDAC6i #1. Accounting for this, linker length in these three cases would be UDCA-HDAC6i #2 > UDCA-HDAC6i #6 > UDCA-HDAC6i #1. However, HDAC6 selectivity for these compounds appeared to be #1 > #2 >>> #6. Therefore, since they share the same chelating group (i.e., hydroxamic acid), the same van der Waals cap (i.e., UDCA) and possess similar linker lengths, it seems that the chemical nature of the spacer is critical to determine selectivity of these compounds, and in this regard 1, 4-phenylene groups provide substantial advantage towards HDAC6 selectivity when compared to alkyl groups. Although there are some important differences in terms of HDAC6 activity between inhibitors containing paraphenyl spacers and compound carrying alkyl spacer (i.e., UDCA-HDAC6i #1 (IC₅₀ = 58 nM), #2 (IC₅₀ = 56,1 nM) and #9 (IC₅₀ = 4.26 nM) *versus* UDCA-HDAC6i #6 (IC₅₀ = 82.1 nM)) this difference becomes much more exacerbated when comparing HDAC6/HDAC1 selectivity between these two type of compounds (i.e., #1 (HDAC6/HDAC1 = 174), #2 (HDAC6/HDAC1 = 160) and #9 (HDAC6/HDAC1 = 3574) vs #6 (HDAC6/HDAC1 = 31)). For this reason, we hypothesized that, at least for this type of compounds, HDAC6 selectivity would be in part dictated by the optimized HDAC6 activity, but largely by the suboptimal capacity to bind the catalytic domain of other HDAC isoforms. Thus, to test this hypothesis we carried out the alignment of the catalytic domains of human HDAC1, 2, 3, 4, 7, 8 and zebrafish HDAC10 (PDB entries: 5ICN, 6G3O, 4A69, 4CBT, 3ZNR ,5VI6 and 5TD7) with our docking model of human HDAC6 CD2 (Figure R12 and Figure R13).



HDAC isoforms: ● HDAC6 ● HDAC2 ● HDAC4 ● HDAC8
 ● HDAC1 ● HDAC3 ● HDAC7 ● HDAC10

Figure R12. Upper and side views of the three-dimensionally aligned active sites of different HDAC isoforms (HDAC1, 2, 3, 4, 6, 7, 8 and zebrafish HDAC10 (PDB entries: 5ICN, 6G3O, 4A69, 4CBT, 5EDU, 3ZNR, 5VI6 and 5TD7)).

Alignment of the catalytic domains of the different isoforms revealed some differences in the architecture of the outer rim, the hydrophobic channel, and the active site (Figure R12). In this regard, while isoforms 2, 6 and 8 share similar features in terms of depth and width of the hydrophobic channel, isoforms 4 and 7 possess a wider cavity and isoform 10 becomes wider at the bottom of the channel. In addition, isoforms 1 and 3 extend the hydrophobic channel deeper into the protein internal face. Interestingly, in all cases the Zn(II) cation is located in a very similar position. However, although there are some differences in the particular architectures of the hydrophobic channels of the different HDAC isoforms, these are not enough to explain the substantial differences in terms of selectivity observed between UDCA-HDAC6i #6 and compounds carrying 1, 4-phenylene spacers (Figure R10 and table R3). Outstandingly, analysis of the surface topography of the catalytic sites of the different HDAC isoforms aligned to our docking model revealed fundamental information to understand HDAC6 selectivity in UDCA-HDAC6is and most probably in other HDAC inhibitors (Figures R12 and R13). In this regard, we observed that the surface cavity preferentially occupied by the UDCA moiety in the compounds containing 1, 4-phenylene linkers is not present in the other HDAC isoforms, while the other two cavities occupied by less active/selective UDCA-HDAC6is (UDCA-HDAC6i #6) remained almost intact (Figure R13).

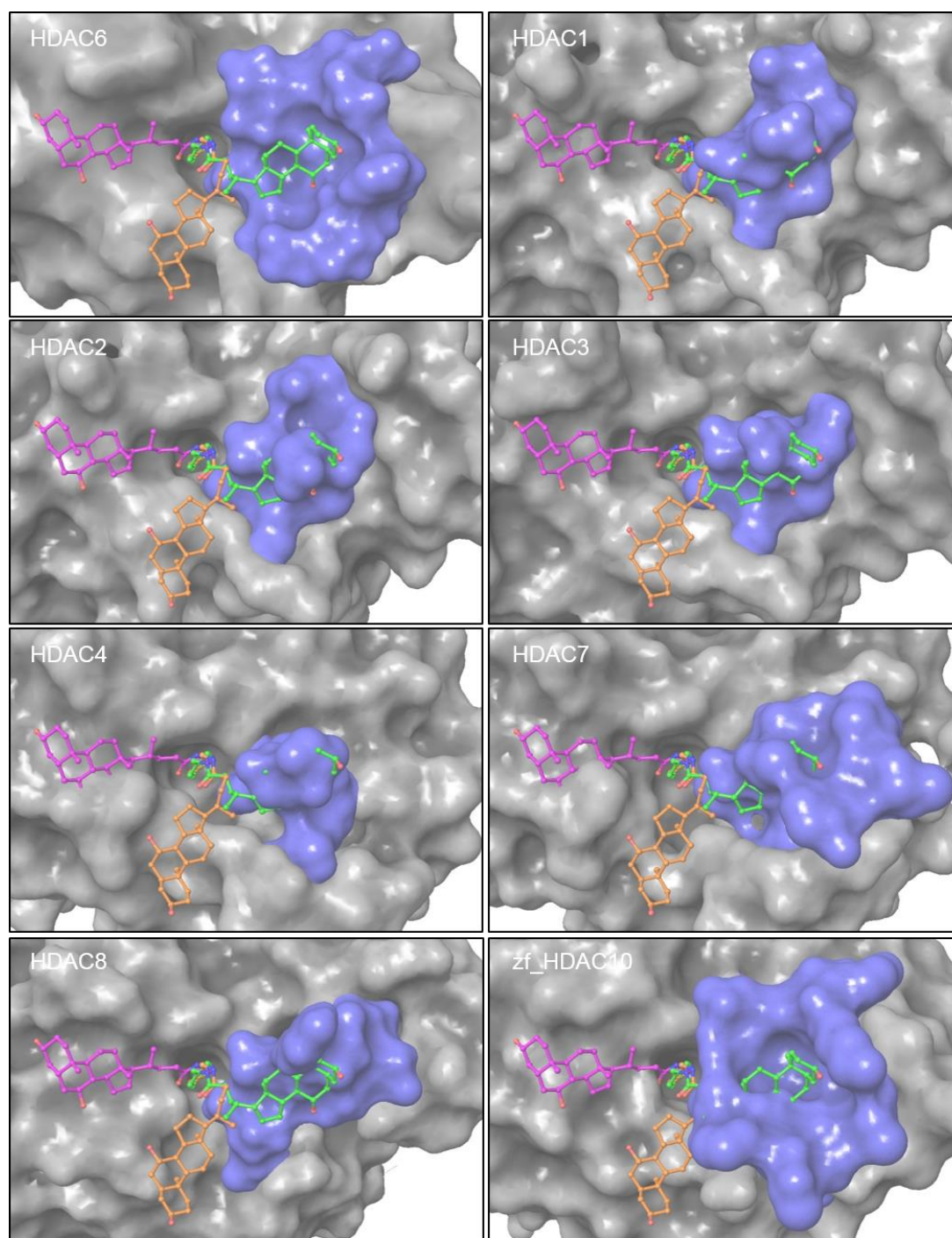


Figure R13. 3D structural alignment of the catalytic domains of different HDAC isoforms with the docking model of human HDAC6 CD2. In blue, surface region in which the three most active/selective UDCA-HDAC6is preferentially accommodate UDCA in HDAC6.

Accordingly, sequence alignment of the mentioned HDAC isoforms confirmed a very low degree of sequence identity in the mentioned region between HDAC6 and the other HDAC isoforms (Figure R14).

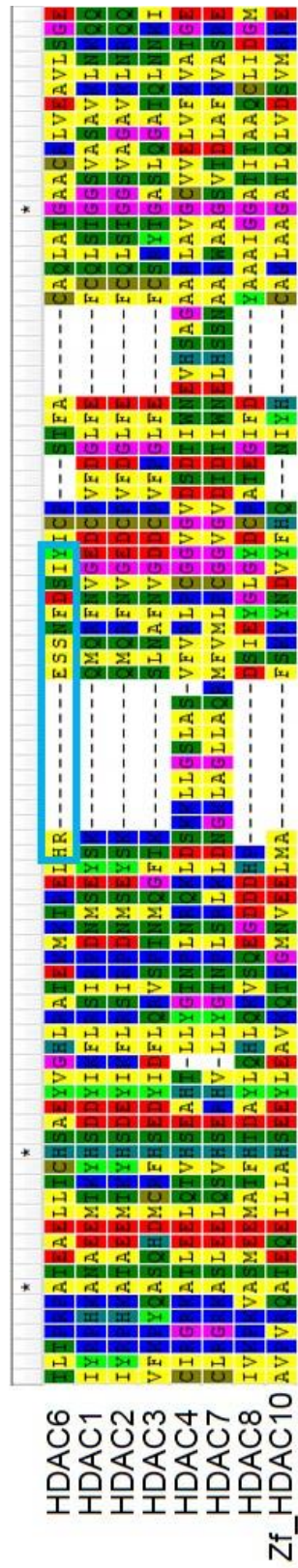


Figure R14. Sequence alignment of human HDACs 6, 1, 2, 3, 4, 7, 8 and zebrafish HDAC10. Light blue rectangle includes the amino acids within the external cavity of HDAC6 CD2 preferentially occupied by UDCA hydrocarbon skeleton in UDCA-HDAC6i #1, #2 and #9. Alignment performed with MEGA6 software.⁴¹

R.6 Potency and selectivity, pharmacokinetic properties and synthetic cost make UDCA-HDAC6 #1 the best candidate for potential clinical translation

Once the HDAC6 inhibitory potency and selectivity were confirmed on four of the newly synthesized UDCA-HDAC6is, we had to select the best candidate for further characterization and evaluation of its therapeutic potential *in vivo*. Although UDCA-HDAC6i #9 showed the highest HDAC6i activity and selectivity values in enzymatic assays, we considered some other important factors for the selection of the lead compound. First, the synthetic route for UDCA-HDAC6i #9 is substantially longer than that for other UDCA-HDAC6is. For this reason, the synthesis of UDCA-HDAC6i #9 in larger scales would come out to be very expensive, raising some concerns about its clinical translation. For example, while UDCA-HDAC6i #1 requires only two synthetic steps with an overall yield of 51%, UDCA-HDAC6i #9 needs four steps what requires more starting materials and leads to a substantial drop in the overall yield to only 27 % (Figure R2).

The pharmacokinetic properties of the compound should also be considered for the final selection. One of the main components of our therapeutic strategy was to benefit from the intrinsic hepatotropic features of UDCA to target and maintain the compound into the enterohepatic circulation after oral administration and gastrointestinal absorption. In order to reduce the number of animals used for experimentation, we applied QikProp software included in Maestro package 10.4 to perform an *in silico* prediction of several pharmacokinetic parameters for all the designed UDCA-HDAC6is, obtaining considerably better values for UDCA-HDAC6i #1 than for the other three candidates in terms of oral absorption (Table R5).

Range of recommended values		UDCA-HDAC6#1	UDCA-HDAC6#2	UDCA-HDAC6#3	UDCA-HDAC6#4	UDCA-HDAC6#5	UDCA-HDAC6#6	UDCA-HDAC6#7	UDCA-HDAC6#8	UDCA-HDAC6#9	UDCA-HDAC6#10
Percent Human oral absorption	>80% is high	55.1	25.9	58.7	54.4	53.2	44.4	57.3	60.2	38.7	47.9
#stars	0-5	1	4	0	0	0	1	9	5	8	1
#rotor	0-15	10	12	9	10	11	13	12	11	13	10
mol_MW	130-725	540.7	597.8	478.7	478.7	492.7	520.8	692.0	615.9	673.9	530.7
dipole	1-12.5	12.6	10.7	5.7	6.3	6.3	6.4	3.5	11.3	8.1	9.1
SASA	300-1000	895.9	993.7	805.3	809.0	842.1	908.2	1148.2	1021	1111.1	882.1
FOSA	0-750	513.1	554.6	567.4	547.5	580.5	646.4	506.8	513.3	544.6	511.8
FISA	7-330	254.4	301.4	237.8	261.5	261.7	261.8	214.4	219.1	307.5	272.2
PISA	0-450	128.3	137.7	0	0	0	0	427.0	288.6	258.9	98.1
WPSA	0-175	0	0	0	0	0	0	0	0	0	0
volume	500-2000	1695.4	1868.3	1517.7	1519.5	1580.4	1701.7	2182.7	1941.4	2101.9	1649
donorHB	0-6	5	5.25	4.25	4	5	5	5.5	5.5	6	5
accptHB	2-20	10.1	11.85	9.35	9.1	10.1	10.1	9.4	9.4	12.6	10.6
glob	0.75-0.95	0.8	0.7	0.8	0.8	0.8	0.8	0.7	0.7	0.7	0.8
QPpoltz	13-70	56.5	62.2	48.8	48.2	50	53.6	77.6	67.2	72.1	54.4
QPlogPC16	4-18	18	20.3	15	15.2	16	17.3	25.2	21.6	23.9	17.5
QPlogPoct	8-35	33.1	36.1	27.7	27.2	29.7	30.8	39.7	36.8	40.7	32
QPlogPw	4-45	21.5	26.1	21.1	20.5	22.8	22.5	23.7	22.5	26.8	22.1
QPlogPo/w	-2-6.5	2.8	2.2	1.5	1.5	1.3	2	6.6	4.9	3.9	2.2
QPlogS	-6.5-0.5	-5.9	-5.6	-3.9	-3.8	-3.8	-4.5	-9.8	-7.9	-7.9	-5.4
QPlogBB	-3-1.2	-2.9	-3.8	-2.5	-2.8	-3	-3.2	-3	-2.8	-4.2	-3.1
IP(eV)	7.9-10.5	9.6	9.7	9.6	9.8	9.7	9.7	8.2	8.2	9.7	9.5
EA(eV)	-0.9-1.7	0.4	0.7	-0.6	-0.7	-0.7	-0.7	0.7	0.5	0.7	0.5
#metab	1-8	4	5	4	4	4	4	5	7	5	5
QPlogKhsa	-1.5-1.5	0.3	-0.1	-0.3	-0.2	-0.4	-0.2	1.4	0.9	0.6	0.1
PSA	7-200	142.8	181.2	140.8	145.1	145.1	145.1	137.1	138	179.8	153.4

Table R5. QikProp predicted values. Percent Human Oral Absorption, predicted on 0 to 100% scale, based on a quantitative multiple linear regression model. #stars, number of property or descriptor values that fall outside the 95% range of similar values for known drugs. #rotor, number of non-trivial (not CX3), non-hindered (not alkene, amide, small ring) rotatable bonds. MW, molecular weight of the molecule. Dipole†, computed dipole moment of the molecule. SASA, total solvent accessible surface area (SASA) in square angstroms using a probe with a 1.4 Å radius. FOSA, hydrophobic component of the SASA (saturated carbon and attached hydrogen). FISA, hydrophilic component of the SASA (SASA on N, O, and H on heteroatoms). PISA π, (carbon and attached hydrogen) component of the SASA. WPSA, weakly polar component of the SASA (halogens, P, and S). Volume, total solvent-accessible volume in cubic angstroms using a probe with a 1.4 Å radius. donorHB, estimated number of hydrogen bonds that would be donated by the solute to water molecules in an aqueous solution. accptHB, estimated number of hydrogen bonds that would be accepted by the solute from water molecules in an aqueous solution. For donorHB and accptHB, values are averages taken over a number of configurations, so they can be non-integer. glob, globularity descriptor, where r is the radius of a sphere with a volume equal to the molecular volume. Globularity is 1.0 for a spherical molecule. QPpolrz, predicted polarizability in cubic angstroms. QPlogPC16, predicted hexadecane/gas partition coefficient. QPlogPoct‡, predicted octanol/gas partition coefficient. QPlogPw, predicted water/gas partition coefficient. QPlogPo/w, predicted octanol/water partition coefficient. QPlogS, predicted aqueous solubility, log S. S in mol dm⁻³ is the concentration of the solute in a saturated solution that is in equilibrium with the crystalline solid. QPlogBB, predicted brain/blood partition coefficient. IP(ev)†, PM3 calculated ionization potential. EA(ev)†, PM3 calculated electron affinity. #metab‡, number of likely metabolic reactions. QPlogKhsa, prediction of binding to human serum albumin. PSA, Van der Waals surface area of polar nitrogen and oxygen atoms.

Furthermore, while UDCA-HDAC6i #1 displayed values within the recommended range for all parameters except one, UDCA-HDAC6i #9 fell out of the recommended range in eight different parameters (Table R5). Nevertheless, despite UDCA-HDAC6i #9 inhibitory activity was higher in the enzymatic assays (Figure R10), when compared to UDCA-HDAC6i #1, activity assays performed in PLD cells revealed a similar degree of α -tubulin acetylation at the same concentrations (Figure R8). Last but not the least, one of the main parts of our hypothesis was to maintain the therapeutic potential of UDCA for PLD treatment within our molecules. In this sense we hypothesized that UDCA could trigger some of its therapeutic effects either directly as part of the UDCA-HDAC6#, or upon hepatic metabolism of the amide bond and further liberation of an intact UDCA molecule. However, a potential limitation for the dual activity of these compounds could be the difference in the concentration ranges required for their individual activities (μ M for UDCA *versus* nM for UDCA-HDAC6#s), which was clearly most exacerbated in the case of UDCA-HDAC6i #9. Taking into account all of these considerations, we selected UDCA-HDAC6i #1 for further investigations about its therapeutic potential for PLDs.

R.7 UDCA-HDAC6i #1 halts hepatorenal cystogenesis in PCK rats

The therapeutic value of UDCA-HDAC6i #1 was evaluated in PCK rats (*Pkhd1* mutant), a well-characterized animal model that spontaneously develops hepatorenal cystogenesis overtime.^{183,184} Eight weeks-old PCK rats were treated (15 mg/kg day by oral gavage) with UDCA-HDAC6i #1 for 5 months.

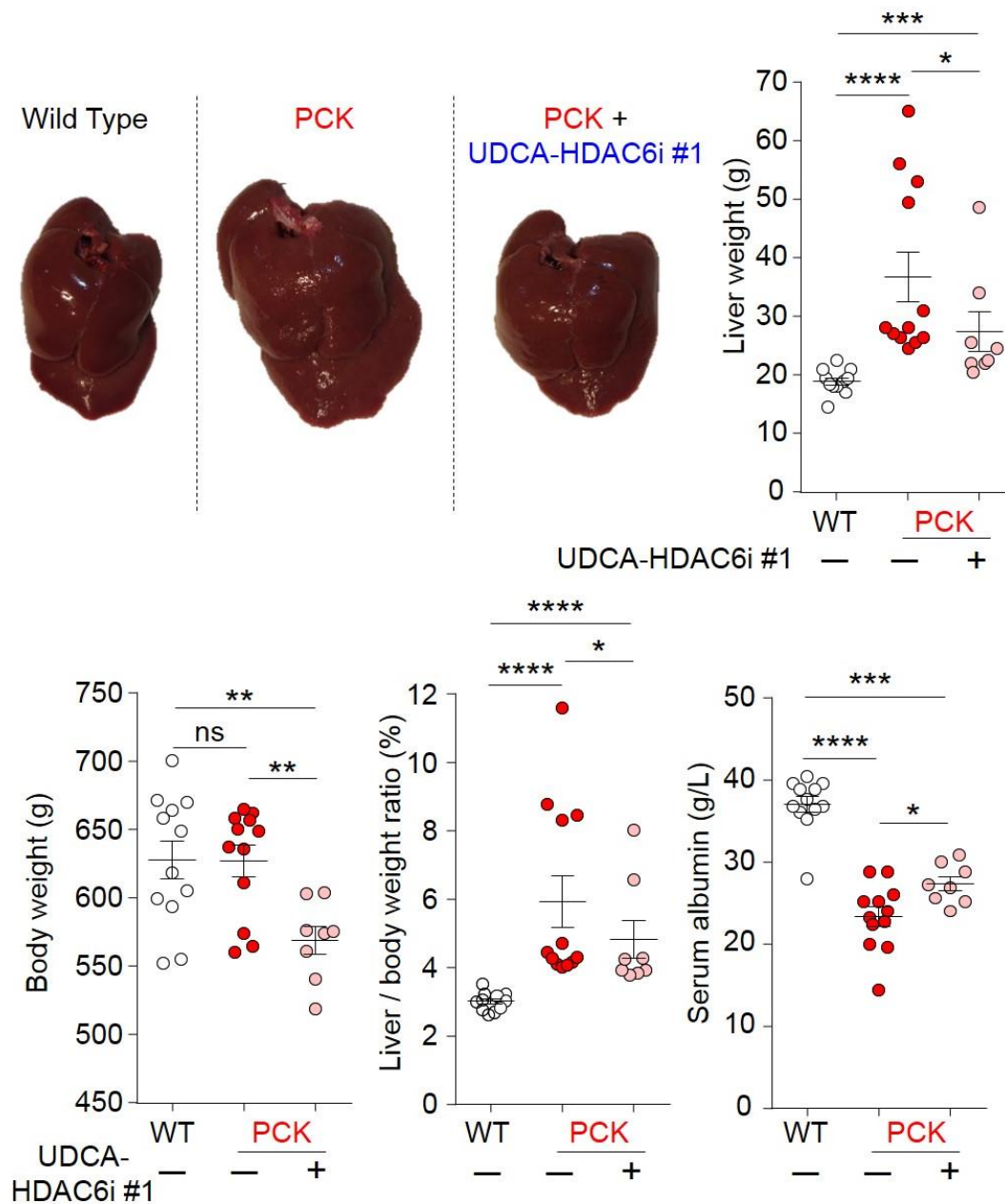


Figure R15. Representative livers of a control rat, as well as non-treated and a UDCA-HDAC6i #1-treated PCK rats. Graphical representation of the relative comparisons of liver weight, total body weight, liver/body weight ratio, and serum albumin concentration in the three assayed groups. Statistical unpaired two-tailed t test analysis was applied to determine significance in all cases with exception of PCK treated *versus* non treated liver to body weight in which unpaired one-tailed t test analysis was applied.

Remarkably, the characteristic hepatomegaly that PCK rats develop over time was found significantly reduced after their daily and chronic treatment with UDCA-

HDAC6i #1. In this regard, liver to body weight ratio was found also reduced compared to untreated PCK rats (Figure R15). Nevertheless, these effects were associated with a significant improvement in liver function, as reflected by the increased albumin levels observed in serum. (Figure R15).

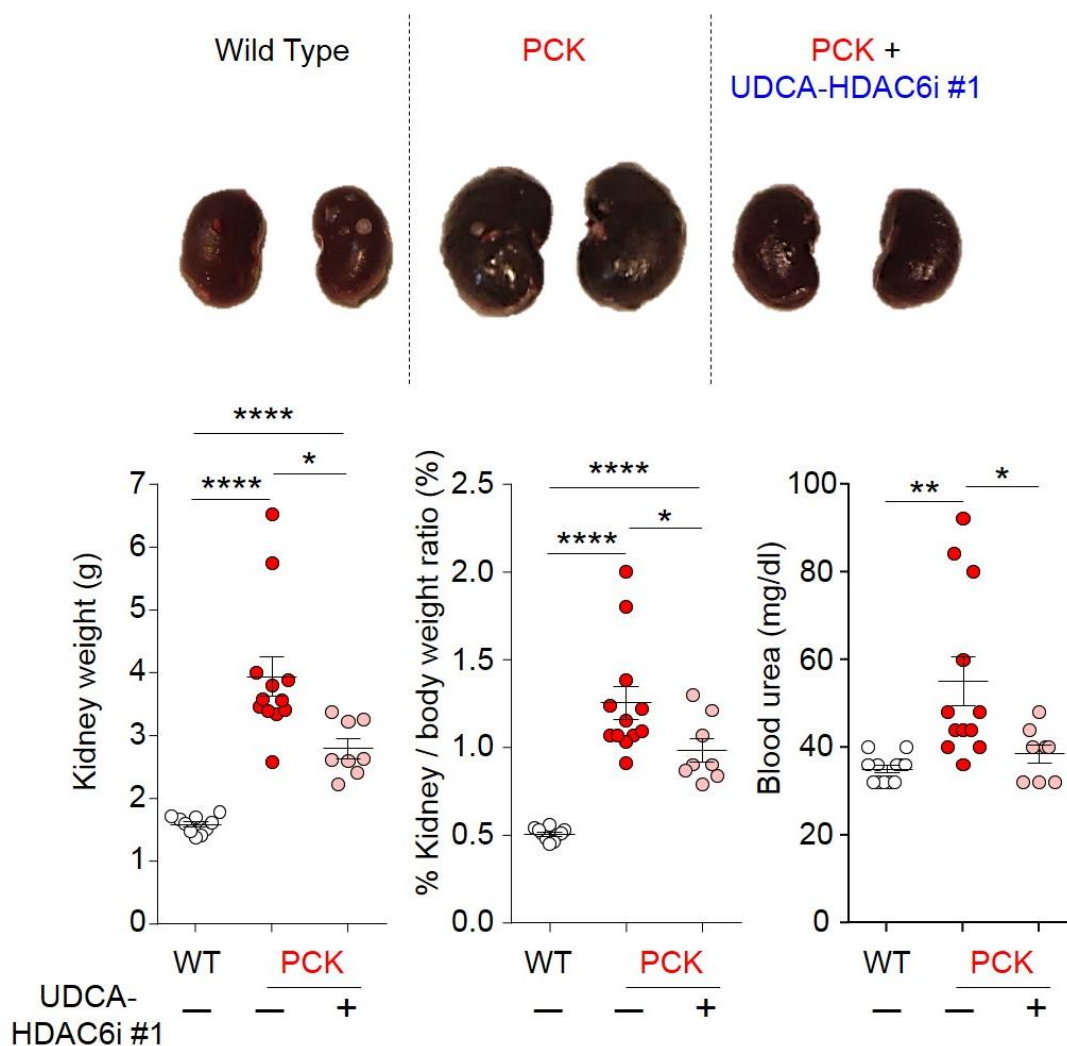


Figure R16. Representative kidneys of a control rat, as well as non-treated and a UDCA-HDAC6i #1-treated PCK rats. Graphical representation of the relative comparisons of kidney weight, kidney/body weight ratio, and serum urea concentration in the three groups. Statistical unpaired two-tailed t test was applied to determine significance.

In agreement, treated animals showed a significant reduction in disease-associated nephromegaly as well as in the kidney to body weight ratio (Figure R16). Importantly, chronic treatment of PCK rats with UDCA-HDAC6i #1 resulted in a significant reduction of the increased serum urea levels observed in PCK rats, to values similar to the ones observed in healthy rats, suggesting a substantial improvement in renal function upon treatment (Figure R16).

In order to obtain some insights into the pharmacokinetic features of UDCA-HDAC6i #1 we measured the biodistribution of this compound to liver, bile, systemic and portal blood of treated animals at the moment of sacrifice (Figure R17).

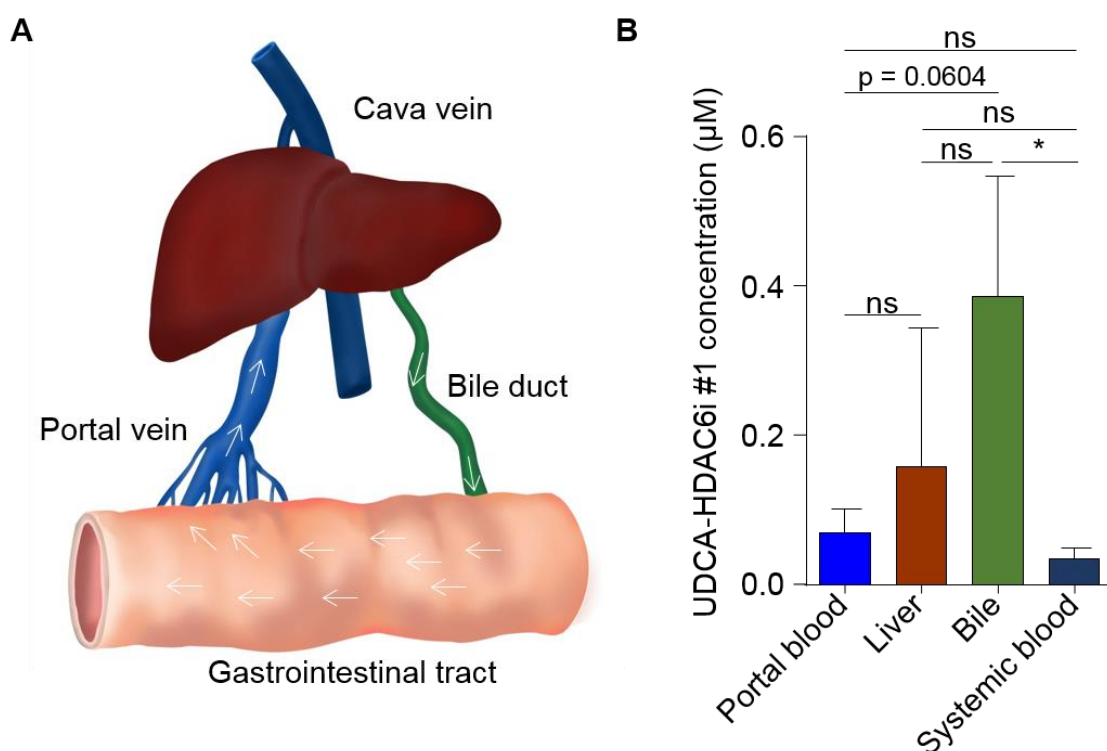


Figure R17. Analysis of UDCA-HDAC6i #1 pharmacokinetics. (A) Schematic representation of the enterohepatic circulation. (B) Graph represents the bioavailability profile of UDCA-HDAC6i #1 on different portal blood (n=8), liver (n=8), bile (n=7, statistical outlier removed) and peripheral blood (n=8) during chronic oral administration. Unpaired two-tailed t test was applied to assess for significance.

These animals presented UDCA-HDAC6i #1 in liver, bile, systemic and portal blood, but particularly in bile (Figure R17).

Next, we analyzed the levels of acetylated α -tubulin in the livers and kidneys of treated and non-treated PCK rats in order to assess the pharmacological targeting of the synthetic derivative (Figure R18). Our results show that levels of acetylated α -tubulin were found increased both in liver and kidney of UDCA-HDAC6i #1-treated animals compared with PCK control rats, confirming their target pharmacological effect on these organs *in vivo* (Figure R18).

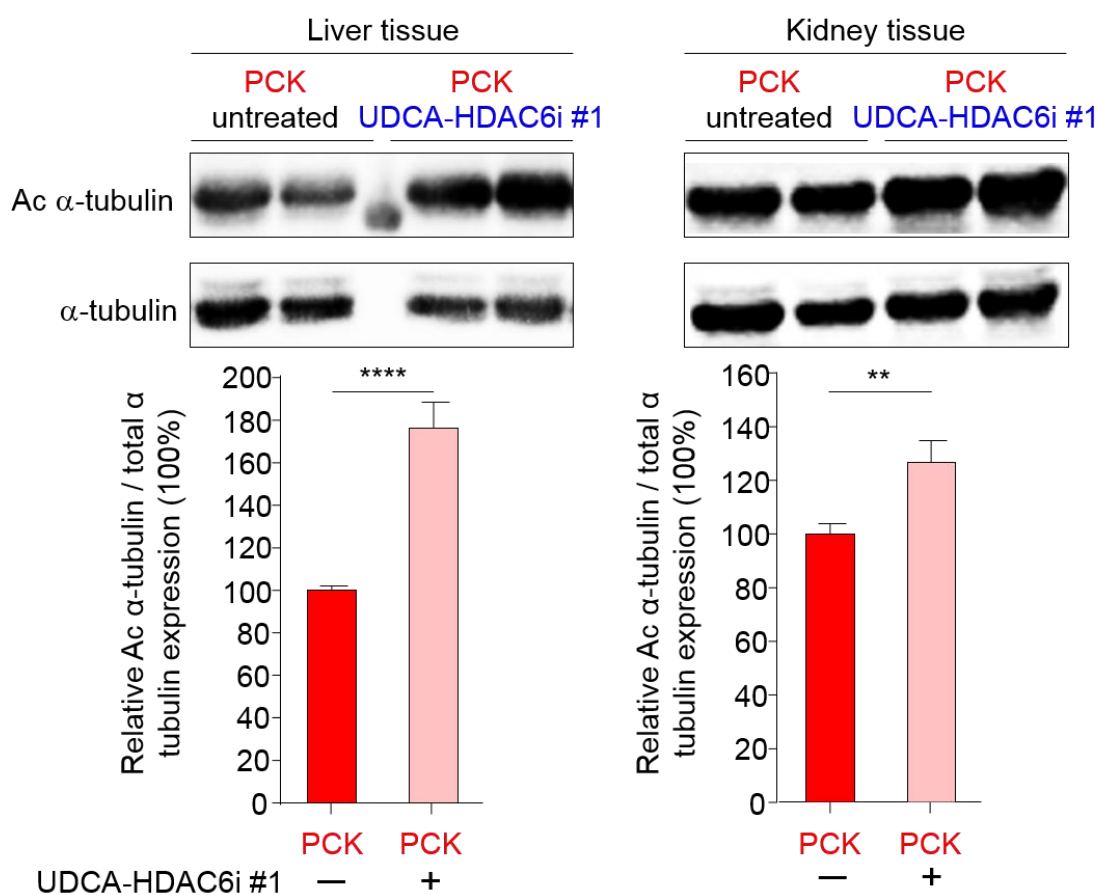


Figure R18. Representative immunoblot of the levels of acetylated α -tubulin in liver and kidney of PCK treated (n=8) and non-treated (n=12) rats. Graph represents the relative amount of acetylated α -tubulin in liver and kidney using total tubulin as normalizing control. For statistical significance assessment unpaired two-tailed t test was used.

R.8 UDCA-HDAC6i #1 modulates the bile acid pool and increases the levels of unconjugated UDCA in PCK rats

The concentration and composition of bile acids was evaluated in liver, bile, as well as in peripheral and portal blood of treated and non-treated PCK rats. As previously described by our group,⁴ the total bile acids concentration was found increased in both liver and peripheral blood of PCK rats compared to normal control animals, and these values were not modified in PCK rats treated with UDCA-HDAC6i #1 (Figure R19). On the other hand, no changes in the total bile acids concentration were found in portal blood and bile between the experimental groups (Figure R19).

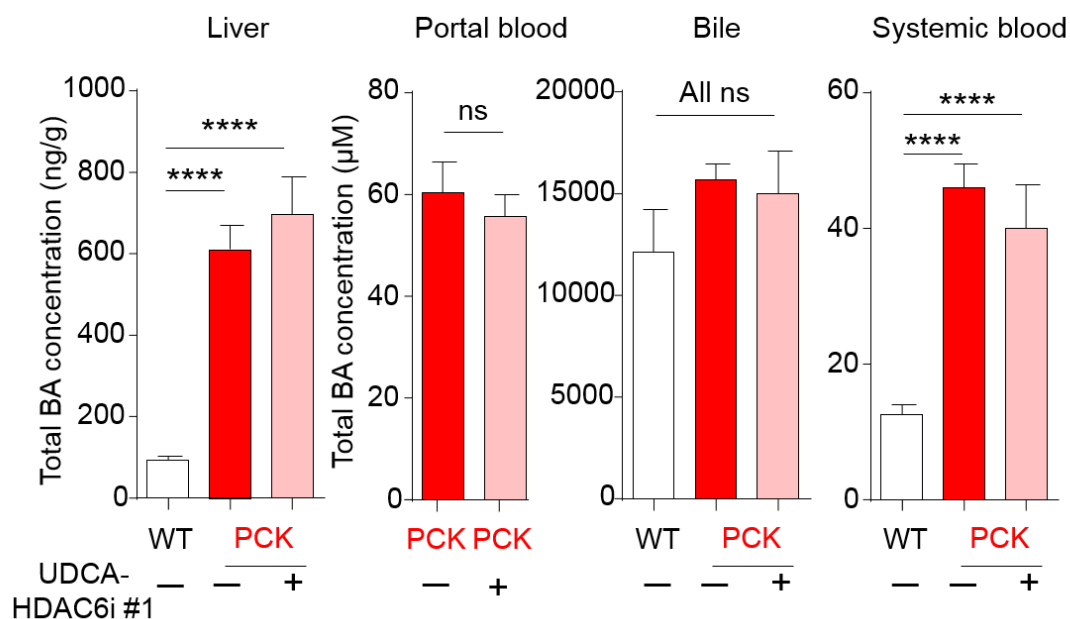


Figure R19. Total bile acids concentration in liver, portal blood, bile and peripheral blood of SD rats (WT) and PCK rats non-treated or treated with UDCA-HDAC6i #1. Statistical unpaired two-tailed t test was applied to determine significance.

In contrast, substantial differences in the composition of the bile acid pool were found in the PCK rats treated with UDCA-HDAC6i #1. In particular, the previously

described⁴ decrease in UDCA concentration in the liver of PCK rats, compared to normal animals, was reversed upon UDCA-HDAC6i #1 treatment (Figure R20).

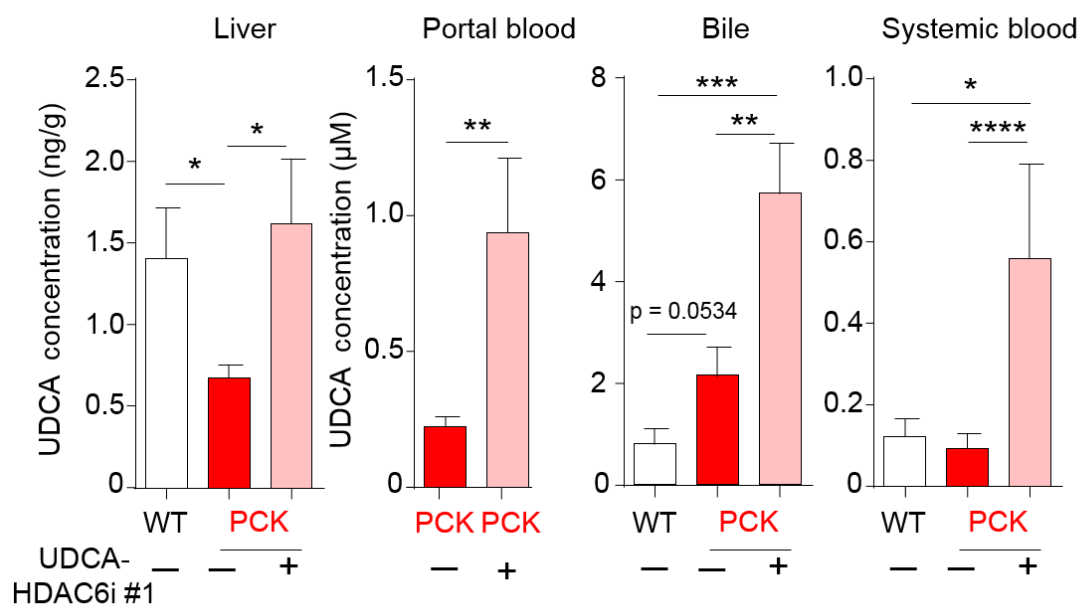


Figure R20. UDCA concentration in liver, portal blood, bile and peripheral blood of SD rats (WT) and PCK treated and non-treated rats with UDCA-HDAC6i #1. Statistical unpaired two-tailed t test was applied to determine significance.

Moreover, increased levels of UDCA were found in portal and peripheral blood, as well as in bile of PCK rats treated with UDCA-HDAC6i #1 compared to both normal and PCK untreated animals (Figure R20). Likewise, a normalization of major unconjugated bile acids (i.e., CA, a/bMCA, SLCA in liver, CA and HyoDCA in bile) was found in liver and bile of treated *versus* untreated PCK animals (Table R6).

	Liver (%)					
	SD	PCK		p		
	Control (a)	Control (b)	UDCA-HDAC6i#1 (C)	a (n=12) vs b (n=12)	a (n=12) vs c (n=8)	b (n=12) vs c (n=8)
TUDCA	13.78	10.58	8.84	0.0827	0.0144	0.2794
TCA	51.62	50.49	49.67	0.7584	0.5420	0.8412
Ta/bMCA	9.09	23.47	13.04	0.0010	0.1556	0.0564
TQDCA	7.23	5.33	5.08	0.0936	0.0830	0.7811
Tauro-conj.	80.52	85.66	76.63	0.1038	0.4078	0.0530
GUDCA	1.80	1.49	3.10	0.3599	0.0575	0.0234
GCA	9.79	10.81	16.93	0.6968	0.0834	0.1193
GQDCA	0.65	0.51	0.81	0.4986	0.4938	0.1229
Glyco-conj.	12.09	12.65	20.85	0.8426	0.0652	0.0678
UDCA	2.14	0.12	0.21	0.0022	0.0157	0.0088
CA	3.23	1.03	1.88	0.0004	0.0638	0.0283
a/bMCA	0.54	0.22	0.31	0.0038	0.0590	0.2551
HyoDCA	1.96	0.32	0.33	0.0001	0.0008	0.8963
SLCA	0.0965	0.0041	0.0199	0.0002	0.0613	0.0330
Unconj.	7.40	1.69	2.53	0.0002	0.0075	0.1042

	Bile (%)					
	SD	PCK		p		
	Control (a)	Control (b)	UDCA-HDAC6i#1 (c)	a (n=8) vs b (n=10)	a (n=8) vs c (n=8)	b (n=8) vs c (n=8)
TUDCA	7.63	8.35	10.32	0.5827	0.1845	0.3464
TCA	54.78	58.89	54.58	0.3998	0.9739	0.4033
Ta/bMCA	14.88	15.86	9.79	0.8296	0.0401	0.0328
TQDCA	5.71	3.91	7.15	0.0070	0.3302	0.0161
Tauro-conj.	82.99	87.01	80.62	0.2921	0.6884	0.1749
GUDCA	2.79	1.61	2.18	0.5001	0.4945	0.8144
GCA	9.80	9.50	11.90	0.9150	0.6672	0.5083
GQDCA	0.50	0.49	0.60	0.8410	0.6388	0.8130
Glyco-conj.	13.09	11.59	14.68	0.6937	0.7902	0.4883
UDCA	0.02	0.01	0.05	0.1858	0.0200	0.0009
CA	3.72	1.31	5.14	0.0196	0.5080	0.0202
a/bMCA	0.09	0.06	0.10	0.1739	0.9337	0.1283
HyoDCA	0.08	0.02	0.07	0.0386	0.9411	0.0310
SLCA	0.0091	0.0020	0.0046	0.0721	0.3101	0.0205
Unconj.	3.91	1.40	4.71	0.0199	0.7039	0.0516

Table R6. Relative abundances of conjugated bile acids in liver, portal blood, bile and peripheral blood of SD rats (WT) and PCK treated and non-treated rats with UDCA-HDAC6i #1. For statistical analysis, two-tailed unpaired t test was performed. Abbreviations: TUDCA, tauroursodeoxycholic acid; TCA, taurocholic acid; Ta/bMCA, tauro α/β murocholic acid; TQDCA, taurochenodeoxycholic acid; GUDCA, glycooursodeoxycholic acid; GCA, glycocholic acid; GQDCA, glycochenodeoxycholic acid; UDCA, ursodeoxycholic acid; CA, cholic acid; a/bMCA, α/β murocholic acid; HyoDCA, hyodeoxycholic acid; SLCA, sulpholithocholic acid.

R.9 UDCA-HDAC6i #1 halts liver cystogenesis *in vivo*, and this event is linked to the restoration of the cholangiocyte primary cilium length and inhibition of cell proliferation

The histological analysis of the liver sections of three different lobes revealed a reduction of the relative cystic area in UDCA-HDAC6i #1-treated animals compared with matched PCK rats without treatment (Figure R21).

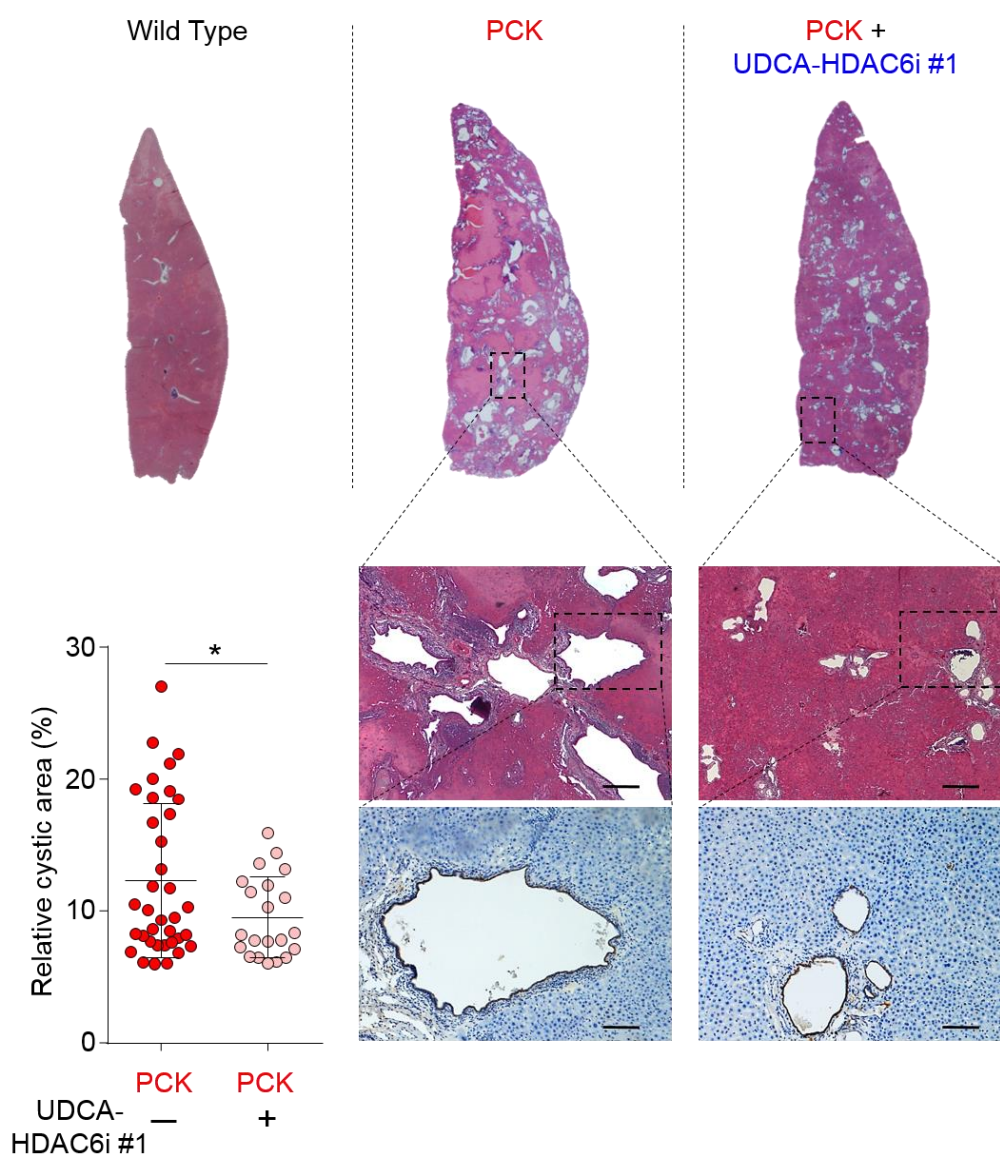


Figure R21. Representative images of hematoxylin eosin staining (scale bar = 500 μ m) and CK19 immunohistochemistry (scale bar = 250 μ m). Graph represents the cystic area relative to total tissue area of individual hepatic lobes (3 for each animal). Statistical unpaired two-tailed t test was applied to determine significance.

At the cellular level, UDCA-HDAC6i #1 restored the primary cilium length in cystic cholangiocytes *in vitro* (~40% increase), which was linked to its direct inhibitory effect on HDAC6 activity and the consequent increase of the levels of acetylation α -tubulin in the cilium (Figure R22).

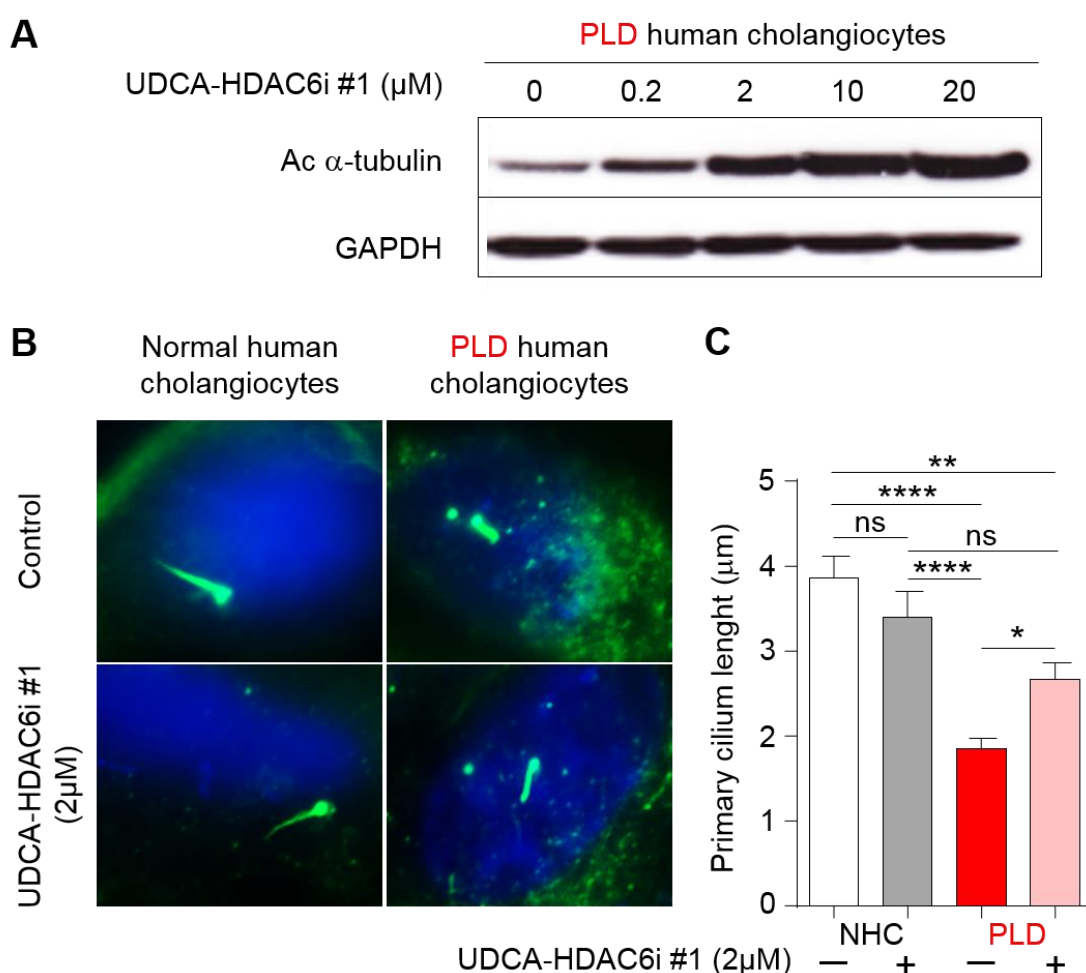


Figure R22. (A) Representative immunoblot of the effect of increasing doses of UDCA-HDAC6i #1 on the α -tubulin acetylation in cultured PLD cholangiocytes. GAPDH was used as a normalizing control. (B) Representative immunofluorescence images of acetylated α -tubulin. Cell primary cilia can be distinguished in green. Blue areas represent cell nuclei stained with DAPI. (C) Bar graph represents the mean ciliary length of baseline (n=23) or 2 μ M UDCA-HDAC6i #1 treated (n=21) normal human cholangiocytes, as well as baseline (n=30) and 2 μ M UDCA-HDAC6i #1 treated (n=27) cystic human cholangiocytes. Statistical method, one-way ANOVA.

In contrast, no changes in the primary cilium length were observed in normal cholangiocytes incubated with UDCA-HDAC6i #1 (Figure R22).

Since the primary cilium promotes the epithelial cell polarity and prevents the cell cycle initiation,^{185,186} we analyzed the effect of UDCA-HDAC6i #1 on the proliferation of cystic cholangiocytes in monolayer cell cultures, and 3D cystic structures. As shown in Figure R23, UDCA-HDAC6i #1 inhibited the 3-dimensional (3-D) growth of cystic cholangioids compared to control conditions.

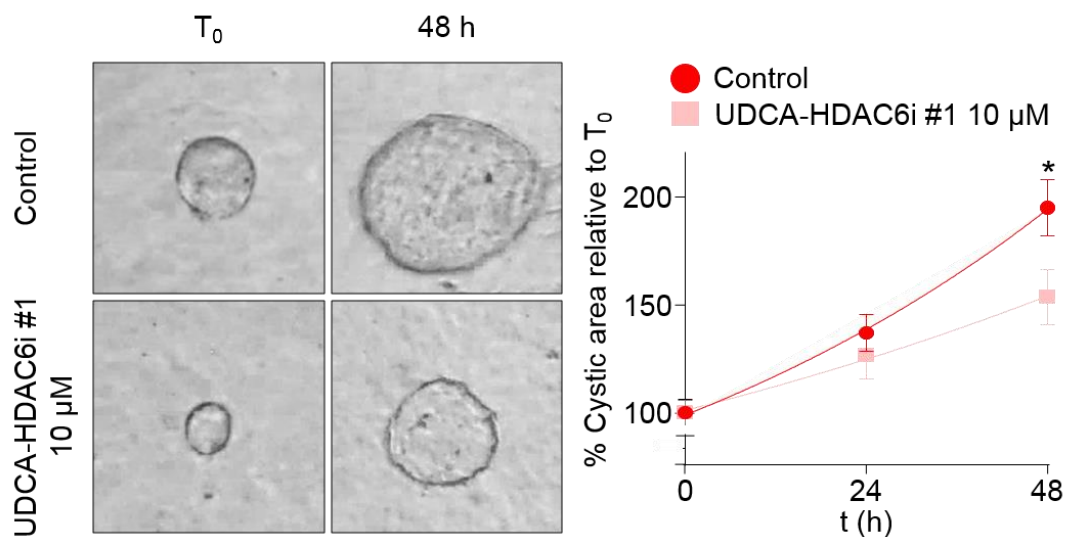


Figure R23. 3D culture in collagen type I of cysts isolated from PCK rats. The graph represents the relative circumferential area of individual non-treated (n=20) and 10 μM UDCA-HDAC6i #1 treated (n=20) cyst-like structures along time.

In accordance, UDCA-HDAC6i #1 inhibited the 2D cystic cholangiocyte proliferation *in vitro* in a dose- and pERK1/2-dependent manner (Figure R24).

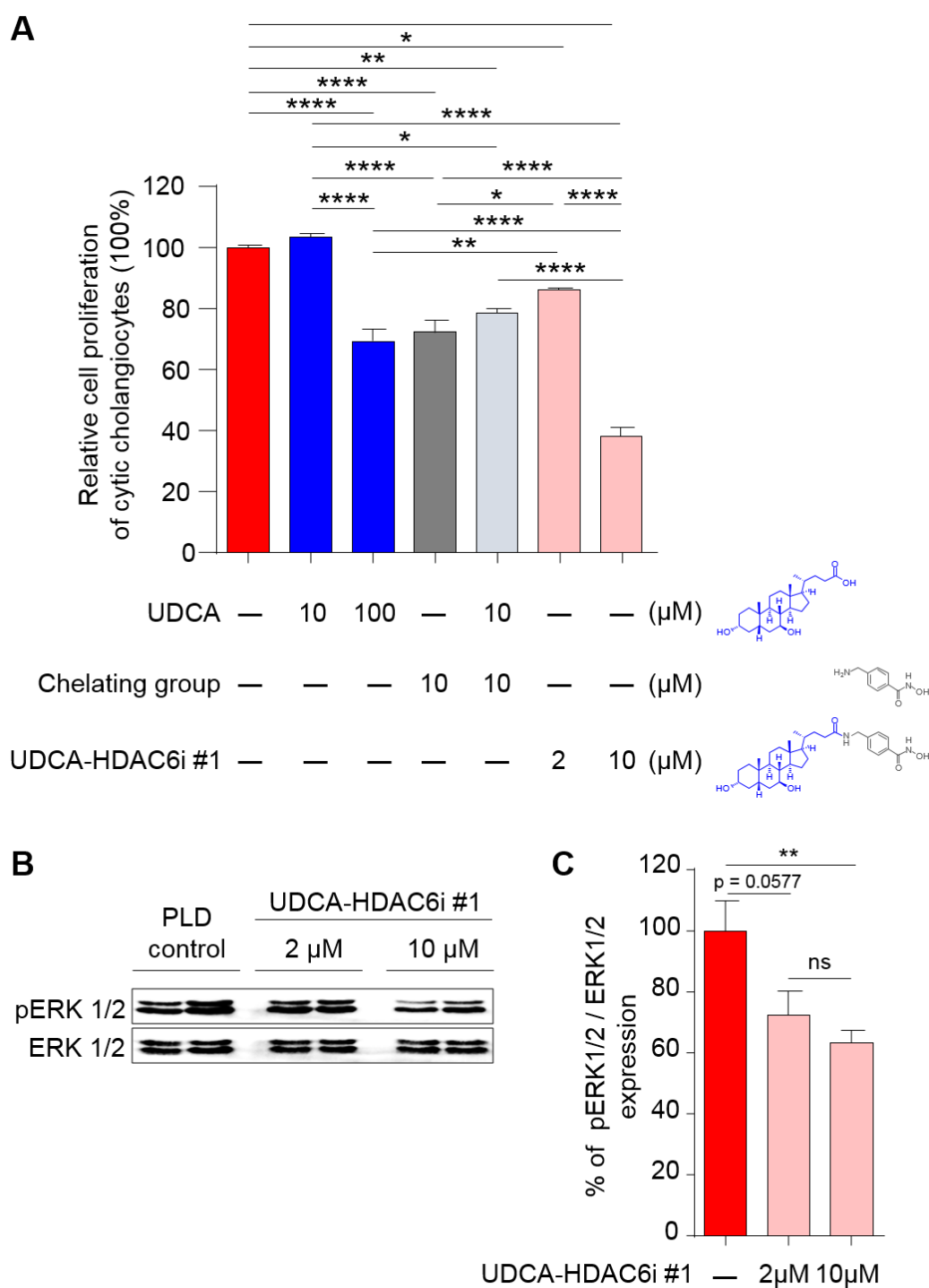


Figure R24. (A) Determination by flow cytometry of the effect on cell proliferation of different treatments on cystic human cholangiocytes stained with CFSE. Bar graph represents the percentage of cell proliferation after 48 hours treatment with 10 μM UDCA (n=7), 100 μM UDCA (n=22), 2 μM UDCA-HDAC6i #1 (n=16), 10 μM UDCA-HDAC6i #1 (n=23), 10 μM chelating group (n=23) or 10 μM UDCA, and 10 μM chelating group combined treatment (n=7) relative to control (n=23) cystic cholangiocytes. (B) Representative immunoblot and (C) relative abundance of phosphorylated ERK1/2 in cystic human cholangiocytes at baseline (n=5) or under incubation with 2 μM (n=5) or 10 μM (n=5) UDCA-HDAC6i #1 using total ERK as normalizing control.

Importantly, this anti-proliferative effect was significantly higher than the one observed upon combined treatment with the two pharmacologically active substructures that compose UDCA-HDAC6i #1 (i.e., UDCA plus HDAC6 chelating group) (Figure R24), indicating the occurrence of fairly a superior therapeutic profile upon covalent coupling of these two elements.

R.10 Hepatotropic properties of UDCA-HDAC6i #1

We next studied the mechanisms of UDCA-HDAC6i #1 uptake by cystic cholangiocytes. For this purpose, cell models of liver-specific plasma membrane transporters were used in transport assays using specific substrates and inhibitors (Figure R25 and R26).

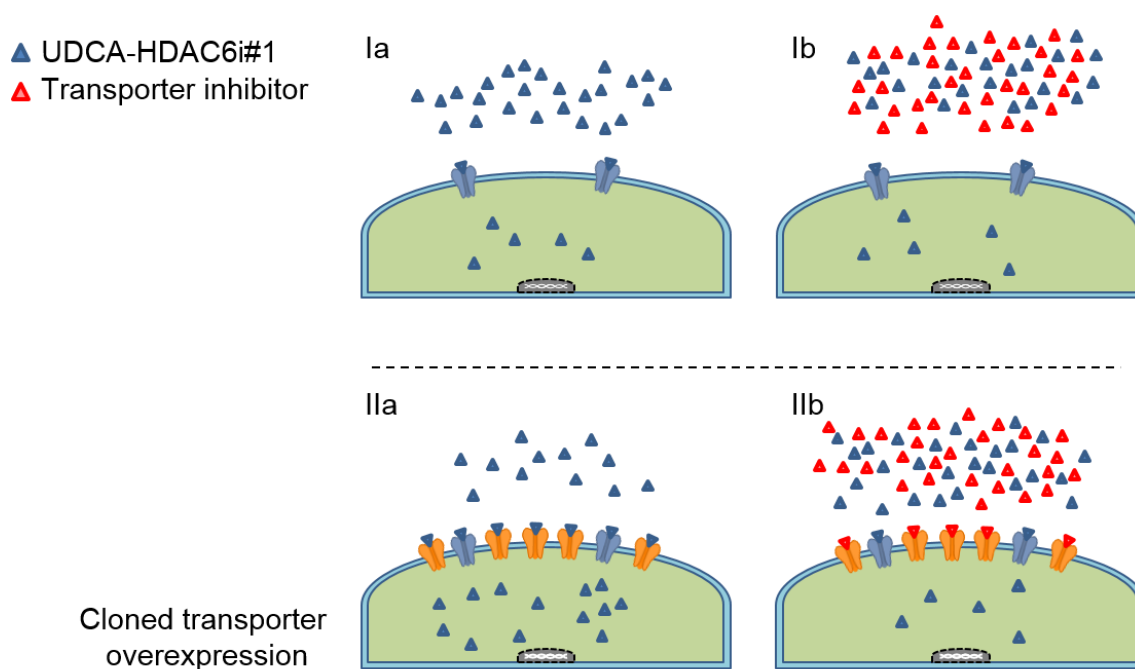


Figure R25. Schematic example of a transport experiment. Ia: Incubation of cells with 100 μM uDCA-HDAC6i #1 in baseline conditions. Ib: Incubation of cells with 100 μM UDCA-HDAC6i #1 in the presence of transporter inhibitor. IIa: Incubation of cells with 100 μM uDCA-HDAC6i #1 after induced transporter overexpression. IIb: Incubation of cells with 100 μM uDCA-HDAC6i #1 in the presence of transporter inhibitor after induced transporter overexpression.

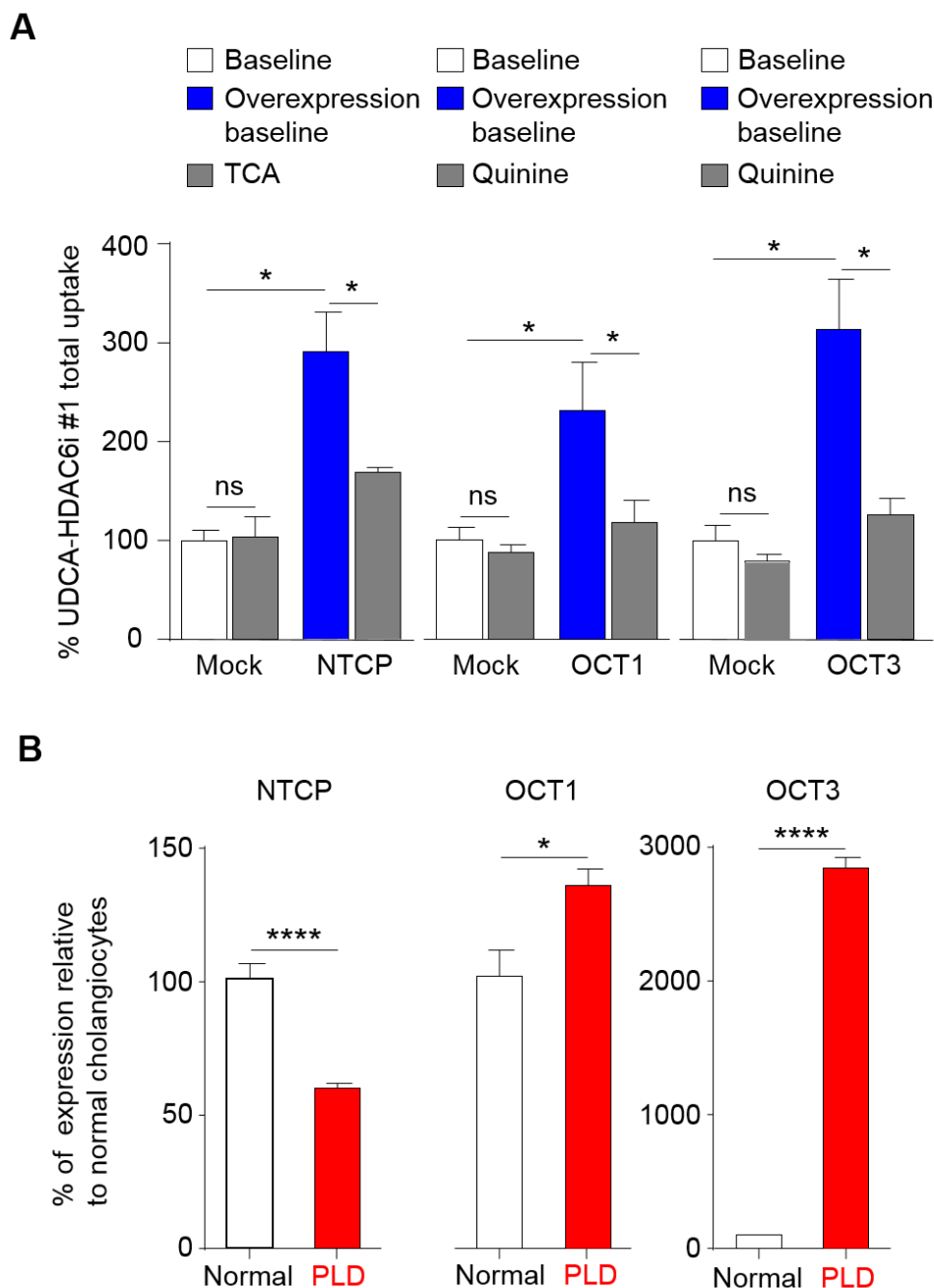


Figure R26. Identification of the molecular transporters involved in the uptake of UDCA-HDAC6i #1. (A) Bar graphs representing UDCA-HDAC6i #1 uptake in baseline and transporter overexpressing conditions in the presence or absence of a transporter inhibitor or a substrate competitor. Transporter overexpression was carried out on CHO cells for NTCP (n=4) and OCT3 (n=5), transporters and in HepG2 cell line for OCT1 (n=4) transporter. (B) RT-qPCR analysis of the mRNA expression of *NTCP*, *OCT1* and *OCT3* transporters in normal (n=6) and cystic (n=6) human cholangiocytes. *RPL22* gene was used as the normalizing control. Two-tailed t-test was applied to determine statistical significance.

Data showed that UDCA-HDAC6i #1 is effectively transported by the sodium-dependent bile acid transporter NTCP (sodium-taurocholate cotransporting polypeptide) as well as the organic cation transporters OCT1 and OCT3 (Solute carrier family 22 members 1 and 3) (Figure R26), two transporters commonly involved in the transport of cationic molecules. In parallel, we evaluated the expression of all these transporters in normal and cystic human cholangiocytes by RT-qPCR (Figure R26). According to our results, the expression of *NTCP* was found downregulated while *OCT1* and *OCT3* were found significantly upregulated in cystic human cholangiocytes compared to normal controls (Figure R26).

DISCUSSION

PLD represents a significant clinical, social and economic burden. Current therapeutic strategies include surgical procedures such as aspiration-sclerotherapy or fenestration of the cysts in highly symptomatic patients, and/or systemic pharmacological treatment based on the use of somatostatin analogues. However, both surgical and pharmacological approaches show short-term and modest beneficial effects without impacting on disease development and progression,² and therefore liver transplantation remains as the only curative option. To date, several genetic defects and related molecular abnormalities triggering cystogenesis have been described, being currently considered potential targets for therapy.^{1,9} For instance, chronic treatment with UDCA inhibits hepatic cyst growth in experimental models of PLD and in a subset of patients with advanced PLD (CURSOR Phase II clinical trial), also improving their symptomatology.^{15,20} Oral administration of UDCA is well tolerated, safe and is currently the first-line therapy internationally approved for the treatment of PBC.²⁷ The beneficial effects of UDCA on PLDs have been linked to the ability of UDCA to increase the iCa^{2+} levels in cystic cholangiocytes, as well as to its choleric properties, that enable it to wash out the increased concentration of cytotoxic and pro-mitotic bile acids in PLD livers. On the other hand, inhibition of the HDAC6 activity has been proposed as a therapeutic strategy for PLD, as it prevents exacerbated deacetylation of α -tubulin, directly contributing to stabilization of the primary cilium of cholangiocytes, restoration of ciliogenesis and cell polarity, and consequently inhibiting hepatic cystogenesis progression *in vivo*. However, the therapeutic benefits of both UDCA and HDAC6 inhibitors are partial, indicating the need to explore new related pharmacological therapies.

The currently available HDAC6 inhibitors do not show preferential targeting to the liver, and in particular to biliary cells. Most HDAC6 inhibitors developed to date comprise on their structure an external cap that accommodates on the shallow cavities located on the protein surface followed by a hydrophobic linker ended on a Zn(II) chelating group that enters into the catalytic sites of HDAC6.⁶² In this regard, HDAC6i molecules usually contain aromatic peptide derivatives and hydrocarbons acting as the closing cap of the inhibitor,^{128-130,187} which are prone to be released into systemic circulation after their hepatic metabolism. These residues have been largely demonstrated to be potentially toxic in humans; the most frequent manifestations of toxicity in clinical trials are fatigue, nausea, diarrhea and cardiotoxicity, including ventricular arrhythmia, which is perhaps the most worrisome adverse effect.^{188,189} Considering these limitations for combination therapies,¹⁹⁰ and taking advantage of our experience in the design of HDAC inhibitors through rational computer aided approaches,⁶² we hypothesized that UDCA could be an appropriate external cap-acting building block for the development of new HDAC6 inhibitors with high selectivity, improved hepatotropism, low toxicity and additional therapeutic features, because:

i) our *in silico* docking experiments indicate that UDCA may actively contribute to reinforce the inhibitory potential and selectivity of the hydrophobic linker plus the Zn(II) chelating group. This reinforcement occurs through the establishment of van der Waals interactions and hydrogen bonds between the two hydroxy groups present on the UDCA structure and the side chains of several amino acid residues located on the external cavities of both CD1 and CD2 HDAC6 catalytic domains;

ii) UDCA would provide hepatotropic features to these new UDCA-HDAC6i entities by promoting its enterohepatic transport through bile acid and/or organic cation transporters;

iii) UDCA is usually conjugated with taurine (TUDCA) or glycine (GUDCA), also termed amidation, in the carbon C-24 within hepatocytes.^{191,192} Therefore, this residue could be used as the conjugation site for the chelating group;

iv) the gut (colon) microbiome deconjugates the taurine or glycine residues of UDCA,¹⁹³ and consequently, UDCA-HDAC6i present in bile and entering the gut could be deconjugated by this process resulting in a secondary increase of the enterohepatic levels of UDCA that would provide additional therapeutic benefits.

With all this information, we designed, synthesized and exhaustively characterized a new family of 10 UDCA derivatives. We applied these 10 structures to docking experiments *versus* three-dimensional structure of human HDAC6 CD2. In these experiments, UDCA-HDAC6 #1, #2 and #9 showed considerably higher binding affinities for this catalytic domain than the other UDCA derivatives. Four of these compounds (UDCA-HDAC6 #1, #2, #6 and #9) exerted highly selective inhibitory activity on HDAC6 both in cell culture and enzymatic assays, while replacement of the hydroxamic acid contained on UDCA-HDAC6i #1 by the orthophenylenediamine present in UDCA-HDAC6i #8 resulted in a complete switch in both the inhibitory activity and selectivity towards nuclear HDACs instead of HDAC6. It is interesting to note that, the accuracy of the computational docking approach was confirmed by comparison of the predicted *in silico* values *versus* the *in vitro* inhibitory effect, thus obtaining a significant correlation between these two parameters.

Importantly, our data showed that UDCA itself has not significant HDAC inhibitory activity. However, its covalent coupling to the structure of the chelating group in order to form UDCA-HDAC6i #1 reduced one order of magnitude the IC50 value on HDAC6 with respect to the isolated chelating group. It is noteworthy that, the three UDCA-HDAC6i molecules displaying the highest *in silico* binding affinities to HDAC6 CD2 (i.e., UDCA-HDAC6i #1, #2, and #9) were also the ones showing the highest levels of activity and selectivity for HDAC6. Interestingly, these three molecules contained 1, 4-phenylene spacers and hydroxamates as chelating groups, and oriented the hydrocarbon skeleton of UDCA towards the same region of the protein surface. These features indicate that the reduced entropy derived from the preorganization of the steroidal scaffold of UDCA, the π - π stacking interactions and the particular geometry provided by the aromatic spacers help to accommodate and stabilize UDCA in a more favorable position to optimize interactions with amino acids located in the outer cavities of HDAC6 CD2. The interactions displayed by UDCA emerged as critical factors to reinforce the HDAC6i activity and selectivity of these compounds. In this regard, the difference in binding energies with the other compounds, which accommodated UDCA in other surface cavities, was more than 3 kcal/mol. In particular, the 3 most active/selective compounds established a hydrogen bond between the UDCA structure and tryptophan 496, a residue that has been recently demonstrated to be important for acetylated α -tubulin recognition by HDAC6 CD2.¹¹⁸ The contribution analysis of the different components of UDCA-HDAC6i molecules to their energy of binding revealed that when analyzing the role of UDCA, both the lipophilic van der Waals interactions energies and the penalty for exposed hydrophobic ligand groups were the main responsible for the

large energy differences between the 3 best scored compounds (i.e., UDCA-HDAC6i #1, #2, and #9) and the other UDCA-HDAC6i molecules.

Focusing in HDAC6 selectivity, structural alignment of different HDAC isoforms with our docking model of human HDAC6 CD2 revealed that the surface cavity preferentially occupied by the three most active/selective compounds remains buried and therefore not accessible in the other HDAC isoforms. This result is of particular interest because to date most published studies have focused attention on the hydrophobic channel and the surface rim in the search for HDAC6 selectivity, most probably because of the lack for any experimental data about HDAC6 3D structure. This lack of accurate structural information has limited further computer aided design of HDAC6 inhibitors to the use of homology models.^{129,187,194} In this regard, these models can be useful tools to predict and optimize inhibitor activity in the cases in which there is a good homolog structure with a sufficient degree of sequence resemblance. However, homology models usually fail when used for optimizing selectivity since one of the main determinants of compound selectivity for a particular target is the degree of structural and physicochemical divergence with respect to other potential targets. In this regard, it is generally agreed that when building a homology model, there is a direct correlation between sequence identity and predicted structure quality, being unaligned target sequences particularly prone to deliver substantially less accurate structures.¹⁹⁵ Accounting for all this, HDAC6 homology models would have introduced a significant degree of structural distortion on the aforementioned surface cavity since all of them were based on X-ray structures of HDAC isoforms with substantial sequence and architectural divergence with HDAC6 on that area. The recent solution of HDAC6 crystallographic structure

highlighted the potential importance of the discussed surface area for HDAC6 inhibitory activity and selectivity.^{118,119} However, to our knowledge this is the first report in which systematic spacer modifications maintaining the same cap structure have demonstrated through experimental and computational approaches the critical role that cap pre-organization and orientation on the protein surface play on HDAC6 selectivity determination.

Interestingly, all compounds that exhibited some binding affinity for HDAC6 CD2 *in silico* were also able to bind HDAC6 CD1 homology model. However, the correlation between the predicted binding affinities in CD1 and the *in vitro* deacetylation activity on acetylated α -Tubulin was substantially lower than that observed for CD2. This result is in accordance with recent findings demonstrating that although catalytically active, CD1 possess a high degree of substrate selectivity for other substrates rather than for acetylated α -Tubulin.¹¹⁸ In particular it has been pointed out the ability of CD1 to catalyze deacetylation in substrates containing C-terminal acetyl lysine residues.¹¹⁹

Once the affinity and selectivity for HDAC6 inhibition was confirmed in 4 of the newly synthesized UDCA-HDAC6i molecules, UDCA-HDAC6i #1 was selected for further *in vivo* analysis based on its predicted pharmacokinetic features and synthetic advantages. One of the points of our hypothesis was that the new UDCA-HDAC6i molecules could benefit from the intrinsic hepatotropic features of UDCA, concentrating them preferentially into the liver and in cystic cholangiocytes after oral administration and gastrointestinal absorption. In addition, these molecules could also be re-absorbed through the enterohepatic circulation. Thus, we applied the *QikProp* software included in the Maestro package 10.4 to *in silico* predict several ADME parameters for all UDCA-HDAC6i

molecules, obtaining considerably better values for UDCA-HDAC6i #1 than for the other three active candidates (including UDCA-HDAC6i #9) in terms of oral absorption. UDCA-HDAC6i #1 displayed values within the recommended range for all the parameters analyzed except one, whereas UDCA-HDAC6i #2 and #9 presented several potential limitations. We also hypothesized that the new UDCA-HDAC6i molecules could preserve some of the previously reported therapeutic features of UDCA for PLD either directly as part of the UDCA-HDAC6i molecule or after intestinal metabolism of the amide bond and further liberation of an intact UDCA molecule. In this regard, the capacity of UDCA to inhibit cystic cholangiocyte proliferation *in vitro* is within the μM range¹⁵ while UDCA-HDAC6is display high HDAC6 inhibitory activity and further anti-proliferative effect in the nM range. Thus, we attempted to select a candidate that could provide a balance in the contribution of both elements to the dual therapeutic effect. Moreover, the chemical synthesis of UDCA-HDAC6i #1 is faster and cheaper than others like UDCA-HDAC6i #9. Thus, while UDCA-HDAC6i #1 requires only two synthetic steps with an overall yield of 51%, UDCA-HDAC6i #9 needs four steps what requires more starting materials and leads to a substantial drop in the overall yield to only 27%.

Oral administration of UDCA-HDAC6i #1 to PCK rats considerably reduced the hepato- and nephromegaly characteristic on these animals, as well as the hepatic cystogenesis. In addition, this new molecule partially normalized the decreased serum levels of albumin, suggesting an improvement of liver function of these animals. Moreover, the levels of urea in serum were reduced upon treatment with the synthetic UDCA derivative, indicating an improvement in renal function. On the other hand, no signs of toxicity were observed at biochemical

and histological levels. Of note, these therapeutic effects were greater and more significant than those observed for UDCA, even using lower doses (i.e., 15 mg/kg/day for UDCA-HDAC6i #1 versus 25 mg/kg/day for UDCA¹⁵ during 5 months, respectively), as only changes in hepatic cystogenesis were observed upon UDCA treatment.¹⁵ At the histological level, increased levels of acetylated α -Tubulin were observed in both liver and kidneys of treated PCK rats compared to untreated animals, supporting that UDCA-HDAC6i #1 is properly absorbed in the gut and is able to reach and exert its pharmacological effect in these tissues. In agreement with these results, UDCA-HDAC6i #1 increased the primary cilium length of human cystic cholangiocytes in an acetylated α -Tubulin dependent manner, whereas it had no effect on the primary cilium length of normal human cholangiocytes *in vitro*. Moreover, UDCA-HDAC6i #1 inhibited the proliferation of cystic cholangiocytes cultured in 2D and 3D conditions. Importantly this anti-proliferative effect was much higher than the one exerted by the combined treatment with its pharmacologically active components (i.e., UDCA + chelating agent) at the same concentration. This result indicates that the covalent combination of these two components into the same chemical entity gives rise to a novel therapeutic profile much superior than the simple sum of their individual pharmacological effects. This phenomenon was also accompanied by a significant reduction in ERK1/2 phosphorylation, one of the main molecular pathways involved in mediating cystic cholangiocyte hyperproliferation.⁶ All these data are consistent with the fact that the primary cilium acts as a checkpoint inhibitor of the cell cycle, being its restoration in cystic cholangiocytes a novel therapeutic strategy.^{185,186,196,197}

Regarding the bile acid metabolism, and similarly to our previous data with UDCA, no significant changes in the total bile acid concentration were observed between UDCA-HDAC6i #1-treated and non-treated animals. However, changes in certain bile acid species in bile and liver were found. Noteworthy, increased levels of free UDCA in liver, bile and serum were found in PCK rats treated with UDCA-HDAC6i #1. This result reinforced the idea that biliary UDCA-HDAC6i #1 could be further metabolized in the gut through the cleavage of the amide bond, resulting in the release of free UDCA that may enter the entero-hepatic circulation in a second round and induce additional therapeutic effect on hepatic cystogenesis.

As indicated above, two important limitations of currently available HDAC6is are their lack of selective affinity towards the hepatic tissue as well as the presence of aromatic peptide derivatives and hydrocarbons in their structures,^{128-130,187} which can be released as potentially toxic metabolites. Our data reveal that oral administration of UDCA-HDAC6i #1 accumulates preferentially in bile, rather than in systemic blood, indicating a superior targeting to the liver and posterior secretion into bile, thus potentially diminishing the off-target effects in peripheral tissues. This preferential biodistribution to the liver could be favored by specific transport activities. UDCA-HDAC6i #1 showed specific transport through the bile acid transporter NTCP and the organic cation transporters OCT1 and OCT3. Although NTCP was found downregulated in cystic cholangiocytes, organic cation transporters OCT1 and OCT3 were markedly upregulated in these cells compared to normal cholangiocytes. The presence of the UDCA moiety in the UDCA-HDAC6i #1 structure may favor its transport through NTCP. These features, together with the fact that OCT3 is strongly overexpressed in cystic

cholangiocytes, may suggest a preferential uptake of these new UDCA synthetic derivatives to target cystic cholangiocytes.

In summary, this study has taken advantage of the last discoveries in the field of PLDs to develop, through a multidisciplinary approach, a novel therapeutic strategy to target several dysregulated molecular mechanisms of pathogenesis (i.e., decreased acetylation of α -tubulin in the primary cilium, downregulated iCa^{2+} levels, increased levels of cytotoxic and pro-mitotic bile acids in the liver) with a single chemical entity. UDCA-HDAC6i #1 showed higher therapeutic benefits than those of UDCA treatment alone. In addition, this synthetic inhibitor exerted superior anti-proliferative effect than the one produced by the combination of its two separate molecular components (UDCA and chelating group). These new UDCA synthetic conjugates possess high hepatotropism, most probably through their uptake via bile acid and cation organic transporter, and are highly concentrated into the entero-hepatic circulation. These particular features also make the UDCA-HDAC6i molecules especially promising for the treatment of other hepatic and gastrointestinal disorders where HDAC6 inhibition is considered a target for therapy, such as acute liver failure, cholangiocarcinoma, pancreatic cancer or colon cancer, among others,^{172,198-203} therefore highlighting the high degree of translational potential of this new family of molecules. Nevertheless, this work has explored through *in vitro* and *in silico* approaches some structural determinants of HDAC6 inhibitory activity and selectivity, providing important novel insights for the understanding of HDAC6 selective inhibition, and highlighting the critical contribution of the UDCA cap to these events.

CONCLUSIONS

- I. Four of the newly synthesized UDCA-HDAC6is exert potent and highly selective HDAC6 inhibitory activity, while a fifth compound exhibited highly selective inhibitory activity towards nuclear HDACs.
- II. UDCA actively contributes to the HDAC6 inhibitory activity of UDCA-HDAC6is by establishing van der Waals and hydrogen bond interactions with residues of the outer cavities of HDAC6 CDs, and this contribution can be up to one third of the total binding energy of the compound.
- III. The pre-organization and preferential orientation of UDCA towards a particular region of the surface of HDAC6 CD2 is critical to determine UDCA-HDAC6i selectivity.
- IV. UDCA-HDAC6i #1 possess the highest degree of translational potential based on its potency and selectivity, pharmacokinetic properties and synthetic cost.
- V. Upon oral administration, UDCA-HDAC6i #1 preferentially accumulates in bile, indicating good targeting capacity towards hepatobiliary system.
- VI. Chronic oral treatment of PCK rats with UDCA-HDAC6i #1 reduced their hepato- and nephromegaly, decreased their hepatic cystogenesis and improved both hepatic and renal functions in these experimental model of PLD. In addition, increased levels of acetylated α -tubulin in liver and kidneys of treated animals confirmed a direct pharmacological effect on these tissues.
- VII. Chronic oral treatment with UDCA-HDAC6i #1 produced significant modification of the bile acid pool in PCK rats, being particularly relevant

the increase in the concentration of free UDCA observed in the liver, bile and serum of the treated animals.

- VIII. The primary cilia of cystic human cholangiocytes is significantly shorter than in normal human cholangiocytes. Incubation of cystic human cholangiocytes with UDCA-HDAC6i #1 increases the levels of acetylated α -tubulin in a dose-dependent manner and significantly elongates the primary cilia of these cells; these effects were not observed in normal human cholangiocytes.
- IX. Incubation of cystic cholangiocytes with UDCA-HDAC6i #1 inhibited the hyperproliferation of these cells in 2D and 3D cultures. This anti-proliferative effect was far superior than the one exerted by the combined treatment with its pharmacologically active components.
- X. Incubation of cystic cholangiocytes with UDCA-HDAC6i #1 reduced the phosphorylation of ERK1/2, providing further explanation of the molecular mechanisms involved in this anti-proliferative effect.
- XI. UDCA-HDAC6i #1 is actively transported through the bile acid transporter NTCP and the upregulated organic cation transporters OCT1 and OCT3 in cystic cholangiocytes.

All together, these findings open a new therapeutic avenue for the treatment of PLDs, and can provide useful data for future drug developments either in the field of HDAC6 activity and selectivity and/or in the field of improved liver targeting pharmacology.

***MATERIALS AND
METHODS***

M.1 Docking

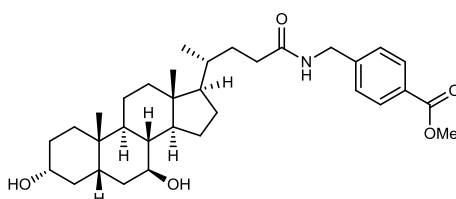
The X-ray structure of the human HDAC6 catalytic domain 2 was obtained from RCSB Protein Data Bank (PDB entry 5EDU). The protein structure was optimized and minimized using the protein preparation wizard software²⁰⁴ included in Maestro 10.4 package (Schrödinger, NY, USA). Ligands were represented with Maestro graphic interface and optimized with LigPrep tool included in Maestro 10.4 package. Flexible docking experiments were carried out using Glide software^{205,206} included in Maestro 10.4 package, using extra precision mode²⁰⁷ to maximize accuracy of the obtained results. Obtained structures and binding predicted energies were analyzed using Maestro and Pymol graphic interfaces.

M.2 Homology modeling

Homology model of Human HDAC6 CD1 was generated with Prime software^{181,182} included in Maestro 10.4 package. Amino acid sequence of human HDAC6 (Uniprot code: Q9UBN7) CD1 comprising residues between 87 and 404 positions was submitted to secondary structure prediction. Next, predicted secondary structure was aligned to that of Danio rerio HDAC6 CD1 (PDB code: 5G0G) by using ClustalW algorithm. Once aligned both structures, a knowledge-based model of human HDAC6 CD1 was constructed based on the tertiary structure of Danio rerio HDAC6 CD1. Finally, protein loops were refined, and protein structure was prepared for docking experiments as explained above.

M.3 Chemical synthesis and characterization

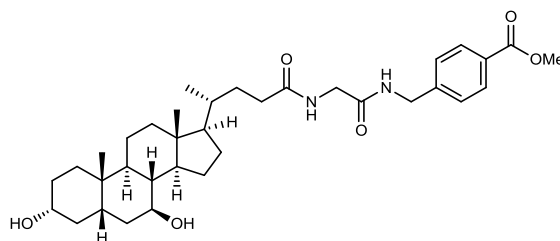
Synthesis of methyl 4-(((R)-4-((3R,5S,7S,8R,9S,10S,13R,14S,17R)-3,7-dihydroxy-10,13-dimethylhexadecahydro-1H-cyclopenta[a]phenanthren-17-yl)pentanamido)methyl)benzoate. (**3a**)



This compound was prepared following the method A described above.

Ursodeoxycholic acid (393 mg, 1 mmol) methyl 4-(aminomethyl) benzoate hydrochloride (202 mg, 1 mmol), TBTU (385 mg, 1.2 mmol), Et₃N in DMF (1.1 mL, 3.26 M). White solid. Yield 84%; m.p.. 114-116 °C; IR 3293, 2927, 2862, 1720, 1650, 1277, 1106 cm⁻¹; ¹H NMR (400 MHz, DMSO-*d*₆) δ: 8.39 (t, *J* = 6.0 Hz, 1H), 7.90 (d, *J* = 8.2 Hz, 2H), 7.37 (d, *J* = 8.1 Hz, 2H), 4.49 (d, *J* = 4.4 Hz, 1H), 4.32 (dd, *J* = 6.0, 2.7 Hz, 2H), 3.88 (d, *J* = 6.7 Hz, 1H), 3.83 (s, 3H), 3.29 (s, 2H), 2.28 – 2.02 (m, 2H), 1.96 – 1.61 (m, 6H), 1.55 – 1.25 (m, 10H), 1.25 – 0.93 (m, 7H), 0.93 – 0.83 (m, 7H), 0.60 (s, 3H); ¹³C NMR (101 MHz, DMSO-*d*₆) δ 172.77, 166.06, 145.50, 129.16, 128.06, 127.26, 69.77, 69.48, 55.89, 54.77, 52.01, 43.10, 43.01, 42.22, 41.80, 39.86, 38.78, 37.74, 37.28, 34.93, 34.86, 33.76, 32.42, 31.67, 30.25, 28.20, 26.71, 23.32, 20.89, 18.44, 12.00; HRMS (ESI) for C₃₃H₄₉NO₅Na calculated [M + Na]⁺: 562.3509. Obtained: 562.3515.

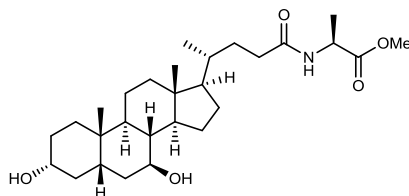
Synthesis of methyl 4-((2-((R)-4-((3R,5S,7S,8R,9S,10S,13R,14S,17R)-3,7-dihydroxy-10,13-dimethylhexadecahydro-1H-cyclopenta[a]phenanthren-17-yl)pentanamido)acetamido)methyl)benzoate. (**6a**)



This compound was prepared following the method C described above.

Glycoursodeoxycholic acid (121 mg, 0.27 mmol) methyl 4-(aminomethyl)benzoate hydrochloride (54 mg, 0.27) TBTU (104 mg, 0.32 mmol) Et₃N (0.3 mL, 3.26 M). White solid. Yield 63%; m.p. 145-147 °C; IR 3354, 2932, 2861, 1720, 1654, 1281, 1111, 847 cm⁻¹; ¹H NMR (400 MHz, DMSO-*d*₆) δ 8.41 (t, *J* = 6.1 Hz, 1H), 8.09 (t, *J* = 5.9 Hz, 1H), 7.90 (d, *J* = 8.2 Hz, 2H), 7.38 (d, *J* = 8.1 Hz, 2H), 4.45 (d, *J* = 4.5 Hz, 1H), 4.35 (d, *J* = 6.0 Hz, 2H), 3.87 (d, *J* = 6.8 Hz, 1H), 3.84 (s, 3H), 3.71 (d, *J* = 5.8 Hz, 2H), 3.29 (2H), 2.25 – 1.96 (m, 2H), 1.95 – 1.59 (m, 5H), 1.55 – 1.25 (m, 9H), 1.25 – 0.93 (m, 7H), 0.93 – 0.85 (m, 7H), 0.60 (s, 3H); ¹³C NMR (101 MHz, DMSO-*d*₆) δ 173.14, 169.42, 166.12, 145.21, 129.17, 128.09, 127.31, 69.75, 69.49, 55.89, 54.79, 52.11, 43.11, 43.04, 42.19, 41.78, 38.75, 38.28, 37.76, 37.29, 35.02, 34.86, 33.79, 32.21, 31.46, 30.27, 28.22, 26.76, 23.35, 20.88, 18.53, 12.08. HRMS (ESI) for C₂₈H₄₇NO₄ calculated [[M + H] + [-H₂O]]⁺: 579.3798. Obtained: 579.3783.

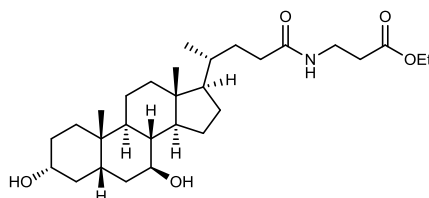
Synthesis of methyl ((R)-4-((3R,5S,7S,8R,9S,10S,13R,14S,17R)-3,7-dihydroxy-10,13-dimethylhexadecahydro-1H-cyclopenta[a]phenanthren-17-yl)pentanoyl)-L-alaninate. **(3b)**



This compound was prepared following the method A described above.

Ursodeoxycholic acid (393 mg, 1 mmol) L-Alanine methyl ester hydrochloride (140 mg, 1 mmol) TBTU (385 mg, 1.2 mmol) and Et₃N (1.1 mL, 3.26 M) White solid. Yield 45%; m.p. 103-105 °C; IR 3296, 2928, 2863, 1739, 1650, 1209, 1049 cm⁻¹; ¹H NMR (400 MHz, DMSO-*d*₆) δ 8.19 (d, *J* = 7.0 Hz, 1H), 4.44 (d, *J* = 4.5 Hz, 1H), 4.23 (p, *J* = 7.2 Hz, 1H), 3.87 (d, *J* = 6.8 Hz, 1H), 3.60 (s, 3H), signal corresponding to 2H overlapped with broad signal of water at 3.29 ppm (confirmed by COSY), 2.19 – 1.88 (m, 3H), 1.88 – 1.57 (m, 4H), 1.56 – 1.27 (m, 9H), 1.27 – 0.93 (m, 12H), 0.93 – 0.82 (m, 7H), 0.61 (s, 3H); ¹³C NMR (101 MHz, DMSO-*d*₆) δ 173.26, 172.52, 69.71, 69.45, 55.87, 54.71, 51.72, 47.41, 43.07, 43.01, 42.16, 38.71, 37.72, 37.27, 34.87, 34.82, 33.75, 31.94, 31.47, 30.24, 28.16, 26.71, 23.31, 20.84, 18.47, 16.93, 12.03; HRMS (ESI) for C₂₈H₄₈NO₅ calculated [M + H]⁺: 478.3532. Obtained: 478.3531.

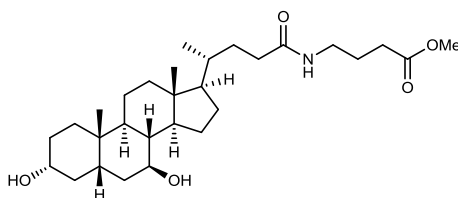
Synthesis of methyl 3-((R)-4-((3R,5S,7S,8R,9S,10S,13R,14S,17R)-3,7-dihydroxy-10,13-dimethylhexadecahydro-1H-cyclopenta[a]phenanthren-17-yl)pentanamido)propanoate. **(3c)**



This compound was prepared following the method A described above.

Ursodeoxycholic acid (393 mg, 1 mmol) β -Alanine ethyl ester hydrochloride (154 mg, 1 mmol), TBTU (385 mg, 1.2 mmol) Et₃N (1.1 mL, 3.26 M). White solid. Yield 66%; m.p. 84-86 °C; IR 3292, 2927, 2862, 1734, 1647, 1180, 1049 cm⁻¹; ¹H NMR (400 MHz, DMSO-*d*₆) δ 7.85 (t, *J* = 5.7 Hz, 1H), 4.43 (d, *J* = 4.6 Hz, 1H), 4.05 (q, *J* = 7.1 Hz, 2H), 3.86 (d, *J* = 6.8 Hz, 1H), 3.29 (2H), 3.24 (q, *J* = 6.5 Hz, 2H), 2.41 (t, *J* = 6.8 Hz, 2H), 2.12 – 1.89 (m, 4H), 1.89 – 1.59 (m, 4H), 1.53 – 1.25 (m, 9H), 1.24 – 0.90 (m, 11H), 0.87 (t, *J* = 3.3 Hz, 7H), 0.61 (s, 3H); ¹³C NMR (101 MHz, DMSO-*d*₆) δ 172.63, 171.30, 69.70, 69.45, 59.86, 55.86, 54.69, 43.06, 43.00, 42.16, 38.71, 37.72, 37.26, 34.90, 34.82, 34.65, 33.90, 33.75, 32.29, 31.60, 30.24, 28.15, 26.70, 23.31, 20.84, 18.45, 14.08, 12.01; HRMS (ESI) for C₂₉H₅₀NO₅ calculated [M + H]⁺: 492.3689. Obtained: 492.3684.

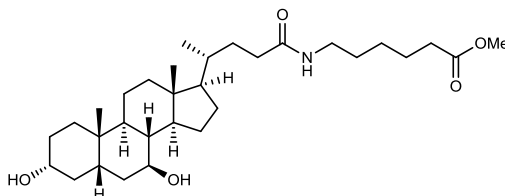
Synthesis of methyl 4-((R)-4-((3R,5S,7S,8R,9S,10S,13R,14S,17R)-3,7-dihydroxy-10,13-dimethylhexadecahydro-1H-cyclopenta[a]phenanthren-17-yl)pentanamido)butanoate. **(3d)**



This compound was prepared following the method A described above.

Ursodeoxycholic acid (393 mg, 1 mmol) 4-aminobutirate methyl ester hydrochloride (154 mg, 1 mmol) TBTU (385 mg, 1.2 mmol) Et₃N (1.1 mL, 3.26 M). White solid. Yield 37 %; m.p. 92-94 °C; IR 3295, 2927, 2862, 1736, 1646, 1170, 1050 cm⁻¹; ¹H NMR (400 MHz, DMSO-*d*₆) δ 7.77 (t, *J* = 5.7 Hz, 1H), 4.42 (d, *J* = 4.6 Hz, 1H), 3.85 (d, *J* = 6.8 Hz, 1H), 3.58 (s, 3H), 3.02 (q, *J* = 6.5 Hz, 2H), 2.29 (t, *J* = 7.5 Hz, 2H), 2.15 – 2.00 (m, 1H), 2.01 – 1.53 (m, 9H), 1.54 – 1.24 (m, 8H), 1.24 – 0.90 (m, 7H), 0.88 (d, *J* = 7.4 Hz, 7H), 0.60 (s, 3H); ¹³C NMR (101 MHz, DMSO-*d*₆) δ 173.04, 172.45, 69.67, 69.41, 55.83, 54.66, 51.20, 43.03, 42.97, 42.13, 38.68, 37.69, 37.60, 37.23, 34.87, 34.79, 33.72, 32.38, 31.63, 30.65, 30.21, 28.14, 26.67, 24.52, 23.28, 20.80, 18.42, 11.96; HRMS (ESI) for C₂₉H₅₀NO₅ calculated [M + H]⁺: 492.3689. Obtained: 492.3686.

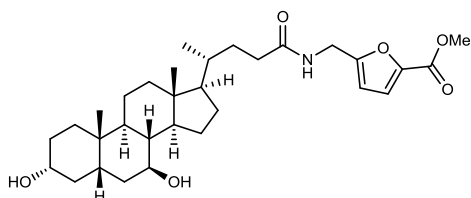
Synthesis of methyl 6-((R)-4-((3R,5S,7S,8R,9S,10S,13R,14S,17R)-3,7-dihydroxy-10,13-dimethylhexadecahydro-1H-cyclopenta[a]phenanthren-17-yl)pentanamido)hexanoate. (**3e**)



This compound was prepared following the method A described above.

Ursodeoxycholic acid (393 mg, 1 mmol), 6-aminohexanoate methyl ester hydrochloride (182 mg, 1 mmol) TBTU (385 mg, 1.2 mmol) and Et₃N (1.1 mL, 3.26 M). White solid. Yield 42%; m.p. 78-80 °C; IR 3299, 2926, 2861, 1736, 1644, 1165, 1050 cm⁻¹; ¹H NMR (400 MHz, DMSO-*d*₆) δ 7.71 (t, *J* = 5.7 Hz, 1H), 4.43 (d, *J* = 4.5 Hz, 1H), 3.86 (d, *J* = 6.7 Hz, 1H), 3.58 (s, 3H), 3.29 (2H), 2.99 (q, *J* = 7.1 Hz, 2H), 2.28 (t, *J* = 7.4 Hz, 2H), 2.14 – 1.56 (m, 10H), 1.56 – 0.91 (m, 20H), 0.88 (d, *J* = 7.2 Hz, 8H), 0.60 (s, 3H); ¹³C NMR (101 MHz, DMSO-*d*₆) δ 173.26, 172.28, 69.70, 69.45, 55.87, 54.70, 51.15, 43.06, 43.00, 42.16, 38.71, 38.12, 37.71, 37.26, 34.90, 34.82, 33.75, 33.22, 32.44, 31.69, 30.24, 28.82, 28.16, 26.70, 25.84, 24.15, 23.30, 20.83, 18.45, 12.00; HRMS (ESI) for C₃₁H₅₄NO₅ calculated [M + H]⁺: 520.4002. Obtained: 520.3997.

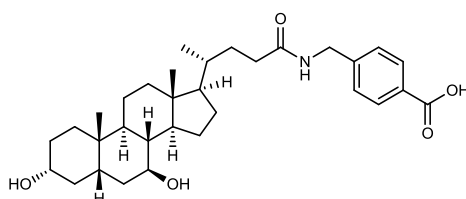
Synthesis of methyl 5-(((R)-4-(((3R,5S,7S,8R,9S,10S,13R,14S,17R) -3,7-dihydroxy-10,13-dimethylhexadecahydro-1H-cyclopenta[a]phenanthren-17-yl)pentanamido)methyl)furan-2-carboxylate. **(3f)**



This compound was prepared following the method A described above.

Ursodeoxycholic acid (145 mg, 0.37 mmol), 5-(aminomethyl)furan-2-carboxylate methyl ester hydrochloride (71 mg, 0.37) TBTU (146 mg, 0.46 mmol) Et₃N (0.41 mL, 3.26 M). White solid. Yield 52%; m.p. 240-242 °C; IR 3463, 3285, 2935, 1705, 1683, 1518, 1210, 763 cm⁻¹; ¹H NMR (400 MHz, DMSO-*d*₆) δ 8.38 (t, *J* = 5.8 Hz, 1H), 7.23 (d, *J* = 3.5 Hz, 1H), 6.40 (d, *J* = 3.4 Hz, 1H), 4.42 (d, *J* = 4.5 Hz, 1H), 4.29 (d, *J* = 5.7 Hz, 2H), 3.85 (d, *J* = 6.8 Hz, 1H), 3.79 (s, 3H), signal corresponding to 2H overlapped with broad signal of water at 3.29 ppm (confirmed by COSY), 2.09 (m, *J* = 39.5, 14.2, 7.9 Hz, 2H), 1.96 – 1.58 (m, 5H), 1.54 – 1.24 (m, 10H), 1.24 – 0.90 (m, 8H), 0.87 (d, *J* = 6.5 Hz, 7H), 0.58 (s, 3H); ¹³C NMR (101 MHz, DMSO-*d*₆) δ 172.63, 158.23, 157.68, 142.62, 119.31, 109.11, 69.71, 69.45, 55.85, 54.69, 51.65, 43.06, 43.00, 42.16, 39.99, 38.71, 37.72, 37.27, 35.57, 34.86, 34.82, 33.75, 32.20, 31.54, 30.24, 28.15, 26.70, 23.30, 20.83, 18.42, 11.99; HRMS (ESI) for C₃₁H₅₁N₂O₆ calculated [M + NH₄]⁺: 547.3745. Obtained: 547.3738.

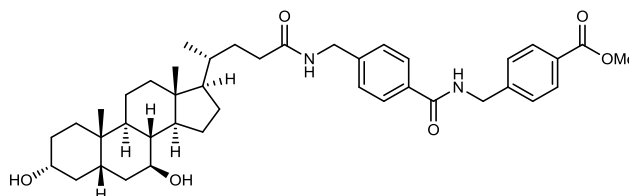
Example 8: Synthesis of 4-(((4R)-4-((3R,5S,7S,8R,9S,10S,13R,14S)-3,7-dihydroxy-10,13-dimethylhexadecahydro-1H-cyclopenta[a]phenanthren-17-yl)pentanamido)methyl)benzoic acid. (**4a**)



This compound was prepared following the method B described above.

4-(((4R)-4-((3R,5S,7S,8R,9S,10S,13R,14S)-3,7-dihydroxy-10,13-dimethylhexadecahydro-1H-cyclopenta[a]phenanthren-17-yl)pentanamido)methyl) benzoate (1079 mg, 2 mmol), NaOH (8.7 mL, 0.5M). White solid. Yield 90%; m.p. 155-157 °C; IR 3288, 2922, 2851, 1638, 1542, 1281, 1015 cm^{-1} ; ^1H NMR (400 MHz, $\text{DMSO-}d_6$) δ 12.85 (s, 1H), 8.37 (t, $J = 6.0$ Hz, 1H), 7.88 (d, $J = 8.2$ Hz, 2H), 7.34 (d, $J = 8.1$ Hz, 2H), 4.48 – 4.39 (m, 1H), 4.34 – 4.28 (m, 2H), 3.86 (d, $J = 6.8$ Hz, 1H), signal corresponding to 2H overlapped with broad signal of water at 3.29 ppm, 2.24 – 2.01 (m, 2H), 1.98 – 1.60 (m, 6H), 1.53 – 1.26 (m, 10H), 1.26 – 0.93 (m, 7H), 0.93 – 0.85 (m, 7H), 0.61 (s, 3H); ^{13}C NMR (101 MHz, $\text{DMSO-}d_6$) δ 172.67, 167.15, 145.01, 129.30, 129.19, 127.10, 69.73, 69.47, 55.88, 54.76, 43.09, 43.01, 42.18, 41.77, 39.84, 38.74, 37.73, 37.27, 34.89, 34.83, 33.76, 32.38, 31.65, 30.25, 28.19, 26.72, 23.32, 20.85, 18.44, 12.01; HRMS (ESI) para $\text{C}_{32}\text{H}_{48}\text{NO}_5$ calculated $[\text{M} + \text{H}]^+$: 525.3532. Obtained: 525.3538.

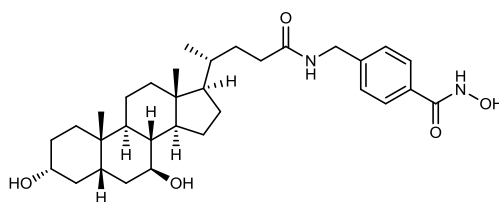
Example 9: Synthesis of methyl 4-((4-(((4R)-4-((3R,5S,7S,8R,9S,10S,13R,14S)-3,7-dihydroxy-10,13-dimethylhexadecahydro-1H-cyclopenta[a]phenanthren-17-yl)pentanamido)methyl)benzamido)methyl)benzoate. **(6b)**



This compound was prepared following the method C described above.

4-(((4R)-4-((3R,5S,7S,8R,9S,10S,13R,14S)-3,7-dihydroxy-10,13-dimethylhexadecahydro-1H-cyclopenta[a]phenanthren-17-yl)pentanamido)methyl)benzoic acid (200 mg, 0.38 mmol) methyl 4-(aminomethyl) benzoate hydrochloride (77 mg 0.38 mmol) TBTU (146 mg 0.46 mmol) Et₃N (0.42 mL, 3.26 M). White solid. Yield 60%; m.p.139-141 °C; IR 3301, 2926, 2861, 1719, 1638, 1276, 1107, 1047 cm⁻¹; ¹H NMR (400 MHz, DMSO-*d*₆) δ 9.08 (t, *J* = 6.0 Hz, 1H), 8.36 (t, *J* = 6.0 Hz, 1H), 7.92 (d, *J* = 8.1 Hz, 2H), 7.85 (d, *J* = 8.1 Hz, 2H), 7.44 (d, *J* = 8.1 Hz, 2H), 7.32 (d, *J* = 8.1 Hz, 2H), 4.55 (d, *J* = 5.9 Hz, 2H), 4.45 (d, *J* = 4.5 Hz, 1H), 4.36 – 4.15 (m, 2H), 3.87 (d, *J* = 6.8 Hz, 1H), 3.83 (s, 3H), 3.29 (2H), 2.23 – 2.01 (m, 2H), 1.97 – 1.59 (m, 6H), 1.55 – 1.25 (m, 10H), 1.25 – 0.93 (m, 7H), 0.93 – 0.82 (m, 7H), 0.61 (s, 3H); ¹³C NMR (101 MHz, DMSO-*d*₆) δ 172.67, 166.11, 145.41, 143.37, 132.52, 129.25, 128.10, 127.29, 126.95, 69.73, 69.48, 55.88, 54.77, 52.06, 43.10, 43.02, 42.40, 42.18, 41.71, 38.73, 37.73, 37.28, 34.91, 34.84, 33.77, 32.41, 31.68, 30.25, 28.20, 26.73, 23.32, 20.86, 18.46, 12.04; HRMS (ESI) for C₄₁H₅₇N₂O₆ calculated [M + H]⁺: 673.4216. Obtained: 673.4214.

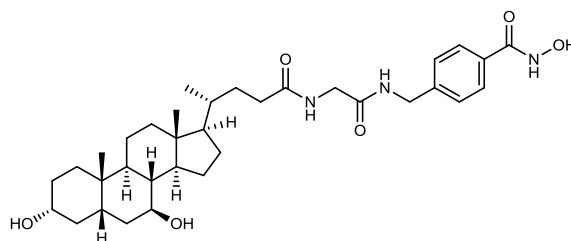
Synthesis of 4-(((4R)-4-((3R,5S,7S,8R,9S,10S,13R,14S)-3,7-dihydroxy-10,13-dimethylhexadecahydro-1H-cyclopenta[a]phenanthren-17-yl)pentanamido)methyl)-N-hydroxybenzamide. **UDCA-HDAC6i #1:**



This compound was prepared following the method A described above.

Methyl 4-(((4R)-4-((3R,5S,7S,8R,9S,10S,13R,14S)-3,7-dihydroxy-10,13-dimethylhexadecahydro-1H-cyclopenta[a]phenanthren-17-yl)pentanamido)methyl)benzoate (539 mg, 1 mmol), hydroxylamine hydrochloride (695 mg, 10 mmol), phenolphthalein (1 mg), sodium methoxide (2000 mg, 37 mmol). White solid. Yield 61 %; m.p. 170-172 °C; IR 3275, 2927, 2862, 1638, 1535, 1012 cm^{-1} ; ^1H NMR (400 MHz, $\text{DMSO-}d_6$) δ 11.17 (s, 1H), 9.01 (s, 1H), 8.34 (t, $J = 6.0$ Hz, 1H), 7.69 (d, $J = 8.1$ Hz, 2H), 7.29 (d, $J = 8.1$ Hz, 2H), 4.44 (d, $J = 4.5$ Hz, 1H), 4.28 (dd, $J = 5.9, 3.6$ Hz, 2H), 3.87 (d, $J = 6.8$ Hz, 1H), 3.29 (2H). 2.24 – 2.01 (m, 2H), 1.99 – 1.59 (m, 6H), 1.56 – 1.26 (m, 10H), 1.26 – 0.94 (m, 7H), 0.94 – 0.84 (m, 7H), 0.62 (s, 3H); ^{13}C NMR (101 MHz, $\text{DMSO-}d_6$) δ 172.63, 163.99, 143.06, 131.18, 126.92, 126.83, 69.73, 69.47, 55.88, 54.76, 43.09, 43.02, 42.18, 41.71, 39.85, 38.73, 37.73, 37.27, 34.93, 34.84, 33.77, 32.38, 31.67, 30.25, 28.21, 26.73, 23.33, 20.86, 18.44, 12.04; HRMS (ESI) for $\text{C}_{32}\text{H}_{47}\text{N}_2\text{O}_4$ calculated $[[\text{M} + \text{H}] + [-\text{H}_2\text{O}]]^+$: 523.3536. Obtained: 523.3536.

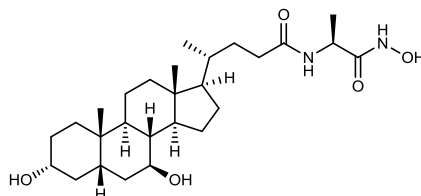
Synthesis of 4-((2-((R)-4-((3R,5S,7S,8R,9S,10S,13R,14S,17R)-3,7-dihydroxy-10,13-dimethylhexadecahydro-1H-cyclopenta[a]phenanthren-17-yl)pentanamido)acetamido)methyl)-N-hydroxybenzamide. **UDCA-HDAC6i #2**



This compound was prepared following the method C described above.

Methyl 4-((2-((4R)-4-((3R,5S,7S,8R,9S,10S,13R,14S)-3,7-dihydroxy-10,13-dimethylhexadecahydro-1H-cyclopenta[a]phenanthren-17-yl)pentanamido)acetamido)methyl)benzoate (84 mg, 0.14 mmol), hydroxylamine hydrochloride (97 mg, 1.4 mmol), phenolphthalein (1 mg), sodium methoxide (2000 mg, 37 mmol). White solid. Yield 42% m.p. 153-155 °C; IR 3217, 2928, 2864, 1641, 1534, 1013 cm^{-1} ; ^1H NMR (400 MHz, $\text{DMSO-}d_6$) δ 11.17 (s, 1H), 8.98 (s, 1H), 8.35 (t, $J = 6.0$ Hz, 1H), 8.05 (t, $J = 5.9$ Hz, 1H), 7.69 (d, $J = 8.1$ Hz, 2H), 7.30 (d, $J = 8.0$ Hz, 2H), 4.46 – 4.40 (m, 1H), 4.31 (d, $J = 6.0$ Hz, 2H), 3.86 (d, $J = 6.7$ Hz, 1H), 3.71 (d, $J = 5.9$ Hz, 2H), 3.29 (2H), 2.11 (m, $J = 57.0, 14.2, 10.0, 5.6$ Hz, 2H), 1.97 – 1.89 (m, 1H), 1.90 – 1.58 (m, 5H), 1.54 – 1.25 (m, 10H), 1.25 – 0.93 (m, 7H), 0.93 – 0.83 (m, 7H), 0.61 (s, 3H); ^{13}C NMR (101 MHz, $\text{DMSO-}d_6$) δ 173.04, 169.24, 164.03, 142.70, 131.21, 126.94, 126.81, 69.71, 69.46, 55.87, 54.73, 43.07, 43.01, 42.17, 42.10, 41.71, 38.72, 37.72, 37.27, 34.98, 34.83, 33.76, 32.18, 31.42, 30.25, 28.18, 26.72, 23.31, 20.85, 18.51, 12.05; HRMS (ESI) for $\text{C}_{34}\text{H}_{52}\text{N}_3\text{O}_6$ calculated $[\text{M} + \text{H}]^+$: 598.3856. Obtained: 598.3857.

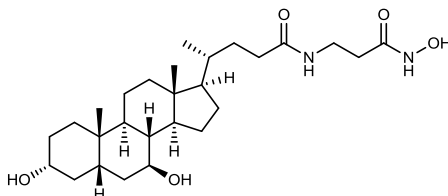
Synthesis of (R)-4-((3R,5S,7S,8R,9S,10S,13R,14S,17R)-3,7-dihydroxy-10,13-dimethylhexadecahydro-1H-cyclopenta[a]phenanthren-17-yl)-N-((S)-1-(hydroxyamino)-1-oxopropan-2-yl) pentanamide. **UDCA-HDAC6i #3**



This compound was prepared following the method A described above.

Methyl ((4R)-4-((3R,5S,7S,8R,9S,10S,13R,14S)-3,7-dihydroxy-10,13-dimethylhexadecahydro-1H-cyclopenta[a]phenanthren-17-yl)pentanoyl)-L-alaninate (193 mg, 0.4 mmol), hydroxylamine hydrochloride (278 mg, 4 mmol), phenolphthalein (1 mg), sodium methoxide (2000 mg, 37 mmol). White solid. Yield 22%. m.p. 170-172 °C; IR 3265, 2928, 2863, 1642, 1537, 1047 cm^{-1} ; ^1H NMR (400 MHz, $\text{DMSO}-d_6$) δ 7.96 (d, $J = 7.8$ Hz, 1H), 4.44 (s, 1H), 4.17 (p, $J = 7.1$ Hz, 1H), 3.86 (d, $J = 6.6$ Hz, 1H), 3.29 (2H), 2.13 (m, $J = 14.8, 10.2, 5.2$ Hz, 1H), 2.04 – 1.89 (m, 2H), 1.89 – 1.55 (m, 4H), 1.54 – 1.24 (m, 10H), 1.22 – 0.93 (m, 11H), 0.88 (d, $J = 6.1$ Hz, 7H), 0.61 (s, 3H); ^{13}C NMR (101 MHz, $\text{DMSO}-d_6$) δ 172.19, 169.09, 69.71, 69.45, 55.87, 54.71, 45.74, 43.07, 43.01, 42.16, 38.72, 37.72, 37.26, 35.03, 34.83, 33.75, 32.10, 31.48, 30.24, 28.18, 26.72, 23.31, 20.84, 18.49, 12.04. HRMS (ESI) for $\text{C}_{27}\text{H}_{47}\text{N}_2\text{O}_5$ calculated $[\text{M} + \text{H}]^+$: 479.3485. Obtained: 479.3483.

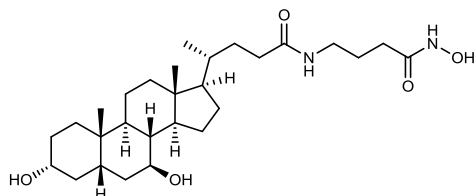
Synthesis of (R)-4-((3R,5S,7S,8R,9S,10S,13R,14S,17R)-3,7-dihydroxy-10,13-dimethylhexadecahydro-1H-cyclopenta[a]phenanthren-17-yl)-N-(3-(hydroxyamino)-3-oxopropyl)pentanamide. **UDCA-HDAC6i #4**



This compound was prepared following the method A described above.

Ethyl 3-((4R)-4-((3R,5S,7S,8R,9S,10S,13R,14S)-3,7-dihydroxy-10,13-dimethylhexadecahydro-1H-cyclopenta[a]phenanthren-17-yl)pentanamido)propanoate (298 mg, 0.61 mmol), hydroxylamine hydrochloride (424 mg, 6.1 mmol), phenolphthalein (1 mg), sodium methoxide (2000 mg, 37 mmol). White solid. Yield 59%; m.p. 180-182 °C; IR 3271, 2927, 2862, 1638, 1542, 1047 cm^{-1} ; ^1H NMR (400 MHz, DMSO-d_6) δ 7.82 (t, $J = 5.7$ Hz, 1H), 4.43 (s, 1H), 3.86 (d, $J = 6.8$ Hz, 1H), 3.30 (s, 2H), 3.19 (q, $J = 6.8$ Hz, 2H), 2.11 (m, 2H), 1.99 – 1.56 (m, 8H), 1.54 – 1.24 (m, 8H), 1.23 – 0.90 (m, 9H), 0.87 (d, $J = 4.4$ Hz, 7H), 0.61 (s, 3H); ^{13}C NMR (101 MHz, DMSO-d_6) δ 172.53, 167.03, 69.71, 69.45, 55.86, 54.70, 43.07, 43.01, 42.16, 39.99, 38.71, 37.72, 37.27, 35.27, 34.98, 34.83, 33.75, 32.53, 32.35, 31.59, 30.24, 28.17, 26.71, 23.31, 20.84, 18.47, 12.04; HRMS (ESI) for $\text{C}_{27}\text{H}_{47}\text{N}_2\text{O}_5$ calculated $[\text{M} + \text{H}]^+$: 479.3485. Obtained: 479.3480.

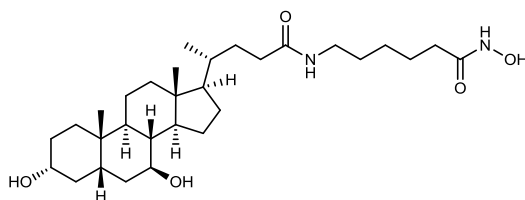
Synthesis of (R)-4-((3R,5S,7S,8R,9S,10S,13R,14S,17R)-3,7-dihydroxy-10,13-dimethylhexadecahydro-1H-cyclopenta[a]phenanthren-17-yl)-N-(4-(hydroxyamino)-4-oxobutyl)pentanamide. **UDCA-HDAC6i #5**



This compound was prepared following the method A described above.

Methyl 4-((4R)-4-((3R,5S,7S,8R,9S,10S,13R,14S)-3,7-dihydroxy-10,13-dimethylhexadecahydro-1H-cyclopenta[a]phenanthren-17-yl)pentanamido)butanoate (165 mg, 0.34 mmol), hydroxylamine hydrochloride (237 mg, 3.4 mmol), phenolphthalein (1 mg), sodium methoxide (2000 mg, 37 mmol). White solid. Yield 54%. m.p. 165-167 °C; IR 3269, 2928, 2862, 1643, 1550, 1047 cm^{-1} ; ^1H NMR (400 MHz, $\text{DMSO-}d_6$) δ 7.81 (t, J = 5.6 Hz, 1H), 4.46 (s, 1H), 3.88 (d, J = 6.6 Hz, 1H), señal correspondiente a 2H superpuesta con señal de agua a 3.29 ppm (confirmado por COSY), 3.00 (q, J = 6.6 Hz, 2H), 2.16 – 1.91 (m, 6H), 1.89 – 1.54 (m, 7H), 1.54 – 1.25 (m, 9H), 1.25 – 0.92 (m, 9H), 0.89 (d, J = 7.8 Hz, 7H), 0.62 (s, 3H); ^{13}C NMR (101 MHz, $\text{DMSO-}d_6$) δ 172.45, 168.69, 69.71, 69.45, 55.87, 54.70, 43.07, 43.01, 42.17, 38.72, 38.05, 37.72, 37.27, 34.97, 34.83, 33.76, 32.43, 31.67, 30.24, 29.91, 28.18, 26.72, 25.45, 23.31, 20.84, 18.48, 12.03; HRMS (ESI) for $\text{C}_{28}\text{H}_{49}\text{N}_2\text{O}_5$ calculated $[\text{M} + \text{H}]^+$: 493.3641. Obtained: 493.3642.

Synthesis of 6-((R)-4-((3R,5S,7S,8R,9S,10S,13R,14S, 17R)-3,7-dihydroxy-10,13-dimethylhexadecahydro-1H-cyclopenta[a]phenanthren-17-yl)pentanamido)-N-hydroxyhexanamide. **UDCA-HDAC6i#6**

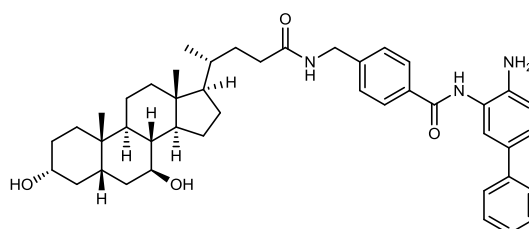


This compound was prepared following the method A described above.

Methyl 6-((4R)-4-((3R,5S,7S,8R,9S,10S,13R,14S)-3,7-dihydroxy-10,13-dimethylhexadecahydro-1H-cyclopenta[a]phenanthren-17-yl)pentanamido)hexanoate (200 mg, 0.38 mmol), hydroxylamine hydrochloride (263, 3.8 mmol), phenolphthalein (1 mg), sodium methoxide (2000 mg, 37 mmol). White solid. Yield 43%; m.p. 125-127 °C; IR 3269, 2927, 2861, 1642, 1547, 1047 cm^{-1} ; ^1H NMR (400 MHz, $\text{DMSO-}d_6$) δ 10.32 (s, 1H), 8.64 (s, 1H), 7.71 (t, $J = 5.6$ Hz, 1H), 4.43 (d, $J = 4.5$ Hz, 1H), 3.86 (d, $J = 6.8$ Hz, 1H), 3.29 (2H), 2.98 (q, $J = 6.5$ Hz, 2H), 2.06 (m, $J = 14.5, 9.7, 5.2$ Hz, 1H), 2.00 – 1.53 (m, 9H), 1.55 – 1.26 (m, 14H), 1.26 – 0.90 (m, 9H), 0.88 (d, $J = 7.3$ Hz, 7H), 0.61 (s, 3H); ^{13}C NMR (101 MHz, $\text{DMSO-}d_6$) δ 172.28, 168.99, 69.71, 69.45, 55.87, 54.70, 43.07, 43.00, 42.16, 38.72, 38.27, 37.72, 37.26, 34.93, 34.82, 33.75, 32.43, 32.20, 31.69, 30.24, 28.93, 28.18, 26.71, 26.04, 24.88, 23.31, 20.84, 18.47, 12.02; HRMS (ESI) for $\text{C}_{30}\text{H}_{53}\text{N}_2\text{O}_5$ calculated $[\text{M} + \text{H}]^+$: 521.3954. Obtained: 521.3955.

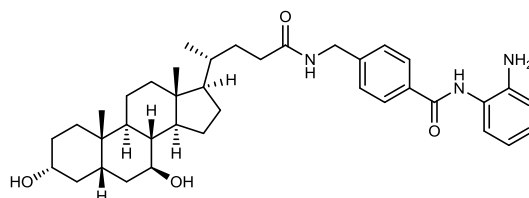
Synthesis of N-(4-amino-[1,1'-biphenyl]-3-yl)-4-(((R)-4-((3R,5S,7S,8R,9S,10S,13R,14S,17R)-3,7-dihydroxy-10,13-dimethylhexadecahydro-1H-cyclopenta[a]phenanthren-17-yl)pentanamido)methyl)benzamide.

UDCA-HDAC6i #7



This compound was prepared following the method B described above. Tert-butyl (3-(4-(((4R)-4-((3R,5S,7S,8R,9S,10S,13R,14S)-3,7-dihydroxy-10,13-dimethylhexadecahydro-1H-cyclopenta[a]phenanthren-17-yl)pentanamido)methyl) benzamido)-[1,1'-biphenyl]-4-yl)carbamate (53 mg, 0.07 mmol) HCl 4M in dioxane (0.3 mL). White solid. Yield 22%; m.p. 163-165 °C; IR 3321, 2927, 2862, 1649, 1489, 1048, 760, 698 cm⁻¹; ¹H NMR (400 MHz, DMSO-*d*₆) δ 9.70 (s, 1H), 8.39 (t, *J* = 6.0 Hz, 1H), 7.95 (d, *J* = 7.9 Hz, 2H), 7.59 – 7.49 (m, 3H), 7.45 – 7.29 (m, 5H), 7.25 (q, *J* = 7.3, 6.6 Hz, 1H), 6.87 (d, *J* = 8.3 Hz, 1H), 5.08 (s, 2H), 4.43 (d, *J* = 4.6 Hz, 1H), 4.33 (dd, *J* = 5.9, 3.8 Hz, 2H), 3.86 (d, *J* = 6.8 Hz, 1H), signal corresponding to 2H overlapped with broad signal of water at 3.29 ppm, 2.29 – 1.88 (m, 3H), 1.89 – 1.59 (m, 6H), 1.54 – 1.26 (m, 10H), 1.26 – 0.97 (m, 4H), 0.97 – 0.83 (m, 9H), 0.62 (s, 3H); ¹³C NMR (101 MHz, DMSO-*d*₆) δ 172.66, 165.23, 143.46, 142.74, 140.17, 132.98, 128.78, 128.13, 127.81, 126.83, 126.00, 125.49, 124.75, 124.65, 123.60, 116.52, 69.71, 69.46, 55.88, 54.75, 43.09, 43.01, 42.16, 41.73, 38.72, 37.72, 37.27, 34.93, 34.83, 33.76, 32.41, 31.70, 30.24, 28.20, 26.73, 23.31, 20.85, 18.46, 12.04; HRMS (ESI) for C₄₄H₅₈N₃O₄ calculated [M + H]⁺: 692.4427. Obtained: 692.4414.

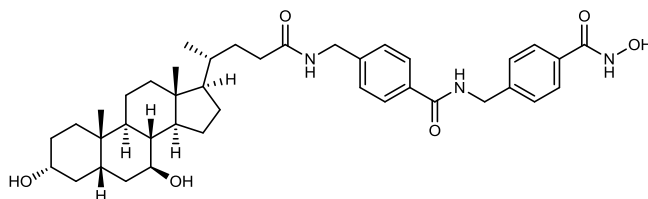
Synthesis of N-(2-aminophenyl)-4-(((R)-4-((3R,5S,7S,8R,9S,10S,13R,14S,17R)-3,7-dihydroxy-10,13-dimethylhexadecahydro-1H-cyclopenta[a]phenanthren-17-yl)pentanamido)methyl)benzamide. **UDCA-HDAC6i#8**



This compound was prepared following the method B described above. 4-(((4R)-4-((3R,5S,7S,8R,9S,10S,13R,14S)-3,7-dihydroxy-10,13-dimethylhexadecahydro-1H-cyclopenta[a]phenanthren-17-yl)pentanamido)methyl) benzoic acid (200 mg, 0.38 mmol) o-Phenylenediamine (41 mg, 0.38 mmol) TBTU (146 mg, 0.46 mmol) Et₃N (0.42 mL, 3.26 M). White solid. Yield 39 %; m.p. 168-170 °C; IR 3294, 2927, 2862, 1647, 1505, 1048, 745 cm⁻¹; ¹H NMR (400 MHz, DMSO-*d*₆) δ 9.61 (s, 1H), 8.38 (t, *J* = 6.0 Hz, 1H), 7.92 (d, *J* = 7.9 Hz, 2H), 7.35 (d, *J* = 7.9 Hz, 2H), 7.16 (d, *J* = 7.9 Hz, 1H), 7.04 – 6.92 (m, 1H), 6.78 (dd, *J* = 8.0, 1.4 Hz, 1H), 6.69 – 6.49 (m, 1H), 4.88 (s, 2H), 4.42 (d, *J* = 4.6 Hz, 1H), 4.37 – 4.25 (m, 2H), 3.86 (d, *J* = 6.8 Hz, 1H), 3.29 (2H), 2.25 – 2.01 (m, 2H), 1.98 – 1.58 (m, 6H), 1.56 – 1.27 (m, 9H), 1.27 – 0.94 (m, 5H), 0.94 – 0.82 (m, 10H), 0.62 (s, 3H); ¹³C NMR (101 MHz, DMSO-*d*₆) δ 172.63, 165.05, 143.38, 143.11, 132.99, 127.74, 126.81, 126.66, 126.43, 123.32, 116.23, 116.11, 69.70, 69.46, 55.87, 54.75, 43.08, 43.01, 42.15, 41.71, 38.71, 37.71, 37.26, 34.91, 34.82, 33.75, 32.39, 31.69, 30.24, 28.19, 26.72, 23.31, 20.84, 18.45, 12.03; HRMS (ESI) for C₃₈H₅₄N₃O₄ calculated [M + H]⁺: 616.4114. Obtained: 616.4110.

Synthesis of 4-(((R)-4-((3R,5S,7S,8R,9S,10S,13R,14S,17R)-3,7-dihydroxy-10,13-dimethylhexadecahydro-1H-cyclopenta[a]phenanthren-17-yl)pentanamido)methyl)-N-(4-(hydroxycarbonyl)benzyl)benzamide.

UDCA-HDAC6i#9



This compound was prepared following the method C described above.

Methyl 4-(((4-(((4R)-4-((3R,5S,7S,8R,9S,10S,13R,14S)-3,7-dihydroxy-10,13-dimethylhexadecahydro-1H-cyclopenta[a]phenanthren-17-

yl)pentanamido)methyl) benzamido)methyl)benzoate (134 mg, 0.2 mmol),

hydroxylamine hydrochloride (139 mg, 2 mmol), phenolphthalein (1 mg), sodium

methoxide (2000 mg, 37 mmol). White solid. Yield 60 %; m.p. 187-189 °C; IR

3288, 2922, 2851, 1638, 1542, 1015 cm^{-1} ; ^1H NMR (400 MHz, $\text{DMSO-}d_6$) δ 9.03

(t, $J = 6.0$ Hz, 1H), 8.35 (t, $J = 6.0$ Hz, 1H), 7.84 (d, $J = 8.0$ Hz, 2H), 7.70 (d, $J =$

7.9 Hz, 2H), 7.33 (dd, $J = 10.4, 8.0$ Hz, 4H), 4.50 (d, $J = 5.9$ Hz, 2H), 4.46 – 4.40

(m, 1H), 4.36 – 4.22 (m, 2H), 3.88 (s, 1H), 3.92 (2H) , 2.28 – 1.99 (m, 2H), 1.99

– 1.56 (m, 5H), 1.54 – 1.25 (m, 9H), 1.25 – 0.94 (m, 8H), 0.94 – 0.84 (m, 8H),

0.61 (s, 3H); ^{13}C NMR (101 MHz, $\text{DMSO-}d_6$) δ 172.63, 166.03, 164.08, 143.29,

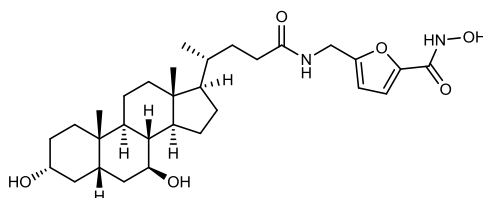
142.96, 132.60, 131.26, 127.24, 126.99, 126.90, 69.71, 69.46, 55.86, 54.74,

43.08, 43.01, 42.35, 42.16, 41.69, 39.99, 38.71, 37.71, 37.27, 34.91, 34.82,

33.76, 32.38, 31.66, 30.24, 28.18, 26.72, 23.31, 20.84, 18.45, 12.03; HRMS (ESI)

for $\text{C}_{40}\text{H}_{54}\text{N}_3\text{O}_5$ calculated $[[\text{M} + \text{H}] + [-\text{H}_2\text{O}]]^+$: 656.4064. Obtained: 656.4054.

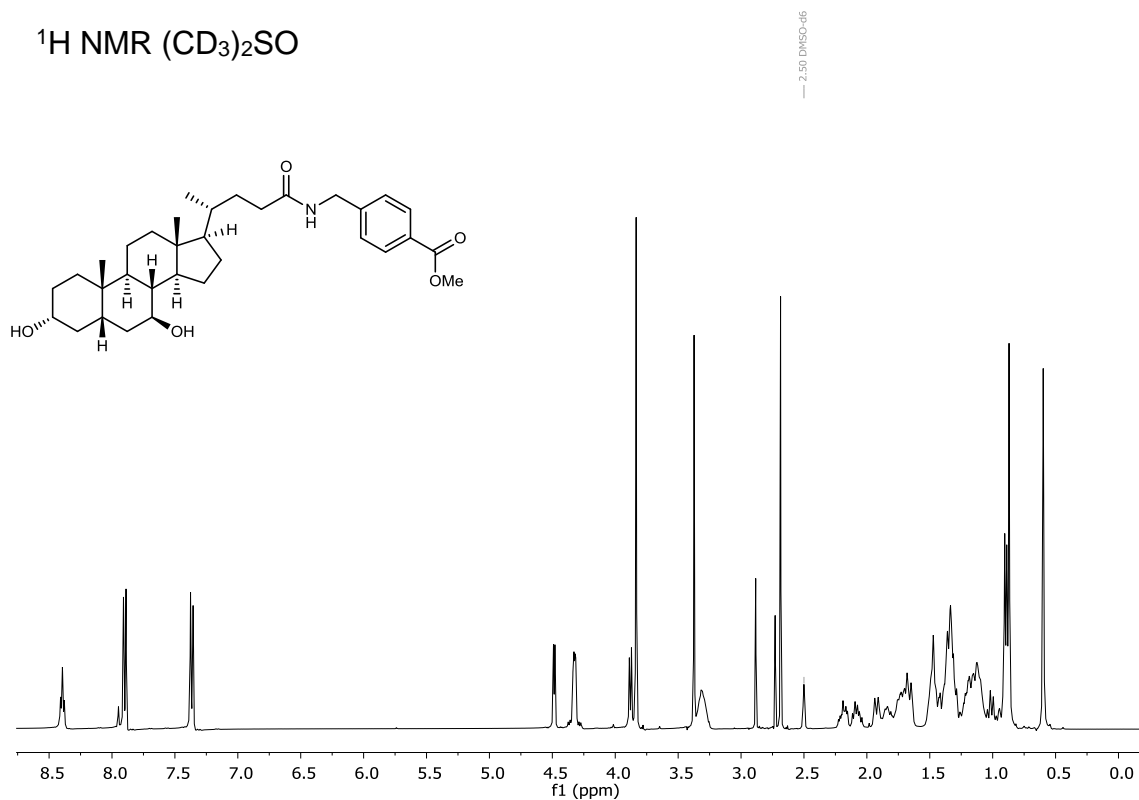
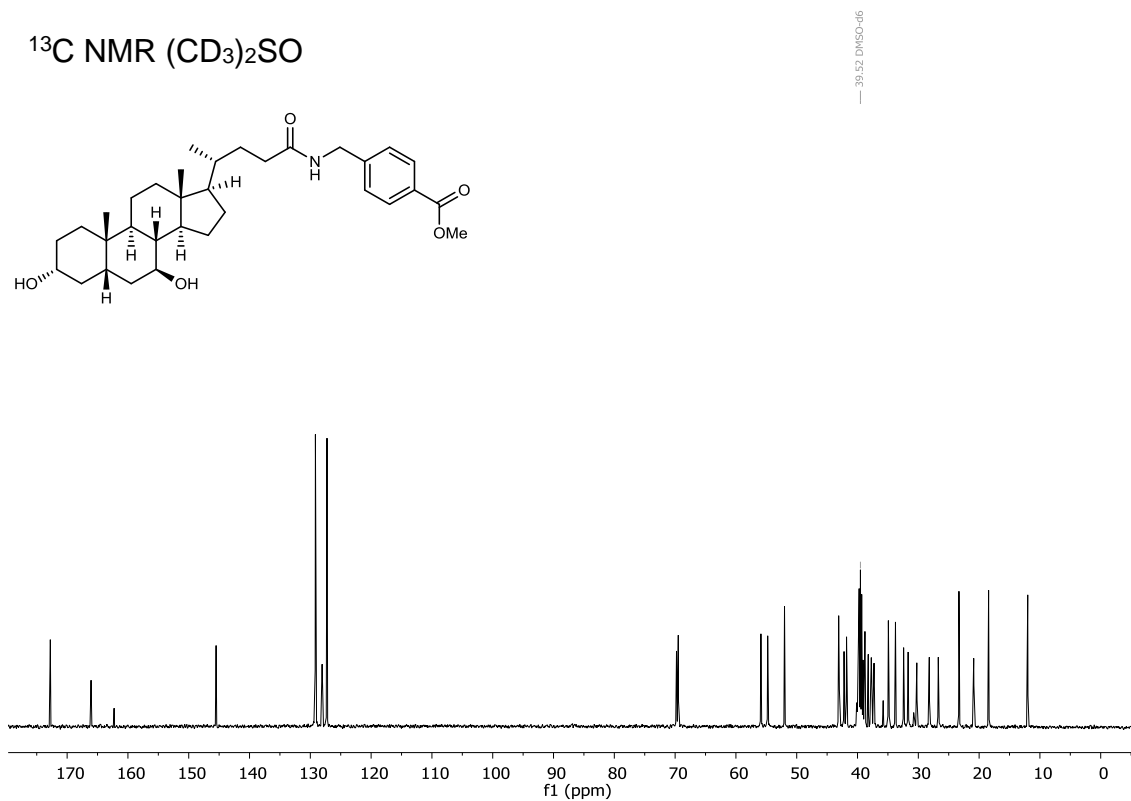
Synthesis of 5-(((R)-4-((3R,5S,7S,8R,9S,10S,13R,14S,17R)-3,7-dihydroxy-10,13-dimethylhexadecahydro-1H-cyclopenta[a]phenanthren-17-yl)pentanamido)methyl)-N-hydroxyfuran-2-carboxamide. **UDCA-HDAC6i#10**



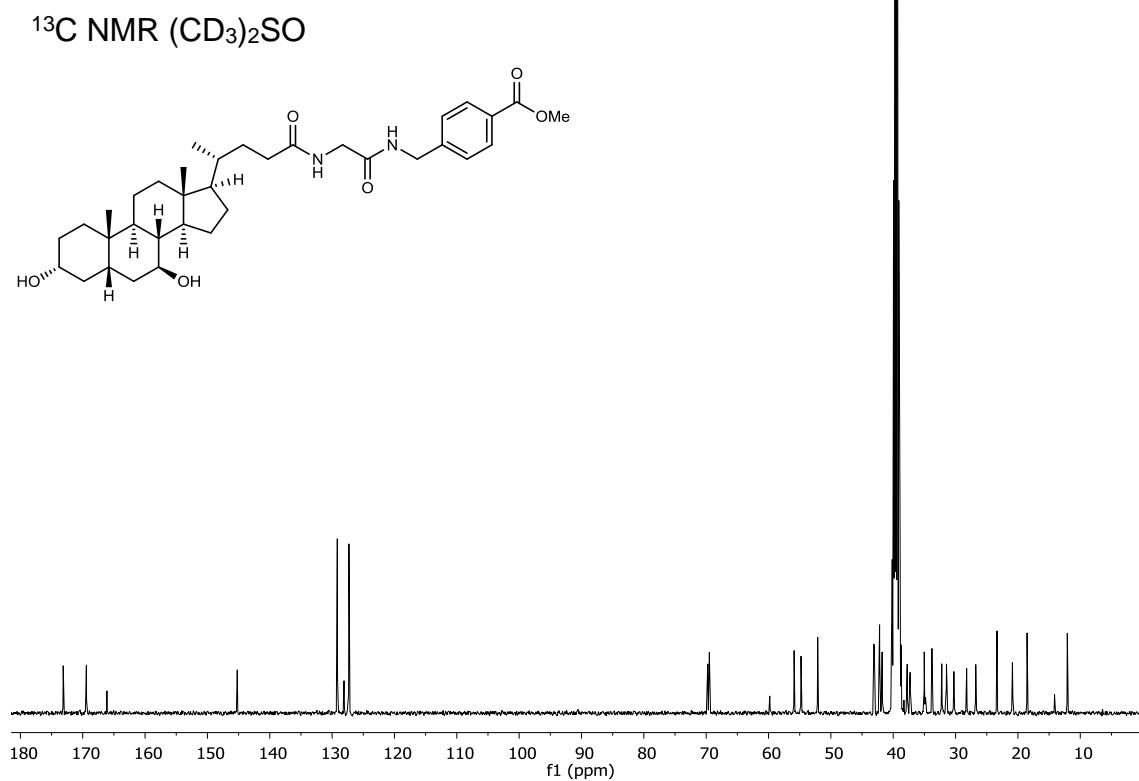
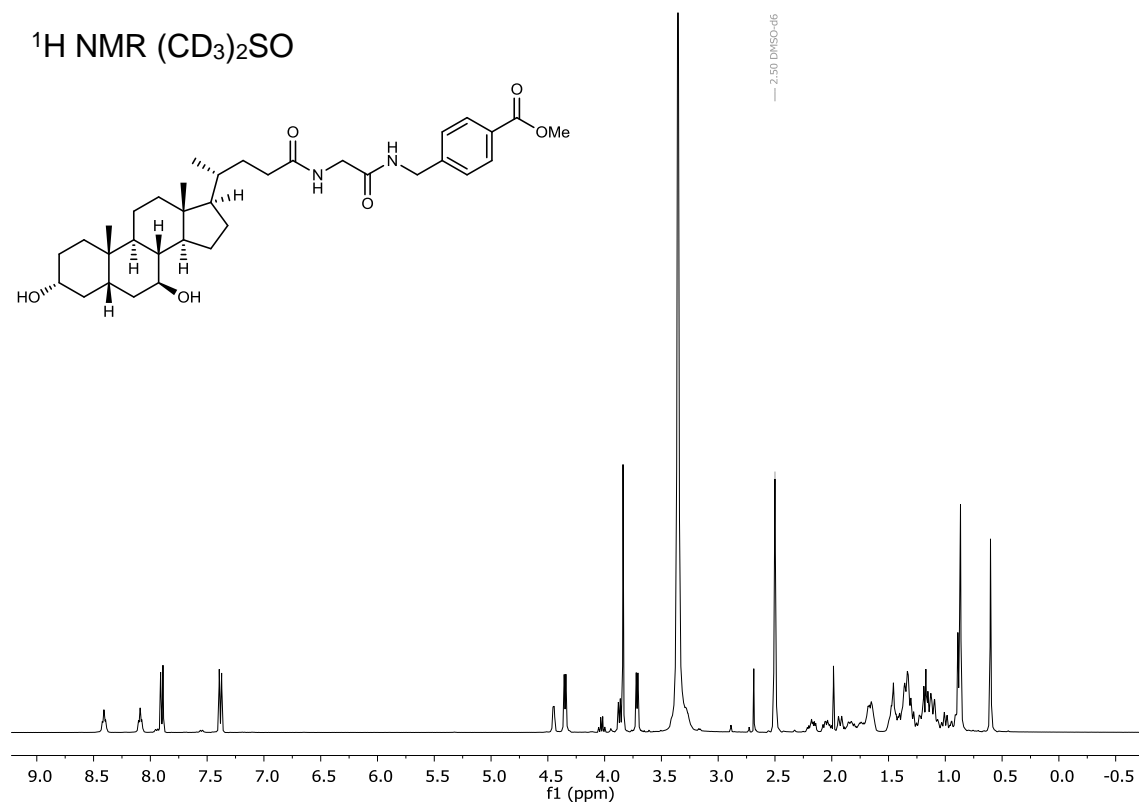
This compound was prepared following the method A described above.

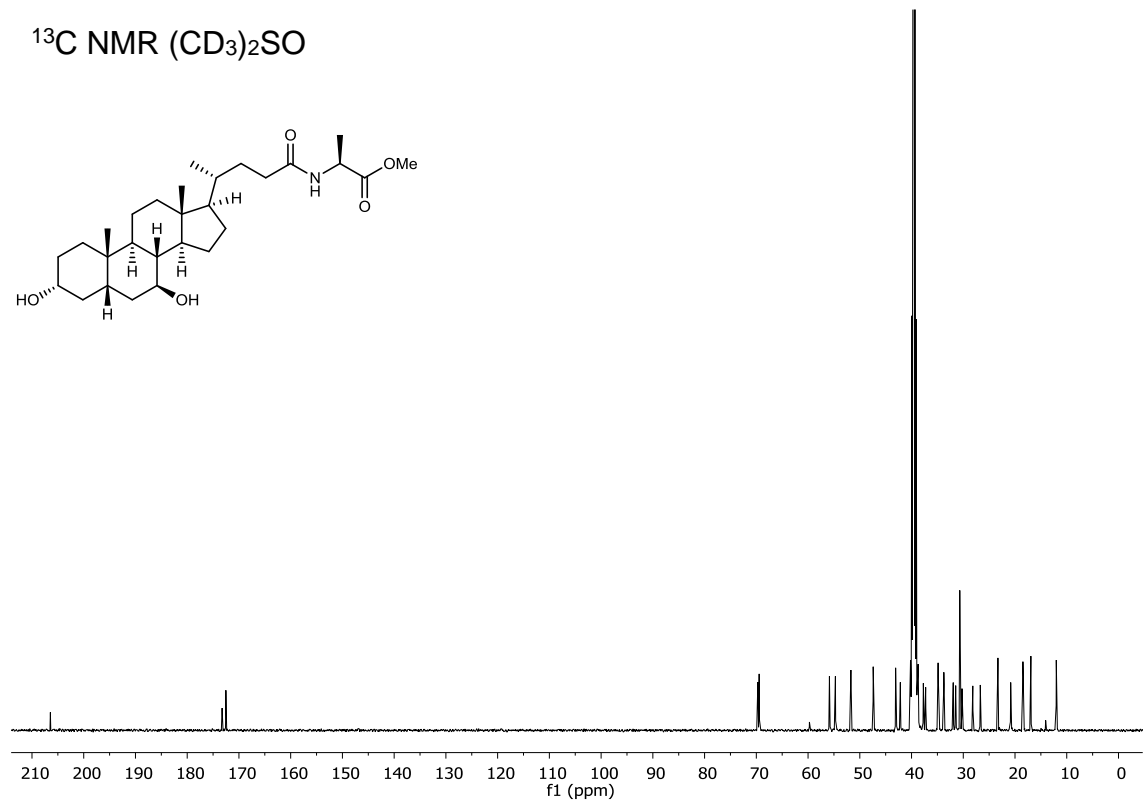
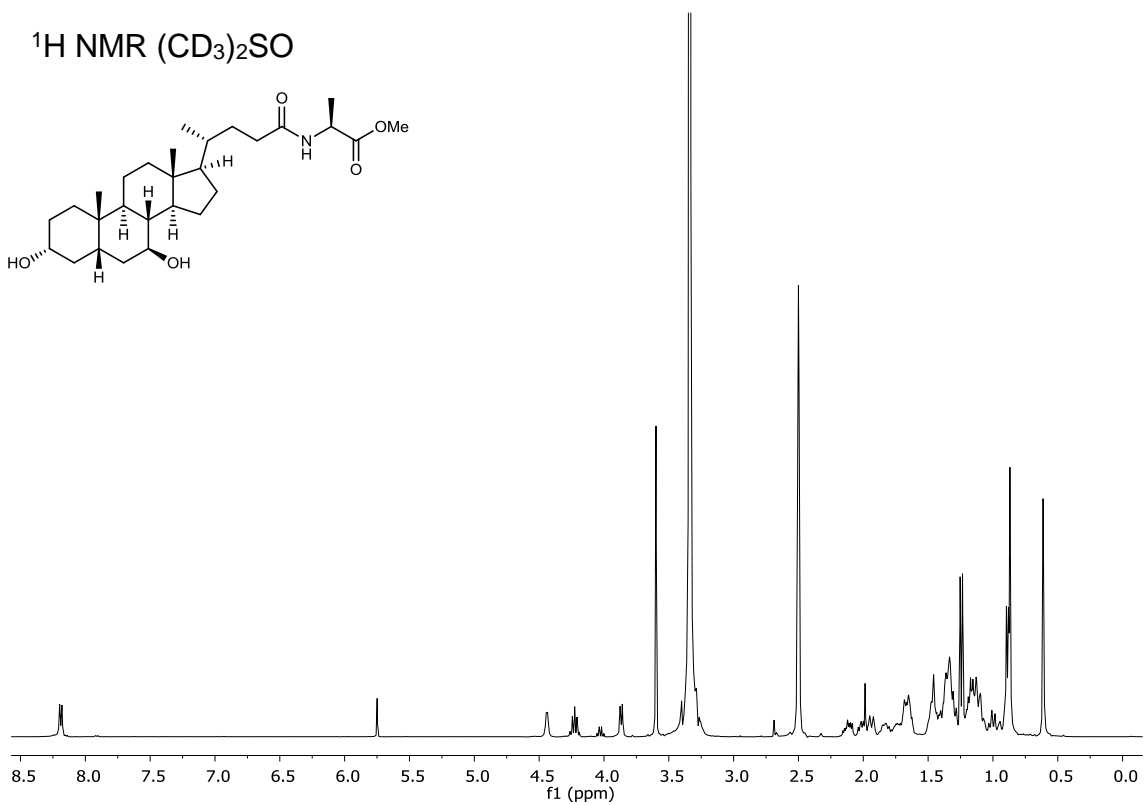
Methyl 5-(((4R)-4-((3R,5S,7S,8R,9S,10S,13R,14S)-3,7-dihydroxy-10,13-dimethylhexadecahydro-1H-cyclopenta[a]phenanthren-17-yl)pentanamido)methyl) furan-2-carboxylate (79 mg, 0.15 mmol), hydroxylamine hydrochloride (104 mg, 1.5 mmol), phenolphthalein (1 mg), sodium methoxide (2000 mg, 37 mmol). White solid. Yield 47%; m.p. 149-151 °C; IR 3272, 2929, 2864, 1644, 1540, 1016 cm^{-1} ; ^1H NMR (400 MHz, $\text{DMSO-}d_6$) δ 11.02 (s, 1H), 9.05 (s, 1H), 8.30 (t, $J = 5.6$ Hz, 1H), 6.95 (d, $J = 3.3$ Hz, 1H), 6.30 (d, $J = 3.4$ Hz, 1H), 4.43 (d, $J = 4.6$ Hz, 1H), 4.26 (d, $J = 5.5$ Hz, 2H), 3.86 (d, $J = 6.8$ Hz, 1H), 3.26 (d, $J = 5.2$ Hz, 0H), 2.24 – 1.97 (m, 2H), 1.97 – 1.56 (m, 6H), 1.56 – 1.25 (m, 9H), 1.25 – 0.93 (m, 7H), 0.93 – 0.83 (m, 8H), 0.60 (s, 3H).; ^{13}C NMR (101 MHz, $\text{DMSO-}d_6$) δ 172.57, 156.39, 154.91, 144.99, 113.56, 108.14, 69.71, 69.45, 55.86, 54.69, 43.07, 43.01, 42.16, 38.71, 37.72, 37.27, 35.62, 34.93, 34.83, 33.76, 32.18, 31.52, 30.24, 28.16, 26.71, 23.31, 20.84, 18.45, 12.03; HRMS (ESI) for $\text{C}_{30}\text{H}_{45}\text{N}_2\text{O}_5$ calculated $[[\text{M} + \text{H}] + [-\text{H}_2\text{O}]]^+$: 513.3329. Obtained: 513.3327.

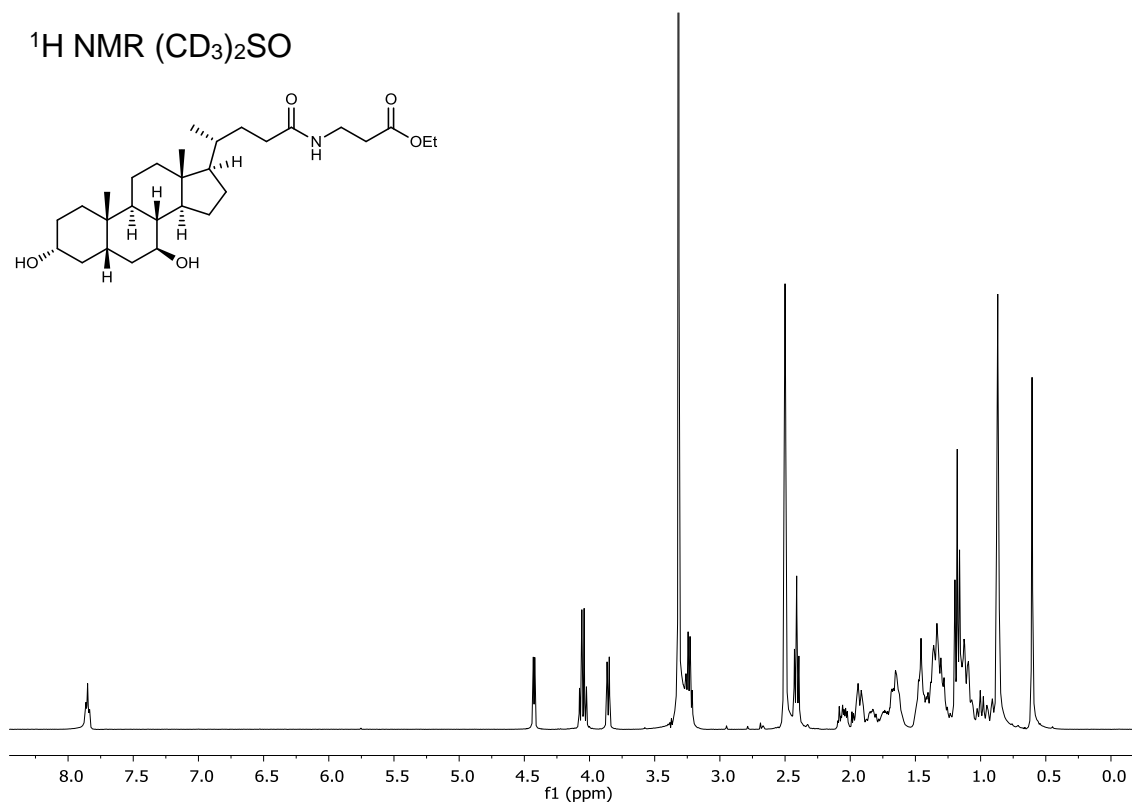
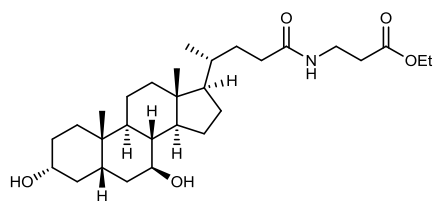
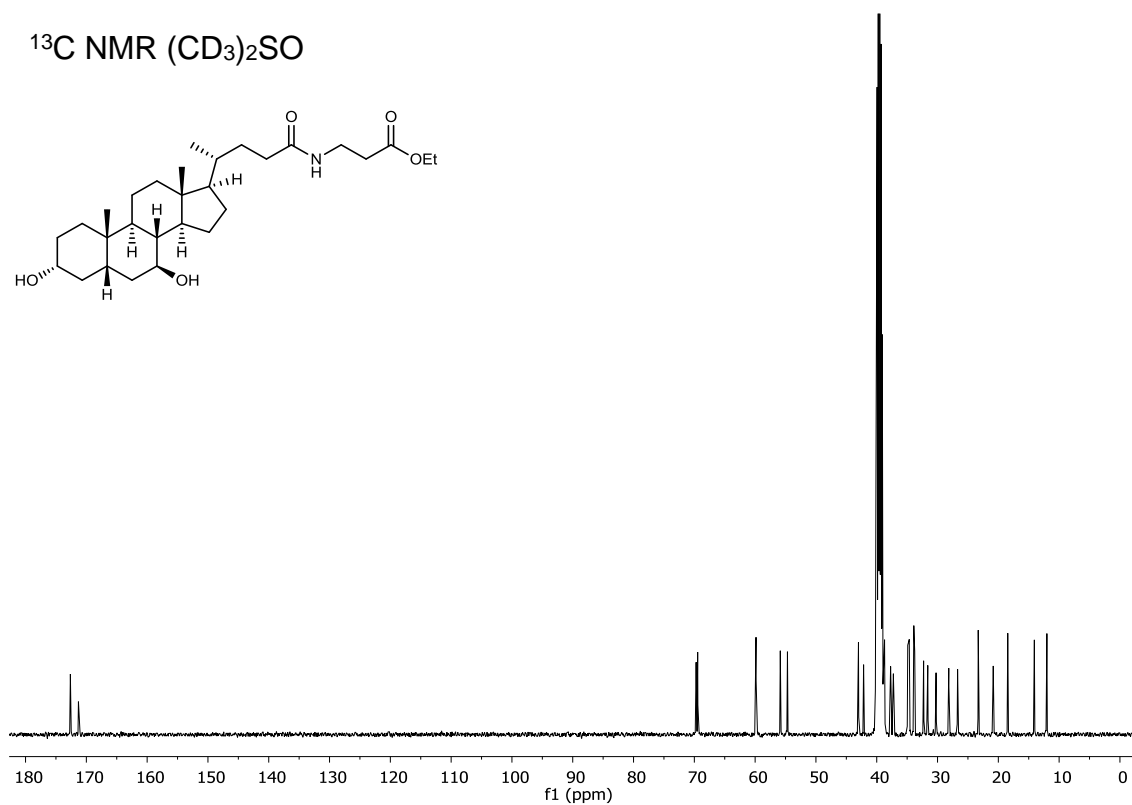
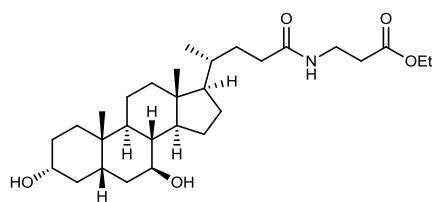
Compound (3a):

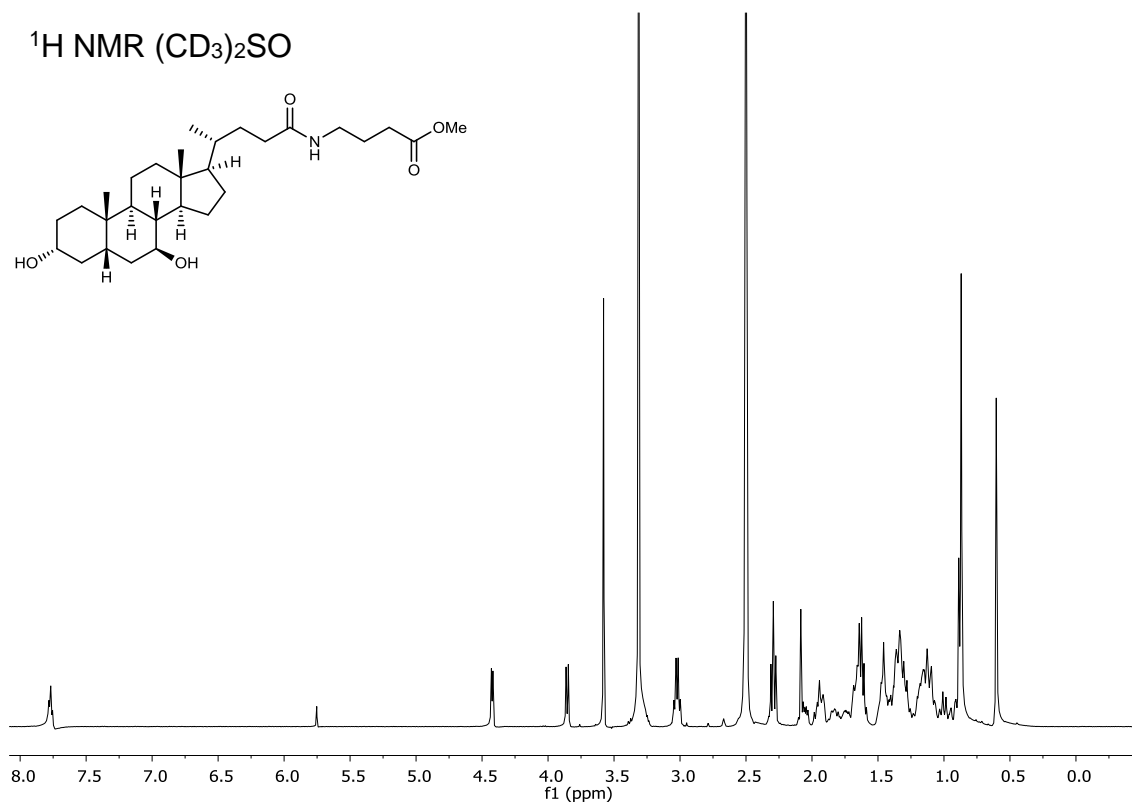
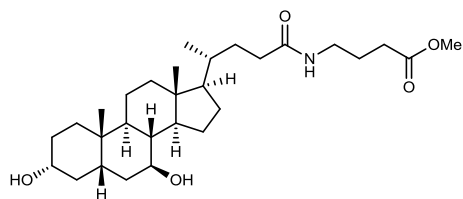
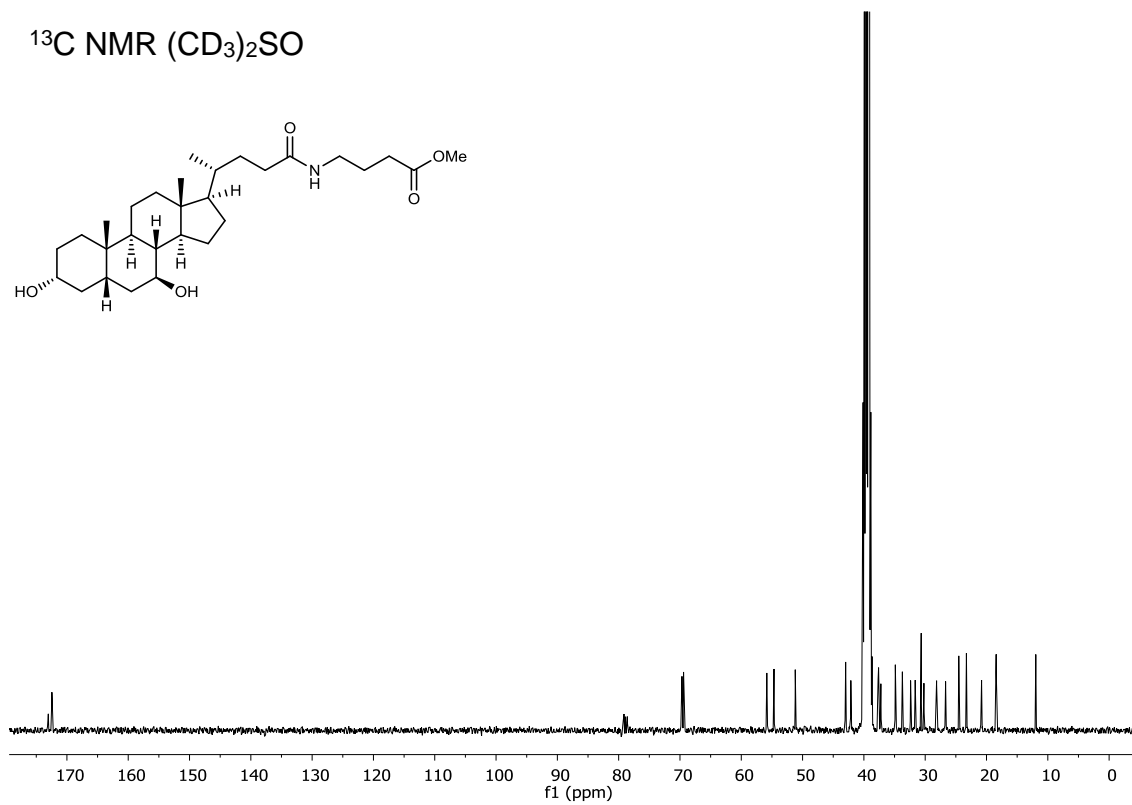
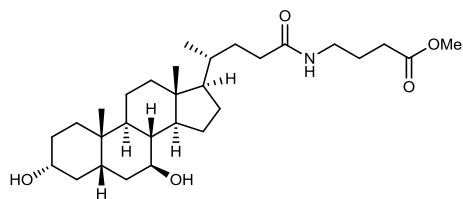
 ^1H NMR ($\text{CD}_3)_2\text{SO}$  ^{13}C NMR ($\text{CD}_3)_2\text{SO}$ 

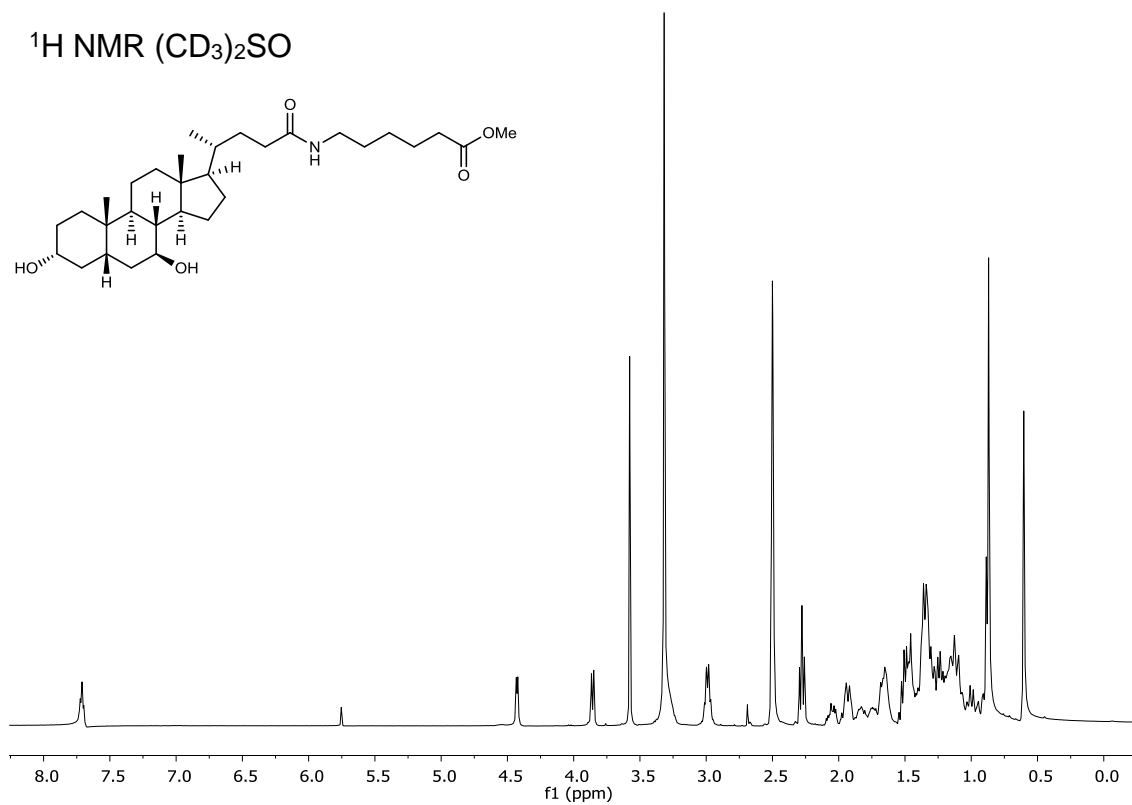
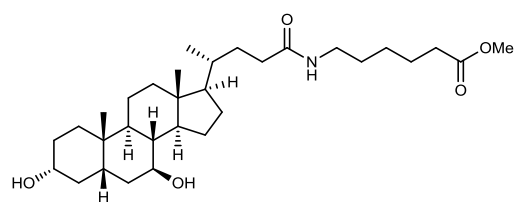
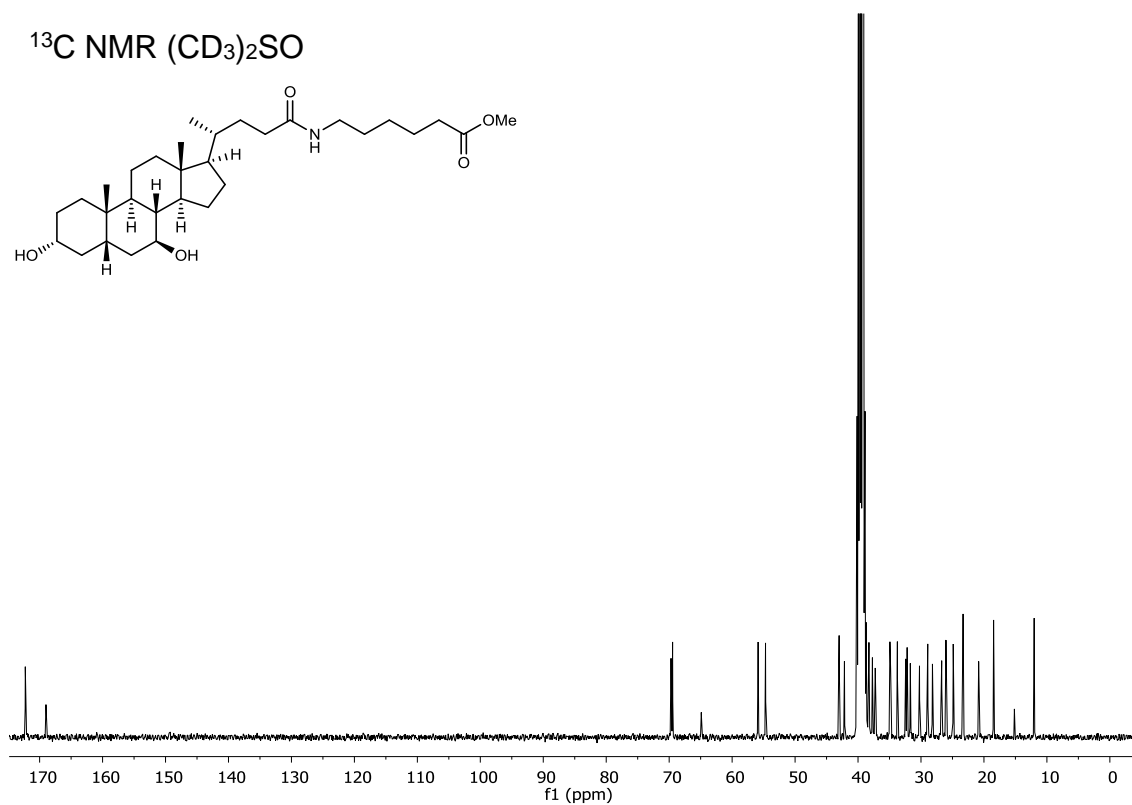
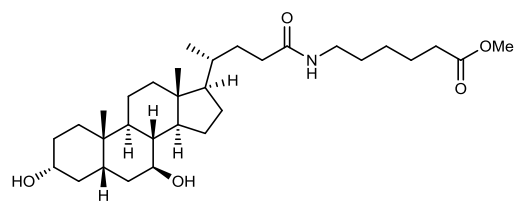
Compound (6a):

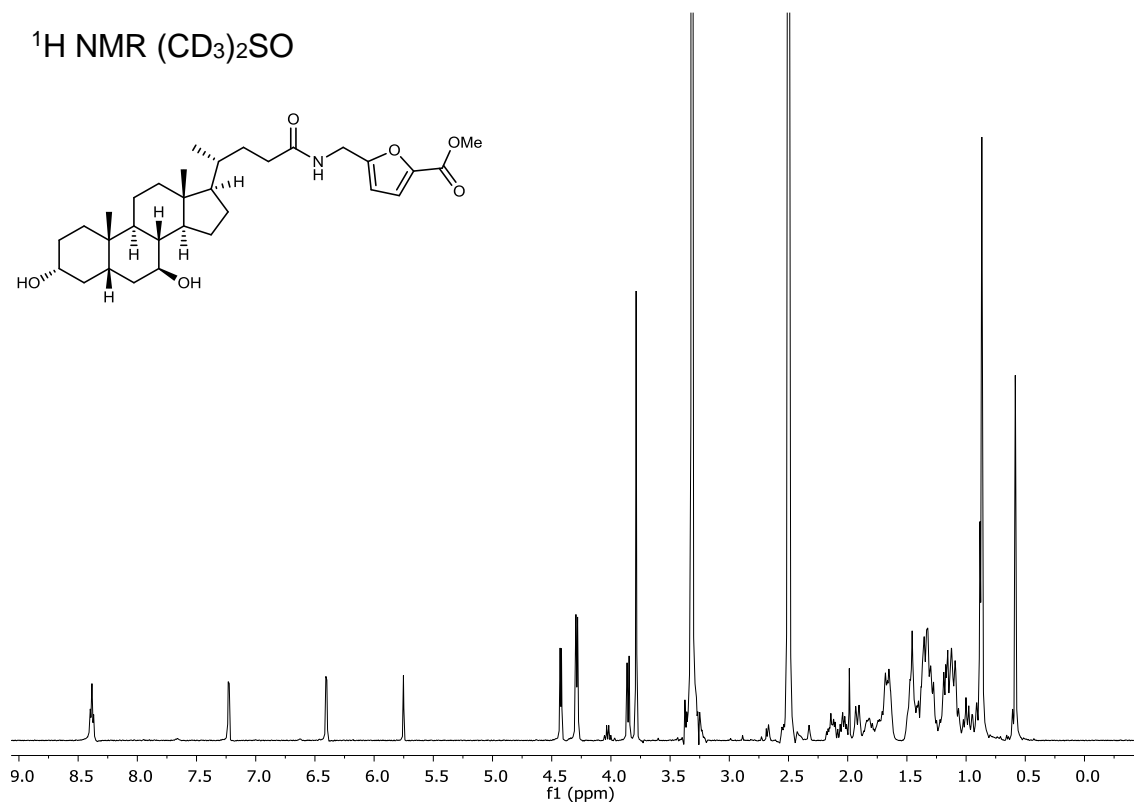
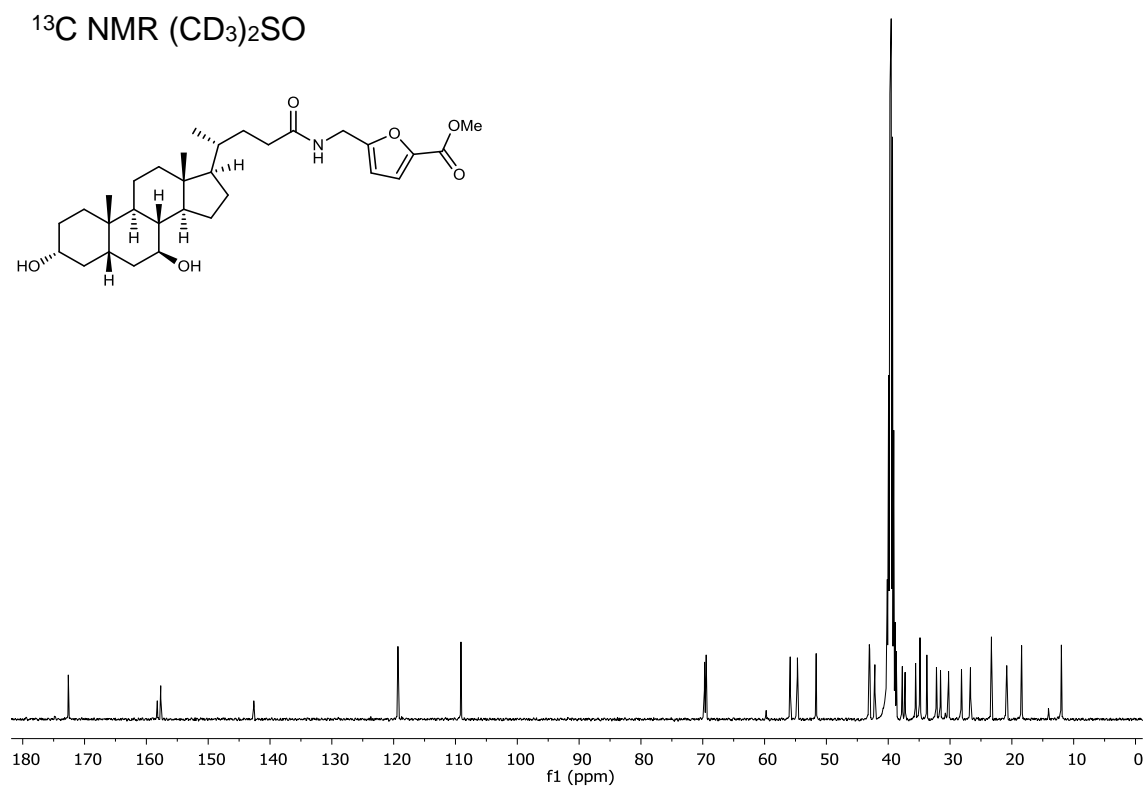


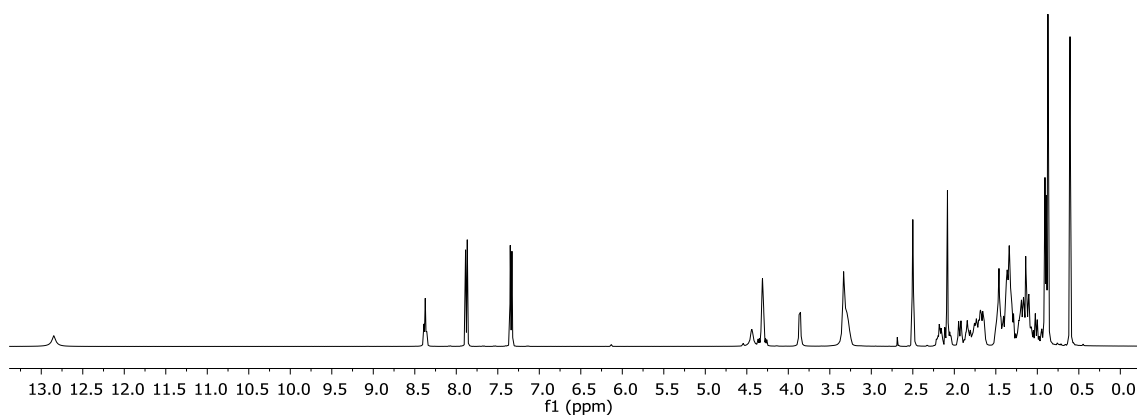
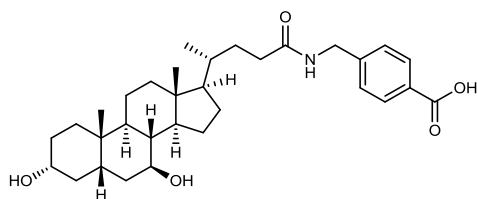
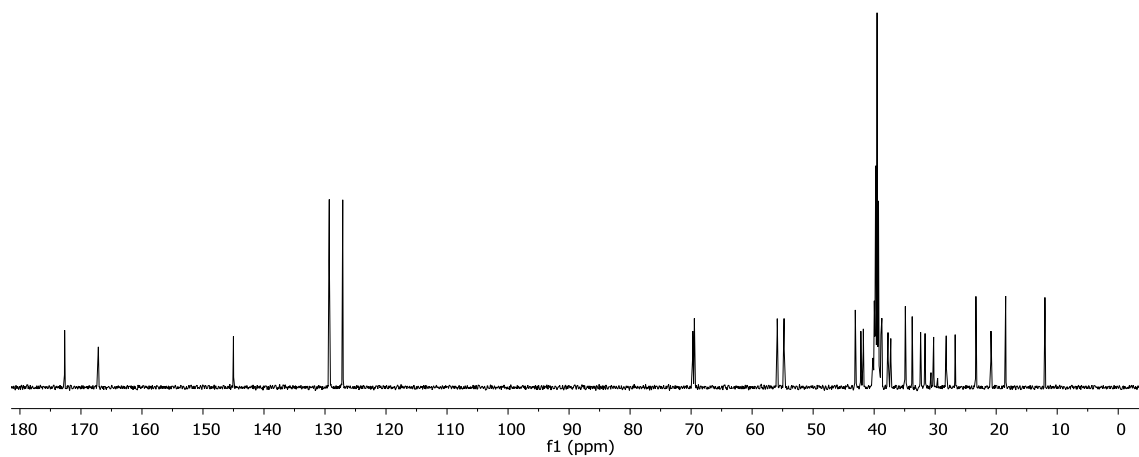
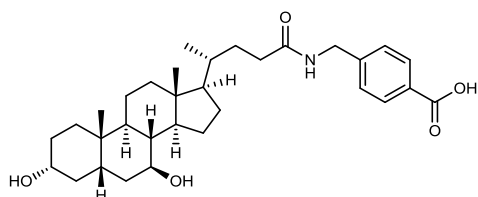
Compound **(3b)**:

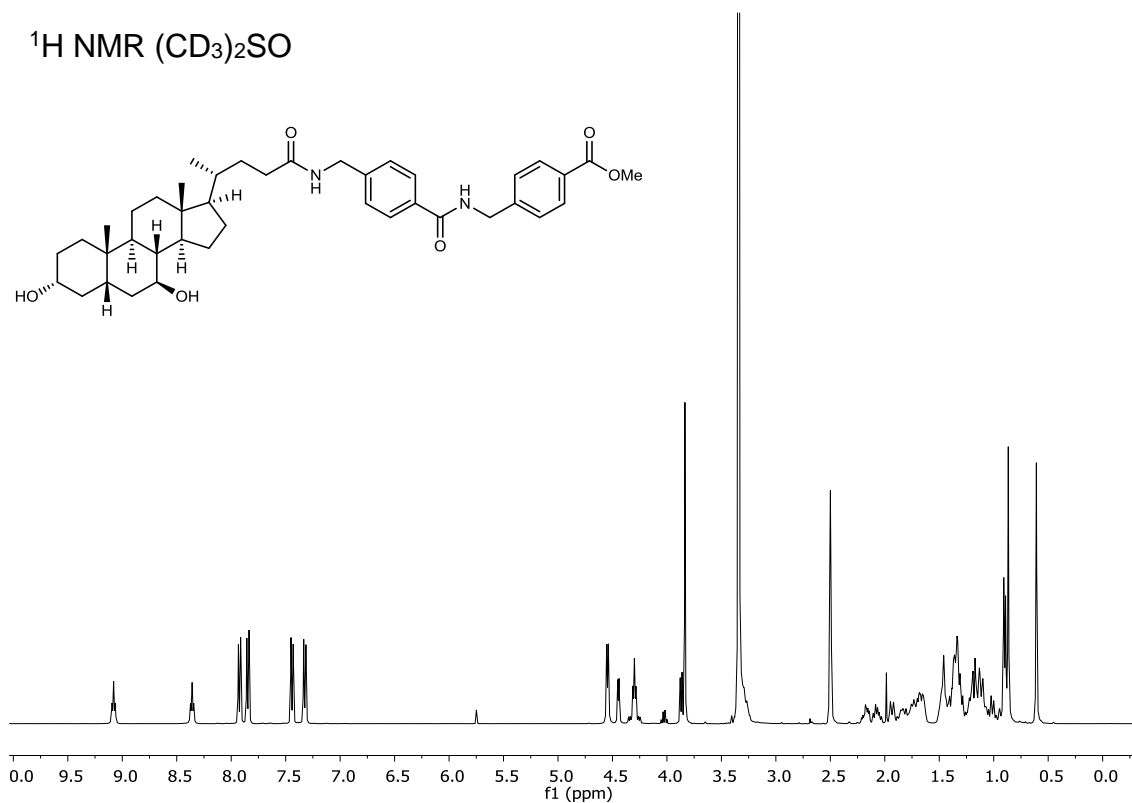
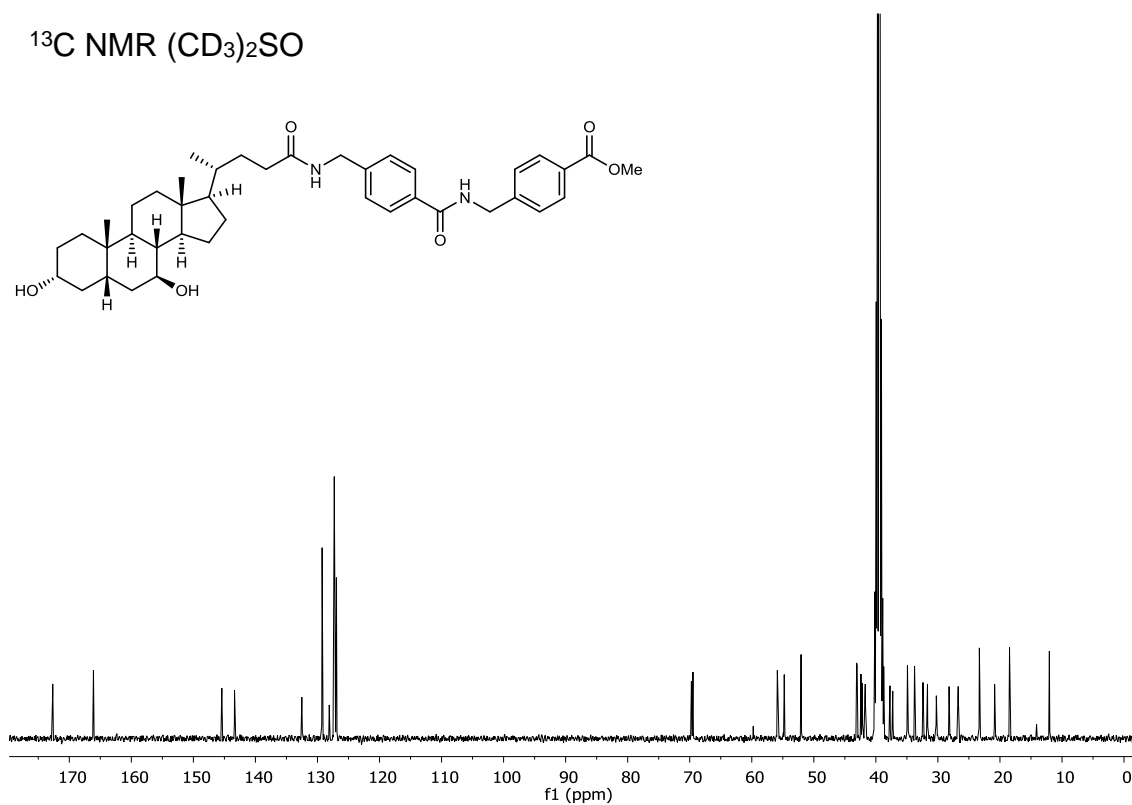
Compound **(3c)**: ^1H NMR ($\text{CD}_3)_2\text{SO}$  ^{13}C NMR ($\text{CD}_3)_2\text{SO}$ 

Compound (**3d**): ^1H NMR ($\text{CD}_3)_2\text{SO}$  ^{13}C NMR ($\text{CD}_3)_2\text{SO}$ 

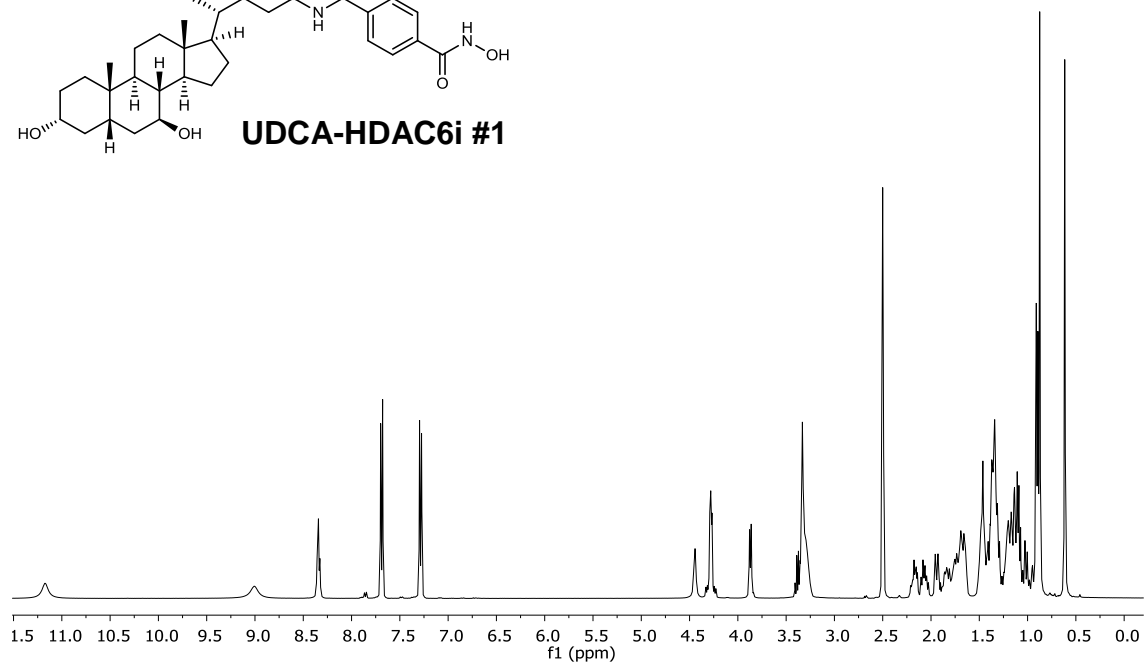
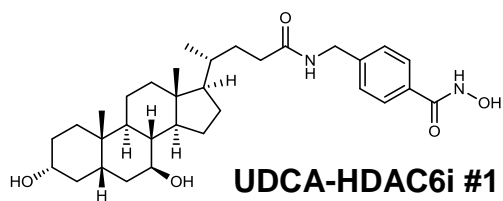
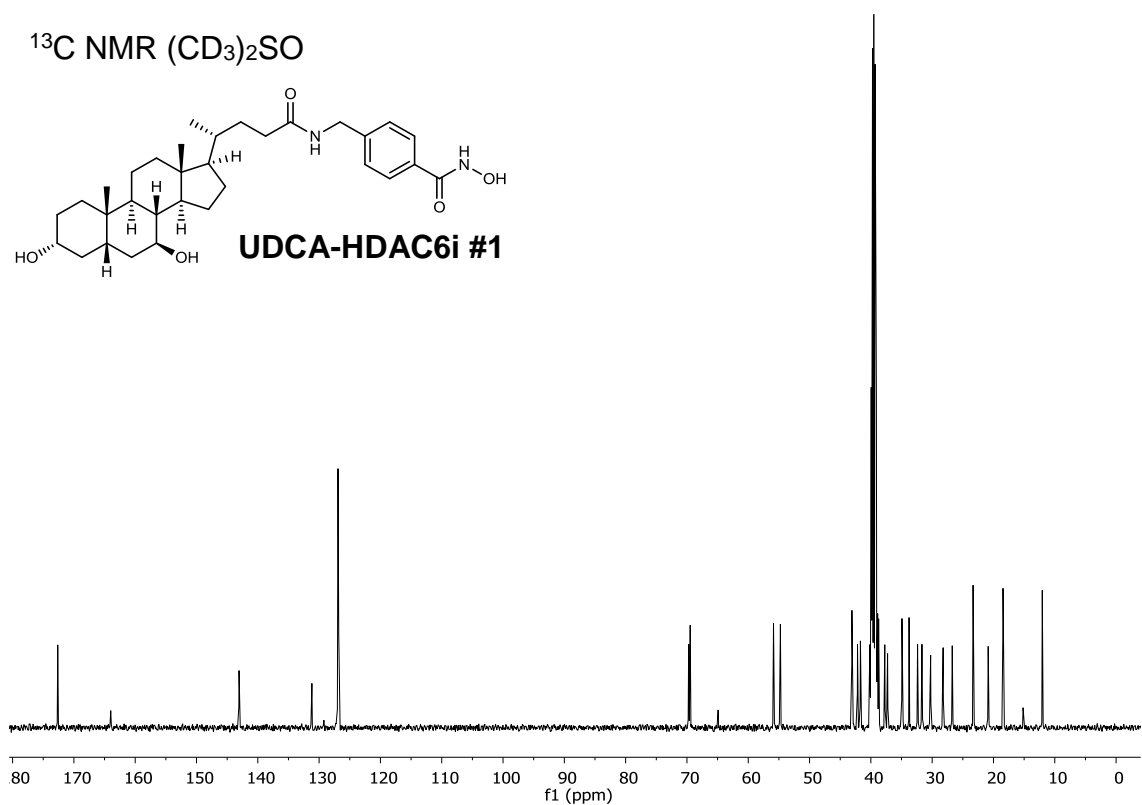
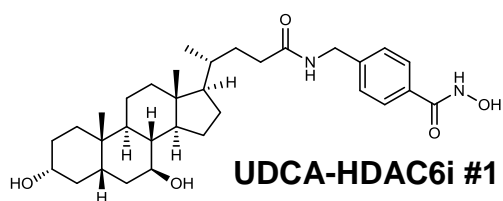
Compound **(3e)**: $^1\text{H NMR}$ (CD_3) $_2\text{SO}$  $^{13}\text{C NMR}$ (CD_3) $_2\text{SO}$ 

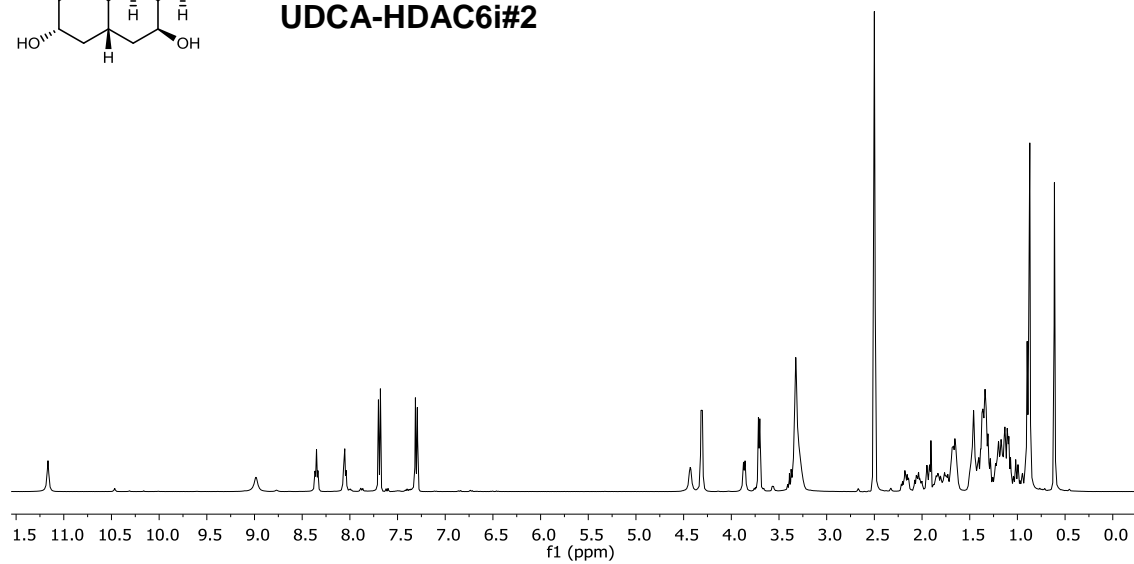
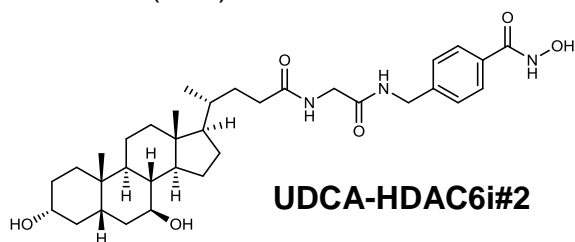
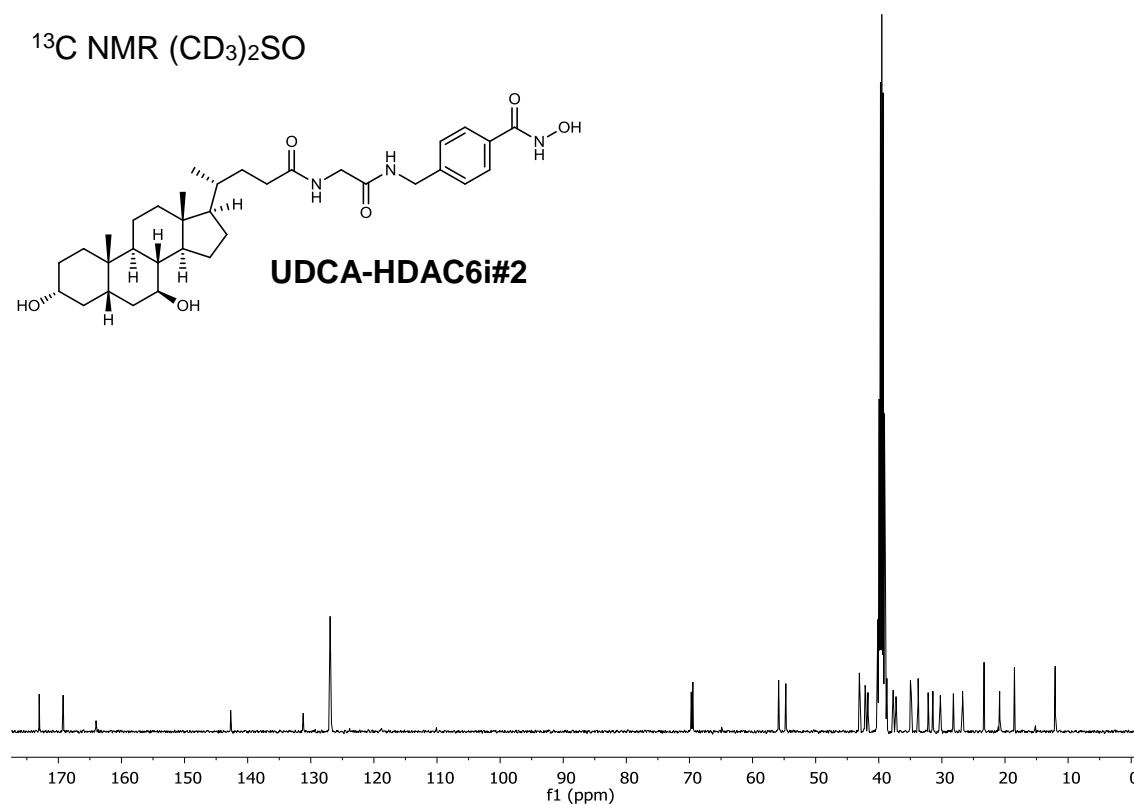
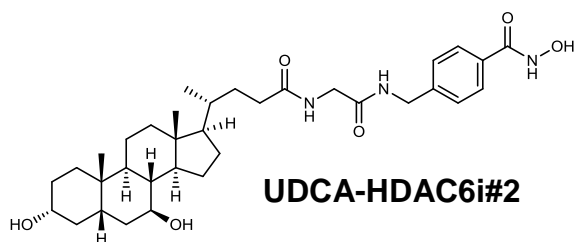
Compound **(3f)**: ^1H NMR ($\text{CD}_3)_2\text{SO}$  ^{13}C NMR ($\text{CD}_3)_2\text{SO}$ 

Compound **(4a)**: ^1H NMR (CD_3) $_2\text{SO}$  ^{13}C NMR (CD_3) $_2\text{SO}$ 

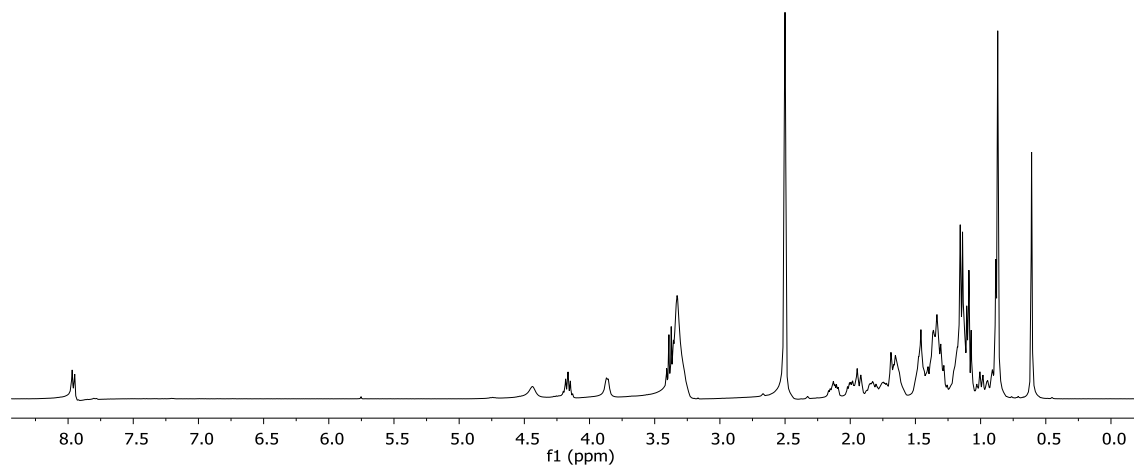
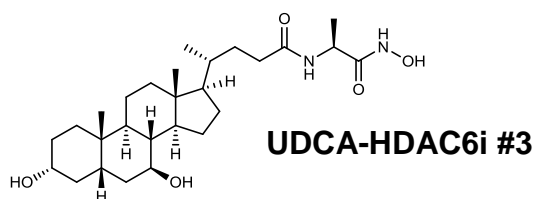
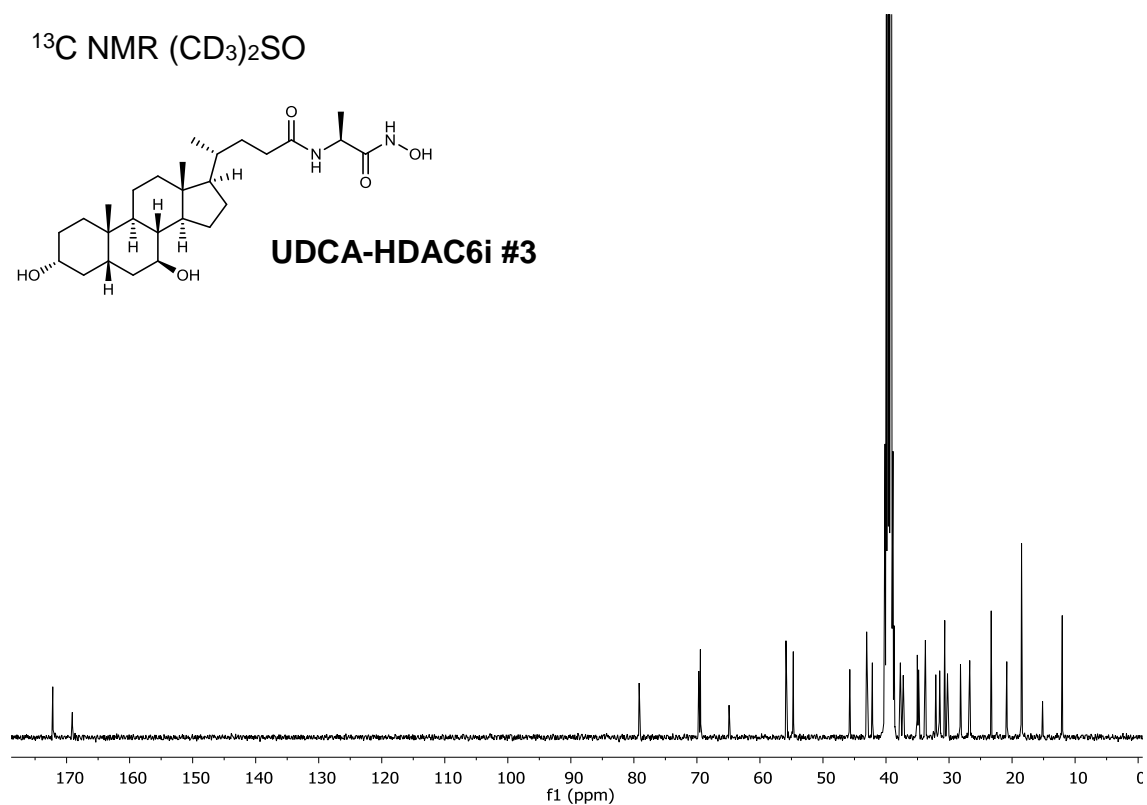
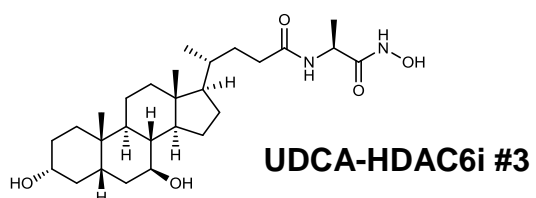
Compound **(6b)**: $^1\text{H NMR}$ (CD_3) $_2\text{SO}$  $^{13}\text{C NMR}$ (CD_3) $_2\text{SO}$ 

UDCA-HDAC6i #1

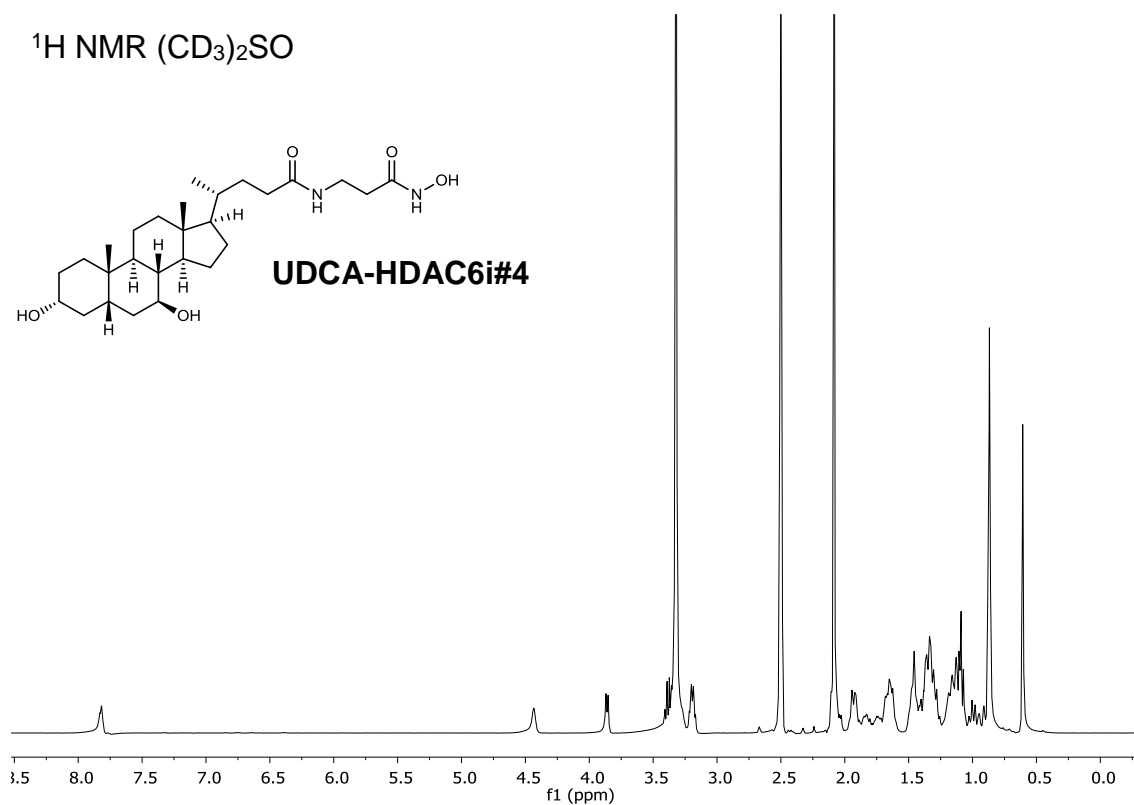
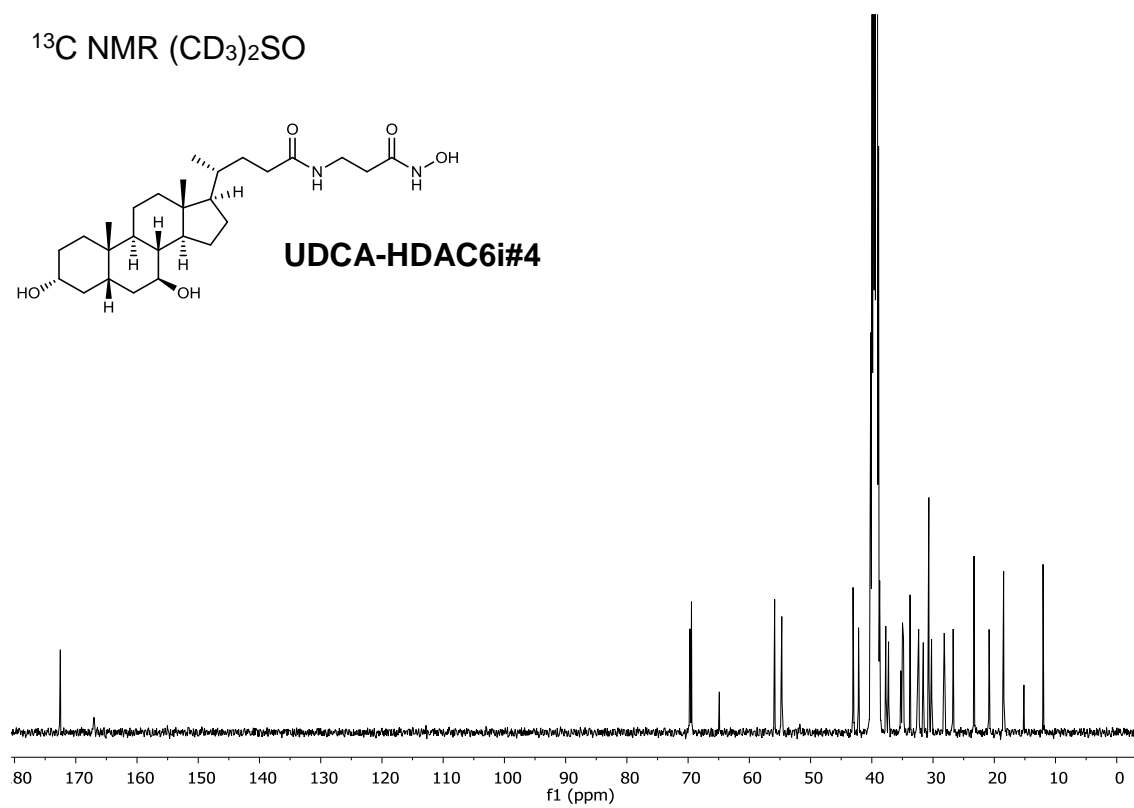
 ^1H NMR (CD_3) $_2\text{SO}$  ^{13}C NMR (CD_3) $_2\text{SO}$ 

UDCA-HDAC6i #2 ^1H NMR (CD_3) $_2\text{SO}$  ^{13}C NMR (CD_3) $_2\text{SO}$ 

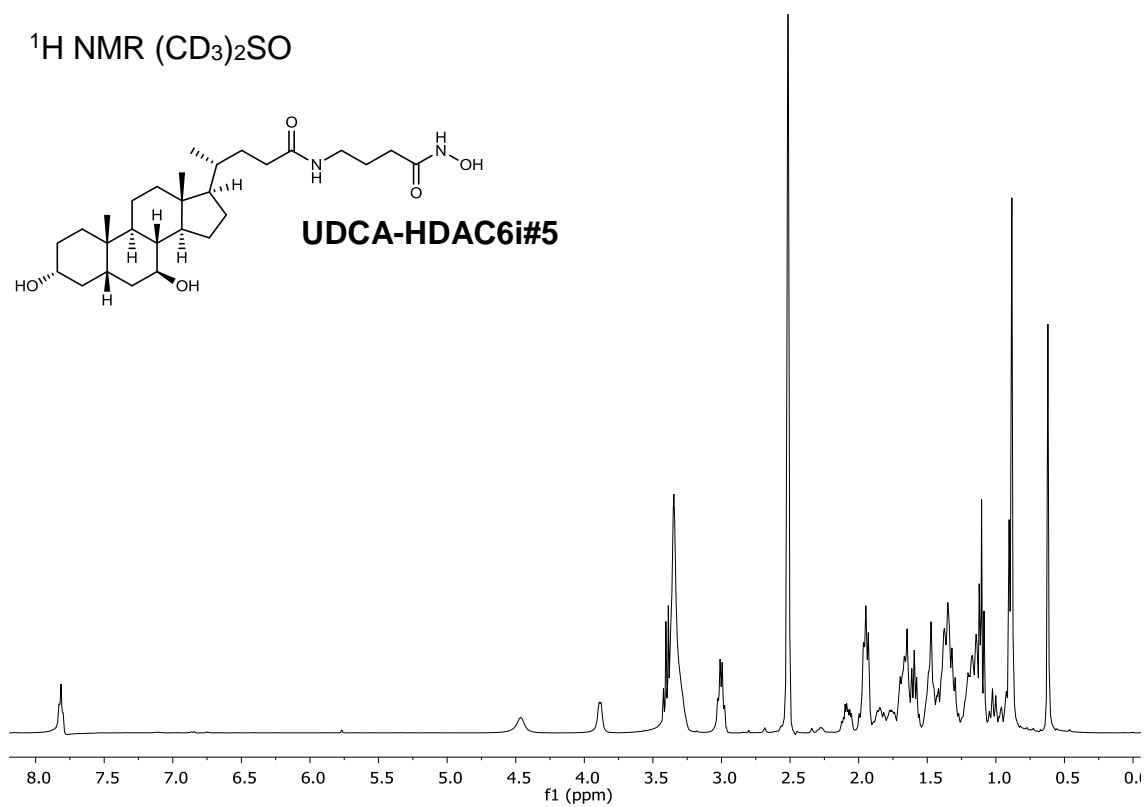
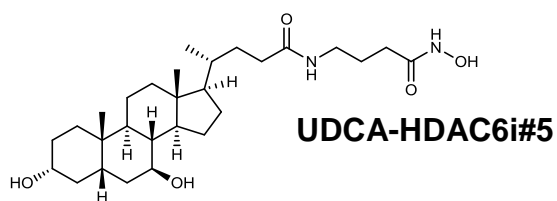
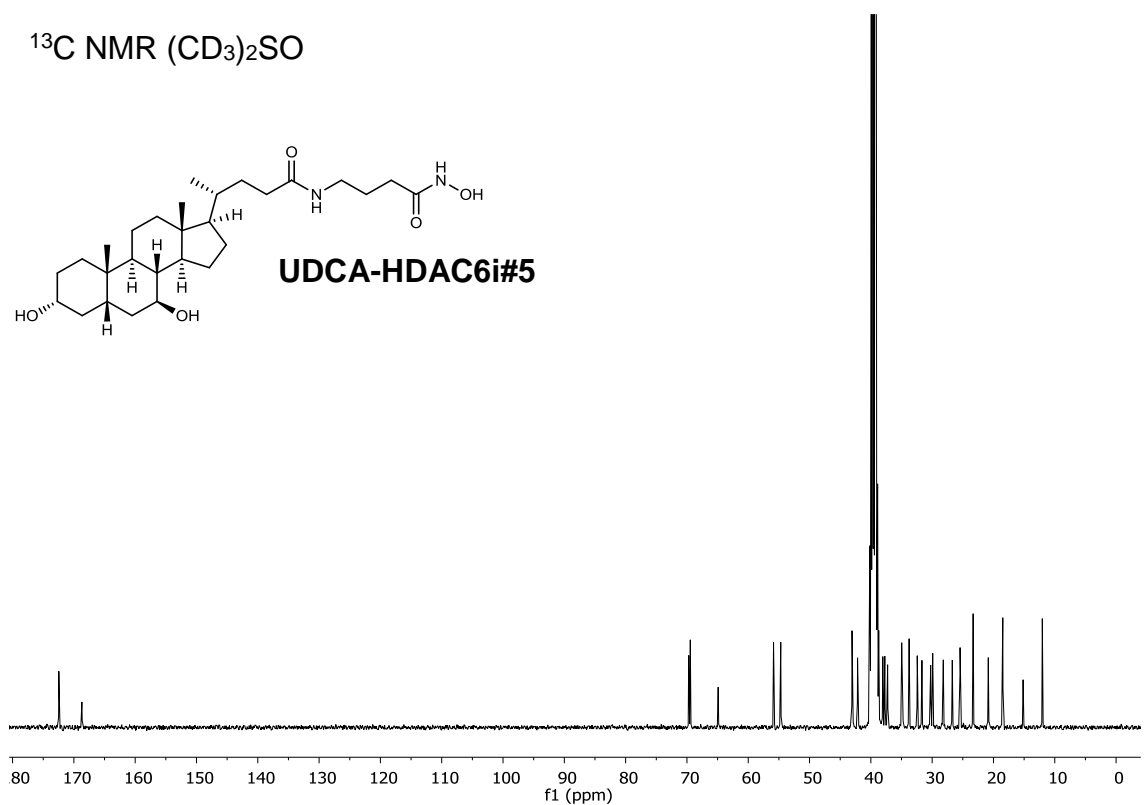
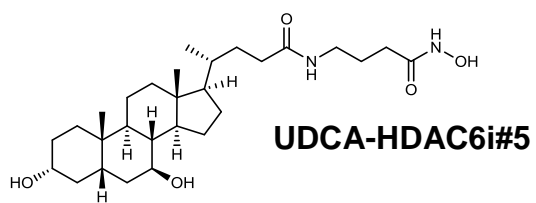
UDCA-HDAC6i #3

 ^1H NMR (CD_3) $_2\text{SO}$  ^{13}C NMR (CD_3) $_2\text{SO}$ 

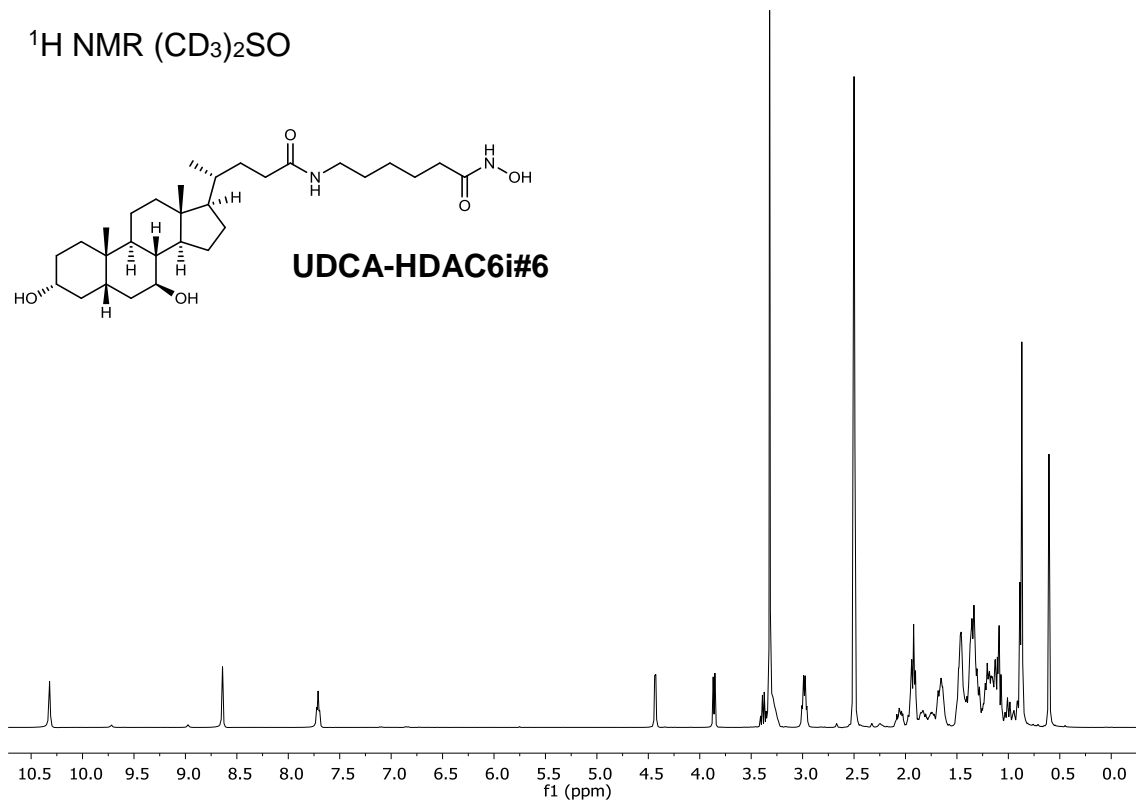
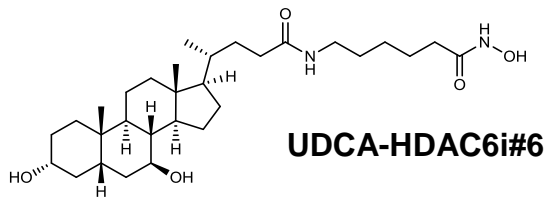
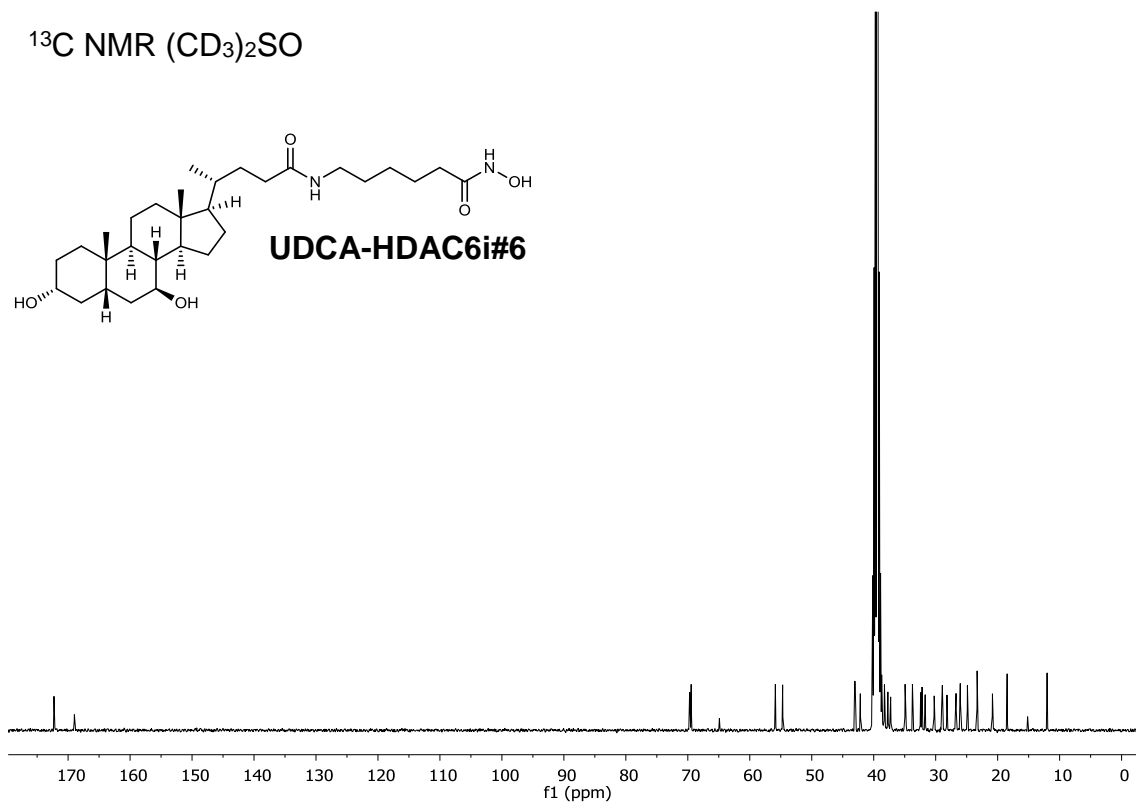
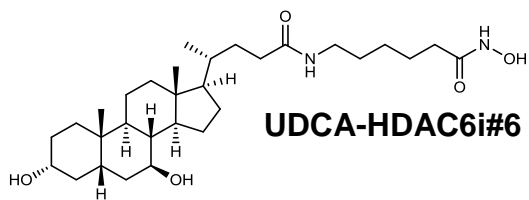
UDCA-HDAC6i #4

 ^1H NMR (CD_3) $_2\text{SO}$  ^{13}C NMR (CD_3) $_2\text{SO}$ 

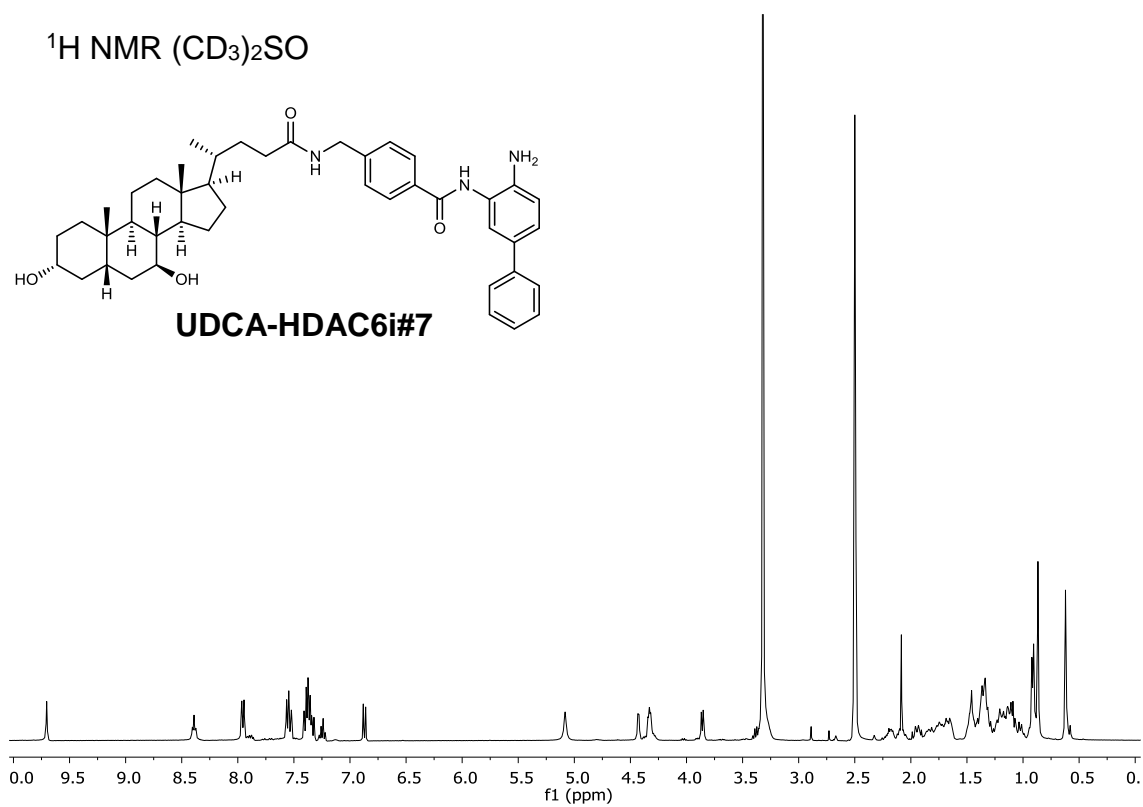
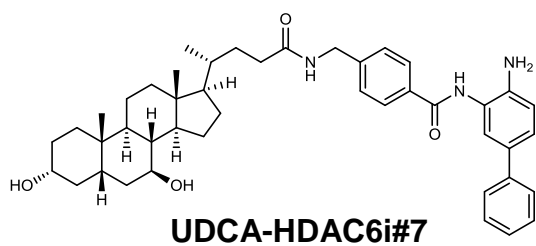
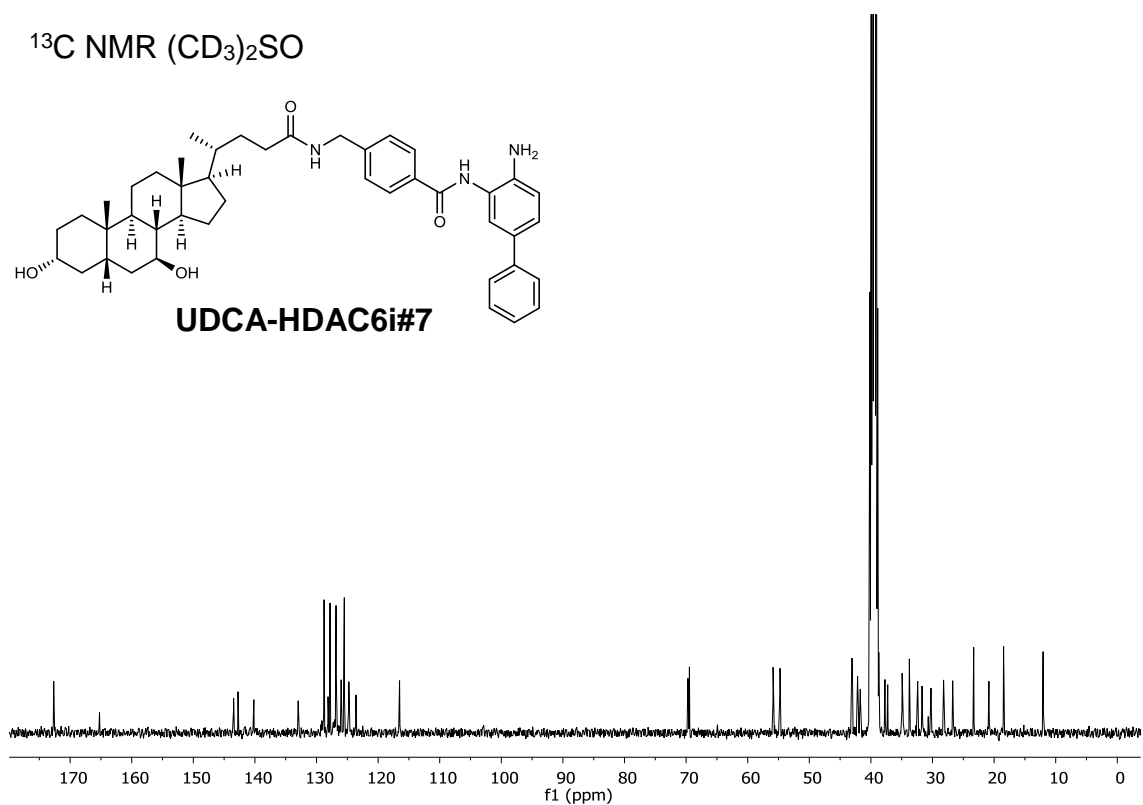
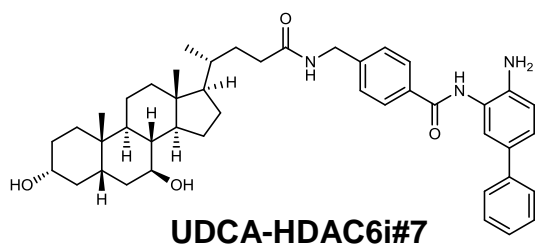
UDCA-HDAC6i #5

 ^1H NMR (CD_3) $_2\text{SO}$  ^{13}C NMR (CD_3) $_2\text{SO}$ 

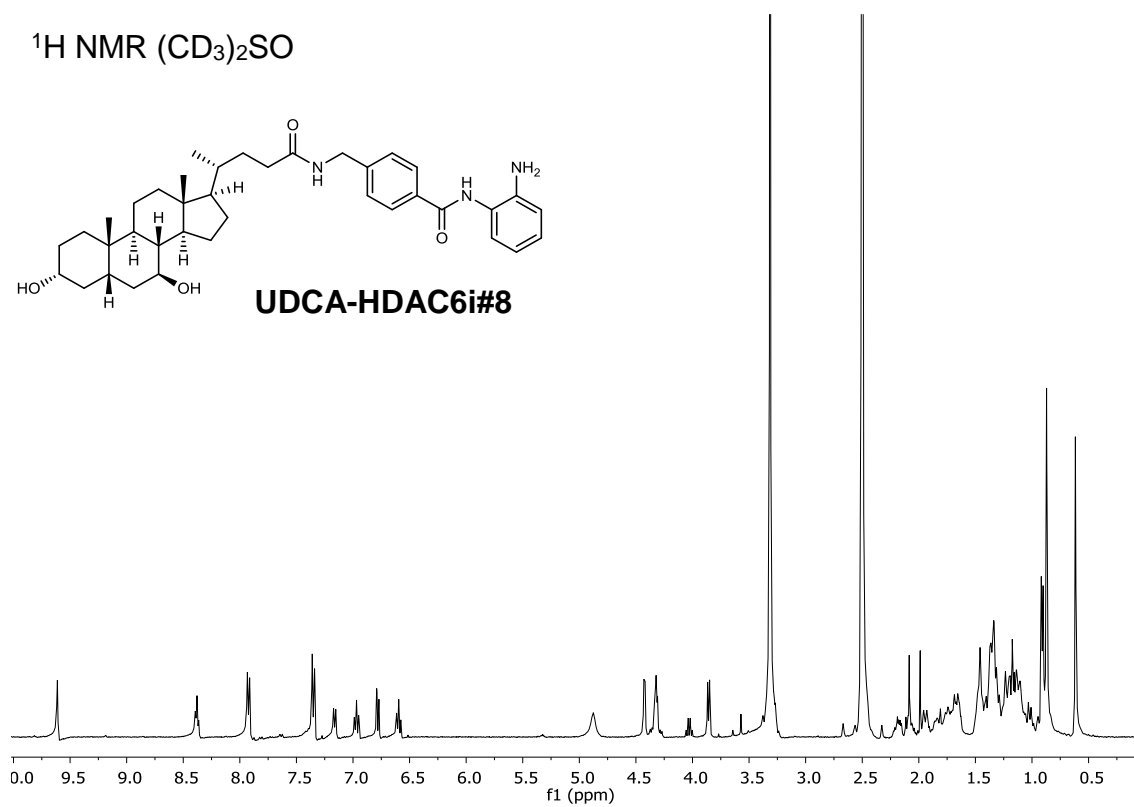
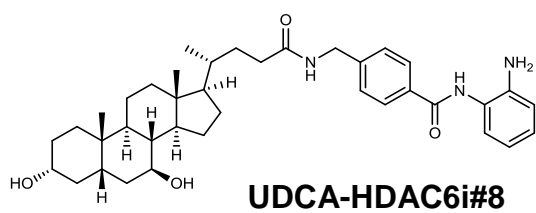
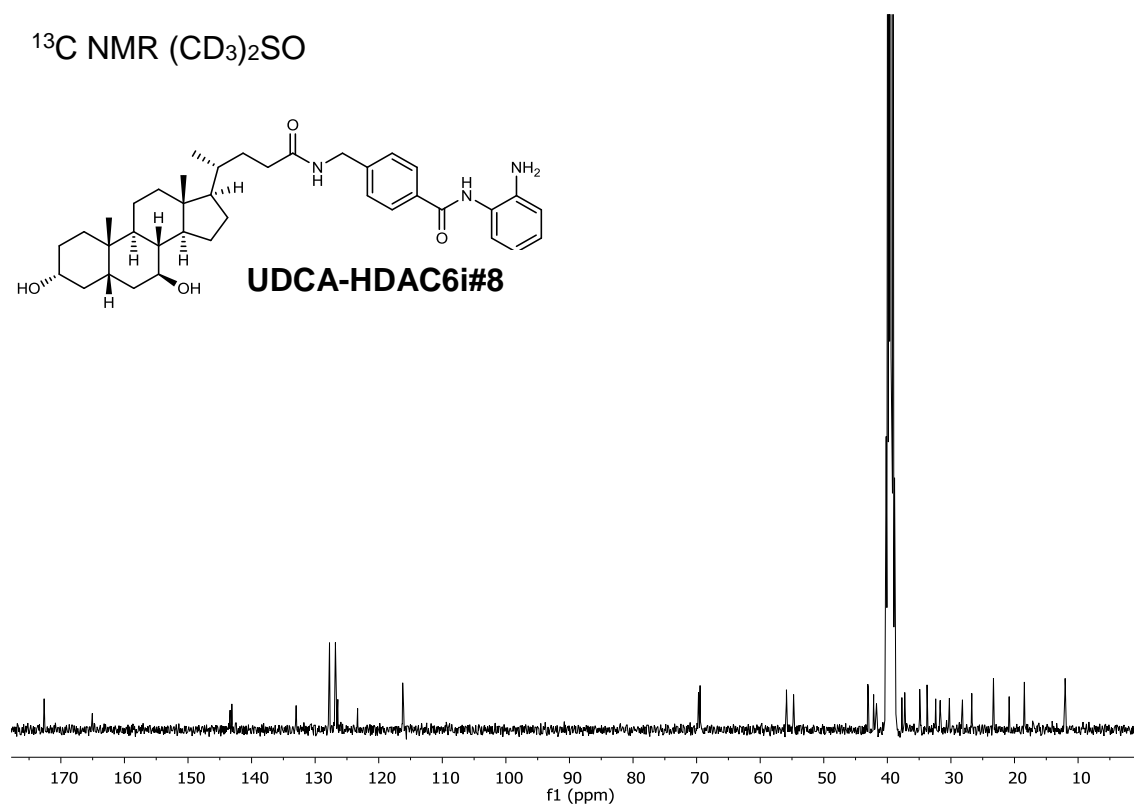
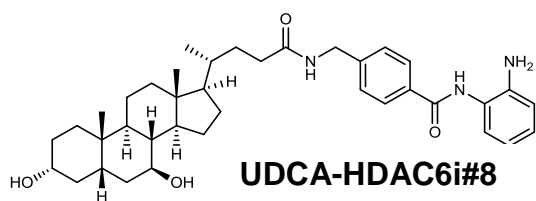
UDCA-HDAC6i #6

 ^1H NMR (CD_3) $_2\text{SO}$  ^{13}C NMR (CD_3) $_2\text{SO}$ 

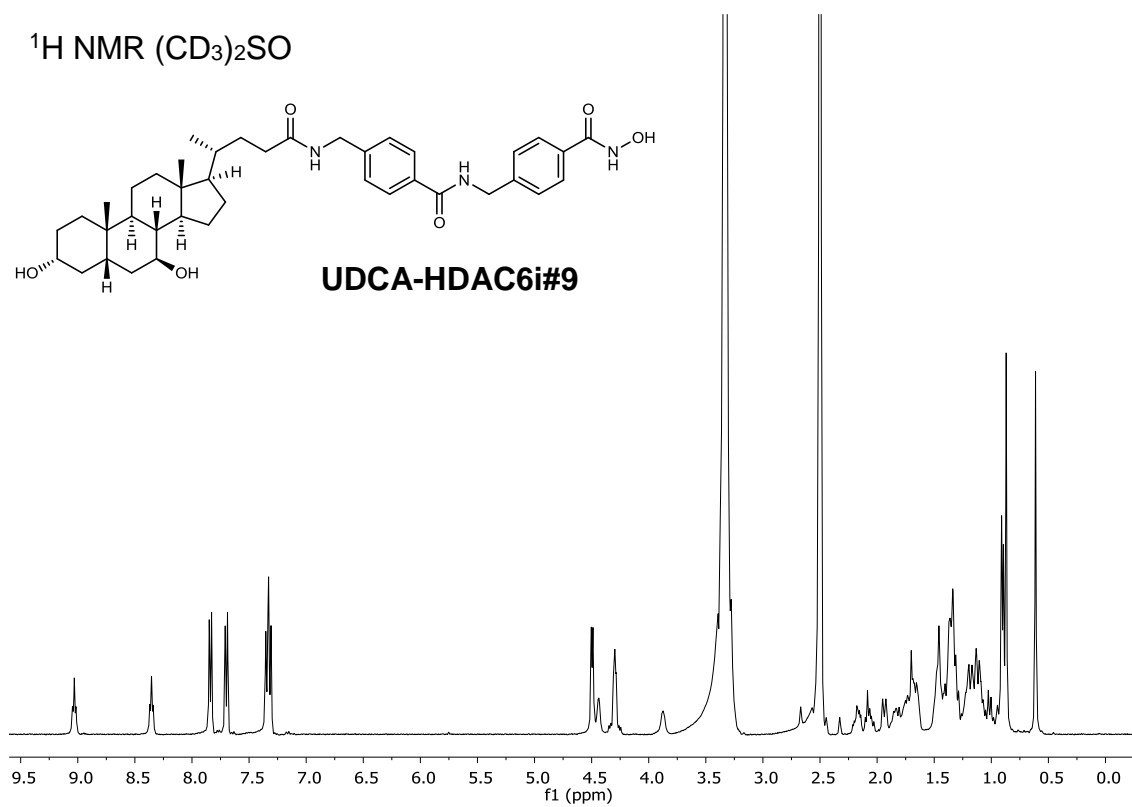
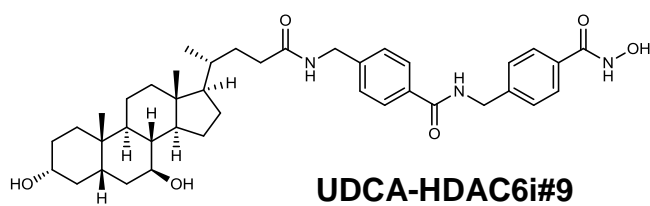
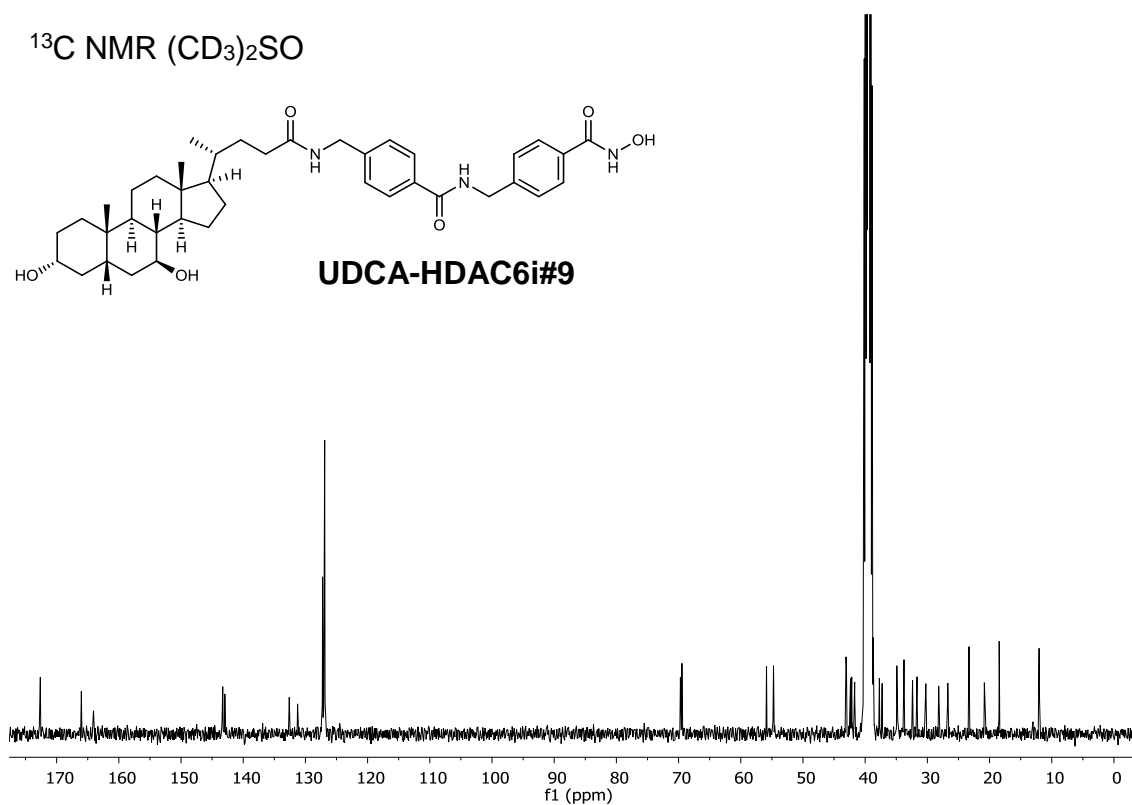
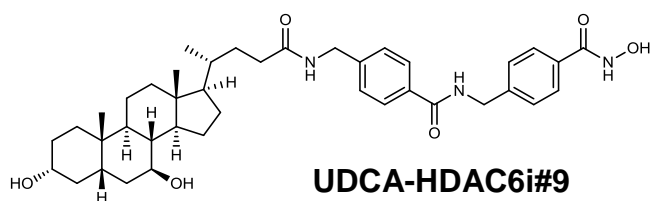
UDCA-HDAC6i #7

 ^1H NMR (CD_3) $_2\text{SO}$  ^{13}C NMR (CD_3) $_2\text{SO}$ 

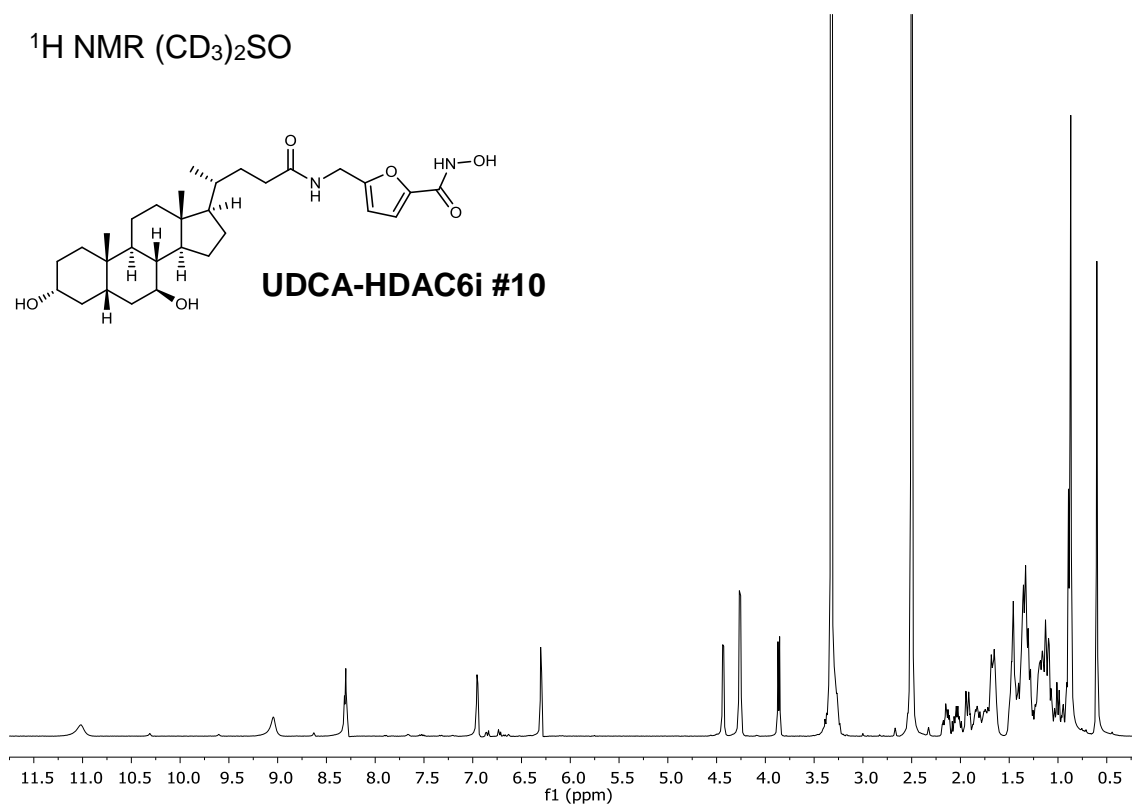
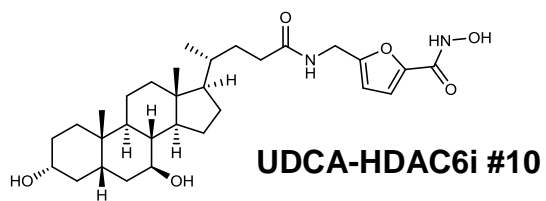
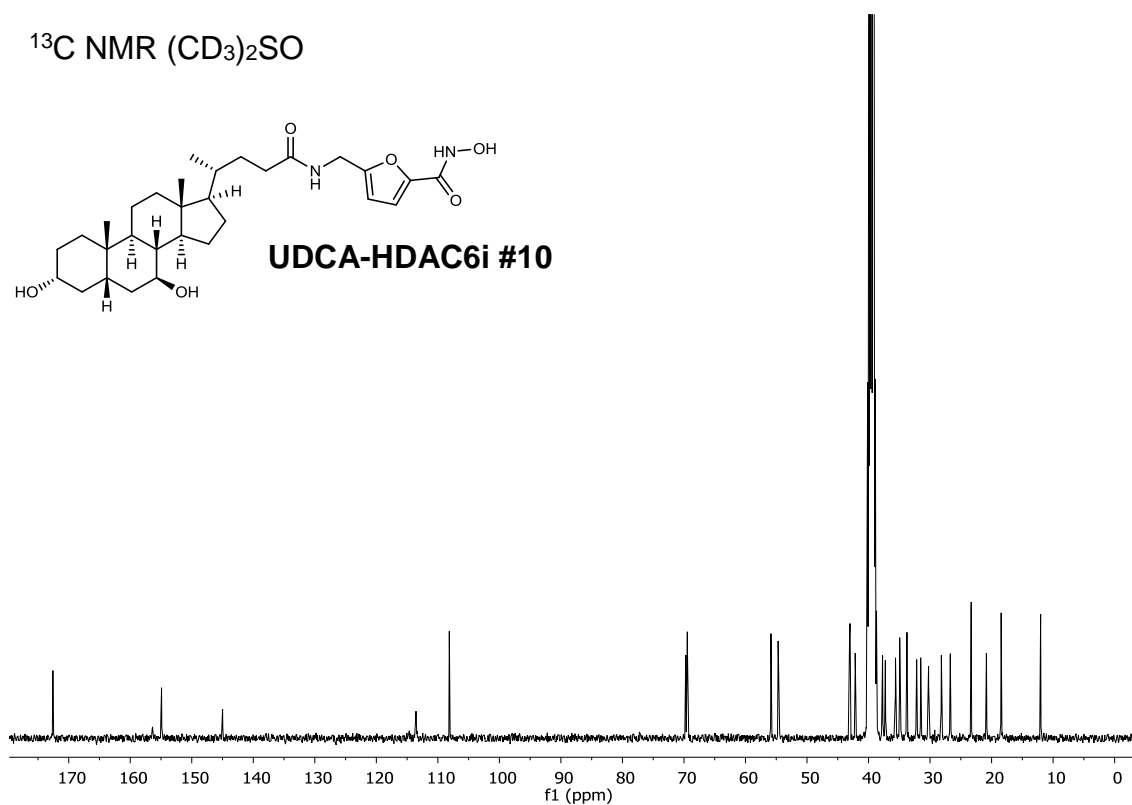
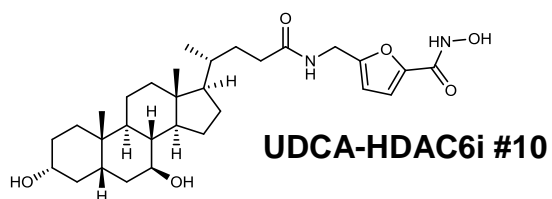
UDCA-HDAC6i #8

 ^1H NMR (CD_3) $_2\text{SO}$  ^{13}C NMR (CD_3) $_2\text{SO}$ 

UDCA-HDAC6i #9

 ^1H NMR (CD_3) $_2\text{SO}$  ^{13}C NMR (CD_3) $_2\text{SO}$ 

UDCA-HDAC6i #10

 ^1H NMR (CD_3) $_2\text{SO}$  ^{13}C NMR (CD_3) $_2\text{SO}$ 

M.4 HDAC activity assays

The HDAC activity assays were performed using acetylated peptide substrates labeled with 7-amino-4-methylcoumarin (AMC) at Reaction Biology Corporation (Pennsylvania, USA). All the enzymes and substrates used in the assays are summarized in Table M1. All assays were performed in a solution buffer (50 mM Tris-HCl, pH 8.0; 137 mM NaCl; 2.7 mM KCl; 1 mM MgCl₂; supplemented with 1 mg/mL of BSA for dilution; BioMol Cat. # KI-143).

Briefly, 50 μ L of peptide substrate and an optimal concentration of the corresponding enzyme (Table M1) were incubated in the assay buffer at a final DMSO concentration of 1% in the presence of increased concentrations of inhibitors at 30°C for 2 hours. The reactions were carried out in 96-well fluorimeter microplates in a final reaction volume of 50 μ L. After the deacetylation reaction, Fluor-de-Lys-Developer (BioMol Cat. # KI-105) was added to each well to digest the deacetylated substrate according to manufacturer instructions, thereby producing the fluorescent signal. The reaction was carried out for 45 min at 30°C with 5% CO₂. Then, the fluorescence signal was measured using an excitation wavelength of 360 nm and an emission wavelength at 460 nm in a fluorimeter (GeminiXS, Molecular Devices, Sunnyvale, CA). All the experiments were performed in triplicate. The IC₅₀ values were calculated by fitting the experimental data with Graphpad Prism 6 software using the equation log(inhibitor) vs. normalized response with variable slope. DMSO was used as a negative control; Trichostatin A (Biomol Cat. # GR-309) was used as a positive control inhibitor.

Enzyme	Accession Number	M _w (kDa)	Expression system	Concentration (nM)	Substrate
HDAC1 Full length with C-terminal GST tag	NM_004964	79.9	Baculovirus in Sf9 cells	75	acetylated fluorogenic peptide from residues of p53, 379-382 (RHKKAc)
HDAC2 Full length with C-terminal His marker	Q92769	60	Baculovirus in Sf9 cells	5	acetylated fluorogenic peptide from residues of p53, 379-382 (RHKKAc)
HDAC3 / NcoR2 Full length with C-terminal His marker (HDAC3) and N-terminal GST label (NcoR2)	NM_003883 (HDAC3) and NM_006312 (NcoR2)	49.7 (HDAC3) and 39 (NcoR2)	Co-expressed in baculovirus	2.3	acetylated fluorogenic peptide from residues of p53, 379-382 (RHKKAc)
HDAC4 Amino acids 627-1085 with N-terminal GST label	NM_006037	75.2	Baculovirus	266	Fluorogenic Boc-L-Lys (s-trifluoroacetyl)-AMC
HDAC5 Full length with N-terminal GST tag	NM_001015053	150	Baculovirus in Sf9 cells	588	Fluorogenic Boc-L-Lys (s-trifluoroacetyl)-AMC
HDAC6 Full length with N-terminal GST tag	BC069243	159	Baculovirus in Sf9 cells	13	acetylated fluorogenic peptide from residues of p53, 379-382 (RHKKAc)
HDAC7 End of 518 amino acids with N-terminal GST label	AY302468	78	Baculovirus	962	Fluorogenic Boc-L-Lys (s-trifluoroacetyl)-AMC
HDAC8 Full length	NM018486	42	E. coli	19	acetylated fluorogenic peptide of p53 residues, 379-382 (RHKKAc)
HDAC9 Amino acids 604-1066 with C-terminal His marker	NM178423	50.7	Baculovirus	986	Fluorogenic Boc-L-Lys (s-trifluoroacetyl)-AMC
HDAC10 Amino acids 1-631 with N-terminal GST tag	NM_032019	96	Baculovirus in Sf9 cells	781	acetylated fluorogenic peptide from residues of p53, 379-382 (RHKKAc)
HDAC11 Full length N-terminal GST tag	NM_BC009676	66	Baculovirus	781	acetylated fluorogenic peptide from residues of p53, 379-382 (RHKKAc)

Table M1. Enzymes and substrates used for HDAC inhibitory activity assays.

M.5 Treatment of PCK rats with HDAC6i-UDCA #1

The PCK rat (Charles River Laboratory, USA) is an animal model of ARPKD, presenting a mutation in the human orthologue *Pkhd1* gene and spontaneously developing both hepatic and renal cystogenesis. All animals used for this experiment were male rats. Both wild-type (WT) (n=12) and PCK rats (n=20) were 8 weeks-old by the beginning of the experiment. PCK rats were randomized into HDAC6i-UDCA #1 treated (n=8; 15 mg/kg/day by oral gavage for 5 months) and non-treated (n=12) groups. Animal randomization of PCK rats into experimental groups was performed based on animal weight as well as different biochemical serum parameters such as transaminase levels (ALT, ALP and AST), urea concentration, total blood protein and albumin concentrations, confirming no significant differences between groups were observed for any of the mentioned parameters at the beginning of the experiment. After 5 months treatment, animals were sacrificed and systemic blood, portal blood and bile were collected to determine BA content and UDCA-HDAC6i #1 concentration. Liver and kidneys were collected, weighted and either fixed in 4% paraformaldehyde (PFA) and embedded in paraffin, or stored at -80°C for further analysis.

M.6 Liver histological analysis

M.6.1 Tissue slides hydration

For histological analysis, 4-5 µm tissue slides were cut from the paraffin-embedded liver tissues using a HM355S microtome (Thermo fisher scientific). Slides were heated for 30 minutes at 60°C and washed in xylene three times to

remove paraffin. Next, slides were immersed for 2 minutes in subsequent solutions of decreasing ethanol concentrations (100%, 96%, 70% and 50%) and washed in phosphate buffered saline (PBS) 1X.

M.6.2 Haematoxylin and eosin (H&E) staining

Tissue slides prepared in the previous step were incubated for 15 minutes at room temperature with Harris Haematoxylin (Merck), washed with distilled water, and placed in a 70% ethanol + 1 % HCl solution for 5 minutes. Next, slides were stained with eosin (Merck) for 5 minutes at room temperature. After washing with distilled water, slides were dehydrated by subsequent immersions of 2 minutes in solutions of increasing ethanol concentrations (50%, 70%, and 100%) and incubated twice in xylene for 5 minutes. Finally stained slides were mounted using Pertex (Sigma Aldrich).

M.6.3 CK19 Immunohistochemistry

Hydrated tissue slides were treated with a solution of 3% hydrogen peroxide in methanol for 15 minutes. Next step consisted in antigen retrieval and subsequent blocking with Avidin/Biotin blocking kit (Vector laboratories). CK19 primary antibody (ARP 03-61029) 1:50 was added and incubated overnight at 4°C. After washing with PBS 1X biotinylated secondary antibody was added and incubated at room temperature. For results development Vectastain ABC Reagent (Vector laboratories) followed by 3,3-diaminobenzidine (DAB) peroxidase substrate Kit (Vector laboratories) were used. Finally, Harris Haematoxylin (Merck) was used for counterstaining and slides were dehydrated and mounted for microscopic analysis

M.7 Bile acid measurement

The concentration of BA species in liver, bile, peripheral and portal blood was measured after methanol precipitation/extraction by HPLC-MS/MS using a modification²⁰⁸ of a previously described method.²⁰⁹ These experiments were performed by the group of Prof. José J. G. Marin at the University of Salamanca.

M.8 Cell lines and culture conditions

Primary cultures of normal and cystic human cholangiocytes, previously isolated and characterized by our group,¹⁷ were seeded at the required cell density for each experimental condition on collagen type I coated plates at 0.05mg/mL (Corning, NY, USA) in complete media, Dulbecco's Modified Eagle Medium/F12 (DMEM/F12 1% (Gibco-Invitrogen), fetal bovine serum (FBS) 5% (Gibco-Invitrogen), MEM-non-essential amino acids 1% (Lonza), Lipid mixture 1% (Sigma-Aldrich), MEM vitamin solution 1% (Gibco-Invitrogen), Penicillin/Streptomycin 1% (Gibco-Invitrogen), Soyben Trypsin Inhibitor 0.05 mg/mL (Gibco-Invitrogen), Insulin Transferrin Selenium 1% (Gibco-Invitrogen), Bovine Pituitary Extract 30 µg/mL (Gibco-Invitrogen), Dexamethasone 393 ng/mL (Sigma-Aldrich), T3 (3, 3' 5-triiodo-L-thyronine) 3.4 µg/mL (Sigma-Aldrich), Epidermal Growth Factor (EGF) 25 ng/mL (Gibco-Invitrogen), Forskolin 4.11 mg/mL (Ascent-Scientific). For transport assays, HepG2 (human hepatoblastoma) and CHO-K1 (Chinese hamster ovary) cells were obtained from the American Type Culture Collection (LGC Standards, Barcelona, Spain). All cell lines were cultured as recommended by the suppliers.

M.9 Experimental overexpression of human transporters in cells

These experiments were performed by the group of Prof. José J. G. Marin at the University of Salamanca. The open reading frame (ORF) of Na⁺-taurocholate cotransporting polypeptide (NTCP, *SLC10A1* gene) and organic cation transporter 3 (OCT3, *SLC22A3*) were amplified from total RNA isolated from human liver by RT followed by high-fidelity PCR using AccuPrime Pfx DNA polymerase (Life Technologies) and specific primers (Table M2). cDNAs were cloned into a pWPI lentiviral vector to obtain transfer vectors encoding both transporters and eGFP as a reporter gene. Using pWPI plasmid, “empty viruses” were generated and used as a negative control. Lentiviral vectors were produced in HEK293T cells and used to transduce target CHO cells as described.²¹⁰ Monoclonal cells stably expressing each transporter were selected by double subcloning using the limiting dilution method. HepG2 cells overexpressing the organic cation transporter 1 (OCT1, *SLC22A1*) were obtained in the same manner.²¹¹

Gene	Protein	Forward (5'-3')	Reverse (5'-3')	Amplicon size (bp)	Accession Number
<i>SLC10A1</i>	NTCP	ATGGAGGCCAC AACGC	GGCTGTGCAAGGG GAGC	1047	NM_003049
<i>SLC22A1</i>	OCT1	ATGCCACCGTG GAT	GGTGCCCGAGGGT TCTGA	1661	NM_003057
<i>SLC22A3</i>	OCT3	ATGCCCTCCTTCG ACG	AAGGTGAGAGCGG GAACTGG	1668	NM_021977

Table M2. Oligonucleotide sequence of primers used to clone the ORF of human transporters . At the 5'-end of the primers an adapter was added containing the sequence of a restriction site for the enzymes MluI (Forward) and SpeI (Reverse).

M.10 Transport assays

These experiments were performed by the group of Prof. José J. G. Marin at the University of Salamanca. Cells were seeded onto 24-well plates at subconfluence. After 24 hours, cells were incubated with “uptake” medium (96 mM NaCl, 5.3 mM KCl, 1.1 mM KH₂PO₄, 0.8 mM MgSO₄, 1.8 mM CaCl₂, 11 mM glucose, and 50 mM HEPES/Tris, pH 7.40) containing 100 μM UDCA-HDAC6i #1 for 1 hour at 37°C. Quinine (OCT1 and OCT3), and taurocholic acid (NTCP) were used as inhibitors or competitors. Transport fluxes were stopped by rinsing the cultures 4 times with 1 mL of ice-cold medium, and then, cells were lysed using pure water. UDCA-HDAC6i #1 concentration was determined by high performance liquid chromatography-tandem mass spectrometry (HPLC-MS/MS) (6410 Triple Quad LC/MS, Agilent Technologies, Santa Clara, CA). Chromatographic separation was carried out in isocratic mode in a Zorbax Eclipse XDB-C18 column (30 mm x 2.1 mm, 3.5 μm) and kept at 35°C. Flow rate was 300 μL/min and mobile phase was 64:36 methanol/water, both containing 5 mM ammonium acetate and 0.1% formic acid. Electrospray ionization (ESI) in negative mode was used, with the following conditions: gas temperature 350°C, gas flow 8 L/min, nebulizer 30 psi, capillary voltage 2500 V. MS/MS acquisition was performed in multiple reaction monitoring (MRM) mode using the specific *m/z* transitions 539.4-539.4 *m/z* for UDCA-HDAC6i #1, and 498.4-80.2 *m/z* for TUDCA. The results were corrected by protein content.²¹²

M.11 Reverse transcription quantitative polymerase chain reaction (RT-qPCR)

M.11.1 RNA extraction

For RNA extraction, 1 mL TriReagent (Sigma, Misuri, USA) was added to each cell culture of human cholangiocytes placed in a 6 well plate. Lysates were collected and placed into 1.5 mL Eppendorf tubes. Next, 200 μ L of chloroform were added to each tube and after 20 seconds vortexing, samples were left for 10 minutes at room temperature. Following this, samples were centrifuged for 15 minutes at 14,500 rpm and 4°C and the aqueous phases (upper part) were transferred to clean 1,5 mL tubes. Next, 0.5 mL isopropanol were added to each tube and after mixing samples were left for 10 minutes at room temperature and further centrifuged at previously mentioned conditions. Liquid phase was discarded and 1 mL of a 75% solution of ethanol was added. Samples were vortexed and centrifuged at 14,500 rpm and 4°C for 5 minutes. Finally, after discarding the supernatant pellets were left to dry and resuspended in 20 μ L Ultrapure™ DNase/RNase-free distilled water (Invitrogen). RNA concentration and purity were measured in a NanoDrop® ND-1000 equipment (Thermo Scientific).

M.11.2 Reverse transcription

Volume of the samples prepared in the previous step containing 1 μ g of RNA was diluted to with Ultrapure™ of DNase/RNase-free distilled water to a final volume of 15 μ L. Subsequently 5 μ L of a mixture containing 4 μ L of iScript mix and 1 μ L of iScript RT (iScript™ cDNA Synthesis Kit (Bio-Rad)) was added to each

sample and reaction was carried out at 25°C for 5 minutes, 42°C for 30 minutes, 85°C for 5 minutes in a Veriti™ Thermal Cycler (Applied Biosystems).

M.11.3 Quantitative real time polymerase chain reaction (qPCR)

The expression levels of particular genes were measured by qPCR using iQ™ SYBR® Green Supermix (Bio-Rad) in a CFX96 Touch apparatus (BioRad). *RPL22* gene was used as a normalizing control. All the primer sequences are summarized in Table M3.

Gene	Protein	Forward (5'-3')	Reverse (5'-3')	Amplicon size (bp)	Accession Number
<i>SLC22A1</i>	OCT1	GTCGCTTTGCCAG AGACCAT	CTTCATCCCTCCA ACACGACA	151	NM_003057
<i>SLC22A3</i>	OCT3	ATCGTCAGCGAGT TTGACCTT	ACCTGTCTGCTGC ATAGCCTA	118	NM_021977
<i>SLC10A1</i>	NTCP	AAGGACAAGGTG CCCTATAAAGG	TTGAGGACGATCC CTATGGTG	80	NM_003049
<i>RPL22</i>	60S ribosomal protein L22	AAAGTGAACGGAA AAGCTGGG	TCACGGTGATCTT GCTCTTGC	76	NM_000983

Table M3. Oligonucleotide sequence of primers used for qPCR.

M.12 Immunoblotting

M.12.1 Protein extraction

Protein extracts were obtained from cell lysates or frozen tissue homogenized with RIPA buffer containing 150 mM NaCl, 50 mM Tris pH 7.5, 0.1% sodium dodecyl sulfate (SDS), 1% triton X100, 0.5% sodium deoxycholate, protease inhibitors (Complete; Roche) and phosphatase inhibitors (1 mM ortovanadate, 10 mM NaF, 100 mM β-glycerophosphate).

M.12.2 Protein quantification

Sample protein concentration was determined by spectrophotometry using Pierce Bicinchoninic kit (Thermo fisher Scientific). Appropriate sample dilutions as well as BSA standards were prepared in distilled water and 25 μ L of each was loaded into a 96 well transparent plate. Parallel, a mixture 1:50 of A and B reagents was prepared, and 200 μ L of this was added to each well. Finally, plate was incubated at 37°C for 30 minutes and measured at a wavelength of 570 nm in a Multiskan Ascent® spectrophotometer (Thermo fisher Scientific).

M.12.3 Protein expression or post-translational modification analysis

Protein expression, acetylation and phosphorylation levels were measured by immunoblotting using either 30 μ g of cell culture protein extract or 40 μ g of PCK rat liver or kidney tissue. Samples were separated by electrophoresis in 10% SDS-PAGE acrylamide gels and electro-transferred onto nitrocellulose membranes (BioRad, Hercules, CA). After blocking with either 2.5% BSA or 2.5% skimmed milk powder, membranes were incubated overnight with primary antibodies (Table M4). Membranes were then washed with TBS (1% Tween 20) and incubated for 1 hour at room temperature with Horseradish peroxidase-conjugated secondary antibodies (Cell Signaling, 1:5,000). Afterwards, membranes were washed with TBS to remove unbound secondary antibody, incubated with Novex® ECL HRP Chemiluminescent Substrate Reagent Kit (Invitrogen) and visualized in an iBright Imaging System (Thermo Fisher Scientific). To determine relative expression or post-translational modification

levels, obtained images were analyzed with ImageJ software (NIH, Bethesda, MD, <https://imagej.nih.gov/ij/>).²¹³

Antigen	Source	Dilution	Reference	Provider
Ac-α-tubulin	Mouse	1:1000	T6793	Sigma
α-tubulin	Rabbit	1:2000	ab52866	Abcam
Ac-H3K9	Rabbit	1:500	6949S	Cell Signalling
β-actin	Mouse	1:2000	a5319	Sigma
GAPDH	Rabbit	1:1000	ab22555	Abcam
p-ERK1/2	Rabbit	1:1000	4370S	Cell Signalling
ERK1/2	Rabbit	1:1000	4695S	Cell Signalling

Table M4. Antibodies used for immunoblot.

M.13 Ciliary length analysis

These experiments were performed by the group of Dr. Sergio Gradilone at the University of Minnesota (Austin, MN, United States). Cholangiocyte cultures in glass cover slips were washed and fixed with ice cold (-20°C) methanol for 10 minutes. Cells were blocked at room temperature for 1 hour, as previously described,¹⁷² and incubated overnight at 4°C with acetylated α -tubulin antibodies (1:1000; Sigma-Aldrich). Afterwards, cells were incubated for 2 hours at room temperature with Alexa Fluor 488 secondary antibody (Life Technologies, USA). Next, coverslips were mounted on slides using Prolong Gold Antifade with Dapi (Invitrogen; Carlsbad, CA, USA). Images were obtained at 60X with a laser scanning confocal microscopy (NIKON C1si Confocal Spectral Imaging System, NIKON Instruments Co., Melville, NY, USA), and the fields were zoomed 4X.

Scale bars were added with EZ-C1 3.90 Freeviewer. Finally, images were analyzed for individual cilia length using ImageJ software.²¹³

M.14 Cell proliferation

Cystic cholangiocytes in culture were stained with CellTrace™ CFSE Cell Proliferation Kit (Invitrogen) according to manufacturer's protocol and seeded them at a density of 3×10^4 cells/well in complete media under collagen type I coated 12-well plates. After overnight incubation at 37°C and 5% CO₂, cells were incubated with 10 μM or 100 μM UDCA, 2 μM or 10 μM UDCA-HDAC6i #1, 10 μM chelating component, or 10 μM UDCA together with 10 μM chelating component in complete media (0.1% DMSO) and were maintained for 48 hours at appropriate incubation conditions. Finally, cells were trypsinized and fluorescence intensities of individual cells were measured by flow cytometry using a Guava® easyCyte 8HT (Merck Millipore). Cell population was gated by size and complexity using forward and side scattering. Fluorescence threshold was established at the fluorescence value in which 50% of control cells were above the threshold and 50% of control cells were below the threshold. Proliferation rates were calculated by measuring the proportion of cells below the fluorescence threshold for each condition.

M.15 3D culturing

Biliary cysts directly isolated from PCK rats were 3D-cultured within a collagen type I matrix of 1.8 mg/mL derived from rat tail (Corning, NY, USA) and incubated

under appropriate culture conditions, as previously reported.²¹⁴ The cyst growth was monitored in HDAC6i-UDCA #1 treated and control groups for 48 hours by the acquisition of images every 24 hours. Circumferential areas were measured with ImageJ software (NIH, Bethesda, MD).²¹³

M.16 Statistical analysis

GraphPad Prism 6 was applied for statistical analysis (GraphPad Software). Data are expressed as mean \pm standard error of the mean (SEM). Unless otherwise indicated, for comparisons between two groups, parametric *t-Student* test or non-parametric *Mann-Whitney* test were used. Statistically significant data represented as *, **, ***, **** denote a *p* value <0.05, <0.01, < 0.001 and < 0.0001 respectively

SUMMARY IN SPANISH
(RESUMEN EN CASTELLANO)

Introducción

Las enfermedades hepáticas poliquísticas (PLDs) son un grupo heterogéneo de trastornos genéticos hereditarios caracterizados por la dilatación de los conductos biliares y/o el desarrollo de múltiples (>10) quistes biliares que contienen fluido quístico. Los síntomas más frecuentes relacionados con estas patologías son distensión y dolor abdominal, así como saciedad temprana tras la ingesta alimenticia. Estos síntomas se originan a partir de distintas manifestaciones hepáticas como hepatomegalia, obstrucción biliar y portal, así como ruptura y/o infección de los quistes. La enfermedad hepática poliquística autosómica dominante (ADPLD, prevalencia de ~ 1:100.000) se caracteriza por el desarrollo de quistes exclusivamente en el hígado, que son la principal causa de morbilidad, mientras que la enfermedad renal poliquística autosómica dominante (ADPKD, prevalencia de ~ 1:1.000) y la enfermedad renal poliquística autosómica recesiva (ARPKD, prevalencia de ~ 1:20.000) también presentan cystogénesis renal, lo que puede conducir a hipertensión y, en última instancia, a enfermedad renal terminal.

Actualmente se cree que los quistes hepáticos se originan a partir de defectos embriológicos durante la formación de la placa ductal y/o como resultado de mutaciones somáticas en la etapa adulta del individuo. En ese sentido, hasta la fecha, se han descrito mutaciones en nueve genes distintos, las cuales se encuentran relacionadas con el desarrollo y la progresión de las PLDs (ver Tabla I1). Dichas mutaciones dan lugar a distintas alteraciones funcionales en los colangiocitos directamente asociadas al aumento de los niveles de monofosfato cíclico de adenosina (AMPC) y disminución de la concentración de calcio intracelular (iCa^{2+}). Entre dichas alteraciones se pueden encontrar

fenómenos como hiperproliferación, hipersecreción, aumento de la actividad metaloproteolítica de la matriz extracelular, cambios en la expresión de microARNs y alteraciones morfológicas y funcionales del cilio primario, siendo estas las principales responsables de la fisiopatología de las PLDs.

Las terapias actuales frente a las PLDs incluyen una serie de procedimientos quirúrgicos, así como estrategias farmacológicas basadas en el uso de análogos de somatostatina. Todos estos tratamientos van dirigidos a paliar la sintomatología mediante una reducción parcial de las manifestaciones hepáticas de la enfermedad. Sin embargo, estas terapias muestran beneficios modestos y de escasa duración, así como algunos efectos secundarios, por lo que su aplicación se reduce a casos particulares en los cuales la sintomatología compromete de manera significativa la calidad de vida del paciente. En ese sentido, actualmente el trasplante hepático continúa siendo la única opción curativa. Sin embargo, además de que su aplicación conlleva los problemas comúnmente asociados al trasplante de órganos, su disponibilidad se ve altamente limitada por la naturaleza no letal de las PLDs. Todo ello pone de manifiesto la urgente necesidad de desarrollar nuevas terapias que resulten más efectivas y accesibles para el tratamiento de las PLDs. En ese sentido, *Bañales JM* y *colaboradores* propusieron evaluar el potencial terapéutico del ácido ursodeoxicólico (UDCA) para el tratamiento de las PLDs.

El UDCA es un ácido biliar (bile acid, BA) endógeno ampliamente aplicado en clínica para el tratamiento de los trastornos colestáticos hepatobiliares. Este BA colerético y hepatoprotector posee importantes propiedades antioxidantes, antiinflamatorias, citoprotectoras y calcio-moduladoras. Dada su particular naturaleza bioquímica, una gran parte del UDCA administrado por vía oral se ve

confinado a la circulación entero-hepática, garantizando de esta manera elevados niveles de biodisponibilidad hepatobiliar. Este hecho unido a la elevada capacidad de señalización tanto del UDCA como de sus derivados conjugados para estimular los niveles de iCa^{2+} , hacen de este BA un potencial candidato para su aplicación en el tratamiento de las PLDs. En ese sentido, se ha observado que el UDCA es capaz de reducir la cistogénesis hepática y mejorar la sintomatología tanto en modelos experimentales (*in vitro* e *in vivo* en ratas PCK) como en pacientes con ADPKD avanzada, induciendo la normalización de los niveles de calcio intracelular en los colangiocitos poliquísticos, así como el descenso en la acumulación intrahepática de ácidos biliares citotóxicos y promitóticos.

Por otra parte, la deacetilasa de histonas 6 (HDAC6) se encuentra sobreexpresada en colangiocitos poliquísticos. Este enzima se encarga de catalizar, entre otras, las reacciones de desacetilación de tubulina- α acetilada, por lo que desempeña un papel fundamental en la regulación celular de la homeostasis de los cilios primarios. Por tanto, y dada la importancia del cilio primario de los colangiocitos en la fisiopatología de las PLDs, *Gradilone et al.* decidieron evaluar el uso de inhibidores selectivos de HDAC6 para el tratamiento de las PLDs. En dos trabajos independientes, los autores demostraron que el uso de distintos inhibidores selectivos de HDAC6 administrados independientemente, o en combinación con la administración de análogos de somatostatina es capaz de inhibir significativamente la cistogénesis hepatorenal en modelos experimentales.

Hipótesis

Los enfoques farmacológicos basados en la administración de UDCA o HDAC6is han proporcionado resultados muy prometedores, pero aún parciales, para el tratamiento de las PLDs. Por esta razón, planteamos la hipótesis de que nuevas entidades químicas que combinen las características de UDCA y de los HDAC6is en una misma estructura química podrían proporcionar un valor aditivo y/o sinérgico para el tratamiento de las PLDs. A ese respecto, se sabe que los sistemas macrocíclicos pre-organizados pueden exhibir elevadas constantes de unión no covalente con las cavidades externas cercanas al canal que conecta los sitios activos de HDAC con la superficie de estas enzimas. Por esta razón, y teniendo en cuenta la naturaleza policíclica del esqueleto del UDCA, racionalizamos que este BA endógeno podría ser un análogo conformacionalmente restringido adecuado para estos sistemas macrocíclicos y, por lo tanto, un excelente elemento estructural para el desarrollo de nuevos HDACis. Además, razonamos que algunas de las propiedades hepatotrópicas inherentes al UDCA podrían transferirse a estos nuevos HDACis, dotándolos propiedades hepatotrópicas, así como como de la capacidad de ser transportados activamente al interior de los colangiocitos poliquísticos. Es importante destacar que en estos nuevos compuestos no se esperaría que la escisión metabólica del enlace amida por la microbiota intestinal generase metabolitos potencialmente tóxicos, sino que diese como resultado la liberación de concentraciones terapéuticas de UDCA libre aumentando de esta manera la efectividad del tratamiento.

Objetivos

Con el fin de evaluar la hipótesis descrita, se propusieron los siguientes objetivos.

1. Diseño, síntesis química y caracterización de los nuevos conjugados sintéticos de UDCA.
2. Predicción computacional de las afinidades de unión de los UDCA-HDAC6is hacia los dominios catalíticos 1 y 2 de HDAC6.
3. Evaluación *in vitro* de la actividad inhibidora y selectividad de los UDCA-HDAC6is en distintas HDAC individuales y colangiocitos poliquísticos.
4. Estudio computacional y experimental de los factores químicos y estructurales que determinan la actividad y selectividad de los UDCA-HDAC6is sobre HDAC6, y análisis de la contribución del UDCA a estos.
5. Selección basada en la evidencia del UDCA-HDAC6i con mayor potencial traslacional para futuros estudios *in vivo* e *in vitro*.
6. Evaluación *in vivo* del potencial terapéutico de los UDCA-HDAC6is para el tratamiento de las PLDs.
7. Caracterización *in vitro* del efecto terapéutico de los UDCA-HDAC6is.

Resultados y discusión

Tomando como referencia la estructura cristalográfica del dominio catalítico 2 (CD2) de la HDAC6 humana (Figura R1), llevamos a cabo el diseño y síntesis química de 10 nuevos derivados sintéticos de UDCA, los cuales contienen grupos espaciadores tanto aromáticos como alifáticos de longitud variable, así como grupos quelantes de Zn (II) de distinta naturaleza química (Figura R2).

La síntesis química de las moléculas UDCA-HDAC6i comenzó con la reacción de acoplamiento de UDCA (**1**) con las aminas **2** para producir distintos ésteres de amida **3**. La hidrólisis de estos últimos intermedios y la reacción *in situ* con hidroxilamina permitieron la obtención y caracterización de los ácidos UDCA-hidroxiámicos UDCA-HDAC6i **#1**, **#3-6** y **#10**, los cuales poseen diferentes longitudes y características estereoelectrónicas dependiendo de la naturaleza de los residuos, tal como se muestra en la Figura R2 (residuos **X**). Estos candidatos incorporan grupos alquilo, fenilo, heteroarilo y quirales en sus respectivos componentes espaciadores. Alternativamente, la hidrólisis de los ésteres **3** permitió la preparación de ácidos carboxílicos **4**, cuyo acoplamiento posterior con ortofenilendiaminas **7** produjo las amidas UDCA-HDAC6i **#7**, **#8**. En otros ejemplos, el espaciador entre el grupo quelante y el UDCA se alargó mediante una secuencia adicional de acoplamiento e hidrólisis, produciendo así los ésteres **6**. La desprotección de estos ésteres metílicos y la reacción con hidroxilamina permitieron el aislamiento y la caracterización de los candidatos UDCA-HDAC6i **#2**, **#9**. En resumen, el esquema sintético que se muestra en la Figura R2 dio lugar a un conjunto de posibles HDACis con diferentes espaciadores y grupos quelantes, conteniendo todos ellos una molécula de UDCA a modo de cierre terminal hidrofóbico común.

Seguidamente se realizó una estimación *in silico* mediante un modelo de docking de la energía de unión de estos compuestos por el dominio (CD2) de la HDAC6 humana (Figuras R3 y R4). Los resultados mostraron que 8 de los 10 compuestos sintetizados mostraban cierta afinidad de unión por el sitio activo del enzima, siendo UDCA-HDAC6i #1, #2 y #9 los compuestos que mejores energías de unión mostraron (Figuras R3 y R4). Es interesante resaltar que, en los tres compuestos en los se obtuvieron mejores energías de unión, el esqueleto esteroideo del UDCA se encontraba orientado hacia la misma región de la superficie proteica, siendo estos tres los únicos casos en los que este se orientaba hacia dicha región (Figuras R3 y R4). Es por ello, que decidimos realizar un análisis más exhaustivo de la contribución de los distintos elementos estructurales a la energía de unión de cada uno de los compuestos (Figura R5). En dicho análisis, observamos que en los tres casos anteriormente mencionados las interacciones ejercidas por el UDCA suponían alrededor de un tercio de la energía total de unión, siendo estas principalmente interacciones de van der Waals y enlaces de hidrogeno (Tabla R1).

A continuación, llevamos a cabo experimentos de docking sobre un modelo de homología generado a partir de la estructura cristalográfica del dominio catalítico 1 (CD1) de HDAC6 de *pez cebra* (Figura R6). En dichos experimentos se pudo observar que mientras que UDCA-HDAC6i #2 y #9 mantenían un alto grado de afinidad por CD1, la afinidad de UDCA-HDAC6i #1 por CD1 era menor que la mostrada por CD2 (Tabla R2).

Una vez confirmada mediante experimentos de inmunoblot la sobreexpresión de HDAC6 en colangiocitos poliquísticos (Figura R7), se propuso estudiar el potencial inhibitorio de los compuestos sintetizados sobre las HDACs.

Para ello, se incubaron cultivos celulares de colangiocitos humanos poliquísticos con los distintos derivados sintéticos de UDCA. A continuación, se analizaron los niveles de acetilación de tubulina- α como medida de la inhibición frente a HDAC6, así como los niveles de acetilación de la lisina 9 de la histona 3 (H3K9) como medida de la inhibición de HDACs nucleares (Figura R8). En estos experimentos se observó que los compuestos UDCA-HDAC6i #1, #2, #6 y #9 inhibieron selectivamente HDAC6, induciendo un aumento substancial en la acetilación de tubulina- α , sin modificar de forma aparente los niveles de acetilación de H3K9 (Figura R8). Paralelamente, se observó que UDCA-HDAC6i #8 aumentó los niveles de acetilación de H3K9, siendo este un potencial inhibidor selectivo de HDACs nucleares (Figura R8). Por último, la comparativa de estos resultados con los resultados previamente obtenidos en los estudios de docking sobre el CD2 de HDAC6 mostró un elevado índice de correlación entre ambos parámetros, confirmando de esta manera la precisión del modelo computacional (Figura R9), cuyas capacidades predictivas pueden ser utilizadas en futuros desarrollos.

Seguidamente, se decidió analizar en enzimas purificadas la capacidad inhibitoria de los 5 compuestos que mejores resultados habían mostrado en cultivos celulares de colangiocitos poliquísticos (Figura R10). En este experimento se confirmaron los elevados índices de actividad y selectividad de UDCA-HDAC6i #1, #2, #6 y #9 sobre HDAC6, siendo especialmente relevantes los resultados obtenidos para UDCA-HDAC6i #1, #2, y #9 (Figura R10). Así pues, estos experimentos revelaron el elevado índice de actividad y selectividad de UDCA-HDAC6i #8 por HDAC1 (Figura R10). Además, a pesar de que el UDCA no mostró por si mismo capacidad inhibitoria sobre ninguna HDAC, se observó

que el valor de IC50 de UDCA-HDAC6i #1 para HDAC6 era un orden de magnitud menor que para el grupo quelante aislado para ese mismo enzima (Figura R10 y Tabla R3). Este resultado es especialmente relevante, ya que la única diferencia estructural entre estos dos compuestos es la presencia de una molécula de UDCA en el primero, lo cual confirma la importancia de la contribución del UDCA al efecto inhibitorio de los UDCA-HDAC6is propuesta a partir de las observaciones realizadas en los experimentos computacionales (Tabla R1).

Análisis exhaustivos de las interacciones individuales más relevantes observadas en los experimentos computacionales sobre el CD2 de la HDAC6 humana, así como comparativas estructurales entre los compuestos ensayados en HDAC purificadas revelaron información importante (Tabla R4 y Figura R11). Por un lado, estos estudios pusieron de manifiesto la importancia del ácido hidroxámico para la actividad inhibitoria de los UDCA-HDAC6is sobre HDAC6. Por otra parte, indicaron el papel fundamental de los espaciadores 1, 4-fenileno en la determinación de la selectividad de estos compuestos mediante la orientación del esqueleto hidrocarbonado del UDCA hacia una región concreta de la superficie enzimática. De acuerdo con esto, el alineamiento mediante métodos computacionales de las estructuras cristalográficas de los dominios catalíticos de las HDAC1, 2, 3, 4, 7, 8 humanas, así como la HDAC10 de pez cebra, con nuestro modelo de docking en HDAC6 CD2, reveló información crucial sobre la importancia de la orientación del UDCA para la selectividad inhibitoria (Figuras R12 y R13). En dicho análisis se observó que la cavidad superficial preferentemente ocupada en HDAC6 por el UDCA presente en los 3 compuestos más selectivos no se encontraba disponible en el resto de isoformas de HDAC,

mientras que las cavidades superficiales ocupadas por el UDCA en el resto de compuestos se encontraban prácticamente intactas en todas las HDACs analizadas (Figuras R12 y R13). Seguidamente seleccionamos UDCA-HDAC6i #1 como el candidato con mayor potencial traslacional basándonos en su potencia y selectividad inhibitorias, así como en sus propiedades farmacocinéticas y su bajo coste sintético (Figuras R2 y R10 y Tabla R5).

Con el objetivo de evaluar el potencial terapéutico de UDCA-HDAC6i #1 para el tratamiento de las PLDs, se llevó a cabo un ensayo *in vivo* de tratamiento crónico en un modelo animal de poliquistosis hepatorenal (ratas PCK). En dicho ensayo se trataron ratas PCK macho de 8 semanas de edad con una dosis oral diaria de 15 mg/kg día durante 5 meses. El tratamiento crónico de estos animales produjo una reducción significativa tanto de la hepatomegalia como de la nefromegalia asociadas al desarrollo de la enfermedad (Figuras R15 y R26). Además, se observó un aumento significativo en los niveles séricos de albúmina, así como un descenso en la concentración de urea en sangre, indicando sendas mejoras de las funciones hepática y renal respectivamente (Figuras R15 y R16). En cuanto a la farmacocinética, se observó una acumulación preferencial del compuesto en bilis en comparación con sangre portal y sistémica, así como tejido hepático (Figura R17). Además, se observó un aumento significativo en los niveles de acetilación de tubulina- α tanto en tejido hepático como renal, confirmando de esta manera un efecto farmacológico directo del compuesto administrado sobre estos tejidos (Figura R18).

En cuanto a la concentración de los distintos BAs, se observaron ciertas diferencias entre los animales tratados y no tratados en los niveles relativos de algunos BAs (Tabla R6). En ese sentido, resultaron particularmente relevantes

los incrementos significativos observados en las concentraciones de UDCA en bilis, hígado, sangre portal y sangre sistémica de los animales tratados, lo cual parecería indicar un aumento importante de la biodisponibilidad del UDCA originado a partir del metabolismo del UDCA-HDAC6i #1 administrado (Figura R20).

Los análisis histológicos revelaron que el tratamiento crónico con UDCA-HDAC6i #1 produjo un descenso significativo de la cistogénesis hepática (Figura R21). Además, a nivel celular el aumento en los niveles de acetilación de tubulina- α se vio traducido en una elongación significativa del cilio primario de los colangiocitos poliquísticos, mientras que no tuvo efecto aparente sobre la longitud del cilio primario de los colangiocitos normales (Figura R22).

La incubación con UDCA-HDAC6i #1 de estructuras quísticas (colangioides) cultivadas en 3D en matrices de colágeno tipo I, reveló un efecto antiproliferativo significativo del compuesto sobre dichas estructuras (Figura R23). A nivel molecular, se observó que la incubación de colangiocitos poliquísticos cultivados en monocapa con UDCA-HDAC6i #1 producía un descenso en los niveles de fosforilación de ERK1/2 (Figura R24). Además, se analizó este efecto antiproliferativo mediante ensayos de citometría de flujo con colangiocitos poliquísticos sometidos a distintos tratamientos. En dichos ensayos, se pudo observar una clara relación de dosis-dependencia en el efecto antiproliferativo de UDCA-HDAC6i #1 (Figura R24). Particularmente interesante resultó el hecho de que la incubación con UDCA-HDAC6i #1 produjo un efecto anti-proliferativo mucho mayor que la incubación combinada con sus dos componentes estructurales farmacológicamente activos (UDCA + grupo quelante) a la misma concentración (Figura R24).

Por último, se estudiaron los posibles mecanismos de transporte celular activo de estos derivados sintéticos de UDCA (Figura R25). En dichos experimentos se observó que UDCA-HDAC6i #1 era activamente transportado tanto por el transportador de ácidos biliares NTCP, como por los transportadores de cationes orgánicos OCT1 y OCT3, encontrándose estos últimos significativamente sobre-expresados en colangiocitos poliquísticos con respecto a colangiocitos normales (Figura R26).

Conclusiones

- I. Cuatro de las entidades moleculares UDCA-HDAC6i sintetizadas poseen una capacidad inhibitoria sobre HDAC6 potente y altamente selectiva, mientras que un quinto compuesto sintetizado exhibe actividad inhibitoria altamente selectiva frente a las HDAC nucleares.
- II. El UDCA contribuye activamente a la actividad inhibitoria sobre HDAC6 de los compuestos UDCA-HDAC6is al establecer interacciones de van der Waals y enlaces de hidrógeno con residuos de las cavidades externas de los dominios catalíticos de dicho enzima. Esta contribución puede representar hasta un tercio de la energía de unión total del compuesto.
- III. La pre-organización y la orientación preferencial del UDCA hacia una región particular de la superficie de HDAC6 CD2 es crítica para la selectividad y la potencia inhibitoria de los compuestos UDCA-HDAC6i.
- IV. UDCA-HDAC6i #1 es el candidato con mayor potencial traslacional debido a su potencia y selectividad inhibitorias sobre HDAC6, así como sus propiedades farmacocinéticas favorables y menor coste sintético.
- V. Tras la administración oral, UDCA-HDAC6i #1, este se acumula preferentemente en bilis, lo que indica una buena capacidad de vectorización hacia el sistema hepatobiliar.
- VI. El tratamiento crónico de ratas PCK con UDCA-HDAC6i #1 redujo su hepato- y nefromegalia, disminuyó su cistogénesis hepática, y mejoró las funciones hepáticas y renales en estos animales. Además, el aumento de los niveles de α -tubulina acetilada en el hígado y los riñones de los animales tratados confirmó un efecto farmacológico directo sobre estos tejidos.

- VII. El tratamiento oral crónico con UDCA-HDAC6i #1 produjo una modificación significativa en la proporción relativa de algunos BAs en ratas PCK, siendo particularmente relevante el aumento en la concentración de UDCA libre observado en el hígado, la bilis y el suero de los animales tratados.
- VIII. Los cilios primarios de los colangiocitos humanos poliquísticos son significativamente más cortos que los de los colangiocitos humanos normales. La incubación de colangiocitos humanos poliquísticos con UDCA-HDAC6i #1 aumentó los niveles de α -tubulina acetilada de una manera dosis-dependiente y produjo una elongación significativa de los cilios primarios de estas células. Por el contrario, estos efectos no se observaron en los colangiocitos humanos normales.
- IX. La incubación de colangiocitos poliquísticos con UDCA-HDAC6i #1 inhibió la hiperproliferación de estas células en cultivos 2D y 3D. Este efecto antiproliferativo fue superior al ejercido por el tratamiento combinado con sus componentes farmacológicamente activos.
- X. La incubación de colangiocitos poliquísticos con UDCA-HDAC6i #1 redujo la fosforilación de ERK1/2, lo que permite profundizar en la naturaleza de los mecanismos moleculares implicados en este efecto antiproliferativo.
- XI. UDCA-HDAC6i# 1 se transporta activamente a través del transportador de ácidos biliares NTCP y de los transportadores de cationes orgánicos OCT1 y OCT3, encontrándose estos últimos sobre-expresados en los colangiocitos poliquísticos.

En conjunto, estos hallazgos abren la posibilidad de una nueva vía terapéutica para el tratamiento de las PLDs y pueden proporcionar datos útiles para futuros desarrollos farmacológicos, ya sea en el campo de la actividad y selectividad de HDAC6 o en el campo del desarrollo de terapias hepáticas dirigidas.

BIBLIOGRAPHY

1. Perugorria, M.J., *et al.* Polycystic liver diseases: advanced insights into the molecular mechanisms. *Nature reviews. Gastroenterology & hepatology* **11**, 750-761 (2014).
2. van Aerts, R.M.M., van de Laarschot, L.F.M., Banales, J.M. & Drenth, J.P.H. Clinical management of polycystic liver disease. *J Hepatol* **68**, 827-837 (2018).
3. D'Agnolo, H.M., *et al.* Center is an important indicator for choice of invasive therapy in polycystic liver disease. *Transpl Int* **30**, 76-82 (2017).
4. van Aerts, R.M.M., *et al.* Severity in polycystic liver disease is associated with aetiology and female gender: Results of the International PLD Registry. *Liver Int* **39**, 575-582 (2019).
5. Hogan, M.C., *et al.* Somatostatin analog therapy for severe polycystic liver disease: results after 2 years. *Nephrol Dial Transplant* **27**, 3532-3539 (2012).
6. Banales, J.M., *et al.* The cAMP effectors Epac and protein kinase a (PKA) are involved in the hepatic cystogenesis of an animal model of autosomal recessive polycystic kidney disease (ARPKD). *Hepatology* **49**, 160-174 (2009).
7. Larusso, N.F., Masyuk, T.V. & Hogan, M.C. Polycystic Liver Disease: The Benefits of Targeting cAMP. *Clin Gastroenterol Hepatol* **14**, 1031-1034 (2016).
8. Gevers, T.J. & Drenth, J.P. Diagnosis and management of polycystic liver disease. *Nature reviews. Gastroenterology & hepatology* **10**, 101-108 (2013).
9. Perugorria, M.J. & Banales, J.M. Genetics: Novel causative genes for polycystic liver disease. *Nature reviews. Gastroenterology & hepatology* **14**, 391-392 (2017).
10. Mamone, G., *et al.* Magnetic resonance imaging of fibropolycystic liver disease: the spectrum of ductal plate malformations. *Abdom Radiol (NY)* **44**, 2156-2171 (2019).
11. Wills, E.S., Roepman, R. & Drenth, J.P. Polycystic liver disease: ductal plate malformation and the primary cilium. *Trends Mol Med* **20**, 261-270 (2014).
12. Fedeles, S.V., *et al.* A genetic interaction network of five genes for human polycystic kidney and liver diseases defines polycystin-1 as the central determinant of cyst formation. *Nat Genet* **43**, 639-647 (2011).
13. Masyuk, T.V., Masyuk, A.I. & LaRusso, N.F. Polycystic liver disease: The interplay of genes causative for hepatic and renal cystogenesis. *Hepatology* **67**, 2462-2464 (2018).
14. Lee-Law, P.Y., van de Laarschot, L.F.M., Banales, J.M. & Drenth, J.P.H. Genetics of polycystic liver diseases. *Curr Opin Gastroenterol* **35**, 65-72 (2019).
15. Munoz-Garrido, P., *et al.* Ursodeoxycholic Acid Inhibits Hepatic Cystogenesis in Experimental Models of Polycystic Liver Disease. *J Hepatol* (2015).
16. Banales, J.M., *et al.* Hepatic cystogenesis is associated with abnormal expression and location of ion transporters and water channels in an animal model of autosomal recessive polycystic kidney disease. *The American journal of pathology* **173**, 1637-1646 (2008).
17. Urribarri, A.D., *et al.* Inhibition of metalloprotease hyperactivity in cystic cholangiocytes halts the development of polycystic liver diseases. *Gut* **63**, 1658-1667 (2014).
18. Lee, S.O., *et al.* MicroRNA15a modulates expression of the cell-cycle regulator Cdc25A and affects hepatic cystogenesis in a rat model of polycystic kidney disease. *The Journal of clinical investigation* **118**, 3714-3724 (2008).
19. Masyuk, T.V., *et al.* Centrosomal abnormalities characterize human and rodent cystic cholangiocytes and are associated with Cdc25A overexpression. *The American journal of pathology* **184**, 110-121 (2014).

20. D'Agnolo HMA, K.W., Takkenberg B, Riaño I, Bujanda L, Neijenhuis MK, Brunenberg EJL, Beuers U, Banales JM, Drenth JPH. Ursodeoxycholic acid in advanced polycystic liver disease: an international multicenter randomized controlled phase 2 trial *Journal of Hepatology* (2016).
21. Gradilone, S.A., *et al.* HDAC6 is overexpressed in cystic cholangiocytes and its inhibition reduces cystogenesis. *The American journal of pathology* **184**, 600-608 (2014).
22. Yu, F., Ran, J. & Zhou, J. Ciliopathies: Does HDAC6 Represent a New Therapeutic Target? *Trends Pharmacol Sci* **37**, 114-119 (2016).
23. Lorenzo Pisarello, M., *et al.* Combination of a Histone Deacetylase 6 Inhibitor and a Somatostatin Receptor Agonist Synergistically Reduces Hepatorenal Cystogenesis in an Animal Model of Polycystic Liver Disease. *The American journal of pathology* **188**, 981-994 (2018).
24. Chiang, J.Y. Bile acids: regulation of synthesis. *J Lipid Res* **50**, 1955-1966 (2009).
25. Li, T. & Chiang, J.Y. Bile acid signaling in metabolic disease and drug therapy. *Pharmacol Rev* **66**, 948-983 (2014).
26. Goossens, J.F. & Bailly, C. Ursodeoxycholic acid and cancer: From chemoprevention to chemotherapy. *Pharmacol Ther*, 107396 (2019).
27. Beuers, U., Trauner, M., Jansen, P. & Poupon, R. New paradigms in the treatment of hepatic cholestasis: from UDCA to FXR, PXR and beyond. *J Hepatol* **62**, S25-37 (2015).
28. Hanafi, N.I., Mohamed, A.S., Sheikh Abdul Kadir, S.H. & Othman, M.H.D. Overview of Bile Acids Signaling and Perspective on the Signal of Ursodeoxycholic Acid, the Most Hydrophilic Bile Acid, in the Heart. *Biomolecules* **8**(2018).
29. Banks, J.L., *et al.* Integrated Modeling Program, Applied Chemical Theory (IMPACT). *J Comput Chem* **26**, 1752-1780 (2005).
30. Igimi, H. & Carey, M.C. pH-Solubility relations of chenodeoxycholic and ursodeoxycholic acids: physical-chemical basis for dissimilar solution and membrane phenomena. *J Lipid Res* **21**, 72-90 (1980).
31. Lazaridis, K.N., Gores, G.J. & Lindor, K.D. Ursodeoxycholic acid 'mechanisms of action and clinical use in hepatobiliary disorders'. *J Hepatol* **35**, 134-146 (2001).
32. Tonin, F. & Arends, I. Latest development in the synthesis of ursodeoxycholic acid (UDCA): a critical review. *Beilstein J Org Chem* **14**, 470-483 (2018).
33. Paumgartner, G. & Beuers, U. Ursodeoxycholic acid in cholestatic liver disease: mechanisms of action and therapeutic use revisited. *Hepatology* **36**, 525-531 (2002).
34. Beuers, U. Drug insight: Mechanisms and sites of action of ursodeoxycholic acid in cholestasis. *Nat Clin Pract Gastroenterol Hepatol* **3**, 318-328 (2006).
35. Halilbasic, E., Claudel, T. & Trauner, M. Bile acid transporters and regulatory nuclear receptors in the liver and beyond. *J Hepatol* **58**, 155-168 (2013).
36. Bouscarel, B., Fromm, H. & Nussbaum, R. Ursodeoxycholate mobilizes intracellular Ca²⁺ and activates phosphorylase a in isolated hepatocytes. *Am J Physiol* **264**, G243-251 (1993).
37. Beuers, U., Nathanson, M.H., Isales, C.M. & Boyer, J.L. Tauroursodeoxycholic acid stimulates hepatocellular exocytosis and mobilizes extracellular Ca⁺⁺ mechanisms defective in cholestasis. *The Journal of clinical investigation* **92**, 2984-2993 (1993).

38. Wang, X.X., Wan, R.Z. & Liu, Z.P. Recent advances in the discovery of potent and selective HDAC6 inhibitors. *Eur J Med Chem* **143**, 1406-1418 (2018).
39. Spange, S., Wagner, T., Heinzl, T. & Kramer, O.H. Acetylation of non-histone proteins modulates cellular signalling at multiple levels. *Int J Biochem Cell Biol* **41**, 185-198 (2009).
40. Hodawadekar, S.C. & Marmorstein, R. Chemistry of acetyl transfer by histone modifying enzymes: structure, mechanism and implications for effector design. *Oncogene* **26**, 5528-5540 (2007).
41. Tamura, K., Stecher, G., Peterson, D., Filipski, A. & Kumar, S. MEGA6: Molecular Evolutionary Genetics Analysis version 6.0. *Mol Biol Evol* **30**, 2725-2729 (2013).
42. Witt, O., Deubzer, H.E., Milde, T. & Oehme, I. HDAC family: What are the cancer relevant targets? *Cancer Lett* **277**, 8-21 (2009).
43. Yang, F., Zhao, N., Ge, D. & Chen, Y. Next-generation of selective histone deacetylase inhibitors. *RSC Advances* **9**, 19571-19583 (2019).
44. Bagchi, R.A. & Weeks, K.L. Histone deacetylases in cardiovascular and metabolic diseases. *J Mol Cell Cardiol* **130**, 151-159 (2019).
45. Yang, X.J. & Seto, E. The Rpd3/Hda1 family of lysine deacetylases: from bacteria and yeast to mice and men. *Nat Rev Mol Cell Biol* **9**, 206-218 (2008).
46. Lopez, J.E., Sullivan, E.D. & Fierke, C.A. Metal-dependent Deacetylases: Cancer and Epigenetic Regulators. *ACS Chem Biol* **11**, 706-716 (2016).
47. McIntyre, R.L., Daniels, E.G., Molenaars, M., Houtkooper, R.H. & Janssens, G.E. From molecular promise to preclinical results: HDAC inhibitors in the race for healthy aging drugs. *EMBO Mol Med*, e9854 (2019).
48. Bolden, J.E., Peart, M.J. & Johnstone, R.W. Anticancer activities of histone deacetylase inhibitors. *Nat Rev Drug Discov* **5**, 769-784 (2006).
49. Haberland, M., Montgomery, R.L. & Olson, E.N. The many roles of histone deacetylases in development and physiology: implications for disease and therapy. *Nat Rev Genet* **10**, 32-42 (2009).
50. Falkenberg, K.J. & Johnstone, R.W. Histone deacetylases and their inhibitors in cancer, neurological diseases and immune disorders. *Nat Rev Drug Discov* **13**, 673-691 (2014).
51. Bennett, R.L. & Licht, J.D. Targeting Epigenetics in Cancer. *Annu Rev Pharmacol Toxicol* **58**, 187-207 (2018).
52. Davis, R., Peters, D.H. & McTavish, D. Valproic acid. A reappraisal of its pharmacological properties and clinical efficacy in epilepsy. *Drugs* **47**, 332-372 (1994).
53. Mann, B.S., Johnson, J.R., Cohen, M.H., Justice, R. & Pazdur, R. FDA approval summary: vorinostat for treatment of advanced primary cutaneous T-cell lymphoma. *Oncologist* **12**, 1247-1252 (2007).
54. Hughes, B. 2009 FDA drug approvals. *Nat Rev Drug Discov* **9**, 89-92 (2010).
55. Lee, H.Z., *et al.* FDA Approval: Belinostat for the Treatment of Patients with Relapsed or Refractory Peripheral T-cell Lymphoma. *Clin Cancer Res* **21**, 2666-2670 (2015).
56. Garnock-Jones, K.P. Panobinostat: first global approval. *Drugs* **75**, 695-704 (2015).
57. Eckschlager, T., Plch, J., Stiborova, M. & Hrabeta, J. Histone Deacetylase Inhibitors as Anticancer Drugs. *Int J Mol Sci* **18**(2017).
58. Bertrand, P. Inside HDAC with HDAC inhibitors. *Eur J Med Chem* **45**, 2095-2116 (2010).

59. Roche, J. & Bertrand, P. Inside HDACs with more selective HDAC inhibitors. *Eur J Med Chem* **121**, 451-483 (2016).
60. Finnin, M.S., *et al.* Structures of a histone deacetylase homologue bound to the TSA and SAHA inhibitors. *Nature* **401**, 188-193 (1999).
61. Whitehead, L., *et al.* Human HDAC isoform selectivity achieved via exploitation of the acetate release channel with structurally unique small molecule inhibitors. *Bioorg Med Chem* **19**, 4626-4634 (2011).
62. Zubia, A., *et al.* Identification of (1H)-pyrroles as histone deacetylase inhibitors with antitumoral activity. *Oncogene* **28**, 1477-1484 (2009).
63. Perez-Salvia, M., *et al.* In vitro and in vivo activity of a new small-molecule inhibitor of HDAC6 in mantle cell lymphoma. *Haematologica* **103**, e537-e540 (2018).
64. Marcaurrelle, L.A., *et al.* An aldol-based build/couple/pair strategy for the synthesis of medium- and large-sized rings: discovery of macrocyclic histone deacetylase inhibitors. *Journal of the American Chemical Society* **132**, 16962-16976 (2010).
65. Vickers, C.J., Olsen, C.A., Leman, L.J. & Ghadiri, M.R. Discovery of HDAC Inhibitors That Lack an Active Site Zn(2+)-Binding Functional Group. *ACS Med Chem Lett* **3**, 505-508 (2012).
66. Villadsen, J.S., *et al.* An azumamide C analogue without the zinc-binding functionality. *MedChemComm* **5**, 1849-1855 (2014).
67. Bauer, L. & Exner, O. The Chemistry of Hydroxamic Acids and N-Hydroxyimides. *Angewandte Chemie International Edition in English* **13**, 376-384 (1974).
68. Bugg, T. Hydroxamic Acids: A Unique Family of Chemicals with Multiple Biological Activities. Edited by Satya P. Gupta. *ChemBioChem* **15**, 2467-2467 (2014).
69. Gupta, S.P. QSAR studies on hydroxamic acids: a fascinating family of chemicals with a wide spectrum of activities. *Chem Rev* **115**, 6427-6490 (2015).
70. Marmion, Celine J., Griffith, D. & Nolan, Kevin B. Hydroxamic Acids – An Intriguing Family of Enzyme Inhibitors and Biomedical Ligands. *European Journal of Inorganic Chemistry* **2004**, 3003-3016 (2004).
71. Neilands, J.B. Hydroxamic acids in nature. *Science* **156**, 1443-1447 (1967).
72. Muri, E.M., Nieto, M.J., Sindelar, R.D. & Williamson, J.S. Hydroxamic acids as pharmacological agents. *Curr Med Chem* **9**, 1631-1653 (2002).
73. Tsuji, N., Kobayashi, M., Nagashima, K., Wakisaka, Y. & Koizumi, K. A new antifungal antibiotic, trichostatin. *J Antibiot (Tokyo)* **29**, 1-6 (1976).
74. El-Faham, A. & Albericio, F. Peptide coupling reagents, more than a letter soup. *Chem Rev* **111**, 6557-6602 (2011).
75. Sarojini, V., Cameron, A.J., Varnava, K.G., Denny, W.A. & Sanjayan, G. Cyclic Tetrapeptides from Nature and Design: A Review of Synthetic Methodologies, Structure, and Function. *Chem Rev* **119**, 10318-10359 (2019).
76. Lauffer, B.E., *et al.* Histone deacetylase (HDAC) inhibitor kinetic rate constants correlate with cellular histone acetylation but not transcription and cell viability. *The Journal of biological chemistry* **288**, 26926-26943 (2013).
77. Zhang, L., Zhang, J., Jiang, Q., Zhang, L. & Song, W. Zinc binding groups for histone deacetylase inhibitors. *J Enzyme Inhib Med Chem* **33**, 714-721 (2018).
78. Khan, N., *et al.* Determination of the class and isoform selectivity of small-molecule histone deacetylase inhibitors. *Biochem J* **409**, 581-589 (2008).

79. Connolly, R.M., Rudek, M.A. & Piekarz, R. Entinostat: a promising treatment option for patients with advanced breast cancer. *Future Oncol* **13**, 1137-1148 (2017).
80. Pauer, L.R., *et al.* Phase I study of oral CI-994 in combination with carboplatin and paclitaxel in the treatment of patients with advanced solid tumors. *Cancer Invest* **22**, 886-896 (2004).
81. Younes, A., *et al.* Mocetinostat for relapsed classical Hodgkin's lymphoma: an open-label, single-arm, phase 2 trial. *Lancet Oncol* **12**, 1222-1228 (2011).
82. Batlevi, C.L., *et al.* A phase 2 study of mocetinostat, a histone deacetylase inhibitor, in relapsed or refractory lymphoma. *Br J Haematol* **178**, 434-441 (2017).
83. Lu, Q., *et al.* Zn²⁺-chelating motif-tethered short-chain fatty acids as a novel class of histone deacetylase inhibitors. *J Med Chem* **47**, 467-474 (2004).
84. Tan, J., *et al.* The role of short-chain fatty acids in health and disease. *Adv Immunol* **121**, 91-119 (2014).
85. Furusawa, Y., *et al.* Commensal microbe-derived butyrate induces the differentiation of colonic regulatory T cells. *Nature* **504**, 446-450 (2013).
86. Koh, A., De Vadder, F., Kovatcheva-Datchary, P. & Backhed, F. From Dietary Fiber to Host Physiology: Short-Chain Fatty Acids as Key Bacterial Metabolites. *Cell* **165**, 1332-1345 (2016).
87. Arpaia, N., *et al.* Metabolites produced by commensal bacteria promote peripheral regulatory T-cell generation. *Nature* **504**, 451-455 (2013).
88. Smith, P.M., *et al.* The microbial metabolites, short-chain fatty acids, regulate colonic Treg cell homeostasis. *Science* **341**, 569-573 (2013).
89. Zagni, C., Floresta, G., Monciino, G. & Rescifina, A. The Search for Potent, Small-Molecule HDACIs in Cancer Treatment: A Decade After Vorinostat. *Med Res Rev* **37**, 1373-1428 (2017).
90. Mwakwari, S.C., *et al.* Non-peptide macrocyclic histone deacetylase inhibitors derived from tricyclic ketolide skeleton. *J Med Chem* **53**, 6100-6111 (2010).
91. Mwakwari, S.C., Patil, V., Guerrant, W. & Oyelere, A.K. Macrocyclic histone deacetylase inhibitors. *Curr Top Med Chem* **10**, 1423-1440 (2010).
92. Maolanon, A.R., Madsen, A.S. & Olsen, C.A. Innovative Strategies for Selective Inhibition of Histone Deacetylases. *Cell Chem Biol* **23**, 759-768 (2016).
93. Maolanon, A.R., Kristensen, H.M., Leman, L.J., Ghadiri, M.R. & Olsen, C.A. Natural and Synthetic Macrocyclic Inhibitors of the Histone Deacetylase Enzymes. *Chembiochem* **18**, 5-49 (2017).
94. Seidel, C., Schnekenburger, M., Dicato, M. & Diederich, M. Histone deacetylase modulators provided by Mother Nature. *Genes Nutr* **7**, 357-367 (2012).
95. Salvador, L.A. & Luesch, H. Discovery and mechanism of natural products as modulators of histone acetylation. *Curr Drug Targets* **13**, 1029-1047 (2012).
96. VanderMolen, K.M., McCulloch, W., Pearce, C.J. & Oberlies, N.H. Romidepsin (Istodax, NSC 630176, FR901228, FK228, depsipeptide): a natural product recently approved for cutaneous T-cell lymphoma. *J Antibiot (Tokyo)* **64**, 525-531 (2011).
97. Furumai, R., *et al.* FK228 (depsipeptide) as a natural prodrug that inhibits class I histone deacetylases. *Cancer research* **62**, 4916-4921 (2002).
98. Nepali, K., Sharma, S., Sharma, M., Bedi, P.M. & Dhar, K.L. Rational approaches, design strategies, structure activity relationship and mechanistic insights for anticancer hybrids. *Eur J Med Chem* **77**, 422-487 (2014).

99. Stazi, G., Fioravanti, R., Mai, A., Mattevi, A. & Valente, S. Histone deacetylases as an epigenetic pillar for the development of hybrid inhibitors in cancer. *Curr Opin Chem Biol* **50**, 89-100 (2019).
100. Hesham, H.M., Lasheen, D.S. & Abouzid, K.A.M. Chimeric HDAC inhibitors: Comprehensive review on the HDAC-based strategies developed to combat cancer. *Med Res Rev* **38**, 2058-2109 (2018).
101. Gediya, L.K., *et al.* Design, synthesis, and evaluation of novel mutual prodrugs (hybrid drugs) of all-trans-retinoic acid and histone deacetylase inhibitors with enhanced anticancer activities in breast and prostate cancer cells in vitro. *J Med Chem* **51**, 3895-3904 (2008).
102. Marin, J.J., *et al.* DNA interaction and cytostatic activity of the new liver organotropic complex of cisplatin with glycocholic acid: Bamet-R2. *Int J Cancer* **78**, 346-352 (1998).
103. Dominguez, M.F., *et al.* Low in vivo toxicity of a novel cisplatin-ursodeoxycholic derivative (Bamet-UD2) with enhanced cytostatic activity versus liver tumors. *J Pharmacol Exp Ther* **297**, 1106-1112 (2001).
104. Martinez-Diez, M.C., *et al.* Relationship between DNA-reactivity and cytostatic effect of two novel bile acid-platinum derivatives, Bamet-UD2 and Bamet-D3. *Anticancer Res* **20**, 3315-3321 (2000).
105. Pai, M.T., *et al.* Solution structure of the Ubp-M BUZ domain, a highly specific protein module that recognizes the C-terminal tail of free ubiquitin. *J Mol Biol* **370**, 290-302 (2007).
106. Kawaguchi, Y., *et al.* The deacetylase HDAC6 regulates aggresome formation and cell viability in response to misfolded protein stress. *Cell* **115**, 727-738 (2003).
107. Xie, Z. & Klionsky, D.J. Autophagosome formation: core machinery and adaptations. *Nat Cell Biol* **9**, 1102-1109 (2007).
108. Lee, J.Y., *et al.* HDAC6 controls autophagosome maturation essential for ubiquitin-selective quality-control autophagy. *EMBO J* **29**, 969-980 (2010).
109. Bjorkoy, G., *et al.* p62/SQSTM1 forms protein aggregates degraded by autophagy and has a protective effect on huntingtin-induced cell death. *The Journal of cell biology* **171**, 603-614 (2005).
110. Chin, L.S., Olzmann, J.A. & Li, L. Parkin-mediated ubiquitin signalling in aggresome formation and autophagy. *Biochem Soc Trans* **38**, 144-149 (2010).
111. Bertos, N.R., *et al.* Role of the tetradecapeptide repeat domain of human histone deacetylase 6 in cytoplasmic retention. *The Journal of biological chemistry* **279**, 48246-48254 (2004).
112. Yang, P.H., Zhang, L., Zhang, Y.J., Zhang, J. & Xu, W.F. HDAC6: physiological function and its selective inhibitors for cancer treatment. *Drug Discov Ther* **7**, 233-242 (2013).
113. Wang, S.H., Li, N., Wei, Y., Li, Q.R. & Yu, Z.P. beta-catenin deacetylation is essential for WNT-induced proliferation of breast cancer cells. *Mol Med Rep* **9**, 973-978 (2014).
114. Hubbert, C., *et al.* HDAC6 is a microtubule-associated deacetylase. *Nature* **417**, 455-458 (2002).
115. Zhang, X., *et al.* HDAC6 modulates cell motility by altering the acetylation level of cortactin. *Mol Cell* **27**, 197-213 (2007).
116. Kovacs, J.J., *et al.* HDAC6 regulates Hsp90 acetylation and chaperone-dependent activation of glucocorticoid receptor. *Mol Cell* **18**, 601-607 (2005).

117. Lernoux, M., Schnekenburger, M., Dicato, M. & Diederich, M. Anti-cancer effects of naturally derived compounds targeting histone deacetylase 6-related pathways. *Pharmacol Res* **129**, 337-356 (2018).
118. Miyake, Y., *et al.* Structural insights into HDAC6 tubulin deacetylation and its selective inhibition. *Nat Chem Biol* **12**, 748-754 (2016).
119. Hai, Y. & Christianson, D.W. Histone deacetylase 6 structure and molecular basis of catalysis and inhibition. *Nat Chem Biol* **12**, 741-747 (2016).
120. Zhao, Z., Xu, H. & Gong, W. Histone deacetylase 6 (HDAC6) is an independent deacetylase for alpha-tubulin. *Protein Pept Lett* **17**, 555-558 (2010).
121. Wang, Z., *et al.* HDAC6 promotes cell proliferation and confers resistance to temozolomide in glioblastoma. *Cancer Lett* **379**, 134-142 (2016).
122. Valenzuela-Fernandez, A., Cabrero, J.R., Serrador, J.M. & Sanchez-Madrid, F. HDAC6: a key regulator of cytoskeleton, cell migration and cell-cell interactions. *Trends Cell Biol* **18**, 291-297 (2008).
123. Saji, S., *et al.* Significance of HDAC6 regulation via estrogen signaling for cell motility and prognosis in estrogen receptor-positive breast cancer. *Oncogene* **24**, 4531-4539 (2005).
124. Zilberman, Y., *et al.* Regulation of microtubule dynamics by inhibition of the tubulin deacetylase HDAC6. *J Cell Sci* **122**, 3531-3541 (2009).
125. Moreno-Gonzalo, O., Mayor, F., Jr. & Sanchez-Madrid, F. HDAC6 at Crossroads of Infection and Innate Immunity. *Trends Immunol* **39**, 591-595 (2018).
126. Pandey, U.B., *et al.* HDAC6 rescues neurodegeneration and provides an essential link between autophagy and the UPS. *Nature* **447**, 859-863 (2007).
127. Seidel, C., Schnekenburger, M., Dicato, M. & Diederich, M. Histone deacetylase 6 in health and disease. *Epigenomics* **7**, 103-118 (2015).
128. Haggarty, S.J., Koeller, K.M., Wong, J.C., Grozinger, C.M. & Schreiber, S.L. Domain-selective small-molecule inhibitor of histone deacetylase 6 (HDAC6)-mediated tubulin deacetylation. *Proceedings of the National Academy of Sciences of the United States of America* **100**, 4389-4394 (2003).
129. Butler, K.V., *et al.* Rational design and simple chemistry yield a superior, neuroprotective HDAC6 inhibitor, tubastatin A. *Journal of the American Chemical Society* **132**, 10842-10846 (2010).
130. Santo, L., *et al.* Preclinical activity, pharmacodynamic, and pharmacokinetic properties of a selective HDAC6 inhibitor, ACY-1215, in combination with bortezomib in multiple myeloma. *Blood* **119**, 2579-2589 (2012).
131. Cossio, F.P., *et al.* New histone deacetylase inhibitors based simultaneously on trisubstituted 1H-pyrroles and aromatic and heteroaromatic spacers. WO2011039353A1. (ed. Ikerchem, S.L., Universidad Del País Vasco - Euskal Herriko Unibertsitatea (UPV-EHU)) (2011).
132. Dompierre, J.P., *et al.* Histone deacetylase 6 inhibition compensates for the transport deficit in Huntington's disease by increasing tubulin acetylation. *J Neurosci* **27**, 3571-3583 (2007).
133. Govindarajan, N., *et al.* Reducing HDAC6 ameliorates cognitive deficits in a mouse model for Alzheimer's disease. *EMBO Mol Med* **5**, 52-63 (2013).
134. Simoes-Pires, C., *et al.* HDAC6 as a target for neurodegenerative diseases: what makes it different from the other HDACs? *Mol Neurodegener* **8**, 7 (2013).
135. Li, T., *et al.* Histone deacetylase 6 in cancer. *J Hematol Oncol* **11**, 111 (2018).
136. Mottamal, M., Zheng, S., Huang, T.L. & Wang, G. Histone deacetylase inhibitors in clinical studies as templates for new anticancer agents. *Molecules* **20**, 3898-3941 (2015).

137. Mariman, E.C., *et al.* The cilium: a cellular antenna with an influence on obesity risk. *Br J Nutr* **116**, 576-592 (2016).
138. Goetz, S.C. & Anderson, K.V. The primary cilium: a signalling centre during vertebrate development. *Nat Rev Genet* **11**, 331-344 (2010).
139. Wheway, G., Nazlamova, L. & Hancock, J.T. Signaling through the Primary Cilium. *Front Cell Dev Biol* **6**, 8 (2018).
140. Wheatley, D.N., Wang, A.M. & Strugnell, G.E. Expression of primary cilia in mammalian cells. *Cell Biol Int* **20**, 73-81 (1996).
141. Pala, R., Alomari, N. & Nauli, S.M. Primary Cilium-Dependent Signaling Mechanisms. *Int J Mol Sci* **18**(2017).
142. Ford, M.J., *et al.* A Cell/Cilia Cycle Biosensor for Single-Cell Kinetics Reveals Persistence of Cilia after G1/S Transition Is a General Property in Cells and Mice. *Dev Cell* **47**, 509-523 e505 (2018).
143. Plotnikova, O.V., Pugacheva, E.N. & Golemis, E.A. Primary cilia and the cell cycle. *Methods Cell Biol* **94**, 137-160 (2009).
144. Satir, P., Pedersen, L.B. & Christensen, S.T. The primary cilium at a glance. *J Cell Sci* **123**, 499-503 (2010).
145. Ainsworth, C. Cilia: tails of the unexpected. *Nature* **448**, 638-641 (2007).
146. Song, Y. & Brady, S.T. Post-translational modifications of tubulin: pathways to functional diversity of microtubules. *Trends Cell Biol* **25**, 125-136 (2015).
147. Gaertig, J. & Wloga, D. Ciliary tubulin and its post-translational modifications. *Curr Top Dev Biol* **85**, 83-113 (2008).
148. Shida, T., Cueva, J.G., Xu, Z., Goodman, M.B. & Nachury, M.V. The major alpha-tubulin K40 acetyltransferase alphaTAT1 promotes rapid ciliogenesis and efficient mechanosensation. *Proceedings of the National Academy of Sciences of the United States of America* **107**, 21517-21522 (2010).
149. Magiera, M.M. & Janke, C. Post-translational modifications of tubulin. *Curr Biol* **24**, R351-354 (2014).
150. Szyk, A., *et al.* Molecular basis for age-dependent microtubule acetylation by tubulin acetyltransferase. *Cell* **157**, 1405-1415 (2014).
151. Yang, Y., *et al.* CYLD mediates ciliogenesis in multiple organs by deubiquitinating Cep70 and inactivating HDAC6. *Cell Res* **24**, 1342-1353 (2014).
152. Ran, J., Yang, Y., Li, D., Liu, M. & Zhou, J. Deacetylation of alpha-tubulin and cortactin is required for HDAC6 to trigger ciliary disassembly. *Sci Rep* **5**, 12917 (2015).
153. Pugacheva, E.N., Jablonski, S.A., Hartman, T.R., Henske, E.P. & Golemis, E.A. HEF1-dependent Aurora A activation induces disassembly of the primary cilium. *Cell* **129**, 1351-1363 (2007).
154. Thompson, C.L., Chapple, J.P. & Knight, M.M. Primary cilia disassembly down-regulates mechanosensitive hedgehog signalling: a feedback mechanism controlling ADAMTS-5 expression in chondrocytes. *Osteoarthritis Cartilage* **22**, 490-498 (2014).
155. Wang, G., *et al.* PCM1 recruits Plk1 to the pericentriolar matrix to promote primary cilia disassembly before mitotic entry. *J Cell Sci* **126**, 1355-1365 (2013).
156. Ehnert, S., *et al.* TGF-beta1 impairs mechanosensation of human osteoblasts via HDAC6-mediated shortening and distortion of primary cilia. *J Mol Med (Berl)* **95**, 653-663 (2017).
157. Bangs, F.K., Schrode, N., Hadjantonakis, A.K. & Anderson, K.V. Lineage specificity of primary cilia in the mouse embryo. *Nat Cell Biol* **17**, 113-122 (2015).

158. Tabibian, J.H., Masyuk, A.I., Masyuk, T.V., O'Hara, S.P. & LaRusso, N.F. Physiology of cholangiocytes. *Compr Physiol* **3**, 541-565 (2013).
159. Banales, J.M., *et al.* Cholangiocyte pathobiology. *Nature reviews. Gastroenterology & hepatology* **16**, 269-281 (2019).
160. Masyuk, A.I., *et al.* Cholangiocyte cilia detect changes in luminal fluid flow and transmit them into intracellular Ca²⁺ and cAMP signaling. *Gastroenterology* **131**, 911-920 (2006).
161. Larusso, N.F. & Masyuk, T.V. The role of cilia in the regulation of bile flow. *Dig Dis* **29**, 6-12 (2011).
162. Gradilone, S.A., *et al.* Cholangiocyte cilia express TRPV4 and detect changes in luminal tonicity inducing bicarbonate secretion. *Proceedings of the National Academy of Sciences of the United States of America* **104**, 19138-19143 (2007).
163. Hohenester, S., *et al.* A biliary HCO₃⁻ umbrella constitutes a protective mechanism against bile acid-induced injury in human cholangiocytes. *Hepatology* **55**, 173-183 (2012).
164. Banales, J.M., Prieto, J. & Medina, J.F. Cholangiocyte anion exchange and biliary bicarbonate excretion. *World J Gastroenterol* **12**, 3496-3511 (2006).
165. Masyuk, A.I., *et al.* Biliary exosomes influence cholangiocyte regulatory mechanisms and proliferation through interaction with primary cilia. *American journal of physiology. Gastrointestinal and liver physiology* **299**, G990-999 (2010).
166. Mansini, A.P., *et al.* The cholangiocyte primary cilium in health and disease. *Biochim Biophys Acta Mol Basis Dis* **1864**, 1245-1253 (2018).
167. Li, Y., Zhang, X., Polakiewicz, R.D., Yao, T.P. & Comb, M.J. HDAC6 is required for epidermal growth factor-induced beta-catenin nuclear localization. *The Journal of biological chemistry* **283**, 12686-12690 (2008).
168. Li, X., Qi, N., Li, L., Wu, M. & Mei, C. Cytosolic HDAC6 is accumulated in cystic kidneys. *Kidney international* **90**, 705 (2016).
169. Yanda, M.K., Liu, Q., Cebotaru, V., Guggino, W.B. & Cebotaru, L. Histone deacetylase 6 inhibition reduces cysts by decreasing cAMP and Ca(2+) in knock-out mouse models of polycystic kidney disease. *The Journal of biological chemistry* **292**, 17897-17908 (2017).
170. Yanda, M.K., Liu, Q. & Cebotaru, L. An inhibitor of histone deacetylase 6 activity, ACY-1215, reduces cAMP and cyst growth in polycystic kidney disease. *American journal of physiology. Renal physiology* **313**, F997-F1004 (2017).
171. Cebotaru, L., *et al.* Inhibition of histone deacetylase 6 activity reduces cyst growth in polycystic kidney disease. *Kidney international* **90**, 90-99 (2016).
172. Gradilone, S.A., *et al.* HDAC6 inhibition restores ciliary expression and decreases tumor growth. *Cancer research* **73**, 2259-2270 (2013).
173. Mansini, A.P., Peixoto, E., Jin, S., Richard, S. & Gradilone, S.A. The Chemosensory Function of Primary Cilia Regulates Cholangiocyte Migration, Invasion, and Tumor Growth. *Hepatology* **69**, 1582-1598 (2019).
174. Mansini, A.P., *et al.* MicroRNA (miR)-433 and miR-22 dysregulations induce histone-deacetylase-6 overexpression and ciliary loss in cholangiocarcinoma. *Hepatology* **68**, 561-573 (2018).
175. Carpino, G., *et al.* Neoplastic Transformation of the Peribiliary Stem Cell Niche in Cholangiocarcinoma Arisen in Primary Sclerosing Cholangitis. *Hepatology* **69**, 622-638 (2019).

176. Erice, O., *et al.* Differential effects of FXR or TGR5 activation in cholangiocarcinoma progression. *Biochim Biophys Acta Mol Basis Dis* **1864**, 1335-1344 (2018).
177. Masyuk, T.V., Masyuk, A.I. & LaRusso, N.F. TGR5 in the Cholangiociliopathies. *Dig Dis* **33**, 420-425 (2015).
178. Cheng, K., Li, S. & Liao, C. Progress in the Discovery of Macrocyclic Histone Deacetylase Inhibitors for the Treatment of Cancer. *Curr Med Chem* **24**, 4166-4179 (2017).
179. Oyelere, A.K., *et al.* Non-peptide macrocyclic histone deacetylase inhibitors. *J Med Chem* **52**, 456-468 (2009).
180. Zou, H., Wu, Y., Navre, M. & Sang, B.C. Characterization of the two catalytic domains in histone deacetylase 6. *Biochem Biophys Res Commun* **341**, 45-50 (2006).
181. Jacobson, M.P., *et al.* A hierarchical approach to all-atom protein loop prediction. *Proteins* **55**, 351-367 (2004).
182. Jacobson, M.P., Friesner, R.A., Xiang, Z. & Honig, B. On the role of the crystal environment in determining protein side-chain conformations. *J Mol Biol* **320**, 597-608 (2002).
183. Mason, S.B., *et al.* Disease stage characterization of hepatorenal fibrocystic pathology in the PCK rat model of ARPKD. *Anatomical record* **293**, 1279-1288 (2010).
184. Masyuk, T.V., *et al.* Biliary dysgenesis in the PCK rat, an orthologous model of autosomal recessive polycystic kidney disease. *The American journal of pathology* **165**, 1719-1730 (2004).
185. Quarmby, L.M. & Parker, J.D. Cilia and the cell cycle? *The Journal of cell biology* **169**, 707-710 (2005).
186. Mansini, A.P., *et al.* The cholangiocyte primary cilium in health and disease. *Biochimica et biophysica acta* **1864**, 1245-1253 (2018).
187. Dallavalle, S., Pisano, C. & Zunino, F. Development and therapeutic impact of HDAC6-selective inhibitors. *Biochemical pharmacology* **84**, 756-765 (2012).
188. Shah, M.H., *et al.* Cardiotoxicity of histone deacetylase inhibitor depsipeptide in patients with metastatic neuroendocrine tumors. *Clin Cancer Res* **12**, 3997-4003 (2006).
189. Lane, A.A. & Chabner, B.A. Histone deacetylase inhibitors in cancer therapy. *J Clin Oncol* **27**, 5459-5468 (2009).
190. Suraweera, A., O'Byrne, K.J. & Richard, D.J. Combination Therapy With Histone Deacetylase Inhibitors (HDACi) for the Treatment of Cancer: Achieving the Full Therapeutic Potential of HDACi. *Front Oncol* **8**, 92 (2018).
191. Hofmann, A.F. Pharmacology of ursodeoxycholic acid, an enterohepatic drug. *Scand J Gastroenterol Suppl* **204**, 1-15 (1994).
192. Hofmann, A.F. & Hagey, L.R. Bile acids: chemistry, pathochemistry, biology, pathobiology, and therapeutics. *Cell Mol Life Sci* **65**, 2461-2483 (2008).
193. Chiang, J.Y.L. Bile acid metabolism and signaling in liver disease and therapy. *Liver Res* **1**, 3-9 (2017).
194. Schafer, S., *et al.* Pyridylalanine-containing hydroxamic acids as selective HDAC6 inhibitors. *ChemMedChem* **4**, 283-290 (2009).
195. Bordoli, L., *et al.* Protein structure homology modeling using SWISS-MODEL workspace. *Nat Protoc* **4**, 1-13 (2009).
196. Pan, J. & Snell, W. The primary cilium: keeper of the key to cell division. *Cell* **129**, 1255-1257 (2007).

197. Masyuk, T.V., Masyuk, A.I. & LaRusso, N.F. Therapeutic Targets in Polycystic Liver Disease. *Curr Drug Targets* **18**, 950-957 (2017).
198. Kanno, K., *et al.* Overexpression of histone deacetylase 6 contributes to accelerated migration and invasion activity of hepatocellular carcinoma cells. *Oncology reports* **28**, 867-873 (2012).
199. Ding, G., *et al.* HDAC6 promotes hepatocellular carcinoma progression by inhibiting P53 transcriptional activity. *FEBS letters* **587**, 880-886 (2013).
200. Zhang, W.B., *et al.* Histone deacetylase 6 inhibitor ACY-1215 protects against experimental acute liver failure by regulating the TLR4-MAPK/NF-kappaB pathway. *Biomedicine & pharmacotherapy = Biomedecine & pharmacotherapie* **97**, 818-824 (2018).
201. Li, D., *et al.* Histone deacetylase 6 and cytoplasmic linker protein 170 function together to regulate the motility of pancreatic cancer cells. *Protein Cell* **5**, 214-223 (2014).
202. Arlt, A., Muerkoster, S.S. & Schafer, H. Targeting apoptosis pathways in pancreatic cancer. *Cancer Lett* **332**, 346-358 (2013).
203. Kaliszczak, M., *et al.* A novel small molecule hydroxamate preferentially inhibits HDAC6 activity and tumour growth. *Br J Cancer* **108**, 342-350 (2013).
204. Sastry, G.M., Adzhigirey, M., Day, T., Annabhimoju, R. & Sherman, W. Protein and ligand preparation: parameters, protocols, and influence on virtual screening enrichments. *J Comput Aided Mol Des* **27**, 221-234 (2013).
205. Friesner, R.A., *et al.* Glide: a new approach for rapid, accurate docking and scoring. 1. Method and assessment of docking accuracy. *J Med Chem* **47**, 1739-1749 (2004).
206. Halgren, T.A., *et al.* Glide: a new approach for rapid, accurate docking and scoring. 2. Enrichment factors in database screening. *J Med Chem* **47**, 1750-1759 (2004).
207. Friesner, R.A., *et al.* Extra precision glide: docking and scoring incorporating a model of hydrophobic enclosure for protein-ligand complexes. *J Med Chem* **49**, 6177-6196 (2006).
208. Nytofte, N.S., *et al.* A homozygous nonsense mutation (c.214C->A) in the biliverdin reductase alpha gene (BLVRA) results in accumulation of biliverdin during episodes of cholestasis. *J Med Genet* **48**, 219-225 (2011).
209. Steiner, C., von Eckardstein, A. & Rentsch, K.M. Quantification of the 15 major human bile acids and their precursor 7alpha-hydroxy-4-cholesten-3-one in serum by liquid chromatography-tandem mass spectrometry. *J Chromatogr B Analyt Technol Biomed Life Sci* **878**, 2870-2880 (2010).
210. Lozano, E., *et al.* Enhanced antitumour drug delivery to cholangiocarcinoma through the apical sodium-dependent bile acid transporter (ASBT). *J Control Release* **216**, 93-102 (2015).
211. Al-Abdulla, R., *et al.* Epigenetic events involved in organic cation transporter 1-dependent impaired response of hepatocellular carcinoma to sorafenib. *Br J Pharmacol* **176**, 787-800 (2019).
212. Markwell, M.A., Haas, S.M., Bieber, L.L. & Tolbert, N.E. A modification of the Lowry procedure to simplify protein determination in membrane and lipoprotein samples. *Anal Biochem* **87**, 206-210 (1978).
213. Schneider, C.A., Rasband, W.S. & Eliceiri, K.W. NIH Image to ImageJ: 25 years of image analysis. *Nat Methods* **9**, 671-675 (2012).

214. Masyuk, T.V., Masyuk, A.I., Torres, V.E., Harris, P.C. & Larusso, N.F. Octreotide inhibits hepatic cystogenesis in a rodent model of polycystic liver disease by reducing cholangiocyte adenosine 3',5'-cyclic monophosphate. *Gastroenterology* **132**, 1104-1116 (2007).